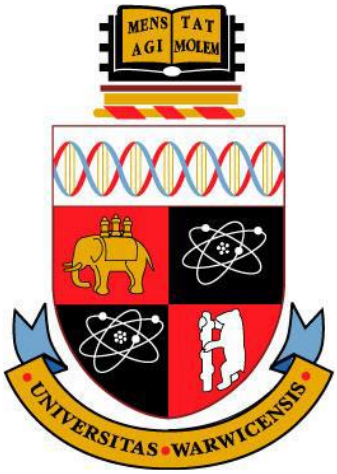

Enzymology and Structural Enzymology of Dye-Decolorizing Peroxidases and a Primary Study of Encapsulin

Rahman Rahman Pour

A thesis submitted in partial fulfilment of the requirements for the degree of

Doctor of Philosophy in Chemistry

THE UNIVERSITY OF WARWICK

University of Warwick
Department of Chemistry

March 2015

Supervisor:

Professor Timothy D.H. Bugg

I. Content

II. List of Figures

III. List of Tables

IV. Abbreviations

ABTS	2,2′-azino-bis(3-ethylthiazoline-6- sulfonate)
Ala	Alanine
APS	Ammonium persulfate
AQs	Anthraquinones
Arg	Arginine
Asp	Aspartate
Asn	Asparagine
A. auricula-judae	*Auricularia auricula-judae*
AU	Arbitrary units
BMC	Bacterial Microcompartment
BLAST	Basic local alignment search tool
BGP	Barley grain peroxidase
B. thetaiotaomicron	*Bacteroides thetaiotaomicron*
B. adusta	*Bjerkandera adusta*
BME	2-mercaptoethanol
Cys	Cysteine
CDE	Chlorite dismutases
Da	Dalton
DMP	2,6-dimethoxyphenol
° C	Degrees Celsius
DMSO	Dimethyl sulfoxide
DNA	Deoxyribonucleic acid
DyP	Dye-decolorizing peroxidases

DCP	2,4-dichlorophenol
dNTPs	Deoxynucleotide triphosphates
E	Enzyme
E. coli	*Escherichia coli*
EDTA	Ethylenediaminetetraacetic acid
Eut	Ethanolamine utilization
ESI	Electrospray ionisation
EPR	Electron paramagnetic resonance spectroscopy
EC	Enzyme commision
Ɛ	Extinction coefficient
FPLC	Fast protein liquid chromatograph
FLP	Ferritin-like protein
Glu	Glutamate
GC-MS	Gas chromatography–mass spectrometry
His	Histidine
HPLC	High pressure liquid chromatography
HRMS	High resolution mass spectrometry
HRP	Horseradish peroxidase
IPTG	Isopropyl β-D-1-thiogalactopyranoside
k_{cat}	Turnover number
K_M	Michaelis constant
kb	Kilo base
LB	Luria broth
LiP	Lignin peroxidase
LC-MS	Liquid chromatography mass spectrometry
LRET	Long-range electron transfer
Leu	Leucine

MnP	Manganese peroxidase
m/z	Mass to charge ratio
mV	Millivolt
MS	Mass spectrometry
Mbp	Mega base pair
MeOH	Methanol
MOPS	3-(N-morpholino)propanesulfonic acid
Ni-NTA	Nickel-Nitrilotriacetic acid
NoP	Novel peroxidase
N-His_6	Hexa-histidine
OD	Optical density
PDB	Protein Data Bank
PBS	Phosphate buffered saline
PCR	Polymerase chain reaction
P. chrysosporium	*Phanerochaete chrysosporium*
pKa	Acid dissociation constant
PMSF	Phenylmethanesulfonylfluoride
Pro	Proline
Pdu	Propanediol utilization
Phe	Phenylalanine
P. fluorescens	*Pseudomonas fluorescens*
RB4	Reactive Blue 4
RB5	Reactive Blue 5
RNA	Ribonucleic acid
R. jostii RHA1	Rhodococcus jostii Rha1
RMSD	Root-mean-square deviation
RubisCO	Ribulose 1, 5-bisphosphate carboxylase/oxygenase

S. enterica	*Salmonella enterica*
S. oneidensis	*Shewanella oneidensis*
$NaBH_4$	Sodium borohydride
NaOH	Sodium hydroxide
SDS	Sodium dodecyl sulfate
SDS-PAGE	Sodium dodecyl sulphate polyacrylamide gel electrophoresi
Trp	Tryptophan
TBE	Tris-borate-EDTA
TEMED	Tetramethylethylenediamine
T. fusca	*Thermomonaspora fusca*
T. maritima	*Thermotoga maritima*
TEV	Tobacco Etch Virus
Tyr	Tyrosine
UV	Ultraviolet
UV-Vis	Ultraviolet-visible
Val	Valine
VP	Versatile peroxidise

V. Acknowledgements

First and foremost I would like to thank my supervisor, Prof. Tim Bugg, for all his help, enthusiasm and encouragement and for giving me the opportunity to change my path in life. I would also like to thank Tim for all the opportunities that he has given me both during my PhD and during my visiting fellow, for keeping me on track and reassuring me when things did not go to plan.

I would also like to offer my thanks to the many members of the Bugg group who have helped me over the years, both past and present. Special mentions must go to Dr Liz Hardiman for being an excellent role model and teaching me most of the things I know about molecular biology, Dr Paul Sainsbury and Dr Peter Harrison for their friendship and helpful advices. Thanks to Goran and Jo for helping me in chemistry and keeping me safe and sane in chemistry lab! Special Thanks to Anne Smith for keeping the place running.

Thanks also to Prof Vilmos Fulop and Dr Dean Rea at Life science for all their help, suggestions and for teaching me the practical protein crystallography. The crystallography work done here would not have been possible without them.

I would like to thank my parents Kazem and Tahereh for all their love and support during over the years and for their faith in me and allowing me to be as ambitious as I wanted. Finally, and most importantly, I would like to thank my wife Shirin who brought me so much happiness in life and without her support, encouragement, quiet patience and unwavering love, this PhD would not have been possible.

VI. Declaration

The work presented herein is my own work and has not been submitted for a degree at another university. All experimental work has been performed by the author in the Department of Chemistry at the University of Warwick, between 2011 and 2015.

Solving the structure of TfuDyP, presented in Chapter 3 was carried out by Prof Vilmos Fulop and Dr Dean Rea at Life science, University of Warwick.

The gene deletion strain *R. jostii* RHA1 Δ encapsulin, used on work presented in chapter 4, was constructed by R. Singh and L. Eltis at Department of Microbiology and Immunology, University of British Columbia.

Rahman Rahman Pour

VII. Abstract

The aim of this project is to provide a detailed comparative study in enzymology of dye-decolorising peroxidases, DyP, from *Pseudomonas fluorescens* and from *Thermobifida fusca*, a thermophile bacterium. Another objective is a primary study of encapsulin, a recently discovered icosahedral nanocompartment protein from *Rhodococcus jostii Rha1*. Three peroxidase genes from *P. fluorescens* and one from *T. fusca* were cloned, expressed, and their products were purified and the enzymes kinetically characterized with different substrates, lignin model compounds and lignocellulose. In addition, encapsulin has been purified, its assembly/disassembly under different pH conditions was studied and finally, its presence or absence in the extracellular fraction of *R. jostii* investigated.

DyP type peroxidases from Gram-positive bacteria have been studied recently and showed oxidation activity toward Mn (II) and lignin model compounds. Gram-negative pseudomonads, also show activity for lignin oxidation and contain DyP-type peroxidase genes. *P. fluorescens* Pf-5 contains three DyP-type peroxidases (35, 40 and 47 kDa). In this study each of them was overexpressed in *Escherichia coli*, purified, and characterised by different substrates, Kraft lignin and lignocellulose. Each of the aforementioned enzymes shows activity for oxidation of most of the substrates, but the 35 kDa DyP1B and 40 kDa DyP2B enzymes show activity for oxidation of Mn (II). Only in the presence of Mn (II) and hydrogen peroxide, incubation of finely powdered lignocellulose with DyP1B leads to the release of a low molecular weight lignin fragment that was identified by mass spectrometry as a β-aryl ether lignin dimer that contains one G unit and one H unit bearing a benzylic ketone. A mechanism for releasing of the β-aryl ether lignin dimer fragment from the lignin molecule via oxidation is proposed.

A DyP-type peroxidase enzyme from the thermophilic cellulose degrader *Thermobifida fusca* was investigated for its catalytic ability for lignin oxidation. TfuDyP was found to oxidise a β-aryl ether lignin model compound, forming an oxidised tetramer. A crystal structure of TfuDyP was determined, to 1.7 Å resolution, which was found to contain a diatomic oxygen ligand bound to the heme centre, hydrogen-bonded to active site residues Asp-203 and Arg-315. For three amino acid residues present in distal heme pocket, site directed mutagenesis was performed and the effect of each mutation on enzyme activity was measured by three different substrates.

Recently DyPB peroxidase from *Rhodococcus jostii* RHA1 has been recognised as a bacterial lignin peroxidase enzyme. The *dypB* gene is next to a gene that encodes an encapsulin protein that previously was shown in *Thermotoga maritima* to assemble and form into a nano-compartment comprised of 60-subunits. DyPB protein contains a C-terminal sequence motif that is supposed to lead the protein to the encapsulin nanocompartment. In this study, *R. jostii* RHA1 *encapsulin* gene was overexpressed in *R. jostii* RHA1, and the encapsulin protein was extracted as a high molecular weight native assembly (Mr $>10^6$ kDa). It was shown that by treatment of the purified nanocompartment at pH 3.0, it is able to be denatured to form a low molecular weight species and most importantly it is able to be re-assembled to form the native nanocompartment at pH 7.0. Dynamic light scattering showed that DyPB peroxidase *in vitro* could be assembled with encapsulin in a monomeric state to form an assembly of encapsulated DyPB in similar size and shape compared to the encapsulin-only nanocompartment. By using a nitrated lignin UV-Vis assay method, it was shown that the assembled complex of DyPB-encapsulin exhibited enhanced lignin degradation activity per mg DyPB present, compared with native DyPB. The stoichiometry of encapsulin/μmol DyPB in the assembled complex was measured, 8.6 mol encapsulin/mol DyPB, that was comparable to the predicted value of 10 obtained from the crystal structure.

Chapter One

Introduction

1.1 Lignocellulose

Cellulose is the most abundant ingredient of lignocellulose, representing over 50% of all woody biomass [1]. The other polysaccharide component of lignocellulose is hemicellulose, a polymer comprised of different five carbon sugar (arabinose and xylose), and six carbon sugar (glucose, galactose, mannose) (Fig. 1.1).

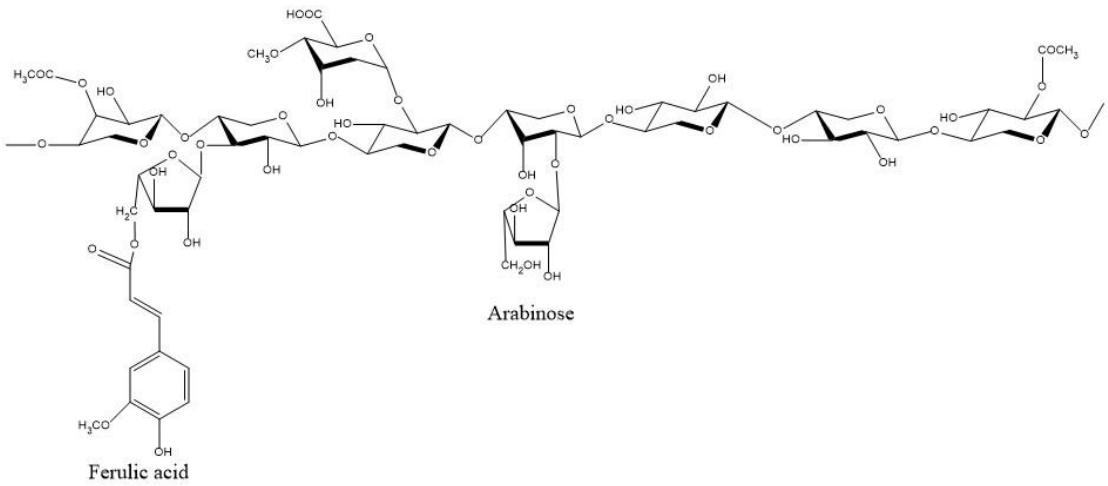

Figure 1.1 – Structure of hemicellulose, comprised of five-carbon sugar and six-carbon sugar

The other part of lignocellulose is lignin; lignin is one of the primary components of plant biomass and comprises 15-30% of its mass [2]. Lignin is a complex structural polymer [3] whose characteristics are high molecular weight, insolubility and lack of stereo-regularity, offering high resistance towards microbial degradation (Fig. 1.2). Lignin is biosynthesised from the phenylpropanoids ρ-coumaryl alcohol, coniferyl alcohol and sinapyl alcohol. These mentioned units, known as monolignols, are connected together by radical-radical coupling reactions [4], [5] (Fig. 1.3).

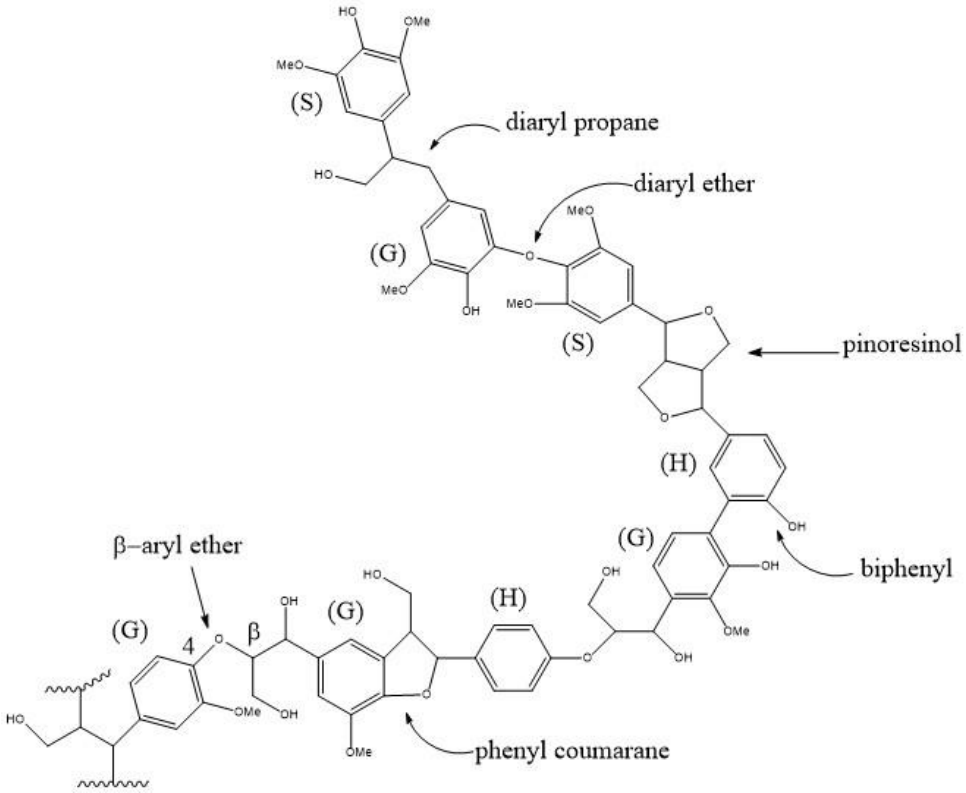

Figure 1.2 - The hypothetical chemical structure of a section of lignin

Polymerisation of these monolignols starts with an enzymatic dehydrogenation reaction, catalysed by peroxidases or laccases that catalyse the production of phenoxy radicals and leads to a dimerisation of two individual units or the addition of one unit to a growing polymeric lignin. This process makes a heterogeneous complex molecular structure that can

then be characterised by the number of guaiacyl (G), syringyl (S) and *p*-hydroxyphenyl (H) units derived from the three main monolignols. Different plant family and species show different polydispersity and contribution of three monolignols in the final lignin structure. For example, grasses have a mixture of G and H, hardwood trees have G and S units, while softwoods have mostly G units [6].

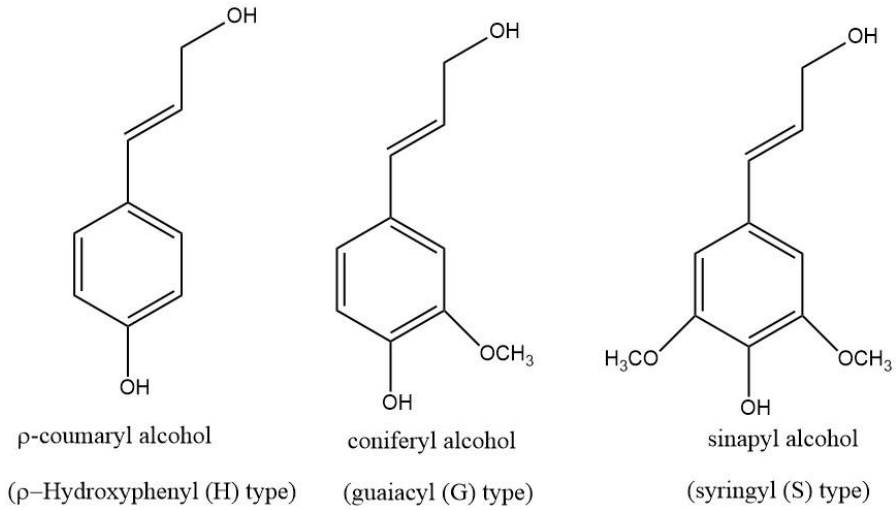

Figure 1.3 - The three monolignols, phenylpropanoids p-coumaryl alcohol, coniferyl alcohol and sinapyl alcohol are building blocks for H, G and S type lignin respectively

These intricate linkage patterns make the lignin a complex, recalcitrant and interesting polymer that can be seen as a potential source of renewable aromatic chemicals.

1.1.2 Kraft lignin

For production of this type of the extracted lignin from lignocellulose, sodium hydroxide and sodium sulphide (Na_2S) are cooked with the wood at 160 °C to 190 °C for two hours [7]. The main lignin degradation reactions that occur during the kraft lignin production involve cleavage of α-aryl ether and β-aryl ether bonds [8].

1.1.3 Organosolv lignin

The other refined form of lignin is produced from lignocellulose by the Organosolv process. In this process, lignocellulose is heated at 180 ℃ in an aqueous organic solvent environment, such as water/ ethanol [9]. The produced organosolv lignin keeps a high proportion of the acid-sensitive -O-4 (aryl ether) linkages that are present in native lignin [10].

1.2 Enzymatic breakdown of lignin

Lignin modification and degradation by basidiomycetes is the key step in environmental lignocellulose decay. In this section, enzymes and mechanisms involved in lignin attack by basidiomycetes are described below. Degradation of lignin by fungi is an oxidative and non-specific process, which decreases the methoxy, phenolic, and aliphatic content of the lignin molecule, and cleaves aromatic rings and generates new carbonyl groups [11, 12]. White-rot basidiomycetes are the most frequent wood-rotting organisms and because of their ability to degrade lignin giving rise to cellulose- enriched white material.

Brown-rot fungi develop mostly on softwoods and represent only 7% of wood-rotting basidiomycetes. They can also degrade wood polysaccharides after only a partial modification of lignin that results in a brown material consisting of oxidized lignin that provides a significant source of aromatic compounds in forest soils [13]. Lignin is degraded to a lesser extent by brown-rot fungi [14].

Several types of extracellular oxidative enzymes are produced by white-rot fungi. These enzymes are resposible for the degradation of lignin in the plant cell wall. Laccases and high redox potential peroxidases such as lignin peroxidase, manganese peroxidase, and

versatile peroxidase are in the first line of attack to the lignin molecules [15]. Studies have shown that the production of these enzymes is a response to nutrient depletion [15].

Both the lignin peroxidase (LiP) and manganese peroxidase (MnP) were purified in the mid-1980s from the white-rot basidiomycetes *Phanerochaete chrysosporium* and later in brown-rot basidiomycetes. LiP shows preference for degradation of non-phenolic contents of lignin (up to 90% of the polymer). MnP participates in the degradation of lignin by generating Mn^{3+}, a diffusible oxidizer, that oxidizes both phenolic and non-phenolic units of the lignin molecule. Finally, versatile peroxidise (VP) from Pleurotus and other fungi acts as a third type of ligninolytic peroxidase. It shows a combination of the catalytic activity of LiP and MnP peroxidises [13, 16]

P. chrysosporium posseses more than a dozen different peroxidase genes in its genome. The genome encode for 16 genes corresponding to lignin degradation; 10 LiP, 5 MnP and 1 NoP (novel peroxidase) [16, 17]. Ten structurally related genes designated *lipA* through to *lipJ* encode for LiPs production. The actual reason behind the presence of so many LiPs is unclear, however the existence of alterations in the oxidation–reduction potential among LiP isoenzymes have been observed [16, 18]. The structures of both LiP and MnP have been determined [19, 20]. They are homologous to each other and to other peroxidases of different classes, which is indicative of divergent evolution [21].

Both lignin peroxidase and manganese peroxidase display catalytic cycles similar to the other peroxidase enzymes. In the resting state the enzyme contains ferric heme, which after reaction with hydrogen peroxide forms a compound **I** intermediate (two-electron oxidized form), and subsequently a compound **II** intermediate (one-electron oxidized form) [13,16, 22]. However, the presence of the two aspects in the molecular structure of these two enzyme differentiate ligninolytic peroxidases from the other peroxidases: first, possesing a heme environment that provides high redox potential for the Cpd **I** (due to the position of N^{ε} of the side-chain of the proximal histidine residue, that increases its electron deficiency and

subsequntly increases the redox potential of the compound **I**); secondly, the presence of particular binding sites in the LiP and the MnP for oxidation of specific substrates, such as non-phenolic aromatics and Mn^{2+} [13, 16, 22].

Both of these enzymes represent a general tertiary fold, a helical topography, they are globular proteins, formed by 11–12 helices arranged in two domains, with a central cavity containing the heme group. In order to stabilize the protein structure, LiP contains four disulfide bridges, and MnP contains a fifth bridge in its C-terminal region, and two Ca^{2+} binding sites [16, 22].

MnP is a glycoprotein and is often produced in multiple forms, up to 11 different isoforms have been described in one fungal strain, *Ceriporiopsis subvermispora*, these isoforms differ mostly in their isolectric points [23].

The Mn peroxidases catalyze the oxidation of complexed Mn^{2+} to Mn^{3+} that leads to oxidation of a large number of phenolic substrates. Mn^{3+} acts as a diffusible oxidant, and is able to oxidize secondary substrates that are distantce from the active site of MnP [21]. The MnP is a potent biochemical tool; it is like a radical generating pump for attacking the recalcitrant lignin polymer. Since Mn^{3+} produced by MnP is very unstable in aqueous media, white-rot fungi secrete oxalic acid and other organic acids that form Mn^{3+} chelates that act as stable diffusing oxidizers of phenolic compounds and dyes [22].

The MnP structure reveals five disulfide-bridging elements and two Ca^{2+} ions, which maintain the structure of the active site. The active site consists of a proximal histidine ligand, H-bonded to an aspartic acid residue and a distal side peroxidase-binding pocket containing catalytic histidine and arginine residues (Fig. 1. 4) [16, 23].

Six different lignin peroxidase isozymes (H1, H2, H6, H7, H8, and H10) have been identified in *P. chrysosporium* in nitrogen-limited cultures. They are glycosylated hemoproteins [16, 24]. All lignin peroxidase isozymes, except for isozyme H1, are

phosphorylated on their N-linked carbohydrate moiety in the form of mannose 6-phosphate [16, 24]. Because of possessing of high redox potential compound **I** [16, 25], the preferred substrates for LiP are nonphenolic methoxy-substituted lignin subunits. One of the important features that distinguishes LiP from other oxidoreductases is its very low pH optimum. The optimum pH for steady-state turnover of LiP is near 2.0, which is lower than those of all other peroxidases [16, 25].

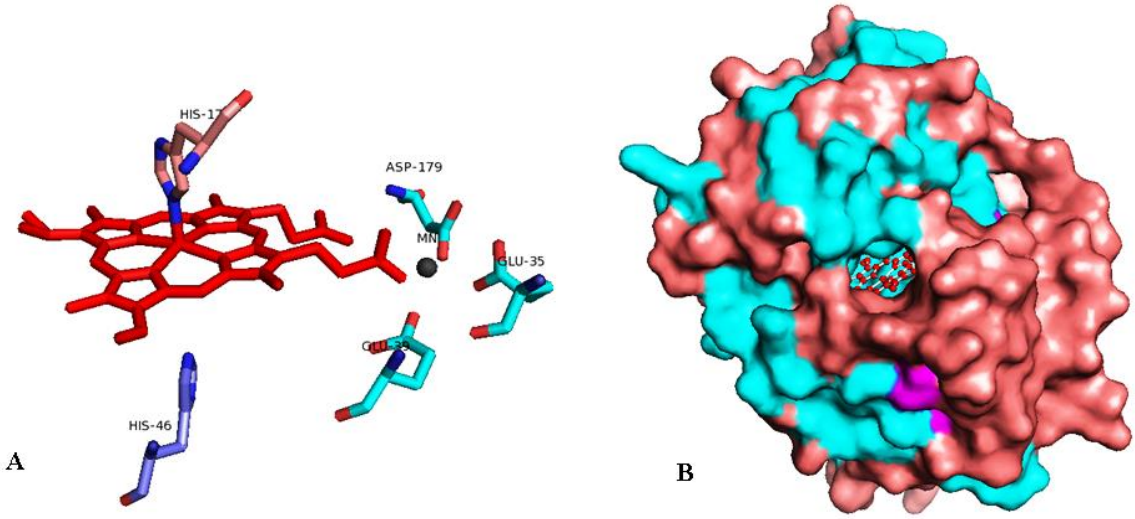

Figure 1.4 - The arrangement of conserved and catalytic residues around heme of Mn peroxidase from *P.chrysosporium* (PDB code 3M5Q) (A). The molecular surface representations of Mn peroxidase, blue and red colours represent helix and loop structures respectively (B). The picture was generated by PyMOL [105].

Veratryl alcohol, produced by ligninolytic fungi has been suggested as a redox mediator for LiP; it is oxidized to its cation radical by LiP and then acts as a diffusible oxidant [16, 26, 27].

Despite the occurrence of direct electron transfer to heme from small substrates of LiP, long-range electron transfer should also be considered. The reason for the presence of the so-called long-range electron transfer phenomena is related to the fact that many aromatic substrates of LiPs including the lignin polymer, cannot penetrate inside the protein for transferring electrons directly to the heme. Therefore, these substrates are oxidized at the

enzyme surface and electrons are transferred to the heme by a protein pathway (Fig. 1.5) and (Fig. 1.6) [13, 16].

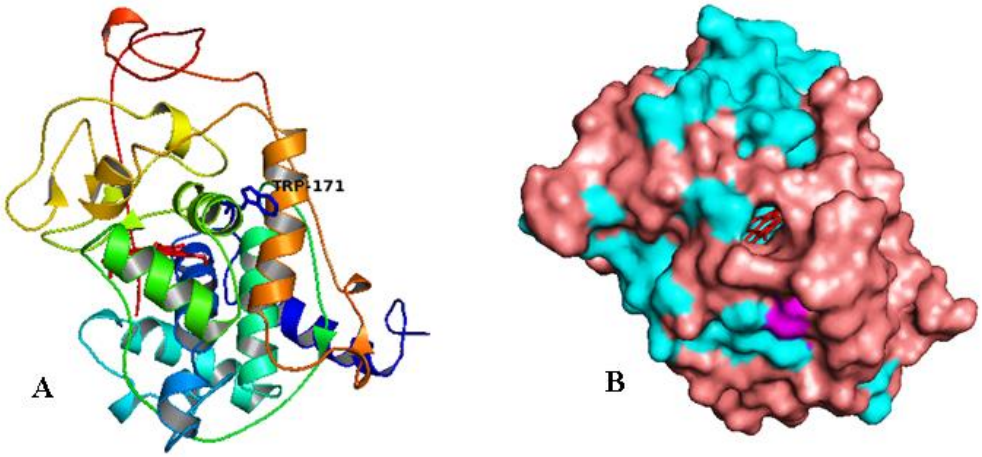

Figure 1.5 - The overall structure of Lignin peroxidase (isozyme H2) from *P.chrysosporium* (PDB code 1LLP) and position of Trp 171 on the surface of the enzyme (A). The molecular surface representation of Lignin peroxidase, blue and red colours represent helix and loop structures respectively (B). The picture was generated by PyMOL [105].

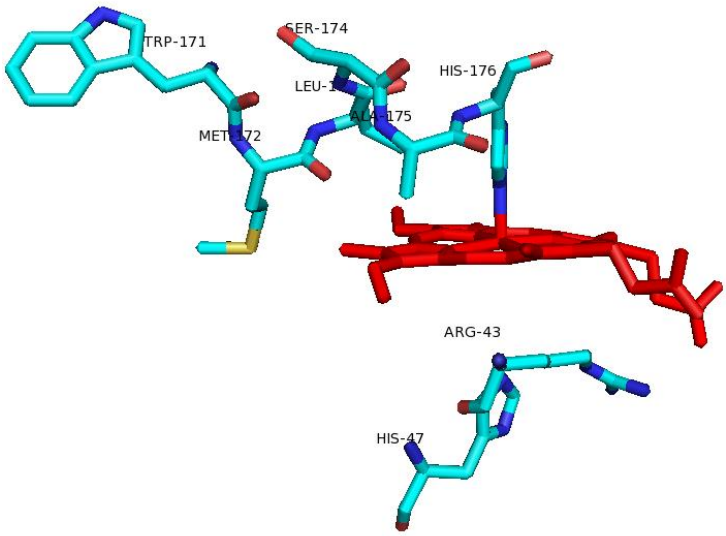

Figure 1.6 - The arrangement of conserved and catalytic residues around heme of Lignin peroxidase (isozyme H2) from *P.chrysosporium* (PDB code 1LLP) and position of Trp 171 compared to heme and distal histidine. The picture was generated by PyMOL [105].

Multiple sequence alignment and side directed mutagenesis experiments suggest that tryptophan 171 is a redox active residue in LiP which could participate in the oxidation of molecules, specially veratryl alcohol on the surface of LiP. The multiple sequence alignment showed that this tryptophan is conserved in all LiP sequences. The W171 is positioned at the LiP surface in a very acidic environment that could stabilize produced veratryl alcohol cation radical from oxidation of veratryl alcohol by compound **I** and subsequently compound **II** during the enzyme catalytic cycle [28].

1.3 *Pseudomonas fluorescens*

Pseudomonas fluorescens belongs to the gamma-proteobacteria and is a Gram-negative rod shaped bacterium. It inhabits the soil, plants, and water surfaces and the best growth temperature suitable for its growth is between 25-30 °C. This species and its strains have been extensively studied to determine their use in bioremediation and biocontrol of pathogens [29]. These organisms are of great interest because of their competency in interacting with plants [29, 30], their effects on crop yield [31, 32] and their benefit as biopesticides [33, 34].

The Pf-5 strain is a plant symbiant and lives in the plant's rhizosphere and makes a collection of secondary metabolites, including antibiotics, that counter plant pathogens originating from the soil [35]. Soluble, green fluorescent pigments are generated while the iron concentration is low.

The genome of two strains of *P. fluorescens* have been sequenced. The *P. fluorescens* Pf-5 genome is one circular chromosome whose size is 7.1 Mbp, with a GC content of 63.3%, and it encodes for 87 RNAs and 6137 proteins. A total of 5.7% of the genome relates to secondary metabolism, that is the largest among the genome of pseudomonads that have been

sequenced so far [35, 36]. The genome of *P.fluorescens* Pf01 contains one chromosome of 6.43 Mbp in size, its GC content is 60.5% and codes for 95 RNAs and 5736 proteins.

P. fluorescens utilizes siderophores to capture iron from the environment. This species makes the siderophore pyoverdine (Fig. 1.7), which is responsible for chelating iron only when iron concentration is low. Pyoverdine is responsible for the fluorescence of *P. fluoresecens*, which explains why the fluorescent pigment is produced whenever the iron concentration is low. When the iron concentration is high, pyoverdine is not required, therefore bacterial colonies do not fluoresce under UV light. *P. fluorescens* is very susceptible to chromate because chromate is a competitor inhibitor of the sulphate transport system which *P. fluorescens* uses [37].

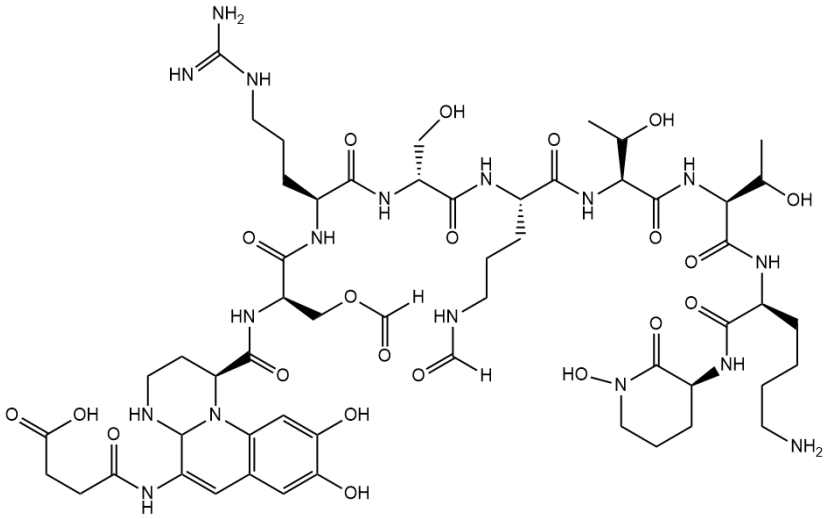

Figure 1.7 - The chemical structure of pyoverdine.

P.fluorescens Pf-5 secretes some hydrolytic enzymes that break down polymers available in the soil, such as hydrolytic enzymes that are active on plant-derived carbohydrates. Furthermore, these enzymes have the capability to degrade and utilize ingredients of plant tissues such as hydrocarbon molecules, fatty acids and oils [35].

P. fluorescens produces a lipopeptide, viscosin, which increases antiviral protection for plants [37]. It also produces some antibiotics and hydrogen cyanide which are destructive for plant pathogens [37].

One of the many by-products of plant cell metabolism includes active oxygen species such as hydrogen peroxide and superoxide that are toxic to microorganisms. Bacteria that inhabit in the rhizosphere such as *P. fluorescens* contain an arsenal of enzymes to survive in these oxidative conditions, including enzymes such as superoxide dismutase for changing superoxide to hydrogen peroxide [35] and catalase to degrade peroxide to water [35]. The availability of these enzymes provides resistance for this organism under oxidative stress conditions [35].

Secondary metabolites produced by microorganisms or plants play a crucial action in defence against plant diseases. *P. fluorescens* Pf-5 produce antibiotics like pyrrolnitrin, pyoluteorin, and 2, 4-diacetylphloroglucinol (Fig. 1.8), that restrict phytopathogen progress [35]. *Rhizoctonia solani* and *Pythium ultimum*, plant pathogenic fungi that act on cotton plants, are inhibited by *P. fluorescens*, by competing for essential iron for growth and restricting pathogens that inhabit in the rhizosphere. The capability of *P. fluorescens* in breaking down environmental contaminants such as Trinitrotoluene, polycyclic aromatic hydrocarbons and styrene has been used in bioremediation [35].

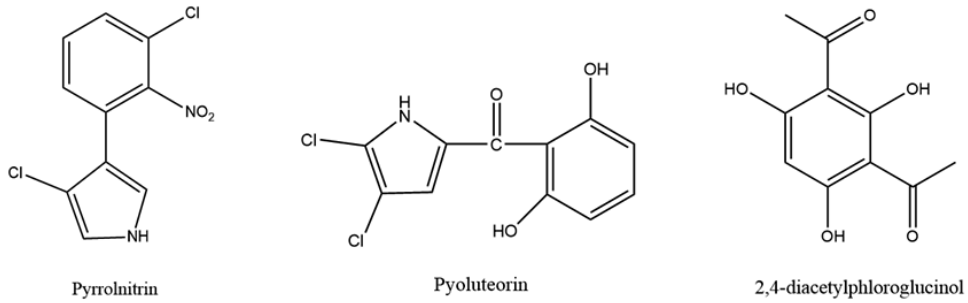

Figure 1.8 - The chemical structure of pyrrolnitrin, pyoluteorin, and 2, 4-diacetylphloroglucinol

Exopolysaccharides such as alginate, a copolymer of mannuronic and guluronic acids, and levan, polymers of fructose, are also made by *P. fluorescens*, which uses them for defence against bacteriophages or conservation of water and for protection against the host immune system [37].

1.4 *Thermobifida fusca*

T. fusca, which previously was known as *Thermomonaspora fusca*, is a moderate thermophilic filamentous bacterium that inhabits soil. Its optimum growth temperature is 55 °C and has a vast optimum growth pH range (4-10) [38]. It degrades most of the plant cell wall polymers in heated organic materials such as rotting hay and compost heaps. It seems that *T. fusca* breaks down all the main plant cell wall polymers except for lignin and pectin polymers, and is able to grow on simple sugars and carboxylic acids [39]. It belongs to the actinomycetes, and its extracellular enzymes, especially cellulases, have been investigated extensively because of their thermostability and high activity. The genus Thermobifida consists of the other member that is a Gram-positive aerobic microorganisms, *Thermobifida alba* [38].

Because of its biotechnological application, the genome of *T. fusca* has been sequenced. The organism secretes different kinds of extracellular enzymes including cellulases, which are responsible for the degradation of cellulose and lignocellulose residues, and which are valuable for decomposing agricultural wastes [38]. *T. fusca* contains a single circular chromosome of 3,642,249 bp with a coding density of 85% that encodes 3,110 proteins and 65 RNA. The G-C content of the genome is 67.5% which is predictable for a microorganism that can withstand high temperatures and a vast pH range from four to ten [39]. *T. fusca* also encodes for other enzymes like glycosyl hydrolases and xylanases, which are essential for the efficient breakdown of plant cell walls [39].

1.5 *Rhodococcus jostii Rha1*

Rhodococcus is a genus and a member of the actinomycetes that contain mycolic acid in their membrane. They can utilise an extraordinary variety of organic compounds as growth nutrients. This degradative ability of Rhodococcus is necessary for maintaining the global carbon cycle and represents a starting point for several applications ranging from the biodegradation of contaminants to the biocatalytic production of hormones and drugs [40].

R. jostii RHA1 is a biphenyl degrading strain that has one of the largest genomes that has yet been sequenced. The size of the genome is 9.7 kb and it is composed of a linear chromosome with a G-C content of 67%, it has been predicted that the genome encodes for 9,145 genes [41]. The linear chromosome is believed to have resulted from recombination between a circular chromosome and linear plasmids [42].

A total of 1,085 oxidoreductases and 192 ligases are encoded by the genome of *R. jostii* RHA1, which is an exception among Actinomycetes. The catabolic power of numerous oxygenases present in the genome of *R. jostii* RHA1 is used in hydroxylation and subsequently degradation of soil and water contaminant aromatic compounds. Nearly 77% of the encoded oxidoreductases by the genome of *R. jostii* RHA1 are within the linear chromosome. Horizontal gene transfer is thought to be responsible for 7% of the oxygenases of *R. jostii* RHA1 [42].

1.6 Peroxidases

Peroxidases are well known in the history of enzymology and in enzyme kinetics, because rapid reaction methods in enzyme kinetics were established through utilizing horseradish peroxidase (HRP) in the 1940s [43] and the obvious spectroscopic characteristics of the Compounds **I** and **II** intermediates resulting from the HRP catalytic cycle, made it relatively easy to discover the green Compound **I** and red Compound **II**.

Peroxidases (EC 1.11.1.x) belong to an abundant group of oxidoreductases that catalyse the oxidation of substrate molecules by utilizing hydrogen peroxide as the oxidiser. The native enzyme possesses a heme cofactor, which is ferriprotoporphyrin IX and by four pyrrole nitrogens binds to the Fe (III). The fifth coordination position on the proximal side of the heme is usually the imidazole side chain of a histidine residue. The sixth coordination position is vacant in the native enzyme on the distal side of the heme [44] (Fig. 1.9).

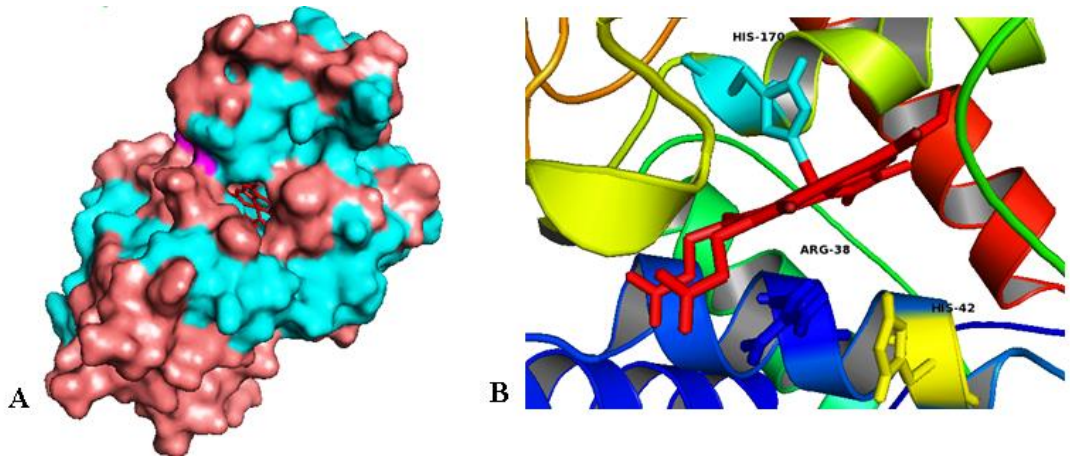

Figure 1.9 - The molecular surface representation of horseradish peroxidase from *Armoracia rusticana* (PDB code 1ATJ) (A). Heme surrounding environment and position of distal and proximal histidine in horseradish peroxidase, blue and red colours represent helix and loop structures respectively (B). The picture was generated by PyMOL [105].

These enzymes can be divided into two large groups: plant peroxidases and animal peroxidases. Twenty years ago, Welinder suggested the idea of a plant peroxidase superfamily [45], at which point prokaryotes including mitochondria, fungal, and plant peroxidases were divided into classes I, II, and III, respectively, based on primary structural homology. For example, yeast cytochrome c peroxidase and chloroplast ascorbate peroxidase are class I peroxidases, while class II enzymes include lignin peroxidase (LiP), manganese peroxidase (MnP) and versatile peroxidase.

Similarly, horseradish peroxidase (HRP) and barley grain peroxidase (BGP) are class III peroxidases [46]. This classification system has proven useful for characterizing the majority of known peroxidases, with the exception of chloroperoxidase which was isolated

from *Caldariomyces fumago*, a fungus, which lacks primary structural homology with other peroxidases [46]. In contrast to plant peroxidases, most enzymes isolated from mammals and other animals have not yet been classified. However, several animal peroxidases have been studied with regards to roles in disease and aging [47].

Peroxidases are ubiquitous in both eukaryotic and prokaryotic organisms and are essential in several vital physiological phenomena, such as biosynthesis of lignin, degradation pathways and host-defense mechanisms [48]. Additionally, the chemical nature of peroxidase-catalysed reactions, exploiting of the oxidising potential of hydrogen peroxide for the oxidation of a extent variety of chemical compounds, has given rise to emergence of peroxidase-based biotechnological applications, such as wastewater treatment, bio-bleaching, and different analytical biosensors [49].

The catalytic cycle of peroxidases is a three step process (Fig. 1.10), briefly iron in the heme molecule in the enzyme's resting state is in ferric form and reaction with hydrogen peroxide leads to formation of compound **I**, a oxo-ferryl intermediate (two- electron oxidized form), and subsequently a compound **II** intermediate (one-electron oxidized form) [13, 23].

The feature of the catalytic mechanism will be discussed in more detail in this chapter.

Ferriperoxidase + H_2O_2 →Compound **I** + H_2O (1)

Compound **I** + AH_2 →Compound **II** + AH (2)

Compound **II** + AH_2 →Ferriperoxidase + AH + H_2O (3)

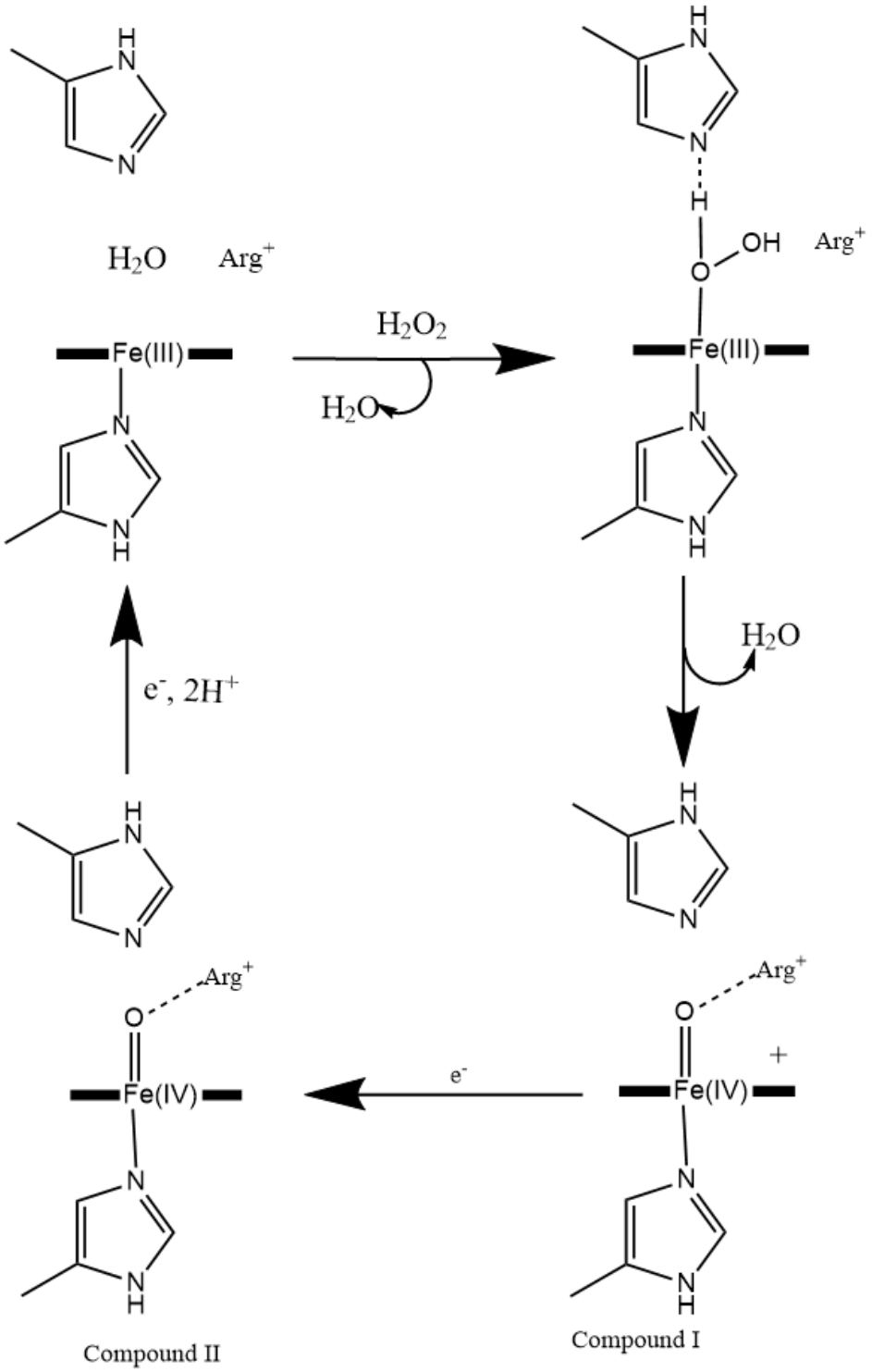

Figure 1.10 - General peroxidase catalytic cycle

1.7 Dye decolorizing peroxidases

A division of this heterogenic group of the peroxidase enzymes is the dye-decolorizing peroxidases or DyPs (EC 1.11.1.19) [50]. In 1995, the basidiomycete *Bjerkandera adusta* (the strain was then known as *Thanatephorus cucumeris*), an isolated basidiomycete from soil, was reported to be able to decolorize acidic and dispersive dyes. Later studies indicated that this organism showed broad degrading activity toward poorly biodegradable materials such as lignin, molasses and synthetic dyes like anthraquinones (AQs) [51-54]. The first dye-decolorizing peroxidase (DyP) was first purified from extracellular solution of basidiomycete *B. adusta*, and its decolorization activity was > 100-fold [55]. Later on, the complete tertiary structure of the enzyme was obtained [56].

Genomic analyses have shown that DyPs occur in a wide variety of fungi and bacteria. Members of this family are listed in the PeroxiBase database (http://peroxibase.isbsib.ch/) and many homologous proteins have been detected by bioinformatics techniques such as PSI-BLAST search. It appears that DyPs are different from general peroxidases because of the distinctive primary sequence and tertiary structures and unique reaction characteristics that they represent [46]. A DyP type peroxidase from *Bacteroides thetaiotaomicron* (BtDyP) is the second reported purified enzyme whose tertiary structure was determined, followed by TyrA protein from *Shewanella oneidensis* as the third structure published for DyP-type peroxidases [57, 58].

According to the aforementioned peroxidase classification [45] and since DyPs enzymes were derived from fungal origins, the DyP family was initially considered to be structurally related to the class II secretory fungal peroxidases; consequently, they were initially grouped in this class of peroxidases. The class comprises fungal peroxidases such as lignin peroxidase, manganese peroxidase, and versatile peroxidase. However, further studies showed that DyPs are phylogenetically as well as structurally unrelated to all previously described peroxidase families. For example, the DyP family exhibits only low sequence

similarity to other fungal peroxidases, such as LiP and MnP, and does not contain the conserved distal histidine and essential arginine found in other plant peroxidase superfamily members [57]. The DyP family is also structurally divergent from all classes of the plant and animal peroxidase superfamilies [57]. Therefore, a new family of enzymes was established to accommodate these new peroxidases [56, 46].

The DyP class of enzymes contains a heme group and catalyzes peroxidase reactions, but shows no primary structural homology to other known general peroxidases. DyPs represent a different molecular architecture and divergent mechanistic behavior compared with other peroxidases that is not fully understood yet. Despite the structural differences, the general physico-chemical properties of DyPs are similar to the classic heme proteins, properties such as UV–vis spectral characteristics, molecular masses or isoelectric points [59, 60].

DyPs were first found in fungi, but were later identified in a wide range of bacterial strains, a recent study in bacteria by genome mining and bioinformatics analysis revealed number of DyP type peroxidases and the number of characterized enzymes is increasing rapidly in the literature. Sturm *et al*. reported that a DyP type peroxidase from *Escherichia coli*, named Ycdb, is exported to the extracellular medium via the Tat translocase system [61]. The first crystal structures of two bacterial dye-decolorizing peroxidases were solved by Zubieta *et al*., BtDyP from *B. thetaiotaomicron* (PDB code 2GVK), and TyrA protein from *S. oneidensis* (PDB code 2IIZ), both revealed a beta-barrel fold with a conserved heme-binding motif in bacterial DyPs [57, 58]. Ogola *et al.,* characterized a unique bacterial dye-decolorizing peroxidase from the cyanobacterium *Anabaena sp*. and showed it efficiently oxidized both recalcitrant anthraquinone dyes (AQ) and typical aromatic peroxidase substrates [62]. In 2009 bacterial DyP discoveries followed by research of van Bloois *et al.*, who characterized robust and extracellular DyP-type peroxidase from *Thermobifida fusca*, a

moderate thermophile. This enzyme showed similar reactivity toward typical peroxidase substrates and, in addition catalyzed enantioselective sulfoxidation [63].

Ahmad *et al*., and Roberts *et al.*, have identified and fully characterized two DyP-type peroxidases enzyme from *Rhodococcus jostii RHA1*, and for the first time they showed a distinct class of DyP type peroxidase that shows manganese-dependent lignin peroxidase activity, which plays a significant role in lignin degradation by *R. jostii RHA1* [64, 65]. The tertiary structure of this enzyme was solved (PDB code 3QNS), and site-directed mutagenesis was carried out for the purpose of increasing manganese oxidation activity, and studying enzyme mechanism [65-67]. Brown *et al.*, reported the identification, characterization and tertiary structure determination of a multifunctional dye-decolorizing peroxidase from *Amycolatopsis sp 75iv2.*, a lignin-reactive bacterium. Their studies indicated that the characterized DyP shows versatile and significant high activity for both peroxidase and Mn peroxidase function compared to other so far characterized bacterial DyPs. The crystal structure of the enzyme (PDB code 4G2C) showed the presence of a Mn^{2+} binding pocket, formed by side chains of three glutamic acid residues near to the heme active site, that supports exhibited manganese peroxidase activity [68]. Ana Santos *et al.*, characterized two new-bacterial DyP-type peroxidases from *Bacillus subtilis* and *Pseudomonas putida MET94* [69]. Their extensive kinetic and spectroscopic results showed that DyP from *P.putida* (PpDyP) is more active and exhibits wider substrate specificity than DyP from *B.subtilis* (BsDyP). Despite its lower activity, BsDyP is more stable in elevated temperature or the presence of chemical denaturation than the PpDyP [69].

Investigation of bacterial DyPs has been more extensive than fungal DyPs, but recently two DyP-like peroxidases (AauDyPI, AauDyPII) from the jelly fungus *Auricularia auricula-judae* were identified and purified from its culture liquids by three chromatographic steps [70]. The crystal structure of AauDyPI was determined (PDB code 4AU9) [71]. AauDyPI can oxidize nonphenolic lignin model compounds and high-redox potential dyes.

Based on kinetics, chemical modification and structural analysis, Strittmatter *et al*., identified a surface-exposed tyrosine on the surface of AauDyPI that acts as an oxidation site for bulky substrates. A long-range electron transfer pathway between the oxidation site and heme environment was proposed [71].

In the next section, based on phylogenetic trees, four different types of DyPs are further investigated by sequence alignment analysis. Prominent similarities and differences that they represent in the primary sequence level will be discussed.

1.7.1 Sub-families of DyP peroxidases

DyP-type peroxidases are considered as a distinct superfamily in databases, such as Peroxibase, Pfam, and InterPro. According to the InterPro database, the DyP superfamily comprises almost 1,000 members of which 881 members are found in bacteria, 11 in cyanobacteria, 39 in fungi, 19 in higher eukaryotes, and one is unclassified [63]. PeroxiBase database and Phylogenetic analyses classify DyP-type peroxidases into four phylogenetically distinct subfamilies A, B, C, and D [62]. A, B and C subfamilies comprise bacterial DyPs, whereas subfamily D is fungal [56, 46, 62, 64]. Class, B and C of DyP-type peroxidases, are predicted to be cytoplasmic enzymes, an indicative of their unknown function in intracellular metabolic pathway.

The first type of reactivity for DyPs to be discovered was the degradation of anthraquinone dyes [46]. However, further enzymes from different subfamilies have shown notably different substrate specificities, for instance, some DyPs catalyze the oxidation of methoxylated aromatic compounds [70] whereas some DyPs could oxidize Mn(II) [64, 65]. DyPs molecular weight range is from nearly 60 kD in fungal DyPs to 30 kD in bacterial DyPs. Phylogenetic analyses suggest that in evolutionary history, subfamilies A and B diverged from C and D counterparts, and in the later steps subfamilies A and B as well as C

and D segregated from each other and their genes have undergone speciation in four directions within the respective subfamilies [69].

The physiological roles of DyP enzymes are ambiguous; they might play roles in bacterial oxidative stress response [72], as virulence factors in plant pathogens [73] in iron removal from heme [74], and porphyrinogen oxidation [75]. Further studies of DyPs from different subfamilies are essential for determining their physiological functions.

Two characterized DyPs from *R. jostii RHA1* were named DyPA and DyPB according to the subfamilies in which they were grouped. Studies have shown that most A-type DyPs contain TAT signal sequences that enable them to be excreted into the periplasmic space but B-type DyPs do not. For instance, TfuDyP from *T.fusca*, Ycdb from *E.coli* and DyPA from *R. jostii RHA1* show the presence of a TAT signal sequnce in their sequence [61, 63, 64].

However, in some bacteria, adjacent to *dypB* gene, there is a gene named *encapsulin* [76, 77]. For example, in the *R. jostii RHA1* genome, next to the *dypB* gene (*ro02407*), there is *ro02408* gene, which encodes an encapsulin protein that has been shown to form an icosahedral nanocompartment [77]. Studies have shown that those B-type DyPs genes that are in the same operon with encapsulin gene exhibit a C-terminal peptide tag that is found in proteins that associate with encapsulin, and this C-terminal tag is found in *R. jostii RHA1* DyPB [64, 76, 77]. There are binding sites for the C-terminal tag in interior of encapsulin cavity that enable B-type DyPs to be encapsulated into the encapsulin [76, 77]. Since *R. jostii RHA1* DyPB has lignin peroxidase activity which occurs extracellularly, there may be some connection between packaging in the encapsulin nanocompartment and cellular export [64].

Fig. 1.11 exhibits a phylogenies tree built by amino acid sequences of characterized DyPs from the above mentioned subfamilies. DyP enzyme such as BtDyP [57], Tyr A [58], PpDyP [69] and DyPB [65] are clustered in clade B, whereas Ycdb [61], TfuDyP [63], BsDyP [69] and DyPA [65] are clustered in Clade A. C-type DyPs are clustered away from the most

prokaryotic DyPs (A and B types) and are much more related to fungal DyPs. DyP2 from *Amycolatopsis sp 75iv2* [68] and DyP from cyanobacterium *AnaPX35* [62] are in the C clade and DyP from *B. adusta* [55] and AauDyPI, AauDyPII from the jelly fungus *A. auricula-judae* belong to subfamily D [70].

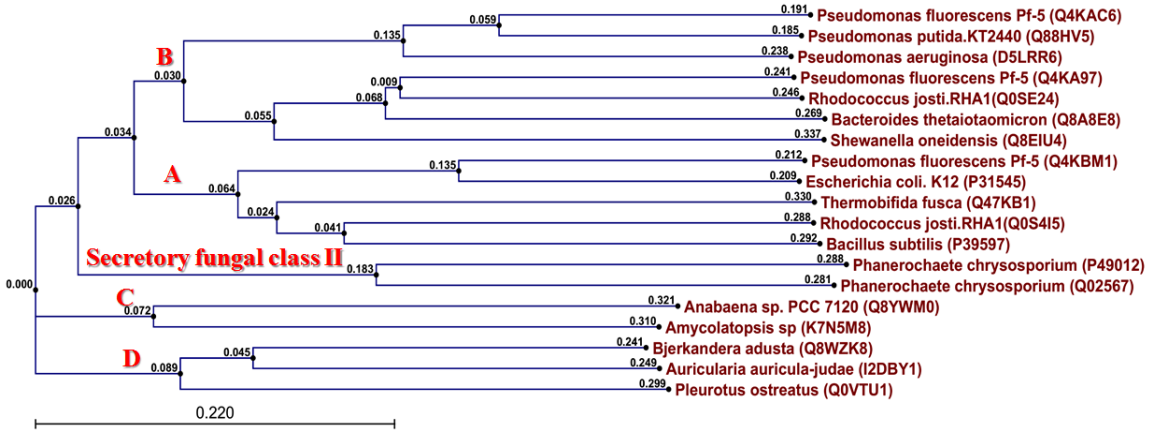

Figure 1.11 - Phylogeny tree of four subfamilies of DyP type peroxidases plus secretory fungal class II peroxidases generated by CLC Main workbench 6 software performed by BLOSUM62 scoring matrix

Steady state kinetics studies have shown that the peroxidase activities of the A and B type DyP members are 3–4 orders of magnitude lower than those exhibited by those of the C or D subfamilies [69].

Analysis at the level of DyPs protein sequence shows conserved residues in the heme-binding site. The presence of an aspartate residue replacing the classical distal histidine in a GXXDG motif is characteristic of all discovered DyPs so far [46].

Fig. 1.12 exhibits the selected parts of protein sequence alignment for four different DyPs type enzyme. DyP from *B. adusta*, DyP2 from *Amycolatopsis sp 75iv2*, TfuDyP from *T. fusca* and DyPB from *R. jostii RHA1* were chosen as a representative of D-type, C-type, A-type and B-type DyP respectively. Red star marks the conserved residues involved in the catalytic action of DyPs.

On the distal face of the heme are three conserved residues; an aspartic acid (Asp 171 in *B. adusta* DyP), an arginine (Arg 329 in *B. adusta* DyP) and a phenylalanine (Phe 356 in *B.*

adusta DyP). The proximal histidine (His 308 in *B. adusta* DyP), the fifth ligand to the heme iron, is also conserved in all of the DyP- type peroxidases. The conserved aspartate is part of the conserved GXXDG motif. Catalytic roles for the distal aspartate and arginine have been proposed based on the structural and mutagenesis studies. The distal Asp acts as a proton shuttle in the formation of compound **I** from H_2O_2 and the arginine stabilizes the negative charge during the heterolytic cleavage of the peroxide group [65].

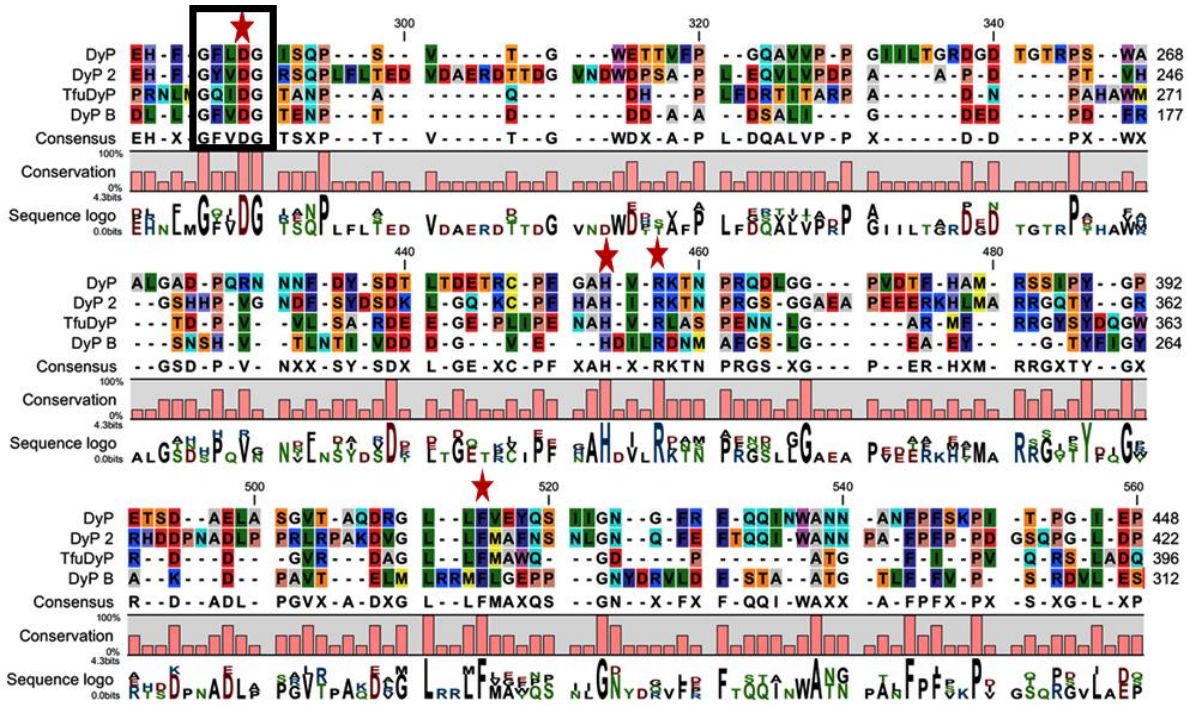

Figure 1.12 - Multiple sequence alignment of four different DyPs enzyme generated by CLC Main workbench 6 software, each enzyme is representative of one DyP-type subfamily. Red stars are indicative of conserved residues

1.7.2 Structure

In this section, the aim is to introduce general structural aspects of DyP-type peroxidases that are present in the both prokaryotic and eukaryotic organisms. For this purpose the structure of D-type DyPs (fungal) from the fungus *B. adusta* is introduced first, followed by the recently solved structure of a DyP-type peroxidase from the jelly fungus *A.*

auricula-judae, and then for each clade of bacterial DyPs a representative structure will be introduced.

Yasushi Sugano *et al.* solved the complete structure of DyP from *B. adusta* [56] (PDB code 2D3Q). They showed that DyP belongs to the α/β superfamily which represents a unique tertiary structure different from other known structures of peroxidases. Contrary to LiP and MnP, which are both like DyP fungal and secretory peroxidases and are primarily α-helical proteins, DyP contains four-stranded antiparallel β-sheets. This is a significantly different arrangement in the distal heme region from that of the most other peroxidases [56].

The tertiary structure revealed that of 442 total residues in DyP, 192 residues form 18 α-helices and 15 β-strands [56]. One of the main characteristics of the DyP structure is the presence of a βαββαβ motif in the secondary structure of DyP, an α/β sandwich with an antiparallel beta-sheet (two βαβ motifs), above the distal area of the heme. This motif is indicative of a ferredoxin-like fold that is not present in other known tertiary structures of peroxidases.

DyP peroxidases comprise two domains that contain α-helices and anti-parallel β-sheets; both domains adopt the ferredoxin-like fold and form an active site crevice with the heme cofactor sandwiched in between [46]. Instead of having a distal histidine residue that is critical in the formation of a iron (IV) oxoferryl center and a porphyrin cation radical intermediate, known as compound **I**, during the catalytic cycle of peroxidases, DyPs possess an aspartic acid and arginine that are involved in the formation of compound **I**. This replacement is one of the main differences between DyP and other peroxidases from plant superfamily that enable DyP to be catalytically active in acidic pH.

The functional importance of the conserved Asp-171 in the GXXDG motif of *B. adusta* DyP was examined [56]. It was discovered that the replacement of Asp-171 by asparagine destroyed enzymatic activity [56]. This is in accordance with the suggested function of acid–base catalyst for the mentioned Asp-171 in the catalytic mechanism at low

pH, as indicated by structural data [56]. DyPs contains a highly conserved histidine residue in the C-terminal domain of the protein which for *B. adusta* DyP is His-308, which is part of the active site [46] and is the fifth ligand of the iron centre in the heme cofactor. Fig. 1.13 shows the overall structure of DyP and arrangement of residues around heme.

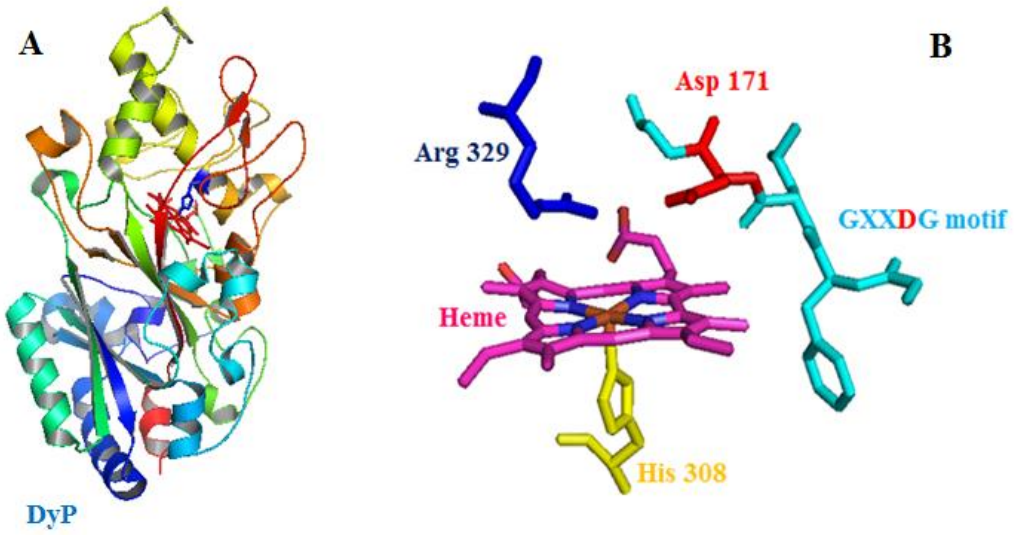

Figure 1.13 -The overall structure DyP from *B. adusta* (A), and arrangement of conserved residues and GXXDG motif around heme molecule (B). The picture was generated by PyMOL [105].

The crystal structure of AauDyPI from *A. auricula-judae* (fungi) was determined at 2.1 A˚ resolution (PDB code 4AU9) by Strittmatter *et al.* [71] AauDyPI is a glycoprotein with a helical basic architecture and the β-sheet motifs typical for DyPs; it shows a ferredoxin-like fold of β-sheets. Like other DyPs, it is structurally very distinct from the classical heme peroxidases.

One of the distinct features of the DyP-type enzymes is the unusual conformation that heme propionate residue at pyrrole C adopts [71, 78]. Structural studies on AauDyPI show that the propionate at pyrrole C is tilted because of the formation of five strong hydrogen bonds to the residues around heme pocket. So it is much more confined than the other propionate at pyrrole D. Hence there is a high energy conformational state to the propionate C, which causes the sp^2-plane of the propionate to lie almost orthogonally to the heme plane [71].

The conserved Asp-168 in the GXXDG motif of AuDyPI, at the distal side of the heme molecule, plays a key role in catalysis. Extensive studies have indicated its involvement in proton rearrangement in the process of compound **I** formation [71]. However, a new investigation by Yoshida *et al*. has shed light on the manner of this involvement and its role in compound **I** formation. By analyzing structural data, they suggested a swinging mechanism for the distal aspartate residue during compound **I** formation [79]. Structural studies [71, 79] revealed that the position of the side chain of the aforementioned aspartate swings toward the heme molecule in the presence of H_2O_2, and thereupon mediates the transfer of a proton. Once compound **I** formation is finished, it swings back to the initial position. These data are consistent with observed flexibility in the atoms of Asp-168 side chain [71, 79]. Strittmatter *et al.* have also proposed an another function for Asp-168, based on its flexibility, acting as a gatekeeper by changing the width of the heme cavity access channel [71]. The conserved arginine is also present in distal face; it is essential for coordinating H_2O_2 at the sixth ligand site of heme-Fe (III) and stabilizing compound **I** [71]. In contrast, studies on prokaryotic DyPs, B-type DyP, indicate that the distal aspartate residue is not essential for catalysis: it effects the stability of compound **I**, but enzymatic activity is retained upon mutation [67].

Another structural feature of AauDyPI is existence of a surface-exposed Tyr-337, involved in the oxidation of bulky substrates. Using the approach of chemical modification and spin-trapping experiments, Strittmatter *et al*. showed that a transient radical on the Tyr-337 is formed which could act as the oxidation site for bulky substrates [71].The presence of a long-range electron transfer (LRET) pathway from the porphyrin ring to an appropriate redox-active amino acid residue at the surface of the enzyme is essential. The existence of a remote oxidation site has been proved in lignin peroxidase, where a hydroxylated tryptophan residue acts as the electron substrate molecules oxidation site [26, 80, 81]. The best-possible long-range electron transfer pathway from the surface of the AauDyPI to the redox heme is via the benzene ring of Tyr-337, to the backbone amide nitrogen of Leu-357, followed by the leucine

side chain, from Cδ1 of Leu-357 to one of the pyrrole rings. The total length of this pathway is about 13 Å, [71] as illustrated in Fig. 1.14.

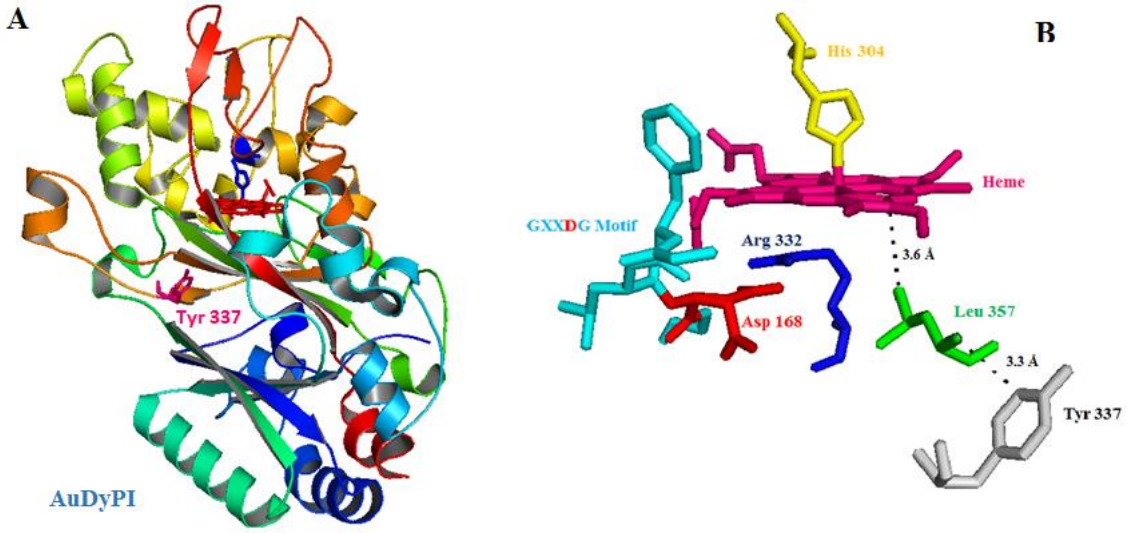

Figure 1.14 -The overall structure of AuDyPI from *A. auricula-judae* (A), and conserved catalytic residues and surface-exposed Tyr-337 involved in long-range electron transfer (B). The picture was generated by PyMOL [105].

EfeB/YcdB is a member of the dye-decolorizing peroxidase (DyP) protein family, and it belongs to A-type DyPs family, a prokaryotic DyP clade. The crystal structure of EfeB from *E. coli O157* was solved at 1.95 A˚ resolution (Protein Data Bank (PDB) code 3O72) by Liu *et. al* [82]. The EfeB monomer represents a ferredoxin-like fold and contains two domains that are composed of 12α-helices and 8β-strands. These structural features are similar to the characteristic of the DyP-type peroxidase protein family [45, 56, 57]. The N-terminal domain (residues 36–221) and C-terminal domain (residues 244–422) are joined by a 22-amino acid-long loop (residues 222–243). The loop takes part in many interactions with the heme molecule, and it is a unique structural characteristic of EfeB structure [82]. Structural analysis indicates the loop is flexible, and it shows significant conformational changes; this property may facilitate the turnover of substrates and products. The C-terminal domain of EfeB is mainly loosely packed, and the heme molecule is positioned in a large hydrophobic pocket in the C-terminal domain [82].

Biochemical studies have indicated the involvement of EfeB in iron acquisition from heme molecule while keeping the tetrapyrrole ring unbroken; this reaction leads to the production of protoporphyrin IX (PPIX) from heme, known as deferrochelation [83-85].

The aforementioned heme interacting distal and proximal residues are also highly conserved in EfeB/YcdB [56, 57, 82]. Due to previous structural and sequences alignment studies, Asp-235 and Arg-347 were recommended as proton acceptor and charge stabilizer, respectively [56]. Site-directed mutagenesis was performed on the Asp-235 and Arg-347 and the proximal histidine (D235N, R347E and H329A) to check their importance for the activity of EfeB [82]. The results showed that except mutant D235N, the other two mutants did not produce PPIX product in the supernatants of cell extracts containing overexpressed H329A and R347E [82]. The mutant D235N also showed approximately the same guaiacol peroxidase activity as the wild-type protein [82]. This observation is entirely incompatible with the previous study on DyP from the fungus *B. adusta* [56], in which the corresponding Asp-171 acts as a proton acceptor and is crucial for the enzymatic activity [56]. The observed differences in the distal aspartate mutants in EfeB and DyP suggest that the DyP peroxidase family may have different mechanisms [82].

The overexpressed cell lysate can catalyse production of a large amount of PPIX, however the purified EfeB protein does not show any catalytic activity [82]. The authors concluded that this reaction requires an unidentified cofactor that is not present in the purified protein [74]. A large amphiphilic tunnel, leading from the surface of EfeB to the heme cofactor, may be a possible passage for accessing the cofactor/substrate to the heme pocket as illustrated in Fig. 1.15. The tunnel diameter is about 4.5 A˚, too narrow for passage of heme or large substrates [82].

In order to prove functional role of the tunnel, its constituent residues were altered by site-directed mutagenesis. Liu *et.al* produced twelve mutants containing bigger side chains than the original residues, in order to block the passage of the unknown cofactor/substrate into

the tunnel. The results showed that all the mutants nearly lost the ability to produce PPIX that strongly supports the idea of the functional role of a tunnel as a route for accessing the active site [82].

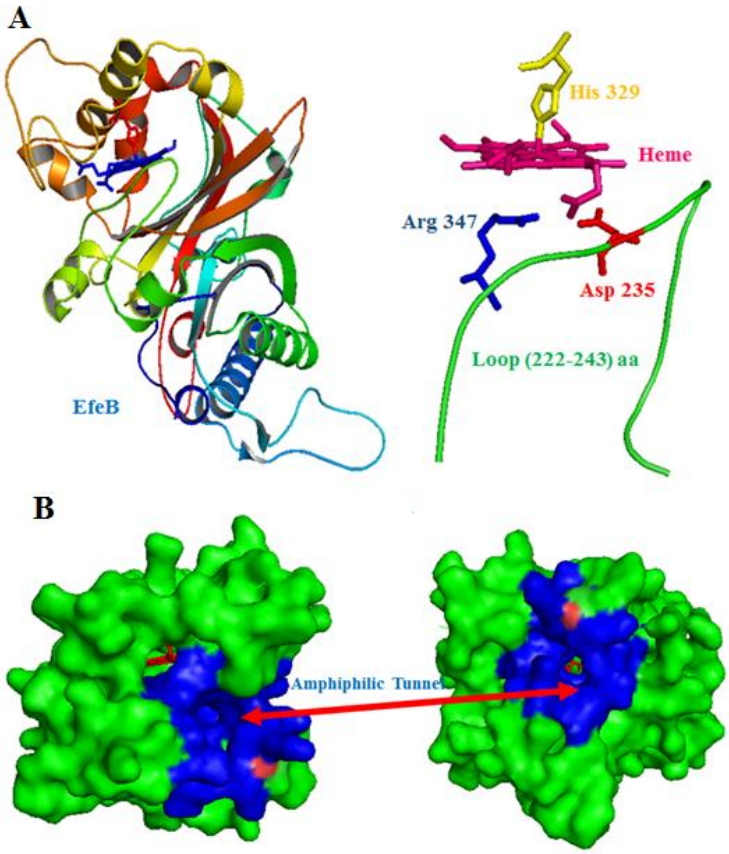

Figure 1.15 - The overall structure of EfeB, arrangement of the conserved residues and the loop around the heme cofactor (A) and location of amphiphilic tunnel in the surface of EfeB (B). The picture was generated by PyMOL [105].

The structure of DyPB from *R. jostii RHA1*, a soil bacterium, is discussed as a representative of B-type DyPs. The structure was determined at 1.4 Å resolution (PDB code 3QNS) [65]. Enzyme activity profile showed that similar to other different DyP type enzymes, DyPB decolorizes dyes, but also catalyses oxidation of lignin and Mn (II). Similar to other DyPs, DyPB represents a fold comprises of two copies of a ferredoxin-like domain, containing two β-sheets sandwiched between two α-helices, in which the heme is bound in the C-terminal domain [56, 57, 58, 82]. The distal face of heme interacts with the two conserved residues, Asp-153 and Arg-244, and a nonconserved one, Asn-246. Both side chains of Asp-

153 and Asn-246 are within hydrogen bonding distance of the iron-bound solvent species [65]. Acting as a proton shuttle in the formation of compound **I** and afterward stabilizing the negative charge has been proposed for Asp-153 and Arg-244 respectively, as in plant-type peroxidases (Fig. 1.16) [46]. However, site-directed mutagenesis along with detailed mechanistic studies showed that the replacement of the Asp-153 with Ala had a relatively weak effect on the enzyme's peroxidase activity and only slightly affected the second order rate constant for compound **I** formation, k_1=2.0 ×10^5 $M^{-1}s^{-1}$ for WT DyPB compared with k_1=0.94 ×10^5 $M^{-1}s^{-1}$ for D153A [67]. The so-called distal aspartate also does not appear to be essential for peroxidase activity in A-type DyPs [82], inconsistent with its accepted acid-base catalyst role in D-type DyPs [56]. The mechanistic studies on DyPB acknowledge the important role for Arg-244 in compound **I** formation instead of Asp-153 possibly via both charge stabilization and proton transfer, since substitution of Arg-244 with leucine abolished the peroxidase activity, and no second order rate constant was obtained for R244L mutant [67].

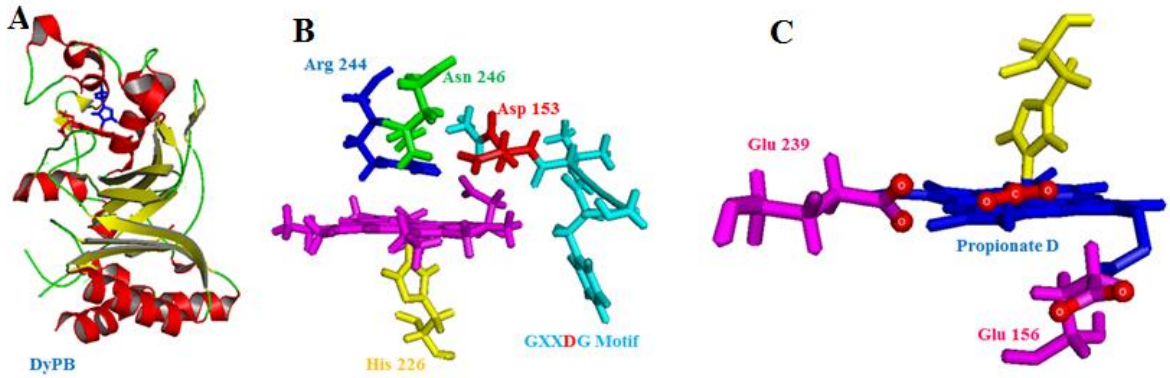

Figure 1.16 -The overall structure of DyPB from *R. jostii RHA1* (A), arrangement of the conserved residues around heme (B) and constituent residues of Mn (II) binding site (C). The picture was generated by PyMOL [105].

Since DyPB showed Mn (II) oxidation activity, the structure was investigated, and a Mn (II)-binding site composed of two acidic residues of Glu-156, Glu-239, and propionate-D

was recognized that is within range of electron transfer to the heme molecule [65, 66]. Site-directed mutagenesis studies showed that substitution of Asn-246 with Ala increased the enzyme's apparent k_{cat} and k_{cat}/K_M values for Mn^{2+} by 80 and 15-fold respectively. The increase in k_{cat} for the N246A variant might be due to raising of the redox potential of the heme molecule in DyPB [66].

The DyPB structure also shows a potential binding site for bulky substrates such as Kraft lignin, which is a hydrophobic groove on the surface of DyPB consisting of Pro-93, Val-94, His-95, Phe-279, and Tyr-287. This site could be involved in long-range electron transfer from a hydrophobic substrate through Tyr-287, and Asp-288, which forms a hydrogen bond with His-226, the fifth ligand to the heme iron [65] shown in Fig. 1.17.

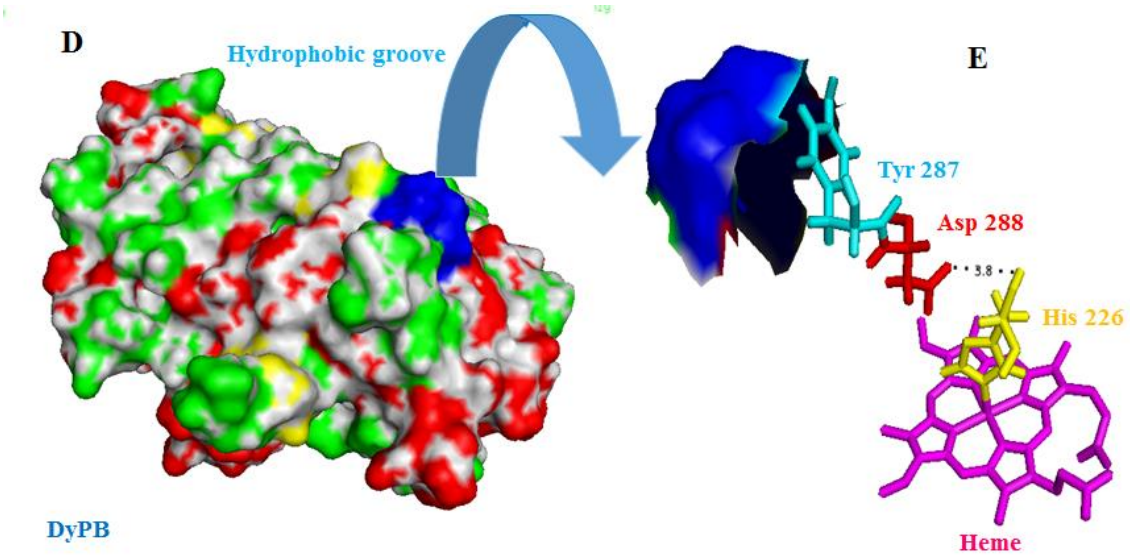

Figure 1.17 - Location of hydrophobic groove that might act as Kraft lignin binding site (D) and proposed long-range electron transfer path from the hydrophobic groove to the heme molecule (E).The picture was generared by PyMOL [105].

The structure of DyPB represents two access paths from bulk solvent to the heme: the distal channel and the propionate pocket. The distal channel is lined by polar and charged residues, and its length is ~19 Å long. Since it leads to the distal face of the heme, it might provide the passage for H_2O_2 entry to heme distal face [65].

Structural analysis indicates that the distal channel is wider in *B. adusta* DyP than in DyPB and is blocked in the A-type EfeB [65]. It appears that there is a correlation between the width of the channel and the reactivity of DyPs toward H_2O_2; as *B. adusta* DyP shows much more efficient peroxidase activity than DyPB, and subsequently EfeB shows the least peroxidase activity compared with DyPB [65].The propionate pocket comprises both heme propionates and several bound water molecules. It is lined by the side chains of three negatively charged residues: Asp-156, Glu-215 and Glu-239 and a positively charged one, Arg-208 [65].

The structural data also might provide an explanation for the observed significant difference reactivity of the DyPB and MnP for oxidation of Mn (II). The arrangement of three acidic residues in the propionate pocket of DyPB provides only low-affinity binding for Mn (II) in DyPB with K_M of 24mM, compared with a group of six carboxylates of negatively charged residues, involved in highly efficient binding of Mn (II) to MnP from *P. chrysoporium* with K_M of 73 μM [20].

The last discussed structure belong to a C- type DyP, DyP2 from *Amycolatopsis sp 75iv2* which represents the only solved structure of this clade so far. The structure of DyP2 from *Amycolatopsis sp. 75iv2* was solved at 2.25 Å resolution (PDB code 4G2C) by Brown *et al* [68]. It shows higher peroxidase and Mn peroxidase activity, ($k_{cat}/K_M \approx 10^5–10^6$ M^{-1} s^{-1}) compared with different DyPs from the other two bacterial clades [68]. DyP2 represents the overall α/β ferredoxin-like fold similar to other structurally characterized DyPs [56, 57, 65, 68, 82], with differences in the arrangements of loops and α-helices that surround the β-barrel core [68]. The surrounding loops provide a deeper active site pocket in DyP2 than for DyPB from *R. jostii RHA1* [68].

The active site of DyP2 shows the same architecture of arrangement of the conserved histidine as the proximal residue and the conserved arginine (Arg-348) and aspartate (Asp-190) in the distal face as the other DyPs [56, 65, 68, 82].

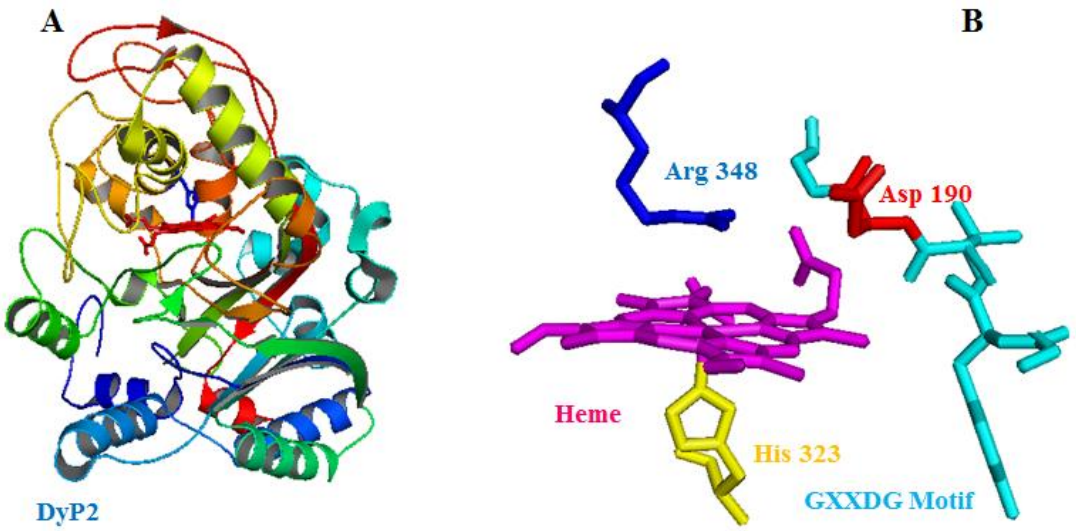

Figure 1.18 - The overall structure of DyP2 from *Amycolatopsis sp 75iv2* (A) and arrangement of conserved catalytic residues around heme (B). The picture was generated by PyMOL [105].

The Mn (II) binding site is formed by the carboxylate groups of three negatively charged residues: Glu-258, Glu-273, Glu-284 and a structural water that chelate Mn (II) ion in the binding site. Tyr-188 in between the heme and Mn (II) binding site could act potentially as a mediator for long-range electron transfer in Mn (II) oxidation [68]. Fig. 1.18 and Fig. 1.19 represent the overall structure of DyP2 and arrangement of residues around heme.

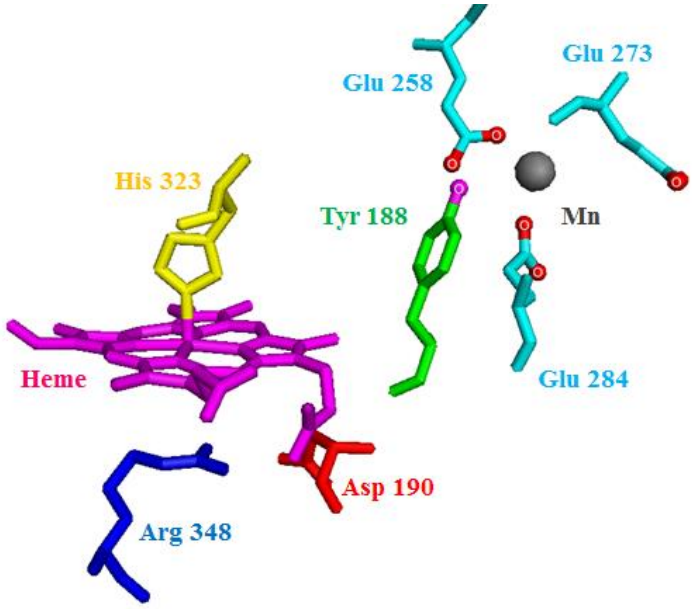

Figure 1.19 - Constituent residues of Mn (II) binding site in DyP2 from *Amycolatopsis sp 75iv2* and probable redox active amino Tyr-188 in between the heme and Mn (II) binding site. The picture was generated by PyMOL [105].

Goblirsch *et al*. recently showed by sequence and structural analysis that the DyP peroxidases shared a similar structure fold to chlorite dismutases. They suggested that the chlorite dismutases, DyP peroxidases and EFeB families comprise a new structural superfamily together, and proposed the name of CDE superfamily [78].

1.7.3 Reactivity and mechanism of DyP Peroxidases

In this section the reactivity of the DyP type peroxidases for the different substrates, the different type of reactions that they catalyse and finally the reaction intermediate and catalytic cycle will be discussed.

1.7.3.1 D-type DyP peroxidases

DyP-type peroxidases show distinctive aspects regarding their reaction features and structures [46]. Results indicate that fungal DyP-type peroxidases are very active against anthraquinone dyes and exhibit modest activity toward standard peroxidase substrates and azo dyes [55, 86]. Substrate specificity experiments have shown that DyP from the fungus *B. adusta* represents significant decolorizing rates for dyes such as reactive blue 5, reactive blue 19, and reactive blue 21. However, dyes like Reactive red 33, reactive black 5, and reactive violet 23 are weakly decolorized [86].

Contrary to LiP, DyP is not able to oxidise veratryl alcohol, however guaiacol and 2,6-dimethoxyphenol are oxidized by DyP from the fungus *B. adusta*. DyP also does not show any reactivity toward oxidation of Mn (II) [86].

Regarding the noteworthy activity of DyP against anthraquinone dyes, particularly Reactive Blue 5 (RB5, a synthetic dye and xenobiotic), Sugano *et al.* inspected the reaction products of RB5 treated with DyP by electrospray ion mass spectrometry (ESI-MS) and nuclear magnetic resonance, and for the first time proposed a degradation pathway for the reaction [87]. One of the characterized compounds from reaction products mixture is phthalic acid (Fig. 1.20) that could be generated not by a peroxidase effect but via a hydrolase- or oxygenase-catalyzed reaction, that suggests that DyP is a bifunctional enzyme [87].

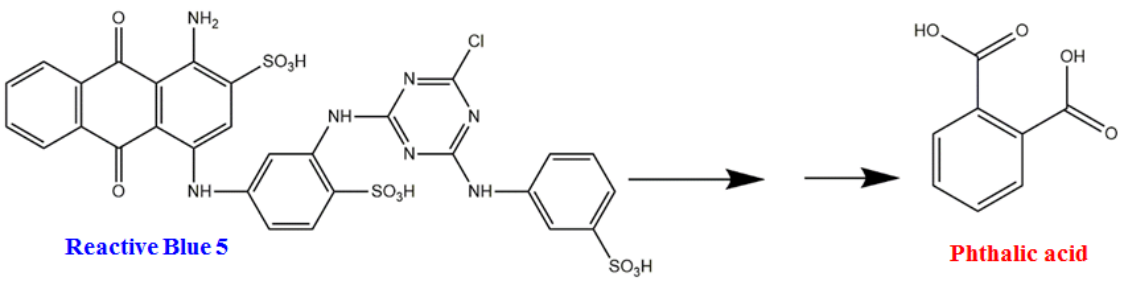

Figure 1.20 - Structure of Reactive Blue 5, an anthraquinone dye, and Phtalic acid, one of the products, produced during the degradation of RB5 by the DyP from *B. adusta*

Liers *et al.* purified and characterized two secreted D-type DyP peroxidases from jelly fungus *A.auricula-judae* [70]. Kinetic data showed that both enzymes not only catalyze the typical peroxidase substrates such as DMP (2,6-dimethoxyphenol) and ABTS (2,2′-azino-bis(3-ethylthiazoline-6- sulfonate)) but, they can also catalyze the decolorization reaction of high-redox potential dyes such as Reactive Blue 5 and Reactive Black 5 [70]. Fig. 1.21 and Fig. 1.22 depict chemical structures of ABTS, Reactive Blue 5 and Reactive Black 5 dyes.

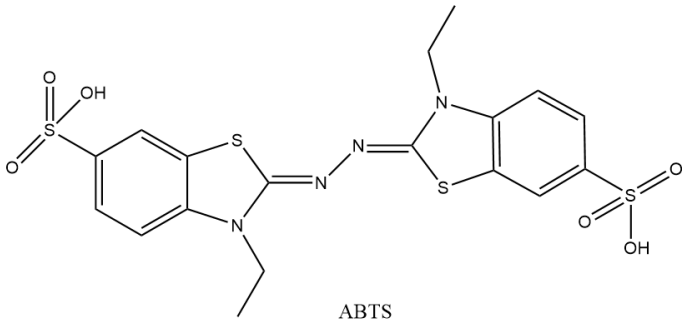

Figure 1.21 - Chemical structure of ABTS (2,2′-azino-bis(3-ethylthiazoline-6- sulfonate))

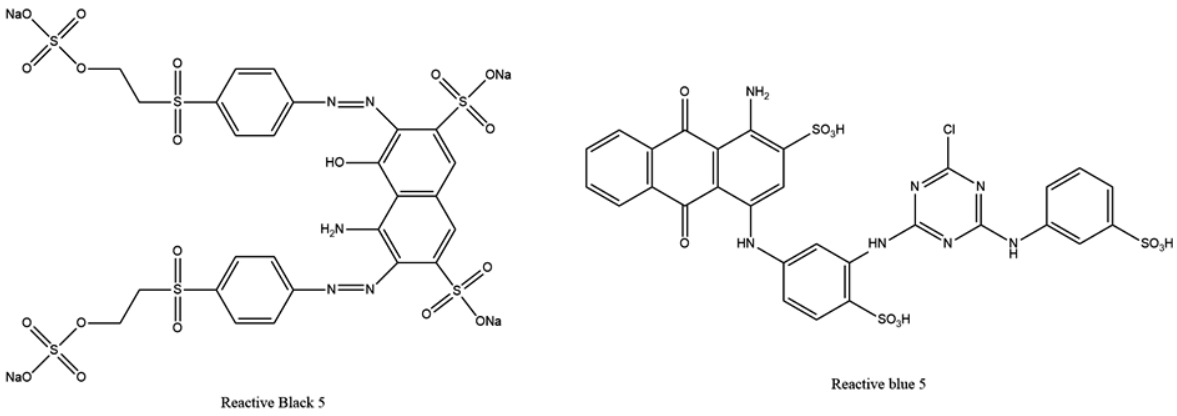

Figure 1.22 - Chemical structure of Reactive Blue 5 and Reactive Black 5

Oxidation of veratryl alcohol into veratraldehyde is considered to be a unique catalytic feature of high-redox potential peroxidases like LiP, VP, whereas the

decolourization of Reactive Blue 5 is a characteristic of DyP-type peroxidases and cannot be performed by LiP or VP [70]. Surprisingly, both AjP I and II exhibit oxidation activity toward nonphenolic lignin model compounds such as veratryl alcohol and adlerol (Fig. 1.23), a nonphenolic β-O-4 lignin model dimer, that is indicative of ligninolytic activity of these two secreted DyP from *A. auricula-judae* [70,88-90].

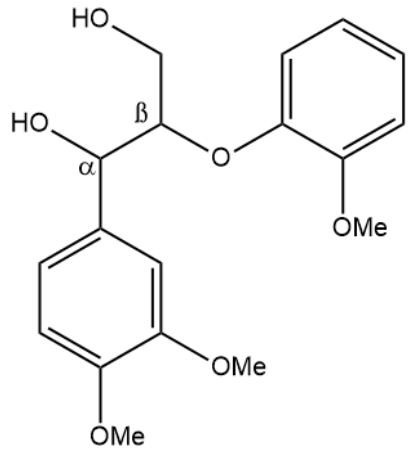

Figure 1.23 - Chemical structure of adlerol, a nonphenolic β-O-4 lignin model dimer

Considering the ability of both AjP I and II for oxidation of various substrates such as veratryl alcohol, non-phenolic lignin model dimers, as well as recalcitrant phenols and dyes, determination of their redox potential could help to understand their reactivity. Liers. *et.al.* determined the redox potential for five fungal DyPs including AjP I and II [60]. Based on the used method, the redox potentials of tested DyPs vary between 1.10 ± 0.02 and 1.20 ± 0.1 V, lower than high-redox potential LiP (1.26 ± 0.17 V) but higher than phenol-oxidizing plant (0.93 ± 0.04 V for SBP) and fungal (1.06 ± 0.07 V for CiP) peroxidases [60].

1.7.3.2 A-type DyP peroxidases

Van Bloois *et al*. characterized TfuDyP, A-type DyP, from *T.fusca*, a moderate thermophile bacteria. Kinetic analysis showed that TfuDyP exhibits dye-decolorizing activity and modest activity towards phenolic compounds such as guaiacol and 2,6-dimethoxyphenol [63]. Similar to the other DyPs [55], TfuDyP shows high activity for anthraquinone dyes such as Reactive Blue 19, and Reactive Blue 4, but low activity for Reactive Black 5, an azo dye [63]. In addition, TfuDyP can catalyze enantioselective sulfoxidation, a type of reaction that had not been reported before for DyP-type peroxidases [63]. For example, TfuDyP converts in to the (*R*)-sulfoxide with 61% ee [63].

Le´toffe *et al*. identified YfeX and EfeB, two *E. coli* paralogs, which belong to DyP-type peroxidase family [74]. They showed that these two enzymes can catalyze the release of iron from heme without tetrapyrrole degradation, a reaction referred to as deferrochelation of the heme. Accumulation of protoporphyrin IX (PPIX) in cells overexpressing these two proteins was an indication of deferrochelation activity [74]. The catalytic mechanism for removing iron from heme is still unknown [82]. Kinetic data has shown that EfeB exhibits modest guaiacol peroxidase activity, so EfeB could be considered as a bi-functional enzyme [82].

1.7.3.3 B-type DyP peroxidases

Ahmad *et al*.[64] and Roberts *et al*. [65] separately identified and characterised two DyPs enzyme from RHA1, A-type and B-type DyP, named DyPA and DyPB respectively. Steady-state kinetic data of these enzymes showed that they represented much lower peroxidase activities than C- and D-type DyPs [65]. By comparing reactivity of DyPA and DyPB towards different substrates, DyPA revealed greater substrate specificity for Reactive

Blue 4, an anthraquinone dye, than ABTS or pyrogallol. However, DyPB exhibited greater specificity for ABTS and showed very modest Mn (II) oxidation activity [65].

The obtained kinetic data stress that the C- and D-type DyPs display much higher peroxidase activities towards AQ dyes than the A- and B-type enzymes [65]. The determined k_{cat}/K_M of DyPB for oxidation of Mn(II), k_{cat}/K_M= 25, is nearly 10^4-10^5-fold lower than of the manganese peroxidases from *P. chrysosporium* by k_{cat}/K_M values of 25 and 4×10^6 respectively[91]. Mutation of the distal heme residue, Asn-246, to Ala raised the enzyme's k_{cat}/K_M for Mn^{2+} by 15-fold [66]. The N246A mutant was studied for catalyzing the manganese-dependent degradation of hardwood Kraft lignin, and the degradation products were identified by GC-MS as 2,6-dimethoxybenzoquinone and 4-hydroxy 3,5-dimethoxybenzaldehyde [66].

DyPB exhibits activity for Kraft lignin as a substrate and shows saturation kinetic behaviour for Kraft lignin at 465 nm [64]. DyPB shows activity toward β-aryl ether lignin model compounds and the reaction produces vanillin, indicating cleavage of Cα-Cβ bond (Fig.1.24) [64]. Moreover, studies on a *R. jostii RHA1*gene deletion mutant for DyPB, using a colorimetric lignin degradation assay [92] showed that Δ*dypB* mutant revealed lower lignin degradation activity than wild-type *R. jostii RHA1*. That is in agreement with the suggested role of lignin breakdown for DyPB in *R. jostii RHA1* [64].

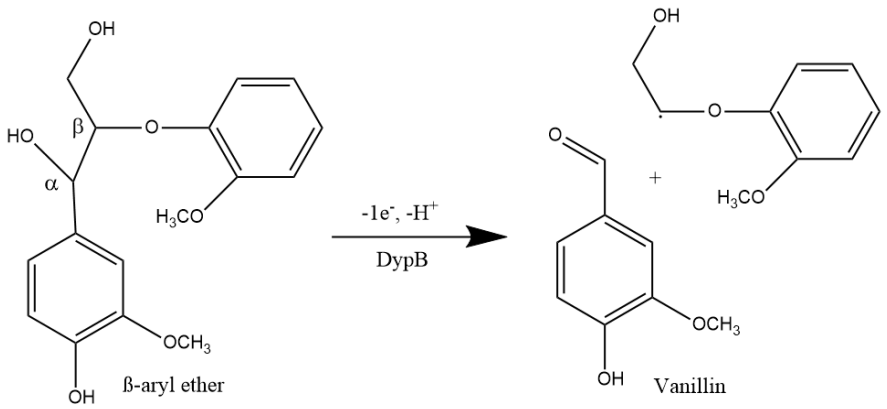

Figure 1.24 - Reactivity of DyPB toward β-aryl ether lignin model compound that leads to production of vanillin, an indication of occurring Cα-Cβ bond cleavage in course of reaction catalysed by DyPB

1.7.3.4 C-type DyP peroxidases

Brown *et al*. characterized DyP2, a C-type DyP from *Amycolatopsis sp*. *75iv2*. The measured redox potential for this enzyme is −85 ± 13 mV, close to the redox potential of manganese peroxidases [68, 93]. DyP2 exhibit an extensive range of peroxidase activity against substrates such as aromatics, azo dyes, anthroquinone dyes, and Mn^{2+}. It shows high activity for oxidation of phenolics compound such 2,4-dichlorophenol. DyP2 represents high specific activity toward Reactive Blue 5 and ABTS, an anthroquinone dye and azo dye respectively. The kinetic parameters for these two dyes are more similar to the D-type DyPs rather than lower values of the characterized bacterial A- and B-type DyPs. Moreover, DyP2 can decolourise Reactive Black 5, an azo dye with high oxidation potential [68]. Among all of the DyPs characterized so far; DyP2 exhibits the highest Mn^{2+}oxidation capacity, k_{cat}/K_M=1.2 ± 0.2 × 10^5, only 10-fold lower than of the versatile peroxidase from *Pleurotus eryngii* and 100-fold lower than that of *P.chrysosporium* Mn peroxidase [68].

1.7.4 Catalytic mechanism of the DyP peroxidases

The principal difference in active site structure between the DyP peroxidase family and the horseradish peroxidase (HRP) family is the replacement of the catalytic histidine residue in the latter family with an aspartic acid residue. As shown in Fig. 1.25, the active site histidine residue of HRP is believed to function as an acid-base residue in the formation of compound **I**, an iron (IV)-oxo cation radical species responsible for substrate oxidation [94-96]. His-42 initially deprotonates hydrogen peroxide, then protonates the distal oxygen of the bound peroxide, generating compound **I**, which is further stabilized by an arginine residue present in the active site [97].

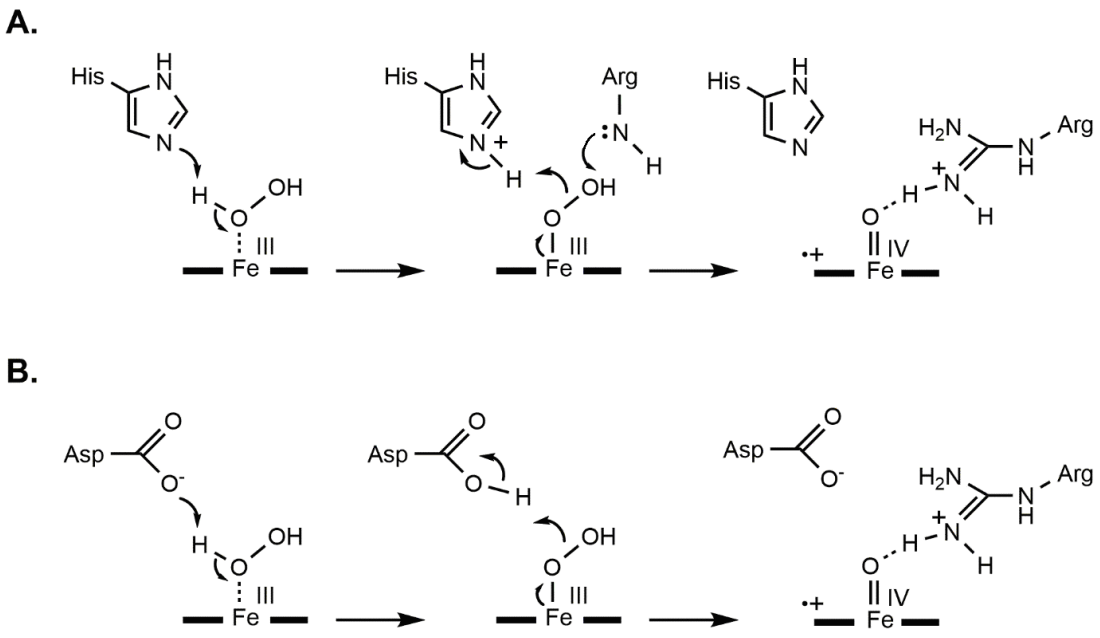

Figure 1.25 - Comparison of mechanisms for compound **I** formation in (A) horseradish peroxidase (B) DyP peroxidase Dec1

In the DyP peroxidase family, the catalytic His residue of HRP is replaced by an aspartic acid residue, whose role in catalysis is reflected in the lower optimal pH of the DyP peroxidases, a pH_{opt} of 3.2 was reported for Dec1 from fungus *B. adusta* [56]. Replacement of Asp-171 in *B. adusta* Dec1 by Asn leads to a 3,000-fold loss in catalytic activity, consistent

with a catalytic role in protonation of the bound peroxide [56]. The crystal structure of the D171N Dec1 mutant and wild-type enzymes shows considerable movement of the Asp/Asn residue, with high measured RMSD values, suggesting that the movement of Asp-171 within the active site is needed for protonation of peroxide [79].

The active site of bacterial DyPB from *R. jostii RHA1* also contains an aspartic acid Asp-153, a nearby Asn-246 residue, and an arginine residue Arg-244 [65]. Surprisingly, Asp-153 and Asn-246 were found not to be essential for compound **I** formation in DyPB, although their mutation did reduce the stability of the intermediate compound **I** [67]. Arg-244 was found to be essential for compound **I** formation in this enzyme; hence it was proposed that Arg-244 may protonate the bound peroxide in this enzyme [67]. Although the high pK_a value of arginine (approximately 13) makes it in theory unlikely to act as a proton donor, there are several enzymes in which Arg residues have been proposed to function as proton donors [98]. Alternatively, it is possible that cleavage of the O-O bond occurs via homolytic cleavage in this case, and that the Arg residue stabilises the iron-oxo species formed, and hence reduces the activation energy for compound **I** formation. It is known that the active site Arg of HRP stabilises compound **I** [97], and a related homolytic O-O bond cleavage mechanism has been proposed for the intradiol catechol dioxygenase family, which also contain a nearby active site Arg residue [99].

The iron-oxo intermediates formed in the two DyP enzymes DyPA and DyPB from *R. jostii* have been analysed by UV-vis and EPR spectroscopy [65]. The intermediate formed in DyPA shows λ_{max} 419 nm, similar to compound **II** of HRP [65]. The intermediate formed in DyPB is particularly long-lived (half-life 9 min), and shows λ_{max} 397 nm, similar to compound **I** of HRP, but the EPR spectrum of this species is different from that of HRP, showing the presence of an organic radical species, suggesting the possible existence of a protein-based radical [65].

Remarkably, *R. jostii* DyPB has been found to show activity as a lignin peroxidase, the first bacterial lignin peroxidase enzyme to be identified [64]. DyPB was found to show activity for oxidation of Mn(II), and also activity towards a β-aryl ether lignin model compound, raising the question of whether this enzyme is similar to the fungal manganese peroxidase [64]. Analysis of these two reactions by pre-steady state kinetics showed similar rate constants for oxidation of Mn(II) (2.35 s^{-1}) and lignin model compound (3.10 s^{-1}) are similar, indicating that DyPB can directly oxidise either substrate, hence this enzyme appears to have different sites for interaction with Mn(II) or lignin. Analysis of the reaction products from cleavage of the β-aryl ether lignin model compound showed that the enzyme catalyses oxidative cleavage of the C_α-C_β bond, similar to the behaviour shown by fungal lignin peroxidases. In the presence of the lignin model compound, the formation of compound **II** species could be observed by pre-steady state kinetics at 417 nm, hence a catalytic cycle for DyPB was proposed, as shown in Fig. 1.26.

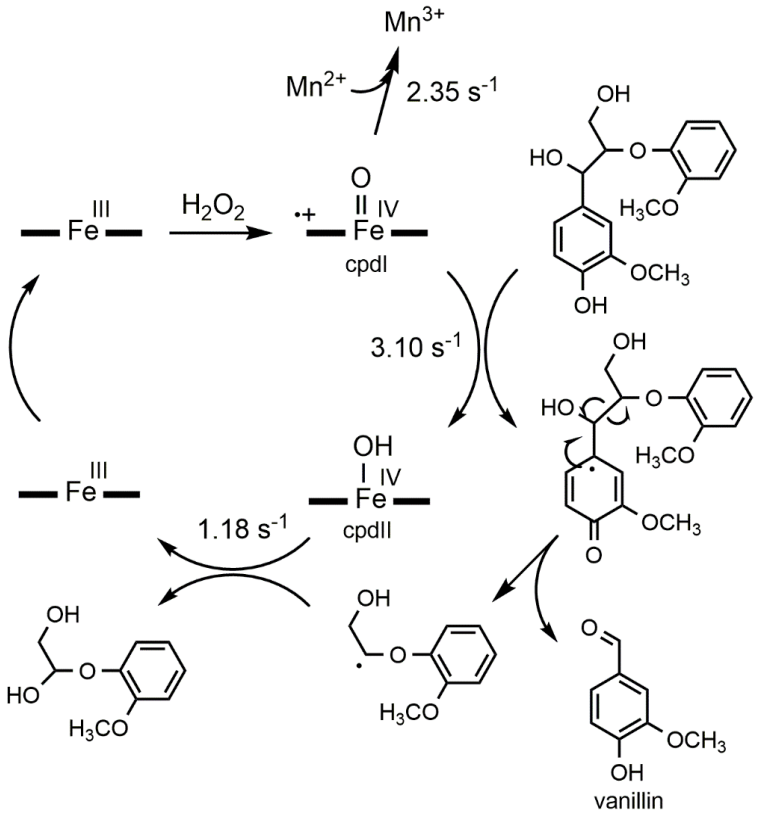

Figure 1.26 - Catalytic cycle for oxidation of lignin model compound by *R. jostii* DyPB

DyPB also showed activity for oxidation of Kraft lignin, and in the presence of Mn (II), time-dependent activity towards lignocellulose was observed [64]. More recently the N246A mutant of *R. jostii* DyPB has been shown to be more active for Mn (II) oxidation, and a Mn (II) binding site identified by X-ray crystallography close to the heme edge [66]. Two aromatic products of wood oxidation were identified, highlighting the potential for the DyP peroxidases for valorisation of lignin [66].

1.7.5 Applications of DyP peroxidases

In this last section, briefly some potential applications of DyPs enzyme based on their exhibited broad reactivity towards different substrate are discussed. DyPs catalyze many reactions, among them several conversions that are biotechnologicaly desirable.

Synthetic dyes are extensively produced and utilized in many industries, some of which are released to the environment mostly as wastewater. DyPs could be used in degradation and bioremediation of dyes in the environment. In particular, fungal and C-type DyP have shown significant ability to degrade anthraquinone dyes and azo dyes. For instance, DyP from *B. adusta* could degrade anthraquinone dyes and modify the molecular structure of several other industrial dyes [87]. DyP2 from *Amycolatopsis sp. 75iv2* is competent to oxidize higher potential dyes such as Reactive Black 5 [68] and both enzymes from fungus *A. auricula-judae,* AauDyPI & AauDyPII also catalyze the decolorization of the high-redox potential dyes such as Reactive Blue 5 and Reactive Black 5 [70]. Certainly the structural analysis and rational mutagenesis along with directed evolution approach will drive the improvement and suitability of DyPs enzyme for bioremediation through altering their substrate specificity and increasing their stability against elevated temperature, industrial denaturant and most importantly high concentration of hydrogen peroxide.

DyPs could be exploited in enzymatic lignocellulose degradation/modification processes. For example DyPB from *R. jostii RHA1,* DyP2 from *Amycolatopsis sp. 75iv2* and AauDyPs from *A. auricula-judae* have shown noteworthy observations in the degradation/modification of lignin model compound [64, 70], kraft lignin [64, 66] and lignocelluse [64]. Further optimization and protein engineering studies undoubtedly will increase their promising potential for degradation of recalcitrant compounds present in Biomass.

1.8 Aim

The aim of this project is to provide a detailed comparative study in enzymology of dye-decolorising peroxidases, DyP, from *Pseudomonas fluorescens* and from *Thermobifida fusca*, a thermophile bacterium. Another objective is a primary study of encapsulin, a recently discovered icosahedral nanocompartment protein from *Rhodococcus jostii Rha1*.

As well as Gram-positive actinobacteria such as *Rhodococcus* [92], *Streptomyces* [92], and *Microbacterium* [100], lignin degradation activity has been detected in Gram-negative aromatic degraders such as *Pseudomonas putida* [92] and *Ochrobactrum* [100], but the enzymology of lignin oxidation in these organisms is unknown. Bioinformatic searches using the BLAST algorithm in genomes of bacteria in the *Pseudomonas* genus revealed that *Pseudomonas fluorescens* Pf-5 contains three sequences related to the DyP family of peroxidase enzymes: DyP1B, DyP2B and DyPA. In this project, we aimed to investigate the enzymology of these three DyP-type peroxidases from Gram-negative Pseudomonas fluorescens Pf-5, and we identified a novel DyP-type peroxidase as an enzyme capable of lignocellulose oxidation. In addition, we also aimed for further steady and pre-steady state kinetic characterization and managed to solve the crystal structure of a DyP enzyme from

Thermobifida fusca, a thermophile bacterium that recently has been shown to belong to DyP family of peroxidase enzymes.

The specific aims of the project are as follows:

- Isolation, cloning, expression and purification of the three DyP genes from *P. fluorescens.*
- Isolation, cloning, expression and purification of the TfuDyP from Thermobifida fusca
- Steady state kinetic characterization of purified enzymes by different substrates and specific dyes.
- Pre-steady state kinetic characterization of DyP1B
- Pre-steady state kinetic characterization of TfuDyP
- Checking reactivity of purified enzyme towards lignin model compounds and lignocellulose and characterization of produced products
- X-ray Crystallography studies for solving the structure of TfuDyP
- Carrying out site- directed mutagenesis based on obtained structural data from TfuDyP for assessing role of residues in the active site of TfuDyP

Another objective in this PhD project is a primary study of encapsulin, a recently discovered icosahedral nanocompartment protein from *Rhodococcus jostii Rha1*. Compartmentalizing materials and enzymatic reactions for increasing metabolic efficiency is one of the outstanding characteristics of living cells. There has been a belief for a long time; that prokaryotic cells are inherently unstructured sacks of cytoplasm and the compartmentalization processes take place only in the eukaryotes. However, recent researches by utilizing electron microscopy, structural and biochemical techniques have changed this view.

Protein-based organelles or so-called the microcompartments, have been recently identified in bacteria. They comprise of a polyhedron-shaped arrays of protein monomers that accommodate particular enzymes/proteins in their inside that catalyse a specific biochemical pathway [101]. For instance carboxysome, an icosahedral protein complex, that sequesters ribulose 1, 5-bisphosphate carboxylase/oxygenase (RubisCO) enzyme along with a carbonic anhydrase [102, 77], Pdu microcompartment that contains enzymes for 1,2-propanediol utilization [103] and Eut microcompartment that contains enzymes for ethanolamine utilization [104] could be mentioned as examples of well characterised of these microcompartment.

A 240 Å icosahedral nanocompartment has been characterized in hyperthermophilic bacterium *Thermotoga Maritima*, whose shell-forming protein is called encapsulin [76]. Encapsulins constitute a class of nanocompartments widespread in bacteria and archaea whose functions have been unclear yet. *Rhodococcus jostii* RHA1 peroxidase DyPB has been recently identified as a bacterial lignin peroxidase and the *dypB* gene is cotranscribed with a gene encoding an encapsulin protein [64]. We wished to investigate whether DyPB is packaged within the encapsulin nanocompartment, and examine what effect the nanocompartment has on lignin degradation activity. In this project the reconstitution of purified recombinant *R. jostii* encapsulin with *R. jostii* DyPB to form a packaged nanocompartment is discussed.

The specific aims of the project are as follows:

- Purification of encapsulin from *R. Rha1*
- Monitoring assembly/disassembly of the encapsulin complex
- Investigation of the interaction of the DyPB enzyme with encapsulin
- Investigation of enzymatic activity of encapsulated DyPB

Some of the results from next chapter have been published in Arch Biochem Biophys.

Rahman Rahmanpour and *Timothy DH Bugg*. Characterisation of DyP-type peroxidases from *Pseudomonas fluorescens* Pf-5: Oxidation of Mn (II) and polymeric lignin by DyP1B.

2015 Jan 3. pii: S0003-9861(14)00447-0. doi: 10.1016/j.abb.2014.12.022.

Chapter Two

Characterisation of DyP-type Peroxidases from *Pseudomonas fluorescens* Pf-5

2.1 Introduction

The DyP family (EC 1.11.1.19) is a branch of the heterogenic group of the peroxidase enzymes. The first dye-decolorizing peroxidase was discovered in basidiomycete *Bjerkandera adusta* in 1995, and showed ability for degrading activity toward lignin, molasses and synthetic dyes like anthraquinones (AQs) [51-54].

Genomic analyses have exhibited that DyPs occur in a wide variety of fungi and bacteria. It appears that DyPs are different from general peroxidases because of the distinctive primary sequence and tertiary structures, and unique reaction characteristics that they represent [46]. A bacterial peroxidase from *Bacteroides thetaiotaomicron* (BtDyP) was the second reported purified DyP enzyme whose tertiary structure was determined, followed by the TyrA protein from bacteria *Shewanella oneidensis* as the third structure published for DyP-type peroxidases [57, 58].

The DyP family was initially considered to be structurally related to the class II secretory fungal peroxidases. However, further studies showed that DyPs are phylogenetically

as well as structurally unrelated to all previously described peroxidase families. Therefore, a new family of enzymes was established to accommodate these new peroxidases [56, 46].

Ahmad *et al*., and Roberts *et al.,* recently have identified and fully characterized two DyP-type peroxidases enzyme from Gram positive bacterium *Rhodococcus jostii RHA1*, and for the first time they showed a distinct class of DyP type peroxidase that shows manganese-dependent lignin peroxidase activity, which plays a significant role in lignin degradation by *R. jostii RHA1* [64, 65]. Brown *et al.,* reported the identification, characterization and tertiary structure determination of a multifunctional dye-decolorizing peroxidase from another Gram positive bacterium *Amycolatopsis sp*. *75iv2*, a lignin-reactive bacterium [68]. Their studies indicated that the characterized DyP shows versatile and significantly high activity for both peroxidase and Mn peroxidase function compared to other bacterial DyPs.

PeroxiBase database and phylogenetic analyses classify DyP-type peroxidases into four phylogenetically distinct subfamilies A, B, C, and D [62]. A, B and C subfamilies comprise bacterial DyPs, whereas subfamily D is fungal [56, 46, 62, 64]. DyPB and DyPA from *R. jostii RHA1* [65] are clustered in clades B and A respectively [65], and DyP2 from *Amycolatopsis sp*. *75iv2* is clustered in clade C [68]. DyPs molecular weight range is from nearly 60 kD in fungal DyPs to 30 kD in bacterial DyPs. Steady state kinetics studies have shown that the peroxidase activities of the A and B type DyP members for ABTS and anthraquinone dyes are 3–4 orders of magnitude lower than those exhibited by those of the C or D subfamilies [69].

There have been some reports that bacteria such as *Streptomyces viridosporus* could break down lignin [3]. However, the enzymology of bacterial lignin degradation was before 2011 poorly understood [4]. DyPB from *Rhodococcus jostii* RHA1 has been identified that can oxidise a β-aryl ether lignin model compound, and can attack Kraft lignin or wheat straw lignocellulose in the presence of Mn^{2+} [5].

As well as Gram-positive actinobacteria such as *Rhodococcus* [12], *Streptomyces* [12], and *Microbacterium* [13], lignin degradation activity has been detected in Gram-negative aromatic degraders such as *Pseudomonas putida* [12] and *Ochrobactrum* [13], but the enzymology of lignin oxidation in these organisms is unknown. In this chapter, three DyP-type peroxidases from Gram-negative *Pseudomonas fluorescens* Pf-5, and a novel DyP-type peroxidase as an enzyme capable of lignocellulose oxidation are investigated.

Bioinformatic searches using the BLAST algorithm in genomes of bacteria in the *Pseudomonas* genus revealed that *Pseudomonas fluorescens* Pf-5 contains three sequences related to the DyP family of peroxidase enzymes. As shown in Figure 1, there is a 35 kDa enzyme (uniprot entry name of Q4KA97_PSEF5), DyP2B, which clusters in the DyPB class of enzymes, and has 47% sequence similarity to *R. jostii* DyPB. Secondly, there is a 47 kDa heme containing peroxidase (uniprot entry name of Q4KBM1_PSEF5), DyPA, which clusters in the DyP class of enzymes, which has 31.7% sequence similarity to *R. jostii* DyPA. Thirdly, there is a 32 kDa enzyme (uniprot entry name of Q4KAC6_PSEF5), DyP1B, which clusters in a group of enzymes slightly distinct from the DyPB enzymes which has 21.4% sequence similarity to *R. jostii* DyPB. Fig. 2.1 shows phylogenetic tree for *Pseudomonas fluorescens* DyP sequences versus DyPB and DyP2C enzymes. It appears that DyPA and DyP2C are sole representatives of their family and are clustered in separate clades whereas DyP2B and Rha1 are clustered together. We would expect that DyP1B would be most similar to the two formerly mentioned DyP type B peroxidases, particularly with DyP2B.

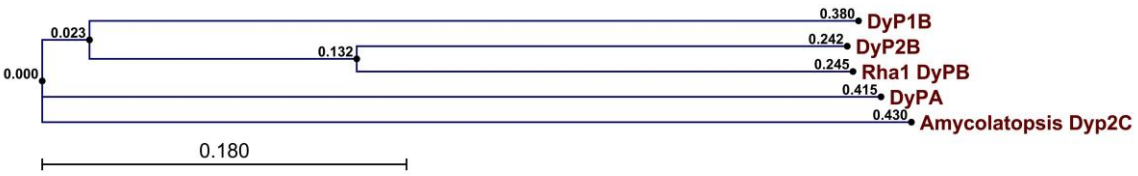

Figure 2.1 - Phylogenetic tree for *Pseudomonas fluorescens* DyP sequences versus DyPB and DyP2C enzymes

Fig. 2.2 exhibits the protein sequence alignment of three DyPs of *P. fluorescens* Pf-5, a Gram-negative bacterium, with DyPB from *R. jostii*, a Gram-positive bacterium. The alignment showed 21 identical and 61 similar positions in these four sequences respectively.

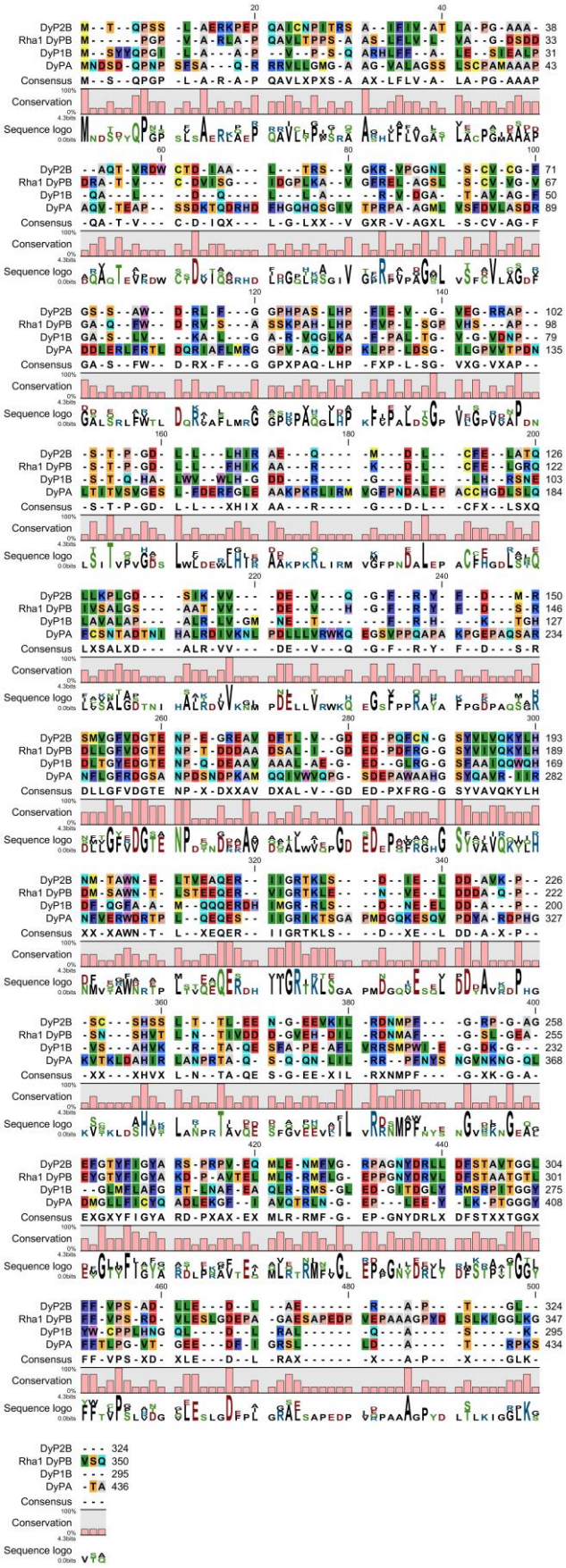

Figure 2.2 - Sequence alignment of three DyPs of *Pseudomonas fluorescens* Pf-5 with DyPB from *Rhodococcus jostii RHA1*

2.2 DyP1B

2.2.1 Expression and purification of DyP1B

For cloning of *dyp1b*, genomic DNA of *P. fluorescens* Pf-5 was extracted using Wizard® Genomic DNA Purification Kit from Promega, from a total 1 ml of overnight culture of *P. fluorescens* Pf-5 in Luria-Bertani broth. Forward and reverse primers were designed for the *dyp1b* and a CACC overhang was added to the forward primers at the 5' end for purpose of performing TOPO cloning method. The designed primers for isolation of *dyp1b* gene are as follows: $_{5'}$C ACC ATG AGT TAC TAC CAG CCC GG$_{3'}$ and $_{5'}$TCA TTT CGA CGC TTG CAG CG$_{3'}$. PCR reactions were carried by using Platinum Pfx-DNA polymerase from Invitrogen, following the manufacturer's instructions. Fig. 2.3 shows the agarose gel picture of PCR product of the amplified *dyp1b* in its predicted size 888 base pair.

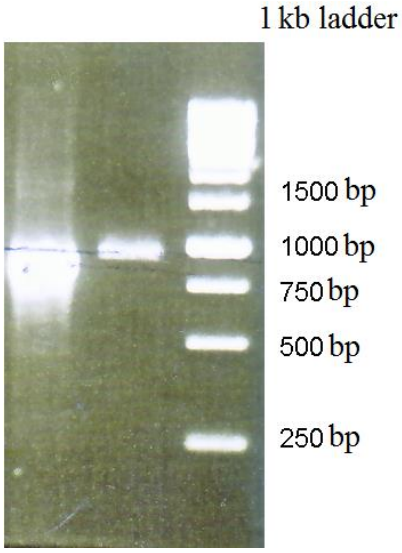

Figure 2.3 - Agarose gel of PCR products of two loading *dyp1b* in the predicted size of 888 base pair.

The amplified gene was cloned using the Champion™ pET 151 Directional TOPO® Expression Kit (Invitrogen) into expression vector pET151, and transformed into *E. coli* TOP10 competent cells (Invitrogen). The extracted plasmids from the obtained colonies were sent for sequencing, to confirm the accuracy of the sequence and the ligation respectively.

The sequencing results showed that the amplified genes did not contain any mutations, and the ligated gene was in the correct orientation in the vector. The recombinant plasmid was then transformed into BL21 *E. coli* (Invitrogen), for protein expression.

The recombinant *dyp1b* was expressed by adding a grown overnight starter culture in the presence of 100 mg/ml ampicillin to 2 litre Luria-Bertani broth for 3 hours at 37 °C, and finally the cells were induced by adding 0.5 mM final concentration of IPTG and shaken overnight at 15°C. Cell pellets were harvested by centrifugation at 4000 × g.

Protein purification was performed by metal affinity chromatography followed by TEV protease cleavage of the $(His)_6$ fusion tag. The harvested cells from a 2 litre culture described above were suspended in 20 ml lysis buffer in the presence of 1 mM final concentration of phenylmethanesulfonylfluoride (PMSF). Cell lysis was carried out using a constant system cell disrupter, followed by centrifugation at 10000 × g for 30 minute. The clear supernatant was loaded onto a Ni-NTA resin FPLC column (HisTrap HP, 1 ml volume) equilibrated with lysis buffer followed by 100 ml of wash buffer, and the recombinant protein was eluted by 7 ml elution buffer, eluting at a flow rate of 0.5 ml min^{-1}.

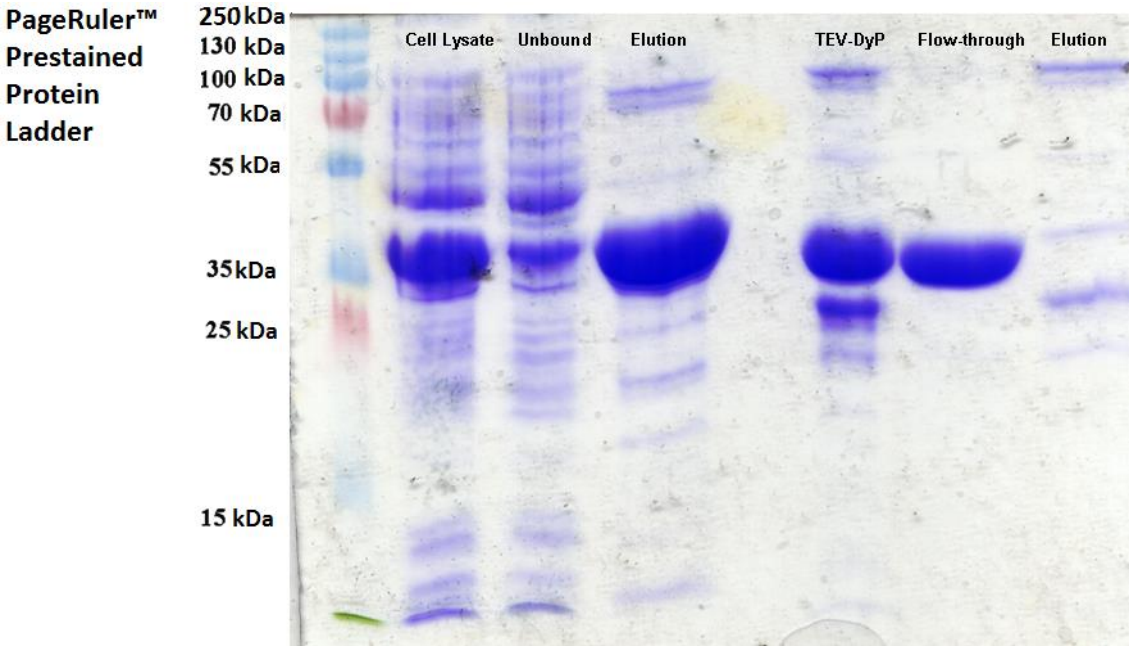

Figure 2.4 - SDS PAGE of DyP1B purification steps

A sample of eluted protein was taken for SDS PAGE and Bradford assay, the remainder of solution was subjected to buffer exchange through a PD-10 column into 10 ml wash buffer. After buffer exchange, the protein solution was mixed with previously purified TEV protease in equal molar ratio overnight in room temperature, then applied again to a Ni-NTA FPLC column, and eluted in elution buffer. The flow-through fraction (25 ml) containing untagged recombinant DyP enzyme was collected. The purified enzyme was buffer exchanged by a PD-10 gel filteration column to 20 mM MOPS 80 mM NaCl buffer pH 7.0.

Fig. 2.4 shows the SDS PAGE of purification steps of DyP1B. The band for purified DyP1B in the flow through lane eluted at 32 kDa, matching the predicted molecular weight is molecular weight of DyP1B protein.

2.2.2 Heme reconstitution

Since the purified protein was in apoprotein form and the majority of enzyme molecules population did not contain heme in their structure, heme reconstitution had to be done. Heme in DyPs is noncovalently bounded to the enzyme; therefore, heme reconstitution of DyPs is generally straightforward.

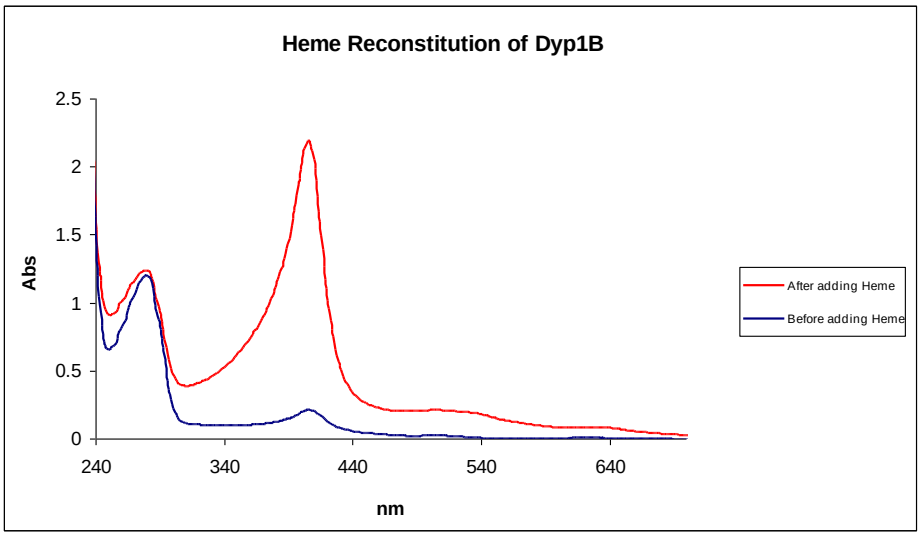

Figure 2.5 - UV/Vis scan of DyP1B before and after heme reconstitution

Heme dissolved in DMSO was added to the protein solution drop wise as explained in the experimental section. The optical absorbance of reconstituted sample was scanned in the range 200 to 800 nm. The appearance of a Soret band at 404 nm indicates the presence of heme in the protein molecules. The observed Rz ratio, (A_{Soret}/A_{280}), obtained from the UV-vis of reconstituted enzyme was 1.76. Fig. 2.5 shows the Uv/vis optical absorption scan of DyP1B protein solution. The protein solution then was concentrated by a 10 kDa Amicon centricon device, and after flash freezing in 50% glycerol using liquid nitrogen, it was stored at -80 °C for further kinetic analysis. The yield of produced DyP1B enzyme from 2 litre bacterial culture was 30 mg.

2.2.3 pH profile of DyP1B

Fig. 2.6 shows the pH profile of DyP1B determined by 2,4-dichlorophenol (DCP) assay at 25 °C using Britton–Robinson buffer in the pH range 3–10, as explained in experimental section. Optimum pH was determined by plotting natural logarithm of obtained enzymatic activity versus corresponding pH value. The optimum pH for DyP1B is 5.5, that is in good agreement with the optimum pH values obtained for other DyPs enzyme [63, 65, 68, 69].

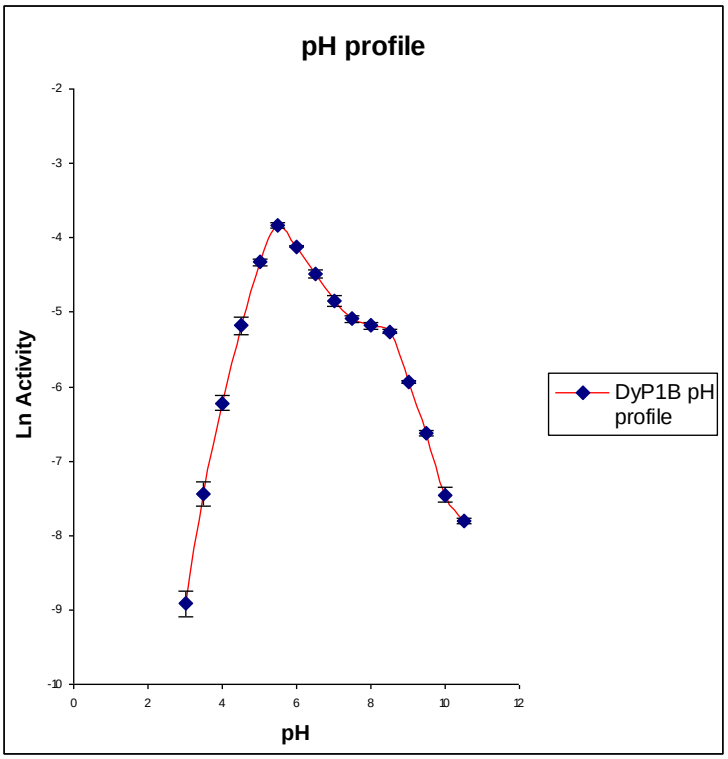

Figure 2.6 - pH profile of DyP1B

2.2.4 Temperature profile of DyP1B

Fig. 2.7 shows the temperature profile of DyP1B determined by 2,4-dichlorophenol (DCP) assay in 100 mM acetate buffer pH 5.5 at different temperature ranging 25 to 75 °C as explained in experimental section. The temperature profile was determined by plotting obtained specific activity versus corresponding temperature. The obtained optimum temperature for DyP1B is 35 to 40 °C, similar to the temperature profile of DyPs enzymes from *Bacillus subtilis* and *Pseudomonas putida* [69].

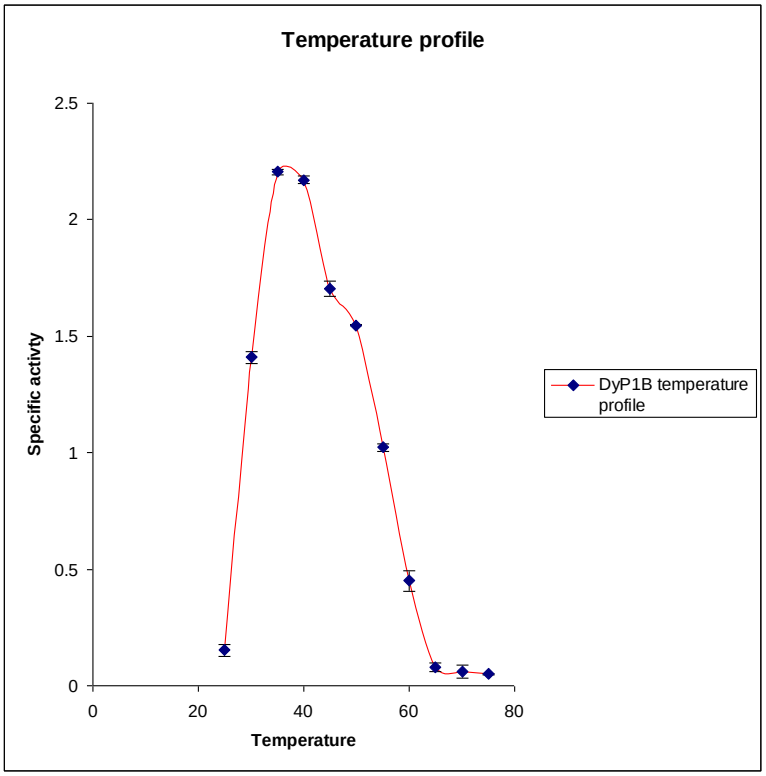

Figure 2.7 - Temperature profile of DyP1B

2.2.5 Kinetics parameters of DyP1B

DyP1B enzyme was characterised using a range of peroxidase and lignin substrates, using UV-vis kinetic assays, and K_M and k_{cat} values measured, as shown in Table 2.1. For each parameter, standard errors were determined by statistical methods and represented along with the reported data. Fig. 2.8 shows steady state kinetic plots for DyP1B for each substrate, fitted by non-linear regression method.

Table 2.1 - Steady-state kinetic data for DyP1B.

	DyP1B		
Substrate	**K_M (mM)**	**k_{cat} (s^{-1})**	**k_{cat}/K_M ($M^{-1}s^{-1}$)**
ABTS	1.13 ± 0.1	13.5 ± 0.4	1.2 x 10^4
H_2O_2 [a]	0.048 ± 0.02	23.3 ± 0.2	4.8 x 10^5
Mn^{2+}	7.3 ± 0.4	2.40 ± 0.04	330
2,4-dichlorophenol	1.25 ± 0.1	0.66 ± 0.02	530
Phenol	1.02 ± 0.08	1.22 ± 0.02	1.2 x 10^3
Guaiacol	0.056 ± 0.006	0.058 ± 0.001	1.0 x 10^3
Pyrogallol	4.0 ± 0.6	2.5 ± 0.1	620
Reactive Blue 4	0.12 ± 0.01	1.04 ± 0.03	9.0 x 10^3
Kraft lignin [b]	0.006 ± 0.001	0.9 ± 0.1	1.4 x 10^5

[a] Using ABTS as substrate, [b] Assuming molecular weight of 10000 M.W.

DyP1B enzyme showed catalytic activity with peroxidase substrate ABTS, and dye substrate Reactive Blue 4 that are characteristic of the DyP family of peroxidases [46, 55, 57, 62, 63, 70].

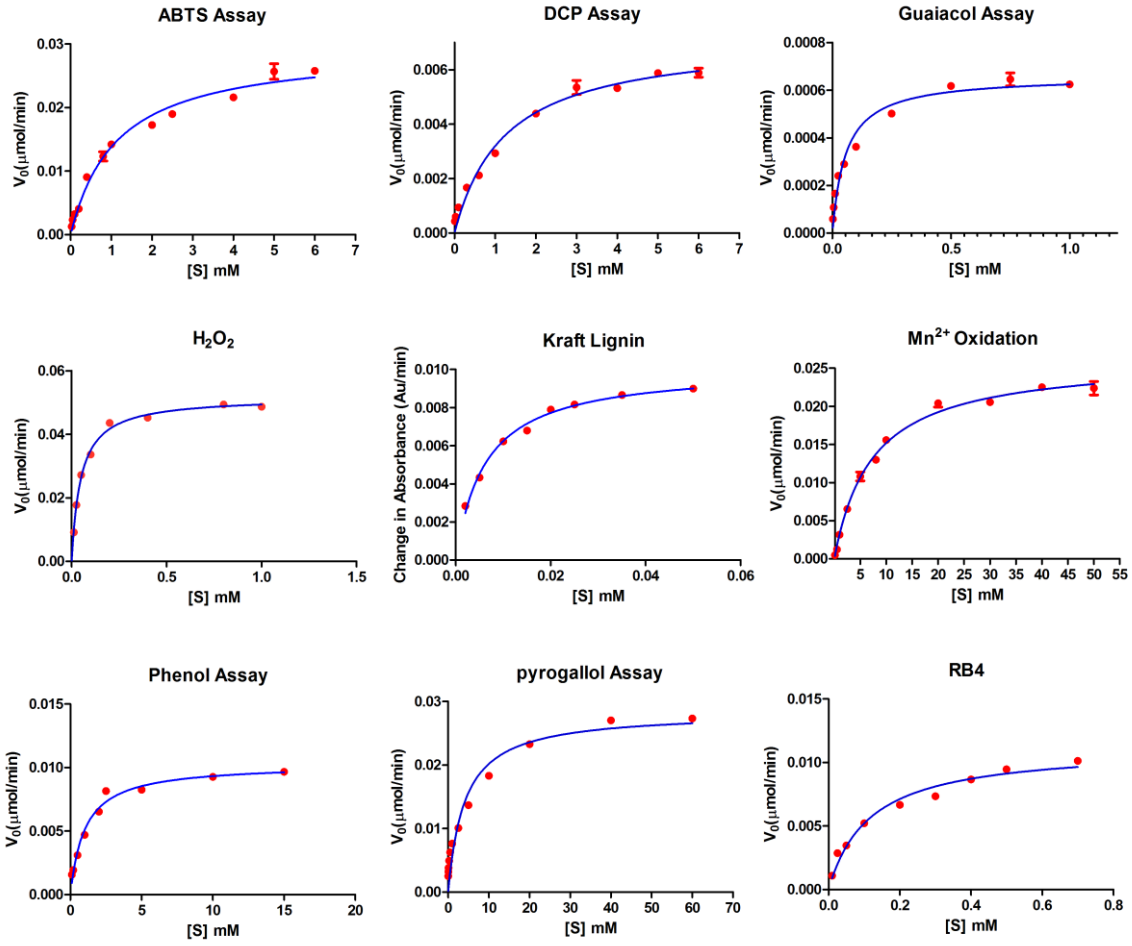

Figure 2.8 - Steady state kinetic plots of DyP1B

DyP1B showed catalytic activity for Mn^{2+} oxidation that for a bacterial peroxidase has been observed for the first time in *R. jostii* DyPB [64, 65]. However, DyP1B is four times more active than *R. jostii* DyPB (k_{cat} =0.59 (s^{-1})).

Incubation of DyP1B with alkali Kraft lignin (Sigma-Aldrich), gave a time-dependent increase in absorbance at 465 nm, also observed previously using *R. jostii* DyPB [64], and this absorbance change was found to show Michaelis-Menten kinetic behaviour, Fig. 2.8 implying

that DyP1B can oxidise Kraft lignin. Fig. 2.9 shows kinetic scanning of Kraft lignin reaction with DyP1B in presence of 1 mM hydrogen peroxide. The reactivity of Kraft lignin with DyP1B might be the result of oxidation of hydroxyl groups present in lignin monomers that leads to formation of quinone products that absorbs in 400 nm region.

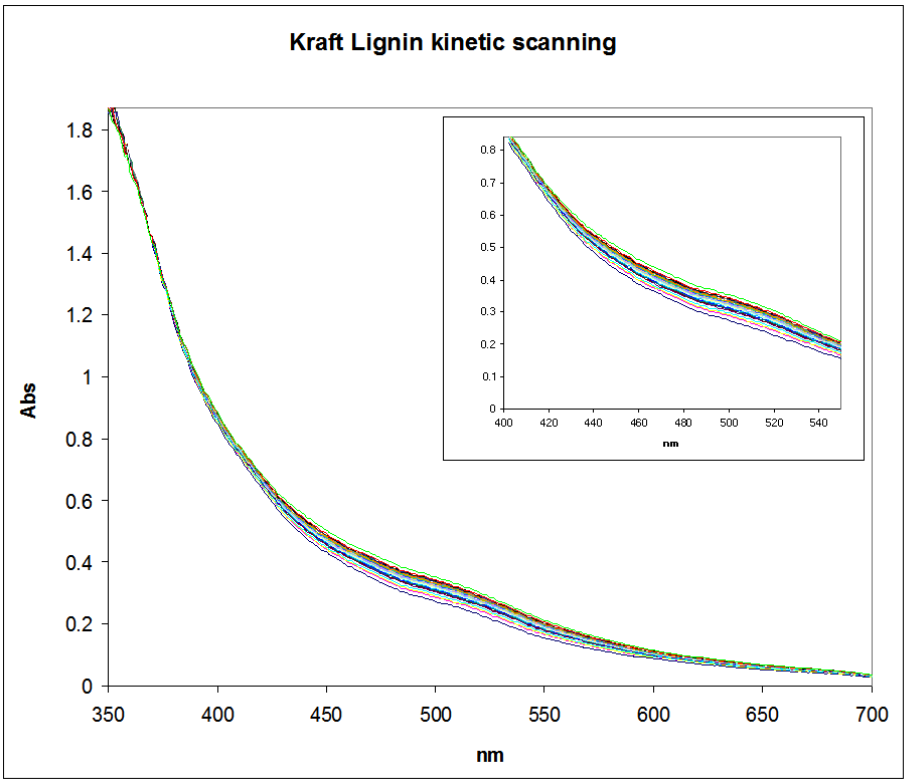

Figure 2.9 - kinetic scanning of Kraft lignin reaction with DyP1B

2.2.6 Pre-steady-state kinetic characterisation of DyP1B

The reactivity of DyP1B was further analysed by pre-steady state stopped flow kinetics. Pre-steady state mixing with hydrogen peroxide leads to the time-dependent disappearance of the Soret band at 406 nm in DyP1B (Fig. 2.10).

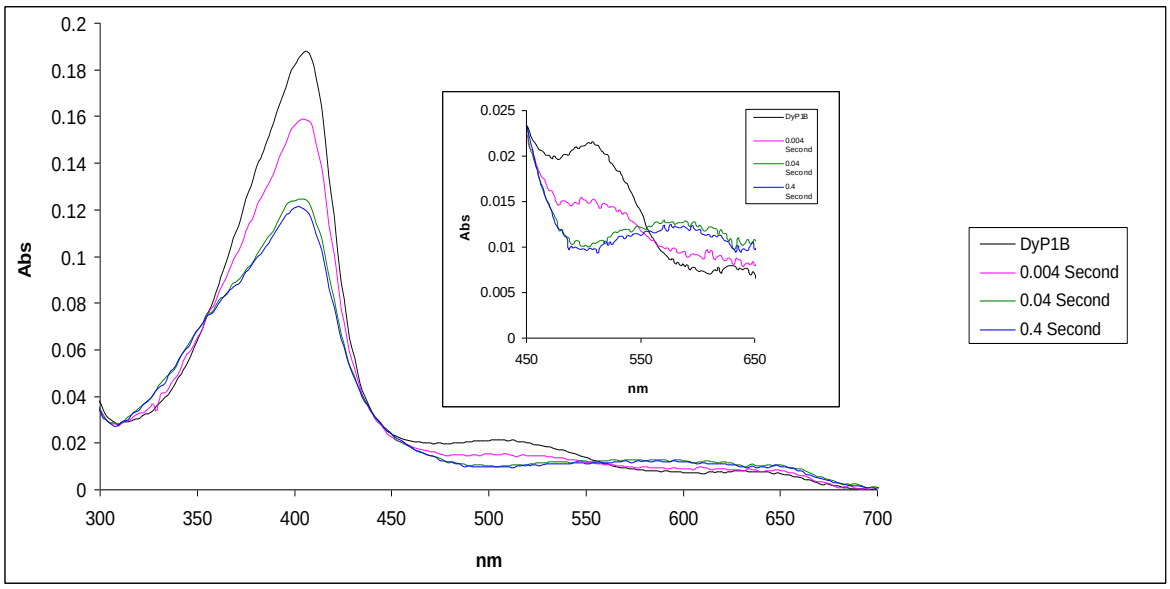

Figure 2.10 - UV–visible spectrophotometric scans of reaction of DyP1B with 5μM hydrogen peroxide from 1 to 400 ms, showing Soret band at 406 nm (gray line, before adding H_2O_2), then transition after 4 ms (pink line) and 40 ms (green line) to compound **I** peak at 402 nm (blue line). Inset shows new absorption at 550–600 nm

At pH 5.5, equimolar rapid mixing of 5 μM DyP1B with5 μM H_2O_2 resulted in decay of the Soret band at 406 nm within ~400 ms with the concomitant appearance of a less intense, broad UV–visible absorption characteristic of compound **I** in the 450-550 nm range and an increase in 550- 650 nm range corresponding to a compound **I** species similar to that observed for *R. jostii* RHA1 DyPB, The inset in Fig. 2.10 shows this UV–visible absorption plot. Fig. 2.11 represents the decay of the Soret band in 406 nm versus time. As is apparent from the plot, within 100 ms, the reaction is completed.

The rate of formation of compound **I** in DyP1B was investigated through enzyme-hydrogen peroxide titration experiments at varying concentrations of hydrogen peroxide (25 μM-250 μM). Measurement and fitting of obtained apparent rate constants by pro-data viewer software provided a second order rate constant of 1.22 $x10^5$ M^{-1} s^{-1}, comparable to that observed for *R. jostii* RHA1 DyPB (1.79 $x10^5$ M^{-1} s^{-1}) [65].

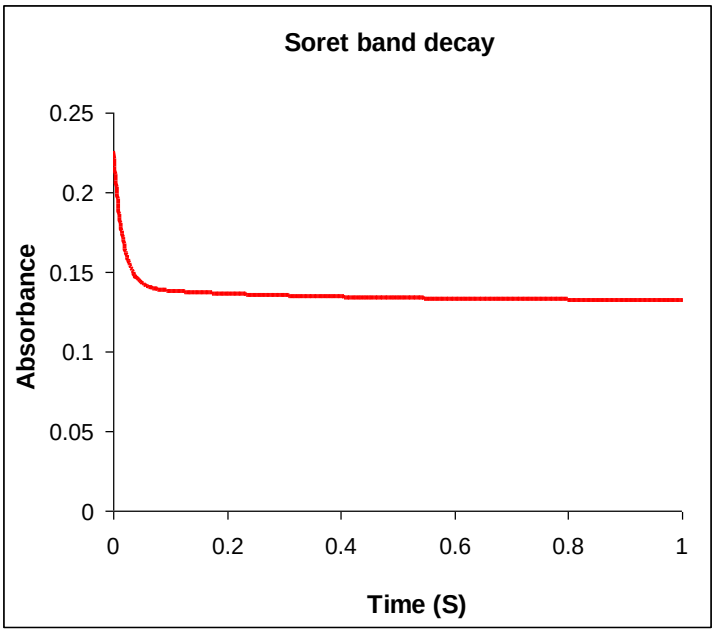

Figure 2.11 - Transient kinetic plot of DyP1B for absorbance at 406 nm

Fig. 2.12 shows plot of first order k_{obs} values for reaction with hydrogen peroxide against hydrogen peroxide concentration.

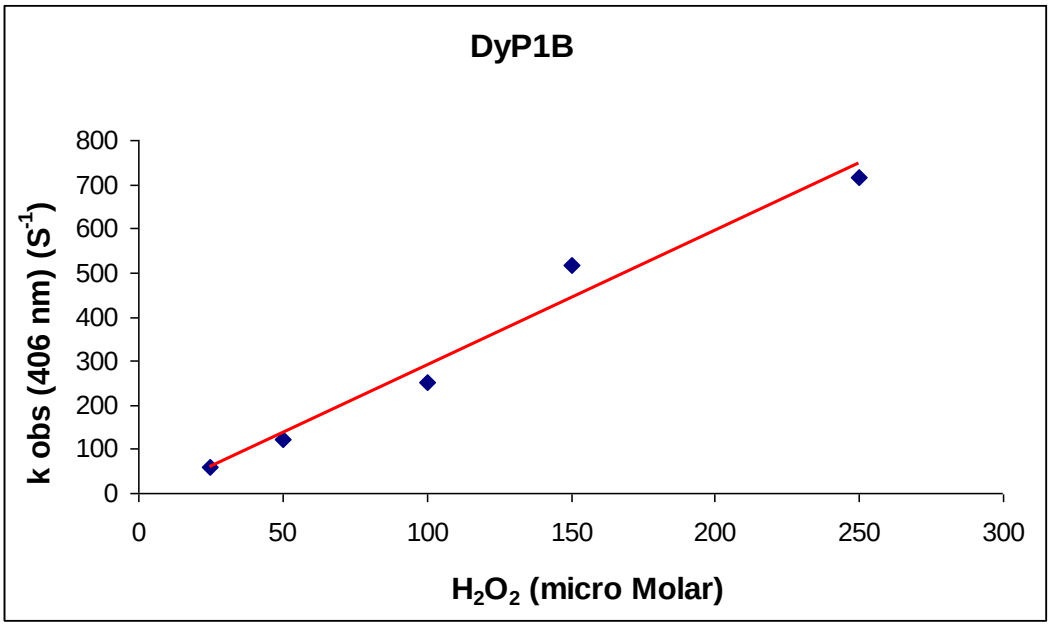

Figure 2.12 - Plot of first order k_{obs} values for reaction of DyP1B with hydrogen peroxide against hydrogen peroxide concentration

2.2.8 Oxidation of wheat straw lignocellulose by DyP1B

DyP1B enzyme was incubated with powdered wheat straw lignocellulose, and product formation monitored by reverse phase HPLC. In the presence of 1 mM $MnCl_2$, and H_2O_2 a visible colour change was observed, Fig. 2.13 represent the colour change in sample containing DyP1B, $MnCl_2$, and H_2O_2.

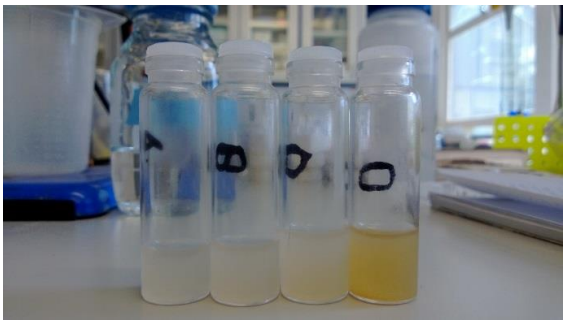

Figure 2.13 -Reaction of *P. fluorescens* DyP1B with wheat straw lignocellulose visual appearance – From left to right: Lignocellulose +Buffer, Lignocellulose+H_2O_2, Lignocellulose+Enz+H_2O_2, Lignocellulose+Enz+H_2O_2 + Mn^{2+}

After analysing of reaction mixture by HPLC a significant new peak was observed at retention time 15.6 min compared with controls, as shown in Fig. 2.14. The new peak was only formed in the presence of $MnCl_2$.

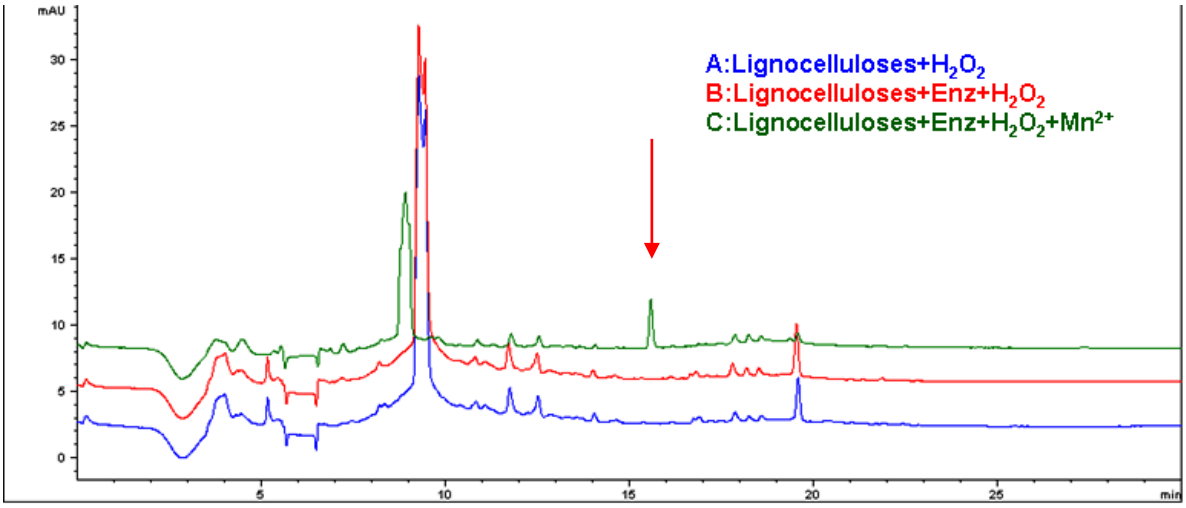

Figure 2.14 - Reverse phase HPLC analysis of DyP1B incubation with wheat straw lignocellulose, showing the formation of a new product peak at 15.6 min

The peak at retention time 15.6 min was collected and analysed by electrospray mass spectrometry, giving a molecular ion at *m/z* 401.1192, matching molecular formula $C_{19}H_{22}NaO_8$ (calculated *m/z* 401.1207), consistent with a lignin fragment containing two aryl-C3 units, containing one G unit and one H unit. Fig. 2.15 shows mass spectra for DyP1B reaction product, compared with calculated values.

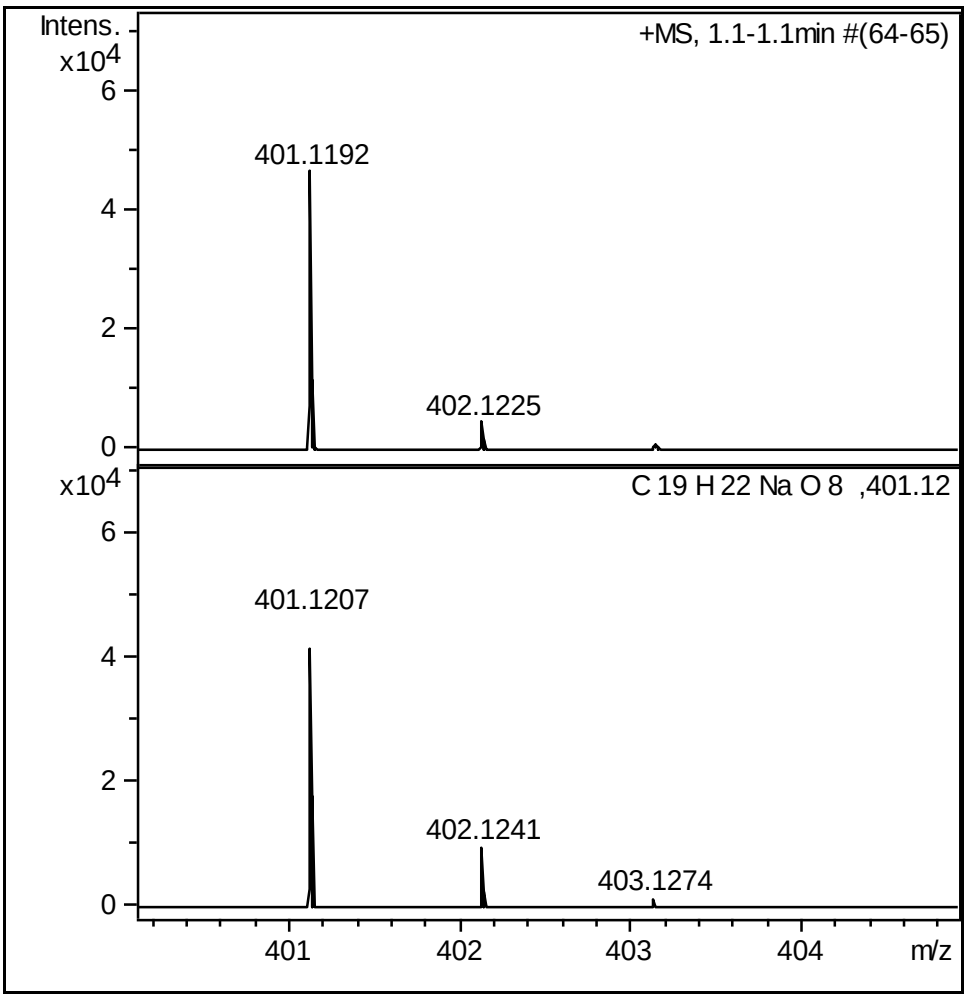

Figure 2.15 - High resolution mass spectra for DyP1B reaction product

MS-MS fragmentation of this compund gave fragments at *m/z* 176.0421 and 217.0434 (Fig.2.16).

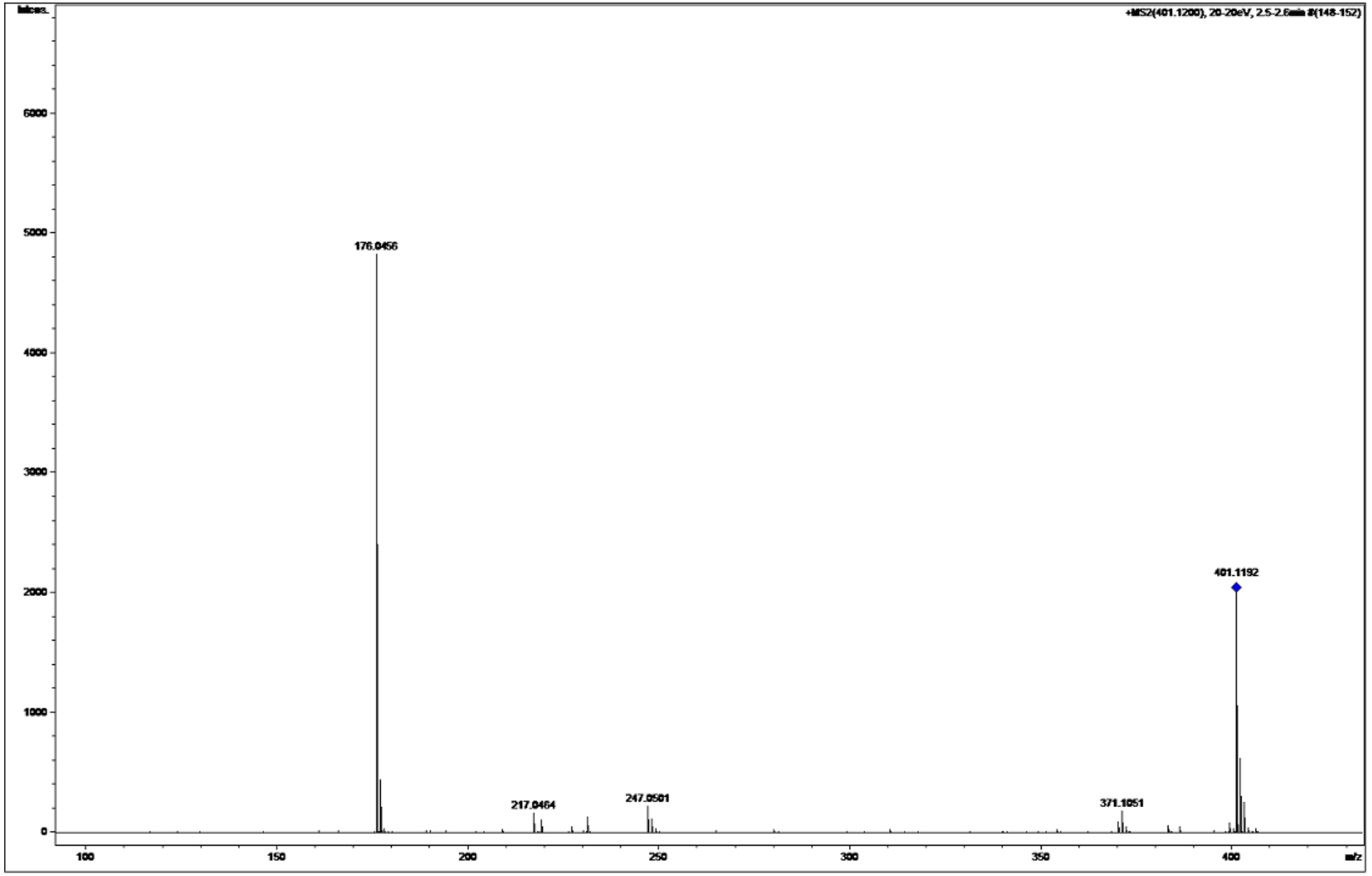

Figure 2.16 - MS-MS fragmentation products of collected product from reaction of DyP1B with wheat straw lignocellulose

As shown in Fig.2.17, these two fragments are consistent with a molecular structure containing a β-aryl ether lignin dimer with a G unit linked via a β-ether linkage to the 4-*O*-position of an H unit bearing a benzylic ketone and β and γ hydroxyl groups.

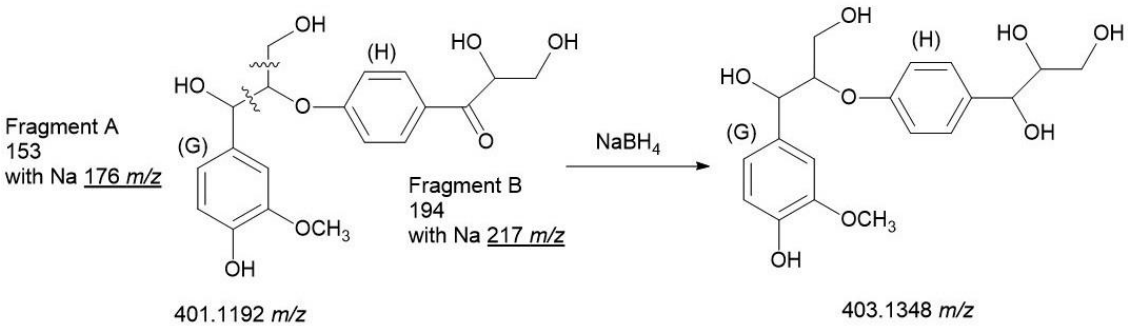

Figure 2.17 - Molecular structure of DyP1B oxidation product, showing fragments observed by MS–MS analysis, and the structure of the reduced product after treatment with sodium borohydride.

In order to seek further evidence for the presence of a benzylic ketone in this compound, a sample of this material was treated with an alkaline solution of sodium borohydride, resulting in the disappearance of the HPLC peak at 15.6 min, and the formation of a new peak at 15.0 min, with weaker absorbance, as it shown in Fig.2.18.

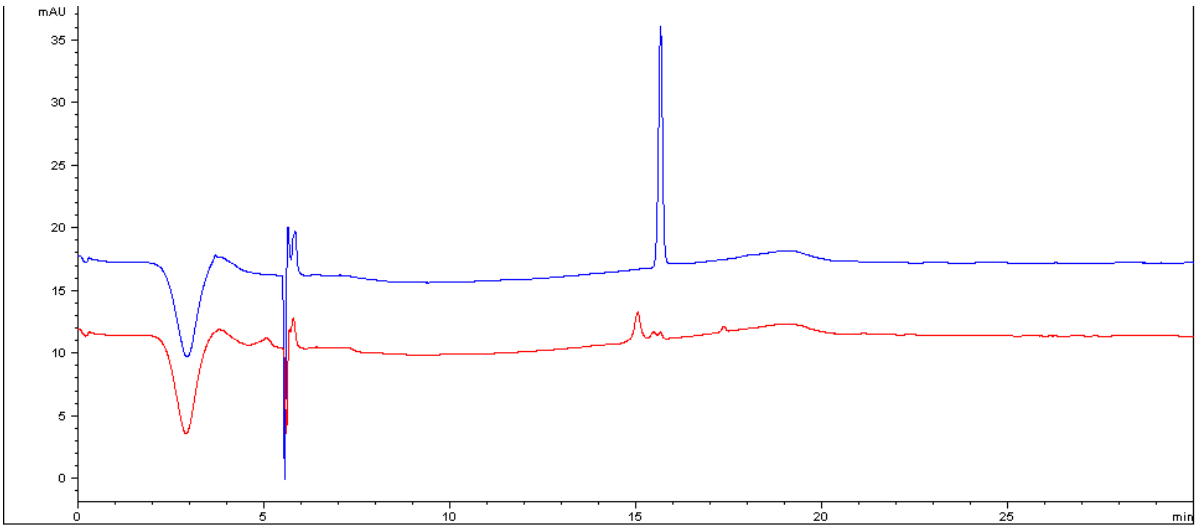

Figure 2.18 -Treatment of DyP1B reaction product at retention time 15.6 min (blue trace) with sodium borohydride, giving a modified product at retention time 15.0 min (red trace)

Analysis of this new species by mass spectrometry gave *m/z* 403, two mass units higher than the first species, consistent with reduction of a benzylic ketone to the corresponding alcohol, Fig. 2.19. Therefore, the structure shown in Fig. 2.17 was proposed for this product.

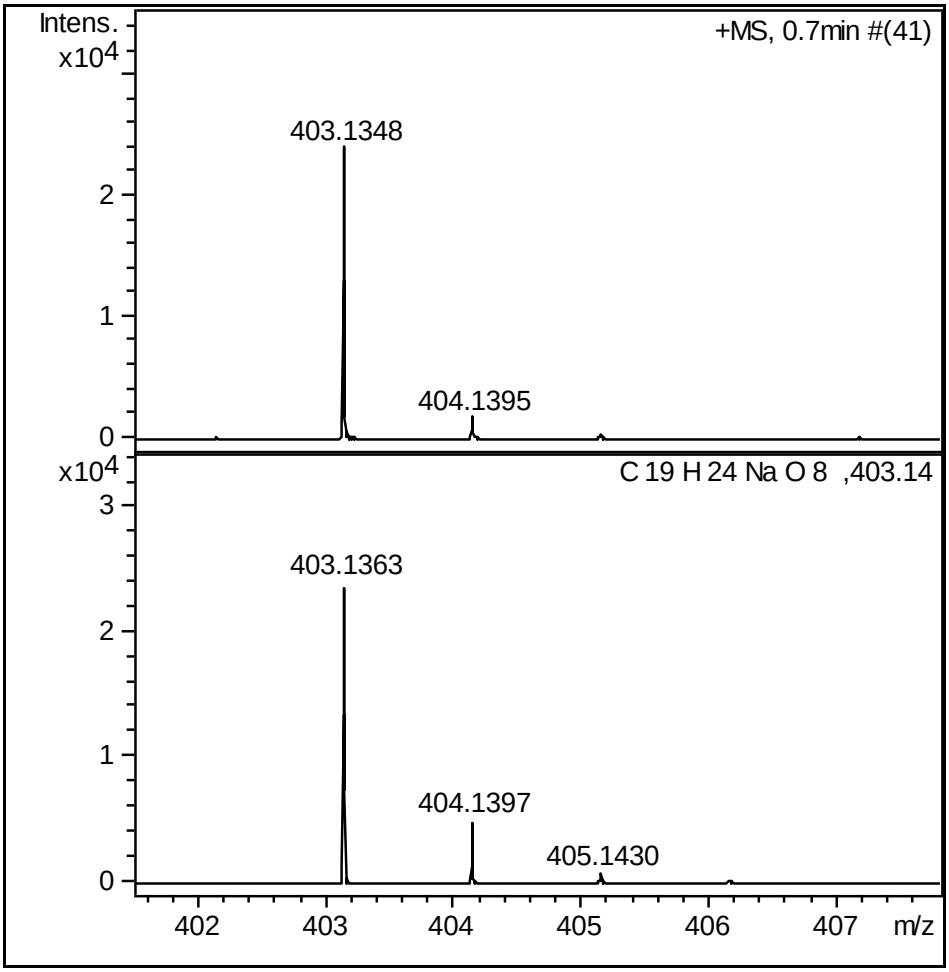

Figure 2.19 - High resolution mass spectra for DyP1B reaction product after treatment with sodium borohydride

2.2.9 Possible route of product formation

Incubation of DyP1B with wheat straw lignocellulose liberates a low molecular weight aromatic product. The molecular structure of this lignin fragment, which contains a G unit linked via a β-aryl ether linkage to an H unit, was determined (Fig. 2.17). It contains a benzylic ketone that is probably the site of oxidative cleavage from the lignin polymer. Two possible pathways for the formation of this product are depicted in Fig. 2.20. The benzylic ketone moiety could be formed from benzylic oxidation of a α-aryl ether linkage to the lignin polymer, or from oxidative cleavage of a phenylcoumarane (β-5) linkage.

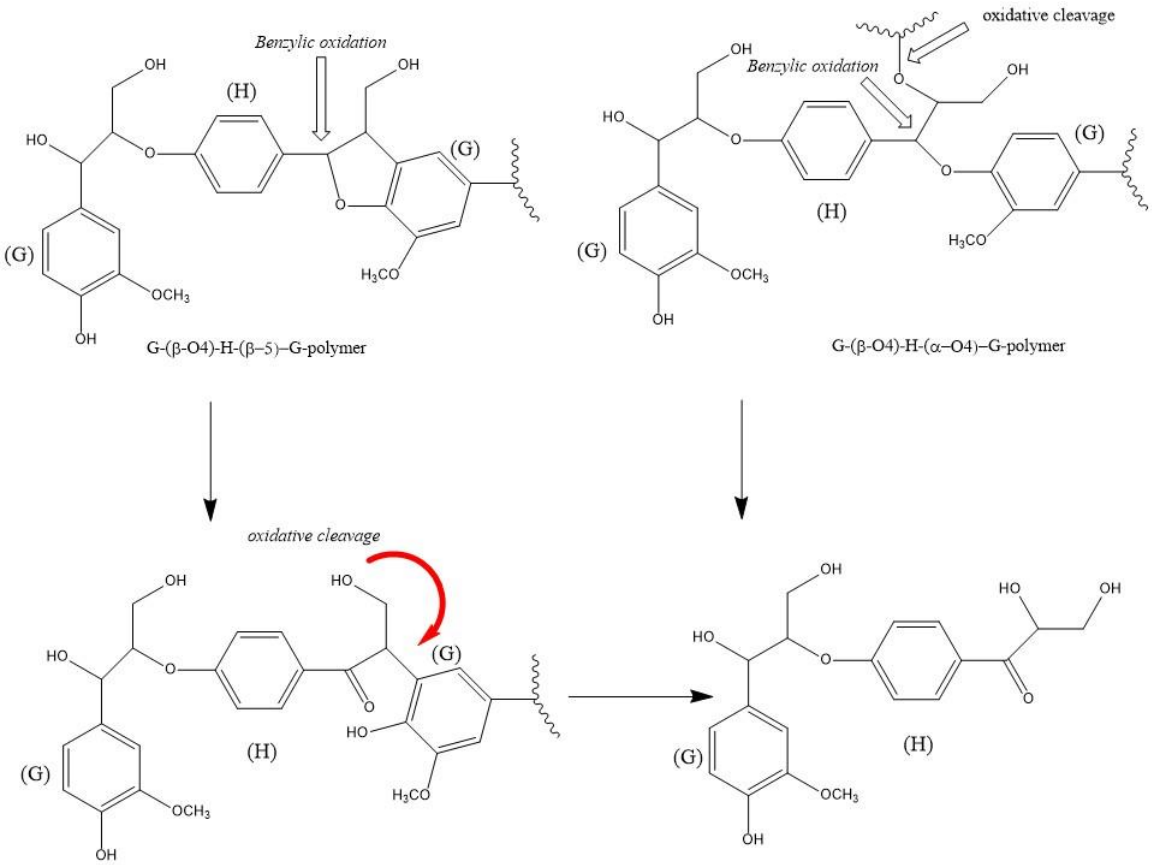

Figure 2.20 - Possible pathways for formation of DyPB1 product from lignin

2.3 DyP2B

2.3.1 Expression and purification of DyP2B

For cloning of *dyp2b*, genomic DNA of *P. fluorescens* Pf-5 was extracted as explained in section of 2.2.1. Forward and reverse primers were designed for the *dyp2b* and a CACC overhang was added to the forward primers in 5' for purpose of performing TOPO cloning method. The designed primers for isolation of *dyp2b* are as following: $_{5'}$C ACC ATG ACC CAG CCG TCC TCC $_{3'}$ and $_{5'}$ CTA CAG GCC GGT GGG CGC $_{3'}$. PCR reactions were carried by using Platinum Pfx-DNA polymerase from Invitrogen, following the manufacturer's instructions. Fig. 2.21 shows the agarose gel picture of PCR product of *dyp2b* in predicted size of 975 base pair.

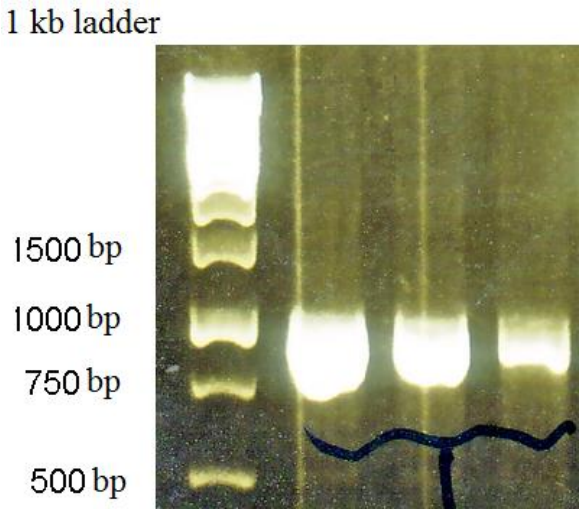

Figure 2.21 - Agarose gel of PCR products of *dyp2b* in predicted size of 975 base pair for different concentration of DNA template

The amplified gene was cloned using the Champion™ pET 151 Directional TOPO® Expression Kit (Invitrogen) into expression vector pET151, and transformed into *E. coli* TOP10 competent cells (Invitrogen). The extracted plasmids from the obtained colonies were

sent for sequencing, to confirm the accuracy of the sequence and the ligation respectively. The sequencing results showed that the amplified genes did not contain any mutations, and the ligated gene was in the correct orientation in the vector. The recombinant plasmid was then transformed into BL21 *E. coli* (Invitrogen), for protein expression.

The recombinant *dyp2b* was expressed by adding a grown overnight starter culture in the presence of 100 mg/ml ampicillin to 2 litre Luria-Bertani broth for 3 hours at 37 °C, and finally the cells were induced by adding 0.5 mM final concentration of IPTG and shaken overnight at 15 °C. Cell pellets were harvested by centrifugation at 4000 × g.

Protein purification was performed as described for DyP1B by metal affinity chromatography followed by TEV protease cleavage of the $(His)_6$ fusion tag.

Fig. 2.22 shows the SDS PAGE of purification steps of DyP2B. The band in the flow through lane reside at 35 kDa matches the predicted molecular weight of DyP2B protein.

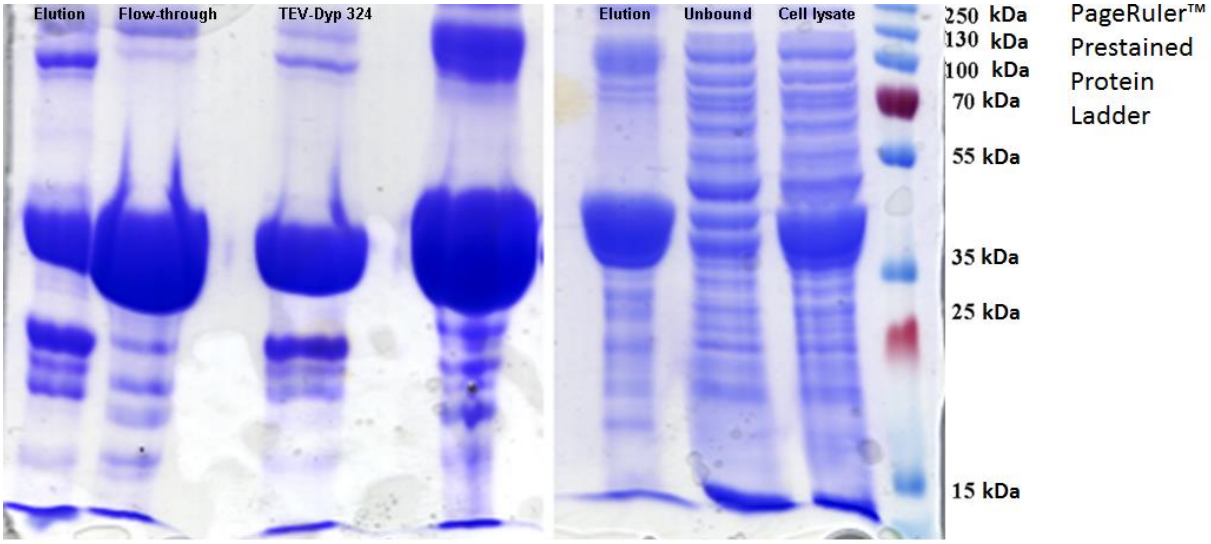

Figure 2.22 - SDS PAGE of DyP2B purification steps

2.3.2 Heme reconstitution

Heme dissolved in DMSO was added to the protein solution dropwise as explained in the experimental section. The optical absorbance of reconstituted sample was scanned in the range 200 to 800 nm. Appearance of a Soret band at 404 nm indicates the presence of heme in the protein molecules. The observed Rz ratio, (A_{Soret}/A_{280}), obtained from the UV-vis of reconstituted enzyme was 1.42. Fig. 2.23 shows the Uv/vis optical absorption scan of DyP2B protein solution. The protein solution then was concentrated by a 10 kDa Amicon centricon device, and after flash freezing using liquid nitrogen, it was stored at -80 °C for further kinetic analysis. The yield of produced DyP2B enzyme from 2 litre bacterial culture was 26 mg.

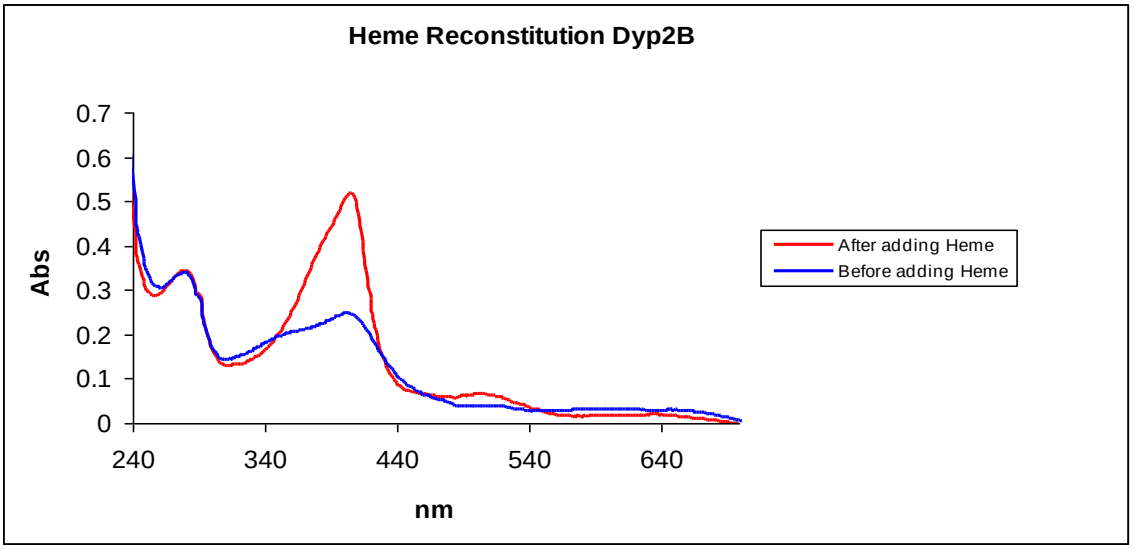

Figure 2.23 - UV/Vis scan of DyP2B before and after heme reconstitution

2.3.3 pH profile of DyP2B

Fig. 2.24 shows the pH profile of DyP2B determined by 2,4-dichlorophenol (DCP) assay at 25 °C using Britton–Robinson buffer in the pH range 3–10, as it is explained in experimental section.

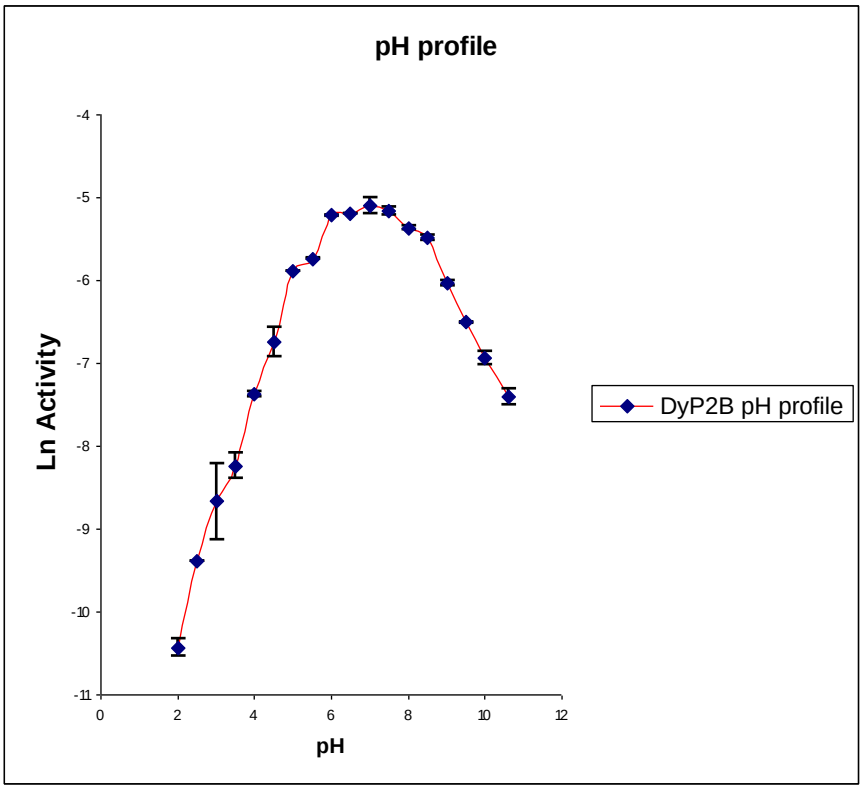

Figure 2.24 - pH profile of DyP2B

Optimum pH was determined by plotting natural logarithm of obtained enzymatic activity versus corresponding pH value. The optimum pH for DyP2B is in range of 6.0-7.5 [63, 65, 68, 69].

2.3.4 Temperature profile of DyP2B

Fig. 2.25 shows the temperature profile of DyP2B determined by 2,4-dichlorophenol (DCP) assay in the 100 mM acetate buffer pH 6.5 at different temperature ranging 25 to 75 °C as explained in experimental section. Temperature profile was determined by plotting obtained specific activity versus corresponding temperature. The obtained optimum temperature for DyP2B is 30 °C that is in good agreement with optimum temperature profile of DyPs enzyme from *Bacillus subtilis* and *Pseudomonas putida* [69].

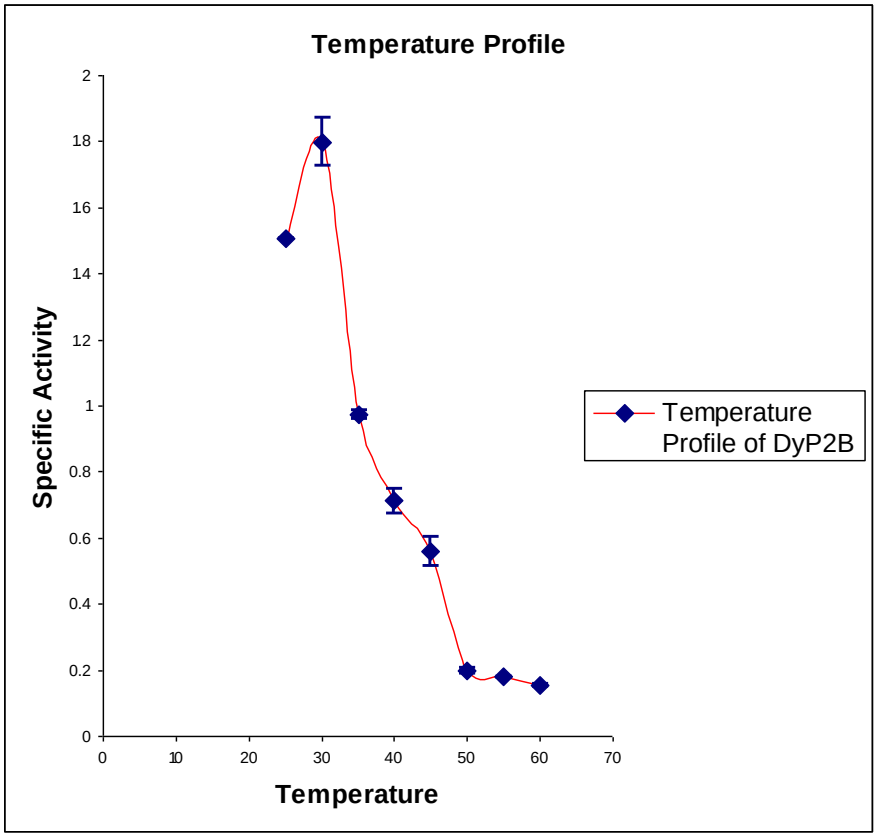

Figure 2.25 - Temperature profile of DyP2B

2.3.5 Kinetic parameters of DyP2B

DyP2B enzyme was characterised using a range of peroxidase and lignin substrates, using UV-vis kinetic assays, and K_M and k_{cat} values measured. Table 2.2 represents kinetics parameters of DyP2B compared with obtained parameters for DyP1B.

Table 2.2 - Steady-state kinetic data for DyP2B compared with DyP1B

	DyP1B			**DyP2B**		
Substrate	K_M (mM)	k_{cat} (s^{-1})	k_{cat}/K_M ($M^{-1}s^{-1}$)	K_M (mM)	k_{cat} (s^{-1})	k_{cat}/K_M ($M^{-1}s^{-1}$)
ABTS	1.13 ± 0.1	13.5 ± 0.4	1.2×10^4	1.7±0.2	10.2±0.44	0.58×10^4
H_2O_2[a]	0.048± 0.02	23.3 ± 0.2	4.8×10^5	0.061±0.005	9.2±0.2	1.5×10^5
Mn^{2+}	7.3 ± 0.4	2.40 ± 0.04	0.33×10^3	1.7±0.3	3.6±0.2	2.09×10^3
2,4-dichlorophenol	1.25 ± 0.1	0.66 ±0.02	0.53×10^3	0.4±0.02	1.3±0.02	3.25×10^3
Phenol	1.02 ± 0.08	1.22 ±0.02	1.2×10^3	0.33±0.02	0.78±0.01	2.36×10^3
Guaiacol	0.056± 0.006	0.058±0.00	1.0×10^3	NA	NA	NA
Pyrogallol	4.0 ± 0.6	2.5 ±0.1	0.62×10^3	10.2±0.8	5.9±0.3	0.58×10^3
Reactive Blue 4	0.12 ± 0.01	1.04 ±0.03	9.0×10^3	NA	NA	NA
Kraft lignin [b]	0.006 ±0.001	0.9 ±0.1	1.4×10^5	NA	NA	NA

[a] Using ABTS as substrate, [b] Assuming molecular weight of 10000 M.W.

For each parameter, standard errors were determined by statistical methods and represented along with the reported data. Fig. 2.26 shows steady state kinetic plots for DyP2B for each substrate, fitted by non-linear regression method.

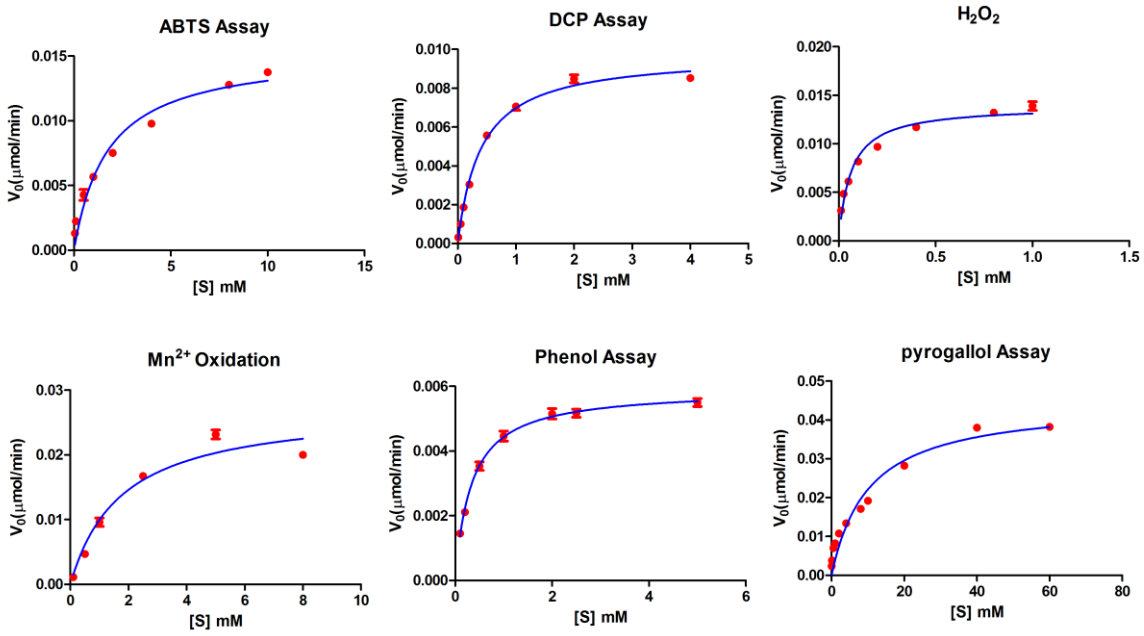

Figure 2.26 - Steady state kinetic plots of DyP2B

DyP2B enzyme showed catalytic activity with common peroxidase substrate ABTS that is characteristic of the DyP family of peroxidases [46, 55, 57, 62, 63, 70]. DyP2B showed catalytic activity for Mn^{2+} oxidation similar to *R. jostii* DyPB [64, 65]. However, DyP2B is six times more active than *R. jostii* DyPB (k_{cat} =0.59 (s^{-1})).

Compared with DyP1B catalytic activity, DyP2B did not show activity towards Kraft Lignin, Reactive Blue 4, guaiacol and no activity towards wheat straw lignocellulose. Comparing the kinetic parameters of these two enzymes also shows that catalytic turn over number of DyP1B for hydrogen peroxide is 2.5 times more than DyP2B, whereas DyP2B represents four times lower Michaelis constant for oxidation of Mn (II) than DyP1B. Both enzymes show similar trend for the oxidation of ABTS. In case of oxidation of phenol and 2,

4-dichlorophenol compounds, DyP2B showed lower Michaelis constant for both of substrates compared with DyP1B, and nearly two times higher k_{cat} for oxidation of 2,4-dichlorophenol over DyP1B, but similar k_{cat}/K_M for this substrate.

2.4 DyPA

2.4.1 Expression and purification of DyPA

For cloning of the *dypa*, genomic DNA of *P. fluorescens* Pf-5 was extracted as explained in section of 2.2.1. Forward and reverse primers were designed for the *dypa* and a CACC overhang was added to the forward primers in 5' for purpose of performing TOPO cloning method. The designed primers for isolation of *dypa* are as following: $_{5'}$C ACC ATG AAC GAT TCA GAT CAG CCC$_{3'}$ and $_{5'}$TCA GGC AGT GCT TTT AGG TCG$_{3'}$. PCR reactions were carried by using Platinum Pfx-DNA polymerase from Invitrogen, following the manufacturer's instructions. Fig. 2.27 shows the agarose gel picture of PCR product of the *dypa* in predicted size of 1311 base pair.

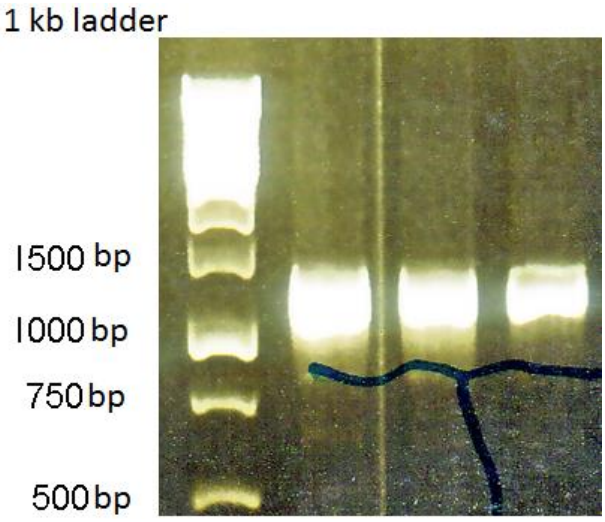

Figure 2.27 - Agarose gel of PCR products of *dypa* in predicted size of 1311 base pair for different concentration of DNA template

The amplified genes were cloned using the Champion™ pET 151 Directional TOPO® Expression Kit (Invitrogen) into expression vector pET151, and transformed into *E. coli* TOP10 competent cells (Invitrogen). The extracted plasmids from the obtained colonies were sent for sequencing to confirm the accuracy of the sequence and the ligation respectively. The sequencing results showed that the amplified genes did not contain any mutations, and the ligated gene was in the correct orientation in the vector. The recombinant plasmid was then transformed into BL21 *E. coli* (Invitrogen), for protein expression.

The recombinant *dypa* was expressed by adding a grown overnight starter culture in the presence of 100 mg/ml ampicillin to 2 litre Luria-Bertani broth for 3 hours at 37 °C, and finally the cells were induced by adding 0.5 mM final concentration of IPTG and shaken overnight at 15 °C. Cell pellets were harvested by centrifugation at 4000 × g.

Protein purification was performed as described for DyP1B by metal affinity chromatography followed by TEV protease cleavage of the $(His)_6$ fusion tag.

Fig. 2.28 shows the SDS PAGE of purification steps of DyPA. The band in the flow through lane at 47 kDa matches the predicted molecular weight of DyPA protein.

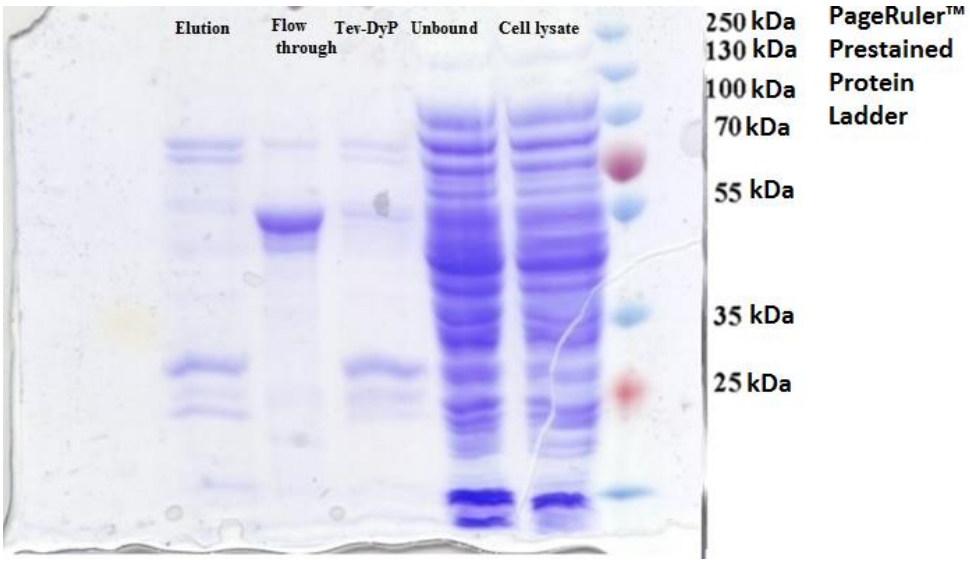

Figure 2.28 - SDS PAGE of DyPA purification steps

2.4.2 Heme reconstitution

Heme dissolved in DMSO was added to the protein solution drop wise as explained in the experimental section. The optical absorbance of reconstituted sample was scanned in the range 200 to 800 nm. Appearance of a Soret band at 409 nm indicates the presence of heme in the protein molecules. The observed Rz ratio, (A_{Soret}/A_{280}), obtained from the UV-vis of reconstituted enzyme was 0.95. Fig. 2.29 shows the Uv/vis optical absorption scan of DyPA protein solution.

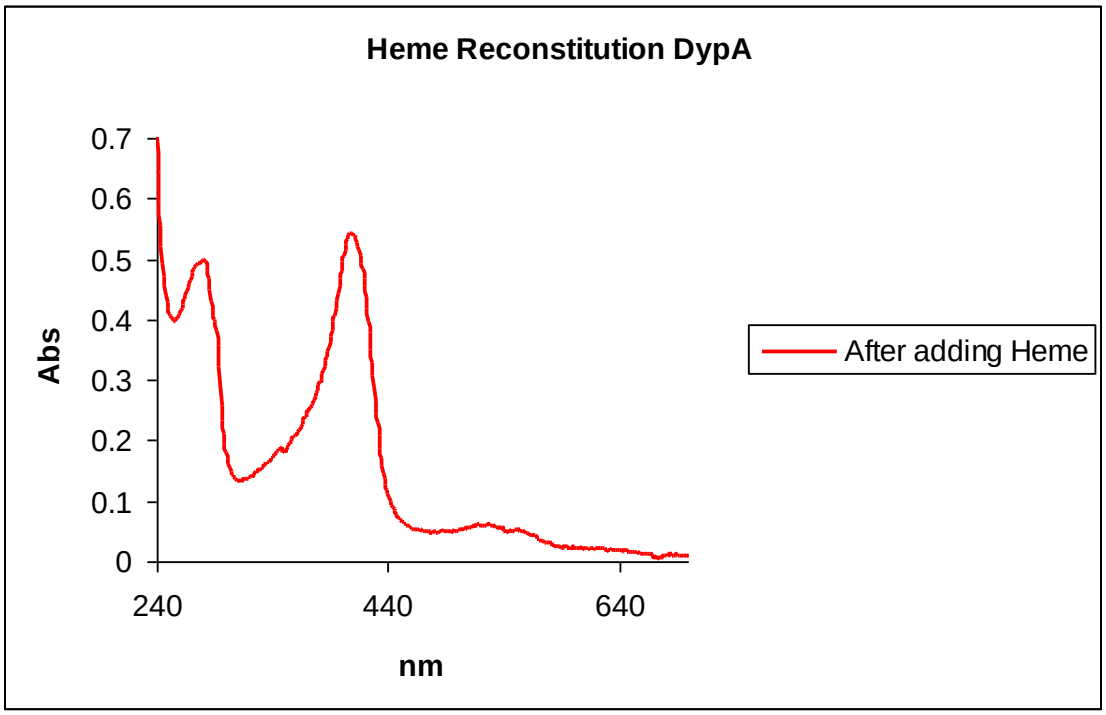

Figure 2.29 - UV/Vis scan of DyPA after heme reconstitution

The protein solution then was concentrated by a 10-kDa Amicon centricon device, and after flash freezing using liquid nitrogen, it was stored at -80 °C for further kinetic analysis. The yield of produced DyPA enzyme from 2 litre bacterial culture was 5 mg.

2.4.3 pH profile of DyPA

Fig. 2.30 shows the pH profile of DyPA determined by 2,4-dichlorophenol (DCP) assay at 25 °C using Britton–Robinson buffer in the pH range 3–10, as explained in experimental section. Optimum pH was determined by plotting natural logarithm of obtained enzymatic activity versus corresponding pH value. The optimum pH for DyPA is 6.0 [63, 65, 68, 69].

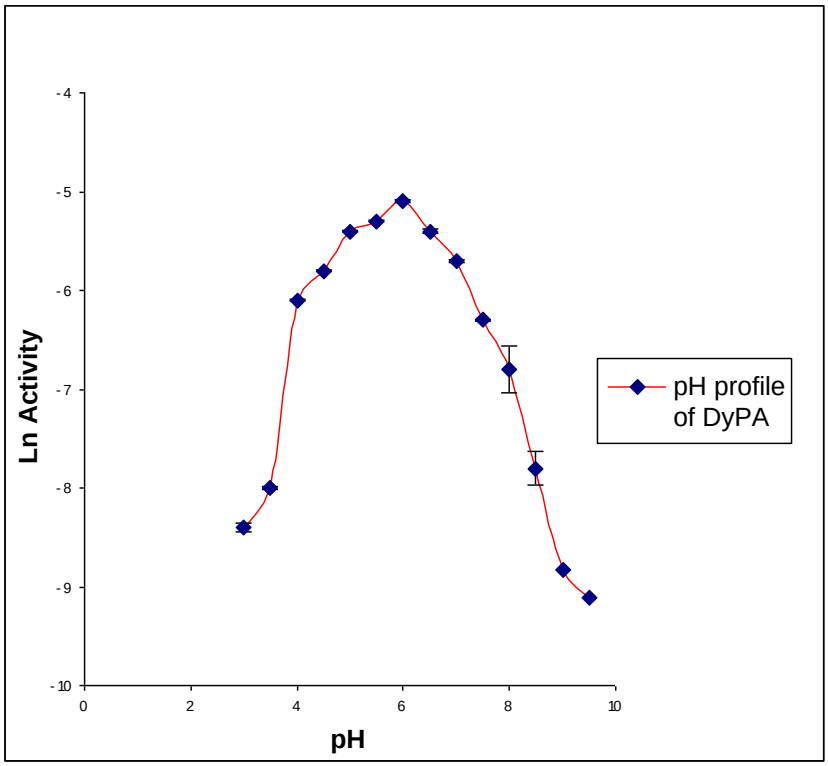

Figure 2.30 - pH profile of DyPA

2.4.4 Temperature profile of DyPA

Fig. 2.31 shows the temperature profile of DyPA determined by 2,4-dichlorophenol (DCP) assay in the 100 mM acetate buffer pH 6 at different temperature ranging 25 to 75 °C as explained in the experimental section. Temperature profile was determined by plotting obtained specific activity versus corresponding temperature. The obtained optimum

temperature for DyPA is 40 °C that is in good agreement with optimum temperature profile of other reported bacterial DyPs enzyme such as *Bacillus subtilis* and *Pseudomonas putida* [69]. Santos *et al.* showed that a DyP type-A enzyme from *B.subtilis* (BsDyP) was more thermo-stable than B-type DyP enzyme from *P.putida* (PpDyP) [69]. In our study also among of these three DyP enzymes from *P. fluorescens*, DyPA also showed higher optimum temperature compared with the other DyPs that might be reflective of presence of more rigidity in DyPs type-A enzyme compared with DyPs type-B.

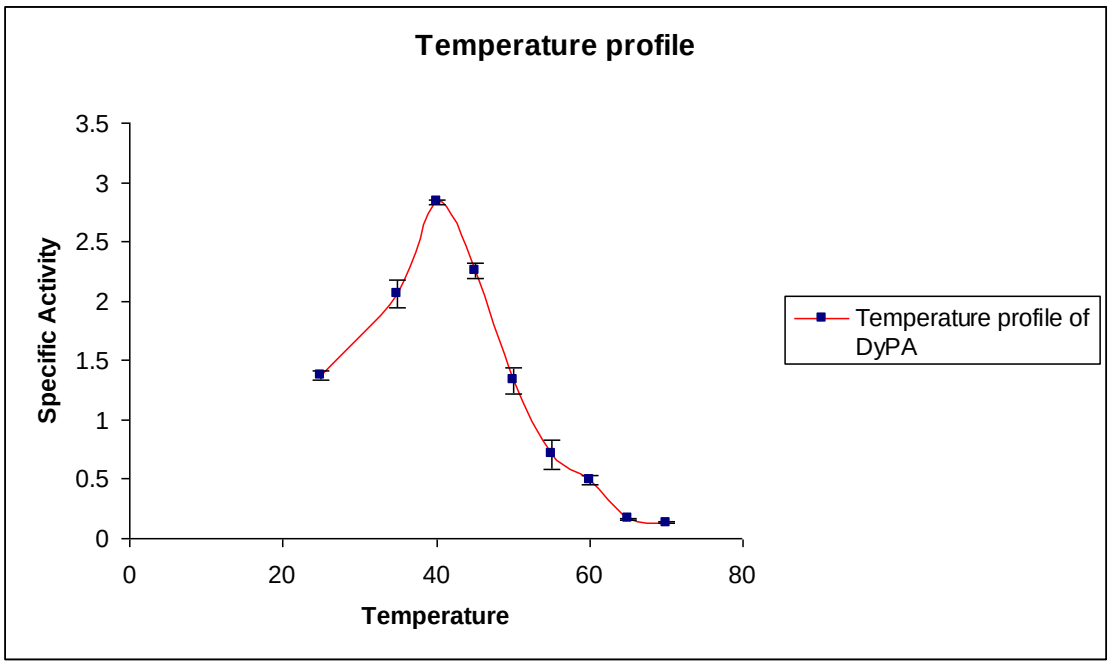

Figure 2.31 - Temperature profile of DyPA

2.4.5 Kinetic parameters of DyPA

DyPA enzyme was characterised using a range of peroxidase and lignin substrates, using UV-vis kinetic assays, and K_M and k_{cat} values measured. Table 2.3 represents kinetics parameters of DyPA. For each parameter, standard errors were determined by statistical methods and represented along with the reported data.

Table 2.3 - Steady-state kinetic data for DyPA

	DyPA		
Substrate	**K_M (mM)**	**k_{cat} (s^{-1})**	**k_{cat}/K_M ($M^{-1}s^{-1}$)**
ABTS	0.82±0.1	23.1±1	2.8 x 10^4
H_2O_2[a]	0.073±0.003	35±0.4	4.79 x 10^5
Mn^{2+}	NA	NA	NA
2,4-dichlorophenol	4.8±0.5	2.61±0.1	0.54 x 10^3
Phenol	0.19±0.02	0.138±0.003	0.72 x 10^3
Guaiacol	NA	NA	NA
Pyrogallol	11.58±1	5.63±0.2	0.48 x 10^3
Reactive Blue 4	0.21±0.017	1.90±0.06	9.04 x 10^3
Kraft lignin[b]	0.011±0.001	1.175±0.03	1.6 x 10^5

[a] Using ABTS as substrate, [b] Assuming molecular weight of 10000 M.W.

Fig. 2.32 shows steady state kinetic plots for DyPA for each substrate, fitted by non-linear regression method.

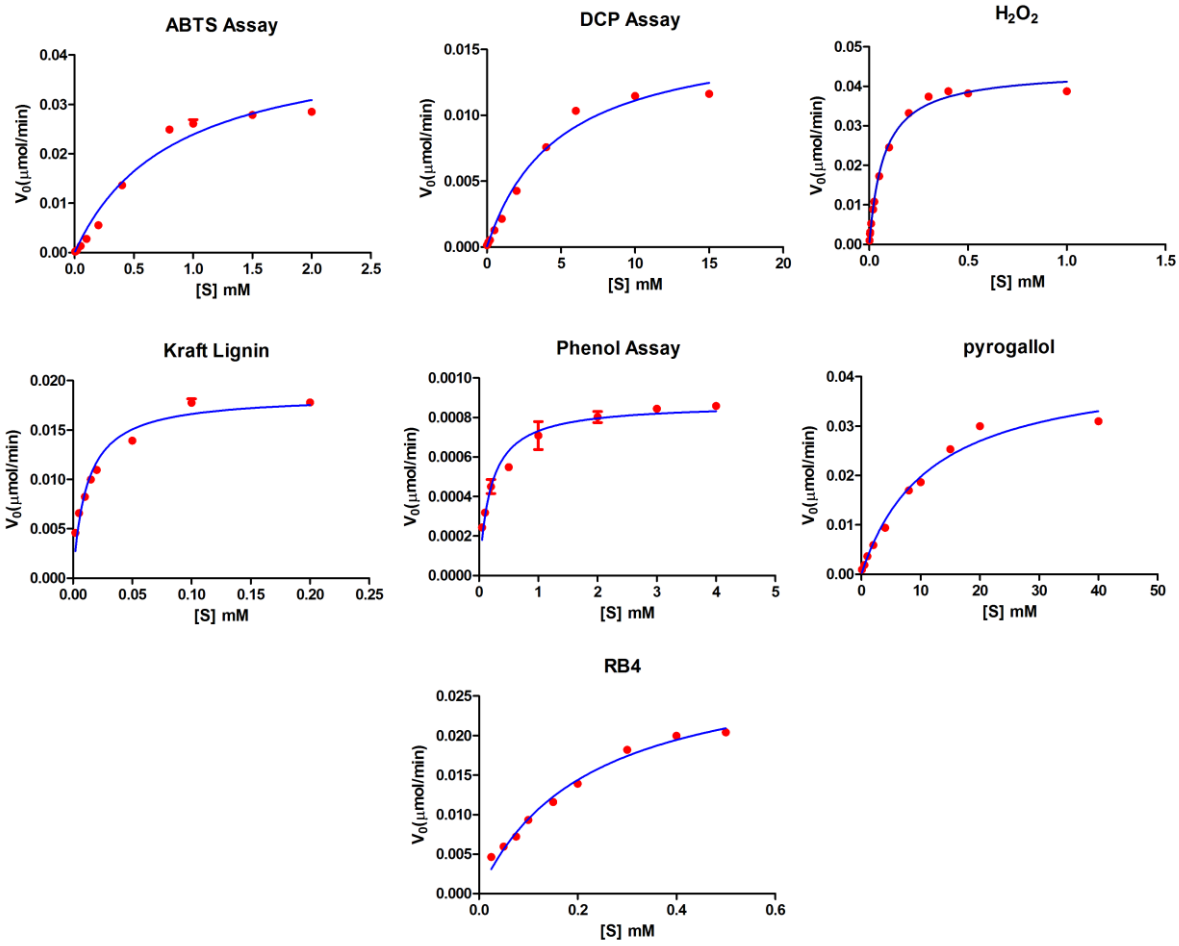

Figure 2.32 - Steady state kinetic plots of DyPA

DyPA from *P. fluorescens* did not show reactivity toward Mn (II) and guaiacol similar to characterised DyPA from *R. jostii*. It showed the highest catalytic turn over number and the lowest Michaelis constant for ABTS as an azo dye compared with the two other characterised DyPs from *P. fluorescens* and DyPB and DyPA from *R. jostii* [65]. DyPA represented the highest k_{cat} number for hydrogen peroxide compared with the other DyPs. DyPA showed the highest Michaelis constant and k_{cat} for oxidation of 2,4-dichlorophenol whereas for phenol oxidation it showed the lowest values for Michaelis constant and k_{cat} compared with the DyP1B and DyP2B. DyPA catalytic parameters of oxidation of pyrogallol were similar to DyP2B, high in Michaelis constant and catalytic turn over number, compared with DyP1B. In case of decolourizing of reactive blue 4, an anthraquinone dye, DyPA showed, more and less higher catalytic turn over number and Michaelis constant compared with DyP1B. In the case of reactivity for Kraft lignin DyPA represented higher catalytic turn over number compared with DyP1B whereas DyP1B showed a Michaelis constant nearly two times lower for Kraft lignin, and finally DyPA did not show any reactivity towards wheat straw lignocellulose.

2.5 Conclusion

This study verifies that Gram-negative bacterial strains such as *Pseudomonas fluorescens* also contain DyP-type peroxidases that can oxidise lignin. There are homologous for DyP2B found in many Pseudomonas strains, and in Burkholderia (e.g. *Burkholderia terrae* BS001, uniprot entry name of I5CHJ6), and Bordetella (e.g. *Bordetella bronchiseptica* M85, uniprot entry name of A0A063K7X2). In addition, none of these three DyP-type peroxidases from *P. fluorescens* shows a signal peptide in its C-terminal for encapsulation by encapsulin compartment compared with *R. jostii* DyPB.

Each enzyme was characterised using a range of peroxidase and lignin substrates, using UV-vis kinetic assays, and K_M and k_{cat} values measured, as shown in Table 2.1, 2.2 and 2.3. All three enzymes showed catalytic activity with peroxidase substrate ABTS, with k_{cat} values of 10.2-23.1 s^{-1}. DyP1B and DyPA were active with dye substrate Reactive Blue 4, characteristic of the DyP family of peroxidases [46, 55, 57, 62, 63, 70]. As shown in Fig. 2.8 and Fig. 2.26 DyP1B and DyP2B showed catalytic activity for Mn^{2+} oxidation (k_{cat} 2.4-3.6 s^{-1}, k_{cat}/K_M 330-2100 $M^{-1}s^{-1}$), whereas DyPA showed no activity for Mn^{2+} oxidation. All three enzymes were able to oxidise some phenolic substrates, less efficiently than ABTS, and only DyP1B showed activity towards guaiacol.

By expressing and characterising the three *P. fluorescens* DyP enzymes, *P. fluorescens* DyP1B was found to be a lignin-oxidising enzyme. Comparing the activity of *P. fluorescens* DyP1B with that of *Rhodococcus jostii* DypB, both show activity for Mn (II) oxidation and Kraft lignin oxidation. The Mn (II) oxidation activity of *P. fluorescens* DyP1B (k_{cat}/K_M 330 $M^{-1}s^{-1}$) is comparable with that of *R. jostii* DyPB (k_{cat}/K_M 275 $M^{-1}s^{-1}$) [65], but not as high as *Amycolatopsis sp*. 75iv2 DyP2 (k_{cat}/K_M 1.2 x 10^5 $M^{-1}s^{-1}$) [68], however, no lignin-oxidising activity was reported for the latter enzyme.

Both *R. jostii* DyPB and *P. fluorescens* DyP1B show time-dependent changes by HPLC when incubated with wheat straw lignocellulose, but uniquely, the *P. fluorescens* DyP1B liberates a low molecular weight aromatic product from wheat straw lignocellulose. The molecular structure of this lignin fragment was identified, which contains a G unit linked via a β-aryl ether linkage to an H unit, which contains a benzylic ketone. The benzylic ketone is probably the site of oxidative cleavage from the lignin polymer. The catalytic activities of these bacterial DyP-type peroxidases towards lignin, Mn (II) and a range of aromatic substrates further demonstrates the potential of DyP peroxidases for biotechnological applications including lignin valorisation, and the potential of pseudomonads for conversion of lignin to aromatic products.

Chapter Three

Characterisation of DyP-type peroxidase from *Thermobifida fusca* and Crystal Structure at 1.7 Å

3.1 Introduction

T. fusca that previously was known as *Thermomonaspora fusca* is a moderate thermophilic bacterium that inhabits soil. Its optimum growth temperature is 55 °C and has a vast optimum growth pH range (4-10) [38]. It degrades most of the plant cell wall polymers in heated organic materials such as rotting hay and compost heaps.

DyP-type peroxidases are considered as a distinct superfamily in databases, such as Peroxibase, Pfam, and InterPro. According to the InterPro database, the DyP superfamily comprises almost 1,000 members of which 881 members are found in bacteria [63]. PeroxiBase database and Phylogenetic analyses classify DyP-type peroxidases into four phylogenetically distinct subfamilies A, B, C, and D [62]. A, B and C subfamilies comprise bacterial DyPs, whereas subfamily D is fungal [56, 46, 62, 64]. Studies have shown that most A-type DyPs contain TAT signal sequences that enable them to be excreted into the periplasmic space but B-type DyPs do not. For instance, TfuDyP from *T. fusca*, Ycdb from

E.coli and DyPA from *R. jostii* RHA1 show the presence of a TAT signal sequnce in their sequence [61, 63, 64].

Van Bloois et al characterized a robust bacterial DyP-type peroxidase from *Thermobifida fusca*, a moderate thermophile. Similar to the other DyPs [55], this enzyme shows high activity for anthraquinone dyes such as Reactive Blue 19, and Reactive Blue 4, but low activity for Reactive Black 5, an azo dye [63]. In addition, TfuDyP catalyzed enantioselective sulfoxidation [63].

In our investigation of detailed enzymology of bacterial DyPs and catalytic activity of these enzymes toward lignin, and in comparison with *P. fluorescens* Pf-5 DyP enzymes from Gram negative origin, we decided to investigate the TfDyP enzyme from *T. fusca*, a Gram positive bacterium, and characterize it with lignin model compounds. Stopped flow studies were performed for characterizing compound **I** formation and the X-ray crystal structure of enzyme was solved. For elucidation of the catalytic role of amino acids present in the active site, three mutant enzymes were generated by site directed mutagenesis and their kinetic constants were determined.

3.2 Expression and purification of TfuDyP

For cloning of the *Tfudyp*, genomic DNA of *T. fusca* was extracted using Wizard® Genomic DNA Purification kit from Promega, from a total 1ml of overnight culture of *T. fusca* in Luria-Bertani broth. Forward and reverse primers were designed for the *Tfudyp* and a CACC overhang was added to the forward primers at the 5' end for the purpose of performing TOPO cloning. The designed primers for isolation of *dyp* are as follows: $_{5'}$C ACC ATG ACC GAA CCA GAC ACG G $_{3'}$ and $_{5'}$ TCA TCC TTC GAT CAG GTC CTG$_{3'}$. PCR reactions were carried by using Platinum Pfx-DNA polymerase from Invitrogen, following the

manufacturer's instructions. Fig. 3.1 shows the agarose gel picture of PCR product of the amplified *Tfudyp* in predicted size 1293 base pair [63].

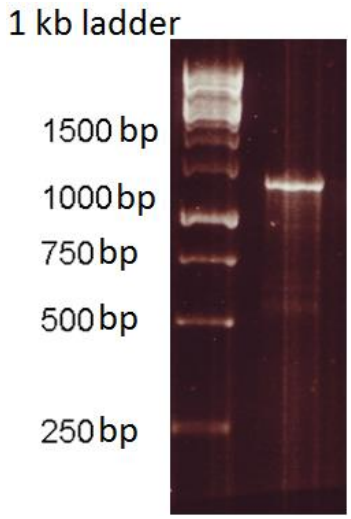

Figure 3.1 - Agarose gel of PCR products of *Tfudyp* in predicted size 1293 base pairs.

The amplified gene was cloned using the Champion™ pET 151 Directional TOPO® Expression Kit (Invitrogen) into expression vector pET151, and transformed into *E. coli* TOP10 competent cells (Invitrogen). The extracted plasmids from the obtained colonies were sent for DNA sequencing, to confirm the accuracy of the sequence and the ligation respectively. The sequencing results showed that the amplified genes did not contain any mutations, and the ligated gene was in the correct orientation in the vector. The recombinant plasmid was then transformed into BL21 *E. coli* (Invitrogen), for protein expression.

The recombinant *dyp* was expressed by adding a grown overnight starter culture in the presence of 100 mg/ml ampicillin to 2 litre Luria-Bertani broth for 3 hours at 37 °C, and finally the cells were induced by adding 0.5 mM final concentration of IPTG and shaken overnight at 15 °C. Cell pellets were harvested by centrifugation at 4000 × g.

Protein purification was performed by metal affinity chromatography followed by TEV protease cleavage of the $(His)_6$ fusion tag. The harvested cells from a 2 litre culture described above were suspended in 20 ml lysis buffer in the presence of 1 mM final

concentration of PMSF. Cell lysis was carried out using a constant system cell disrupter, followed by centrifugation at 10000 × g for 30 minute. The clear supernatant was loaded onto a Ni-NTA resin FPLC column (HisTrap HP, 1 ml volume) equilibrated with lysis buffer followed by 100 ml of wash buffer, and the recombinant protein was eluted by 7 ml elution buffer, eluting at a flow rate of 0.5 ml min^{-1}.

A sample of eluted protein was taken for SDS PAGE and Bradford assay, the remainder of solution was subjected to buffer exchange through a PD-10 column into 10 ml wash buffer. After buffer exchange, the protein solution was mixed with previously purified TEV protease in equal molar ratio overnight in room temperature, then applied again to a Ni-NTA FPLC column, and eluted in elution buffer. The flow-through fraction (25 ml) containing untagged recombinant DyP enzyme was collected. The purified enzyme was buffer exchanged by a PD-10 gel filteration column to 20mM MOPS 80mM NaCl buffer pH 7.0. Fig. 3.2 shows the SDS PAGE of purification steps of TfuDyP. The band for purified TfuDyP in the flow through lane eluted at 45.9 kDa, matching the predicted molecular weight is molecular weight of TfuDyP protein.

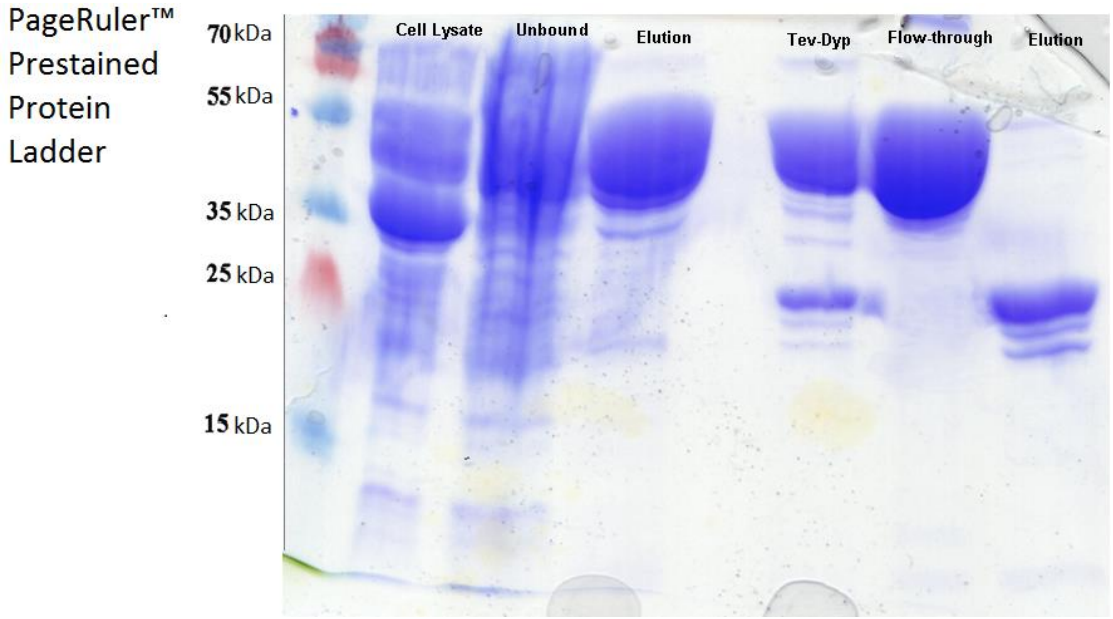

Figure 3.2 - SDS PAGE of TfuDyP purification steps

3.3 Heme reconstitution

Heme dissolved in DMSO was added to the protein solution drop wise as explained in the experimental section. The optical absorbance of reconstituted sample was scanned in the range 200 to 800 nm. Appearance of a Soret band at 404 nm indicates the presence of heme in the protein molecules. The Rz ratio, (A_{Soret}/A_{280}), obtained from the UV-vis of reconstituted enzyme was 1.12. Fig. 3.3 shows the Uv/vis optical absorption scan of TfuDyP protein solution. The protein solution then was concentrated by a 10 kDa Amicon centricon device, and after flash freezing using liquid nitrogen, it was stored at -80 °C for further kinetic analysis. The yield of produced TfuDyP enzyme from 2 litre bacterial culture was 18 mg.

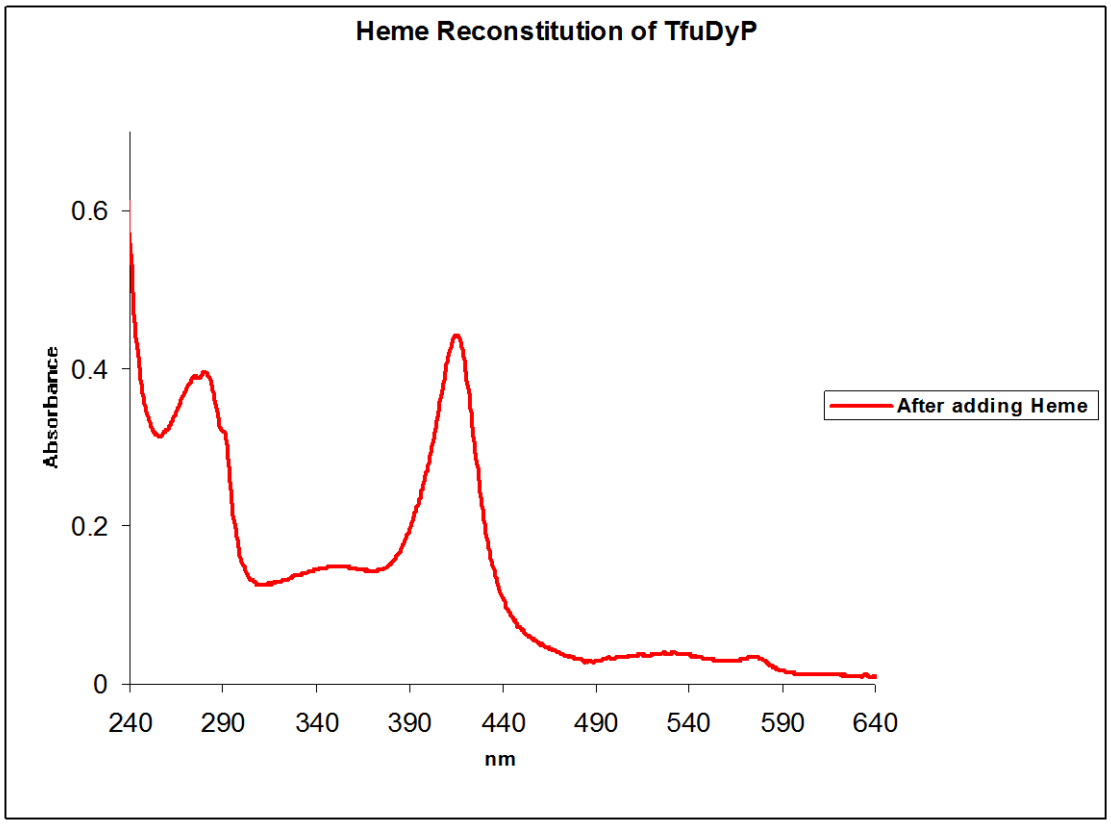

Figure3.3 - UV/Vis scan of TfuDyP after heme reconstitutio

3.4 pH profile of TfuDyP

Fig. 3.4 shows the pH profile of TfuDyP determined by 2,4-dichlorophenol (DCP) assay at 25 °C using Britton–Robinson buffer in the pH range 3–10, as explained in experimental section. Optimum pH was determined by plotting natural logarithm of obtained enzymatic activity versus corresponding pH value. The optimum pH for TfuDyP is 5.0-5.5, that is in good agreement with the optimum pH values obtained for other DyPs enzyme [63, 65, 68, 69].

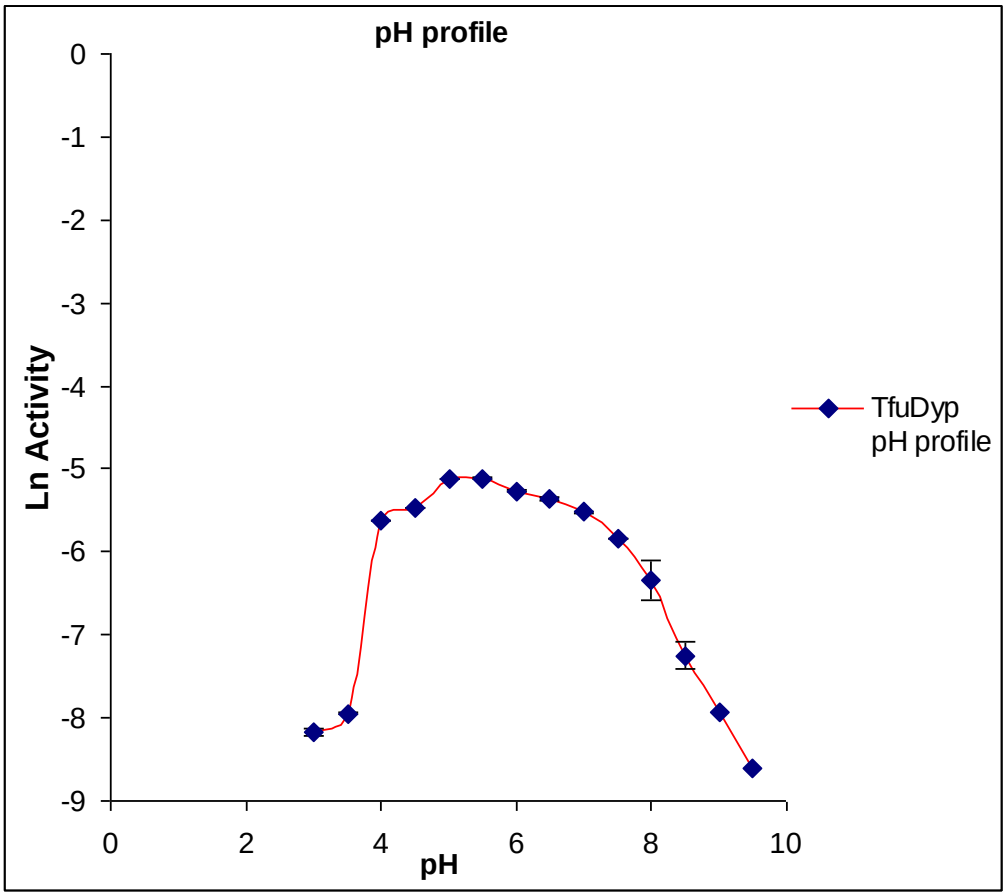

Figure 3.4 - pH profile of TfuDyP

3.5 Temperature profile of TfuDyP

Fig. 3.5 shows the temperature profile of TfuDyP determined by 2,4-dichlorophenol (DCP) assay in 100 mM acetate buffer pH 5.5 at different temperature ranging 25 to 75 °C as explained in experimental section. The temperature profile was determined by plotting obtained specific activity versus corresponding temperature. The obtained optimum temperature for TfuDyP is 50 °C.

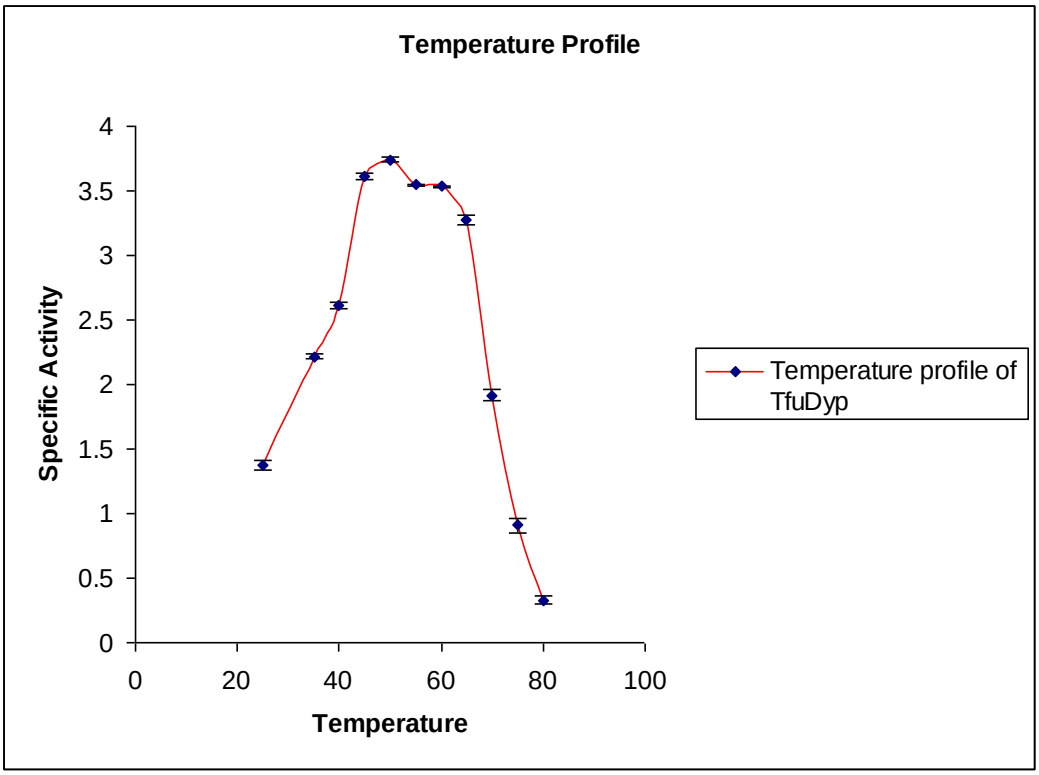

Figure 3.5 - Temperature profile of TfuDyP

3.6 Kinetic parameters of TfuDyP

TfuDyP enzyme was characterised using a range of peroxidase and lignin substrates, using UV-vis kinetic assays, and K_M and k_{cat} values measured, as shown in Table 3.1. For each parameter, standard errors were determined by statistical methods and represented along

with the reported data. Fig. 3.6 shows steady state kinetic plots for TfuDyP for each substrate, fitted by non-linear regression method.

Table 3.1 - Steady-state kinetic data for TfuDyP

	TfuDyP		
Substrate	**K_M (mM)**	**k_{cat} (s^{-1})**	**k_{cat}/K_M ($M^{-1}s^{-1}$)**
ABTS	0.86±0.07	28.1±1	3.26 x 10^4
H_2O_2[a]	0.082±0.003	36.3±0.3	4.39 x 10^5
Mn^{2+}	NA	NA	NA
2,4-dichlorophenol	5.51±0.5	2.86±0.1	0.518 x 10^3
Phenol	0.126±0.01	0.136±0.03	1.077 x 10^3
Guaiacol	NA	NA	NA
Pyrogallol	11.29±1	6.63±0.25	0.587 x 10^3
Reactive Blue 4	0.179±0.01	1.88 ±0.07	10.46 x 10^3
Kraft lignin[b]	0.01±0.0	1.13±0.03	1.057 x 10^5

[a] Using ABTS as substrate, [b]Assuming molecular weight of 10000 M.W.

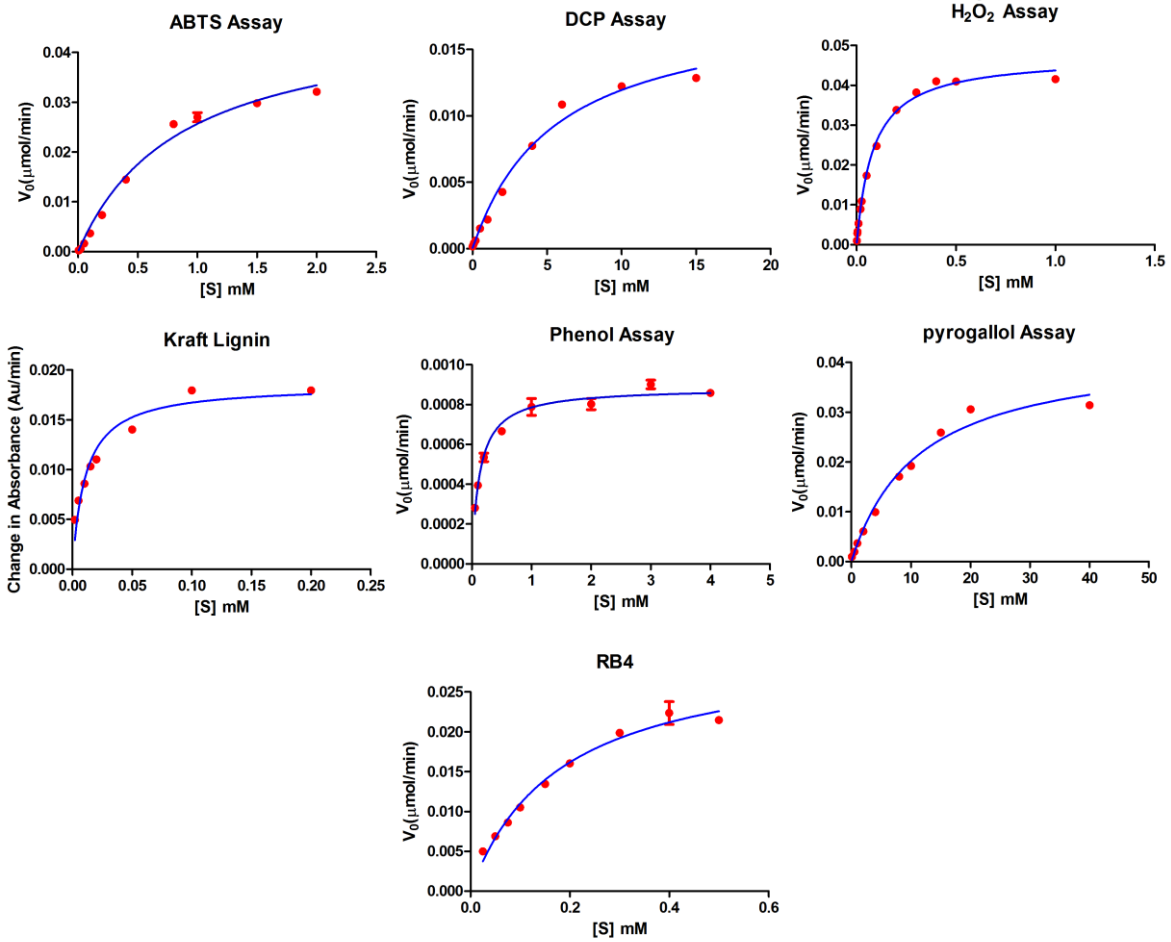

Figure 3.6 - Steady state kinetic plots of TfuDyP

TfuDyP did not show reactivity toward Mn (II) and guaiacol similar to previously characterised DyPA from *R. jostii* and DyPA from *P. fluorescens*. It showed the highest k_{cat} and the lowest Michaelis constant for ABTS as an azo dye among the other tested substrates, except the hydrogen peroxide, this is in agreement with data obtained from other characterised DyPA from *P. fluorescens* and and DyPA from *R. jostii* [65]. Compared with DyP1B and DyP2B from *P. fluorescens* TfuDyP represented the highest k_{cat} number for hydrogen peroxide and showed the highest Michaelis constant for oxidation of 2,4-dichlorophenol whereas for phenol oxidation it showed the lowest values for Michaelis constant and k_{cat}. TfuDyP catalytic parameters of oxidation of pyrogallol were similar to DyP2B and DyPA from *P. fluorescens*, high in Michaelis constant and catalytic turn over number, compared with DyP1B from *P. fluorescens*. For decolourization of reactive blue 4, an anthraquinone dye, TfuDyP showed, higher catalytic turnover number and lower Michaelis constant than DyPA and DyP1B from *P. fluorescens*. TfuDyP showed reactivity towards Kraft lignin, kinetic scanning of Kraft lignin reaction with TfuDyP in presence of 1mM Hydrogen peroxide 400 nm region showed obseved absobance changes. TfuDyP Prepresented higher catalytic turnover number compared with DyP1B from *P. fluorescens* and very similar to DyPA from *P. fluorescens*. However, TfuDyP did not show any reactivity towards wheat straw lignocellulose as analysed by reverese phase HPLC column.

3.7 Pre-steady-state kinetic characterisation of TfuDyP

The reactivity of TfuDyP was further analysed by pre-steady state stopped flow kinetics. Pre-steady state mixing with hydrogen peroxide leads to the time-dependent disappearance of the Soret band at 404 nm and a red shift to 401 nm in TfuDyP (Fig. 3.7).

At pH 5.5, equimolar rapid mixing of 5 μM TfuDyP with 5 μM H_2O_2 resulted in decay of the Soret band at 404 nm within ~400 ms with the concomitant appearance of a less

intense, broad UV–visible absorption characteristic of compound **I** in the 450-550 nm range corresponding to a compound **I** species similar to that observed for *R. jostii* RHA1 DyPB, The inset in Fig. 3.7 shows the UV–visible absorption plot.

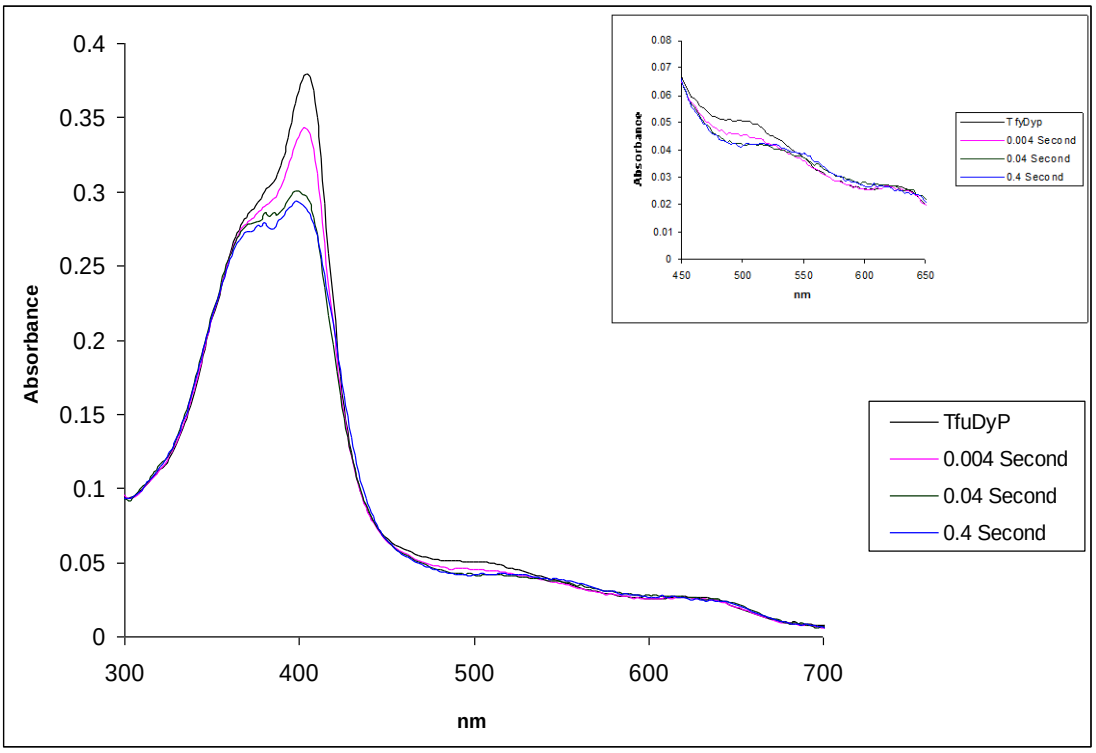

Figure 3.7 - UV–visible spectrophotometric scans of reaction of TfuDyP with 5 μM hydrogen peroxide from 1 to 400 ms, showing Soret band at 404 nm (gray line, before adding H_2O_2), then transition after 4 ms (pink line) and 40 ms (green line) to compound **I** peak at 404 nm (blue line). Inset shows new absorption at 450–600 nm

Fig. 3.8 represents the decay of the Soret band in 404 nm versus time. As is apparent from the plot, within 100 ms, the reaction is completed.

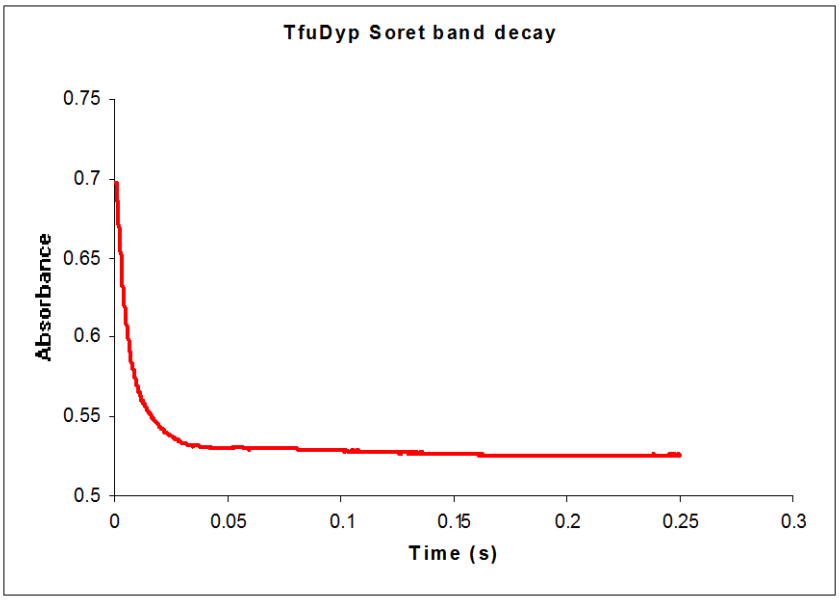

Figure 3.8 - Transient kinetic plot of TfuDyP for absorbance at 404 nm

The rate of formation of compound **I** in TfuDyP was investigated through enzyme-hydrogen peroxide titration experiments at varying concentrations of hydrogen peroxide (25 μM-250 μM). Measurement and fitting of obtained apparent rate constants by pro-data viewer software provided a second order rate constant of 0.55 $x10^5$ M^{-1} s^{-1}, nearly half of the value obtained for DyP1B (1.22 $x10^5$ M^{-1} s^{-1}) and much smaller the observed value for *R. jostii* RHA1 DyPB (1.79 $x10^5$ M^{-1} s^{-1}) [65]. Fig. 3.9 shows plot of first order k_{obs} values for reaction with hydrogen peroxide against hydrogen peroxide concentration.

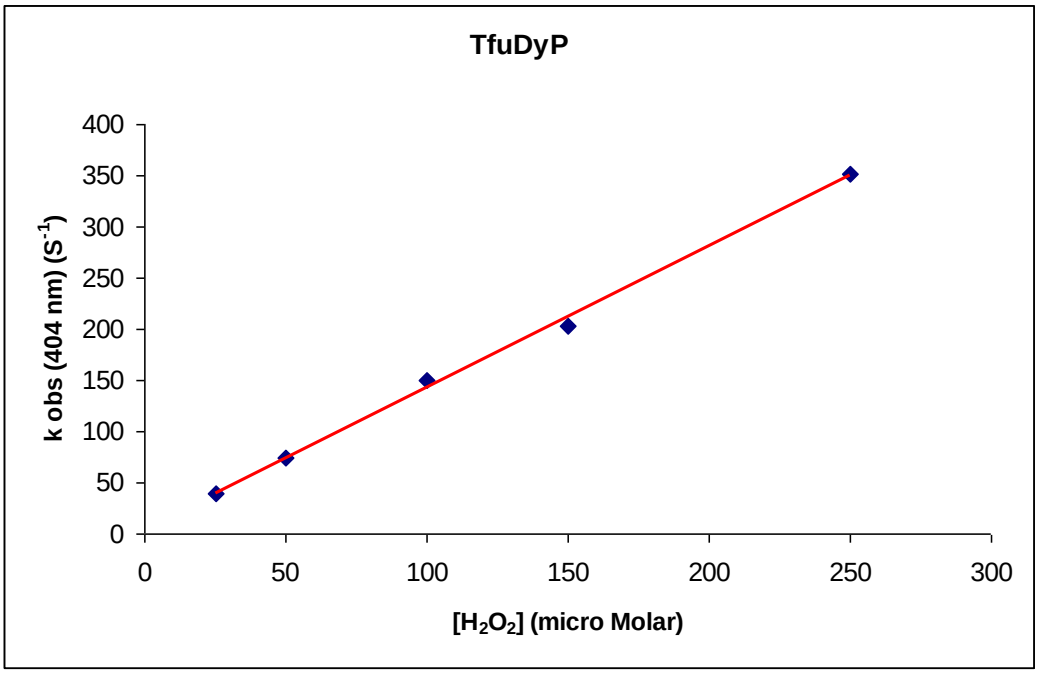

Figure 3.9 - plot of first order k_{obs} values for reaction of TfuDyP with hydrogen peroxide against hydrogen peroxide concentration

3.8 Oxidation of lignin model compound by TfuDyP

TfuDyp enzyme was incubated with a lignin model compound, a β-*O*-4-aryl ether (Fig. 3.10), and product formation monitored by reverse phase HPLC. After analysing reaction mixture by HPLC a significant new peak was observed at retention time 16 min compared with controls, as shown in Figure 3.11. The new peak was only formed in the presence of enzyme and H_2O_2.

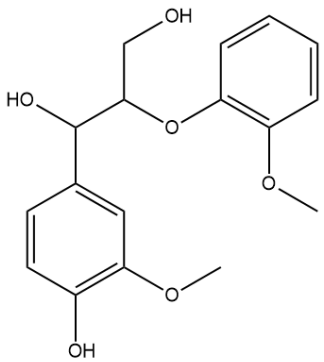

Figure 3.10- Beta-aryl ether lignin model compound (Guaiacylglycerol-beta-guaiacyl ether)

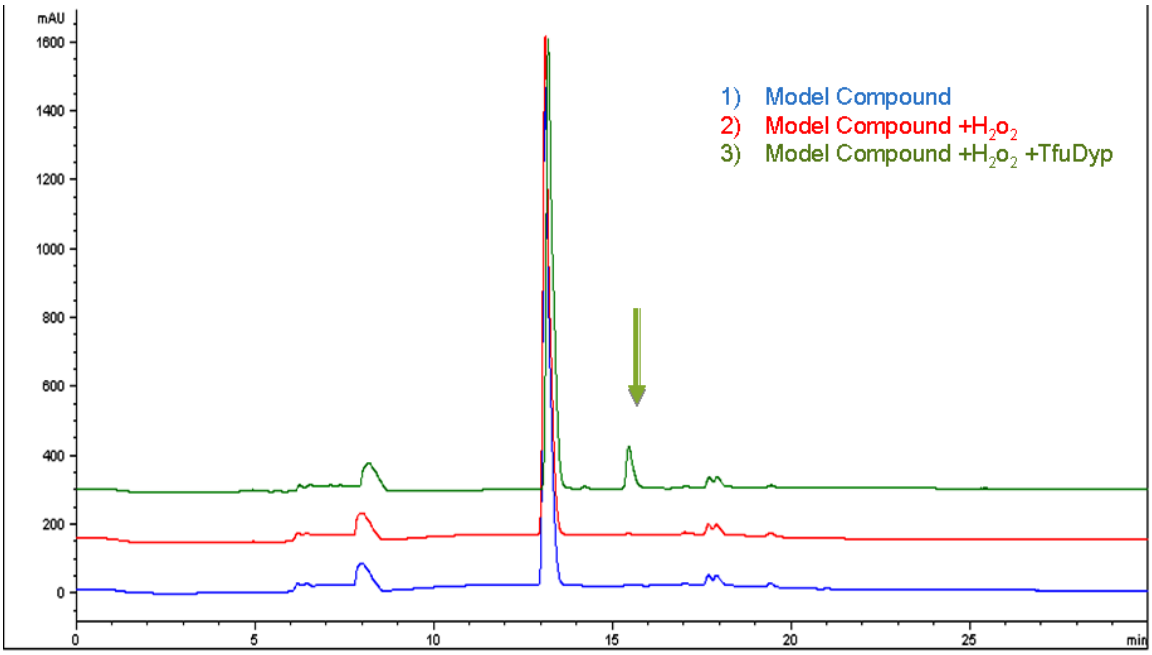

Figure 3.11 - Reverse phase HPLC analysis of TfuDyP incubation with Beta-aryl ether lignin model compound (Guaiacylglycerol-beta-guaiacyl ether), showing the formation of a new product peak at 16 min

The peak at retention time 16 min was collected and analysed by electrospray mass spectrometry, giving a molecular ion at *m/z* 661.2255, matching molecular formula $C_{34}H_{38}NaO_{12}$ (calculated *m/z* 661.23), consistent with dimer of the lignin model compound. Fig. 3.12 shows mass spectra for TfuDyP reaction product, compared with calculated values.

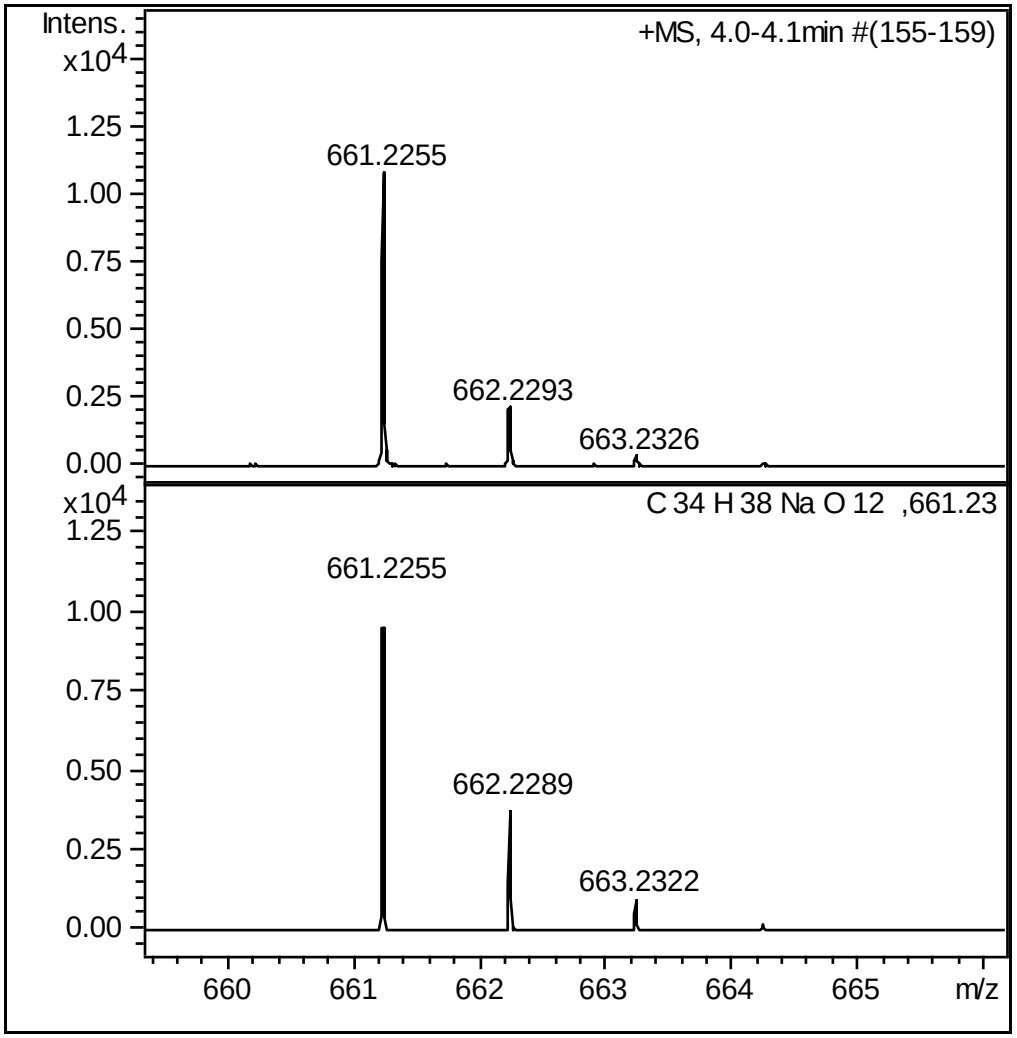

Figure 3.12 - High-resolution mass spectra for TfuDyP reaction product

MS-MS fragmentation of this compund gave fragments at *m/z* 343.2 (Fig.3.13). This fragment is consistent with the molecular structure of monomer, a β-aryl ether lignin model compound. Fig. 3.14 shows the molecular structure of most likely produced product, a dimer of Beta-aryl ether lignin model compound with higher molecular weight.

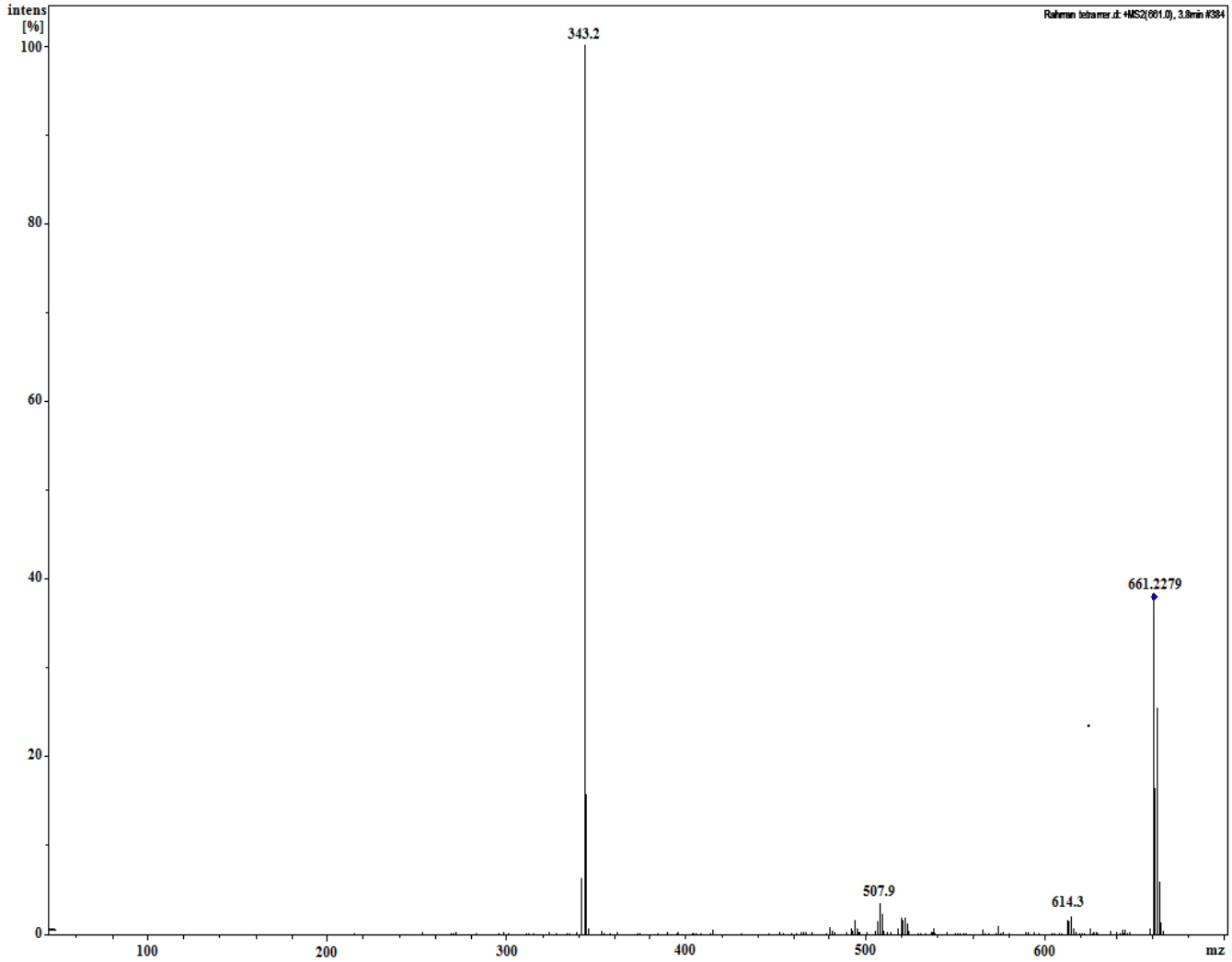

Figure 3.13 - MS-MS fragmentation products of product from reaction of TfuDyP with β-aryl ether lignin model compound (Guaiacylglycerol-beta-guaiacyl ether)

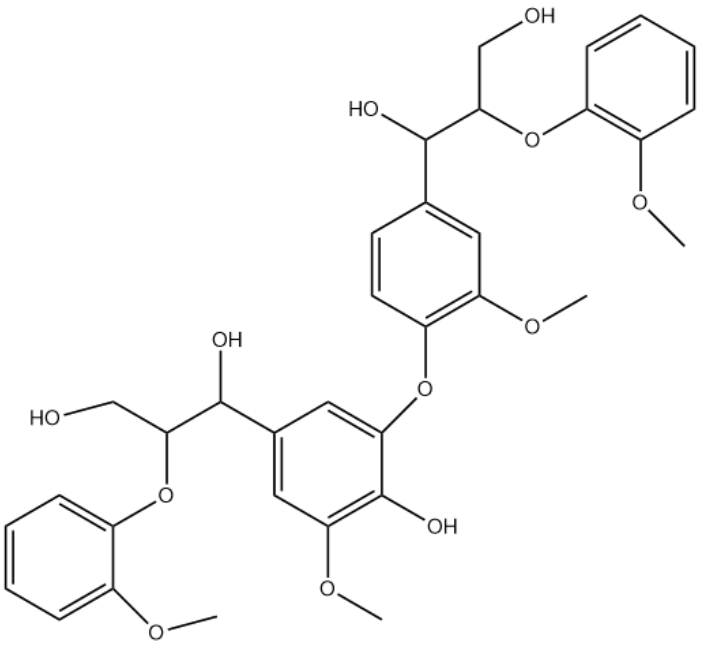

Figure 3.14 - Molecular structure of the product produced from incubation of TfuDyP enzyme with β-aryl ether lignin model compound (Guaiacylglycerol-beta-guaiacyl ether)

3.9 TfuDyP structure determination

Initial screening for crystallization and growing crystal was performed by Rahman Rahman pour and the structure of TfuDyP was solved by Dr. Dean Rea, School of Life Sciences, University of Warwick as explained in experimental section. Fig. 3.15 represents a picture of grown crystal before sending for data collection. Data collection and refinement statistics are given in Table 3.2. Pictures were generated by PyMOL [105].

Figure 3.15- Formed crystal of TfuDyP from *T. fusca*,

Table 3.2- Crystallographic data collection and refinement statistics

Data collection	
Unit cell a,b,c (Å), β (°)	a= 143.36, b= 110.21, c= 75.71, 46.73
Space group	$P2_12_12$
Resolution (Å)	42-1.70 (1.774-1.7)
Observations	418,399
Unique reflections	81,895
I/σ(I)	12.8 (2.0)
R_{sym}[a]	0.079 (0.687)
Completeness (%)	99.5 (97.7)
Refinement	-
Non-hydrogen atoms	6,086 (including 2 haems with the bound oxygens & 412 waters)
R_{cryst}	0.218 (0.405)
Reflections used	78,567 (5,495)
R_{free}	0.264 (0.436)
Reflections used	3,328 (238)
R_{cryst} (all data)	0.220
Average temperature factor (Å^2)	29.6
Rmsds from ideal values	-
Bonds (Å)	0.014
Angles (°)	1.7
DPI coordinate error (Å)	0.126

Numbers in parentheses refer to values in the highest resolution shell.
DPI refers to the diffraction component precision index [106].

TfuDyP structure shows it belongs to α/β superfamily and it reveal the general structural aspects of DyP-type peroxidases, containing a four-stranded antiparallel β-sheets fold and a βαββαβ motif in the secondary structure of TfuDyP that is indicative of a ferredoxin- like fold (Fig. 3.16) [45, 56, 57].

Figure 3.16- The overall structure TfuDyP from T. fusca, it is composed of two four-stranded antiparallel β-sheets domain. The picture was generated by PyMOL [105].

Similar to other DyPs, TfuDyP possesses an aspartic acid (Asp-203) and arginine (Arg-315) in its heme pocket that are involved in the formation of compound **I**. This replacement is one of the main differences between DyP and other peroxidases from plant superfamily that enable DyP to be catalytically active in acidic pH [45, 56, 57]. Fig. 3.17, Fig. 3.18 and Fig. 3.19 show the arrangement of conserved residues of proximal histidine (His-229), the Asp-203 and Arg-315 in heme distal area and GXXDG motif around heme molecule and distances between the key residues and a molecular oxgen in heme distal area.

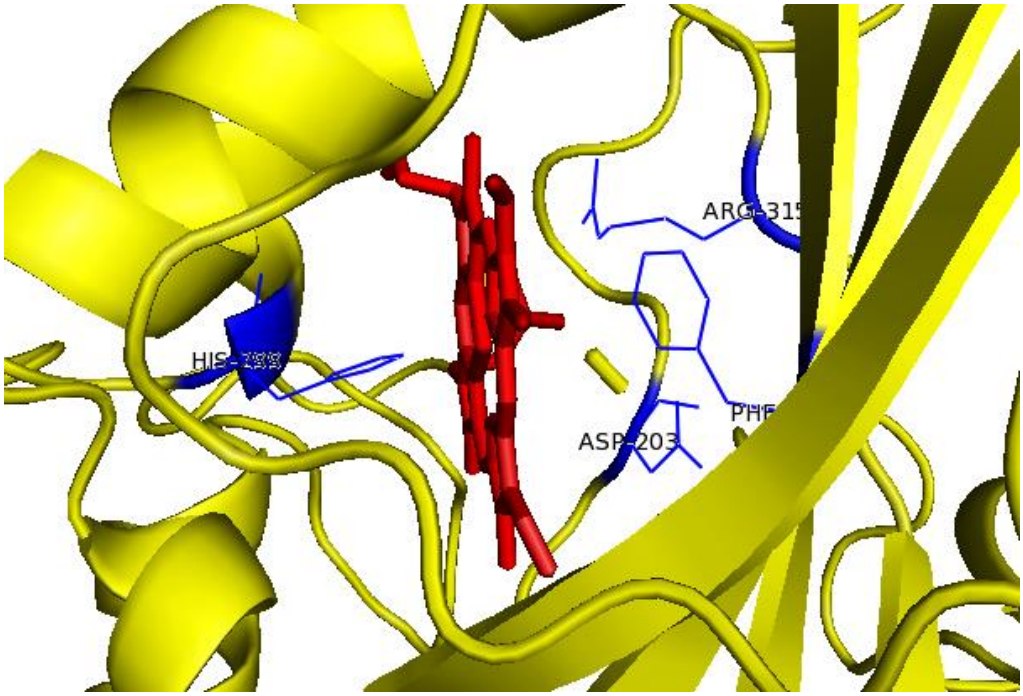

Figure 3.17-Position of heme in heme pocket of TfuDyP and arrangment of conserved residues of Asp-203 and Arg-315 in enzyme active site. The picture was generated by PyMOL [105].

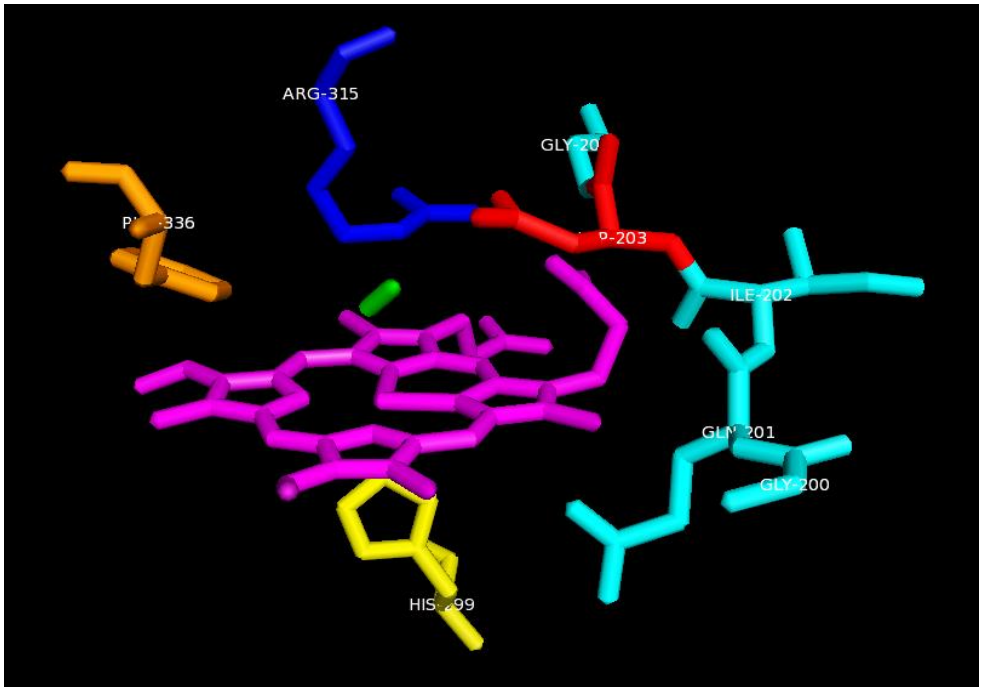

Figure 3.18- Arrangement of conserved catalytic residues and GXXDG motif around heme molecule. The picture was generated by PyMOL [105].

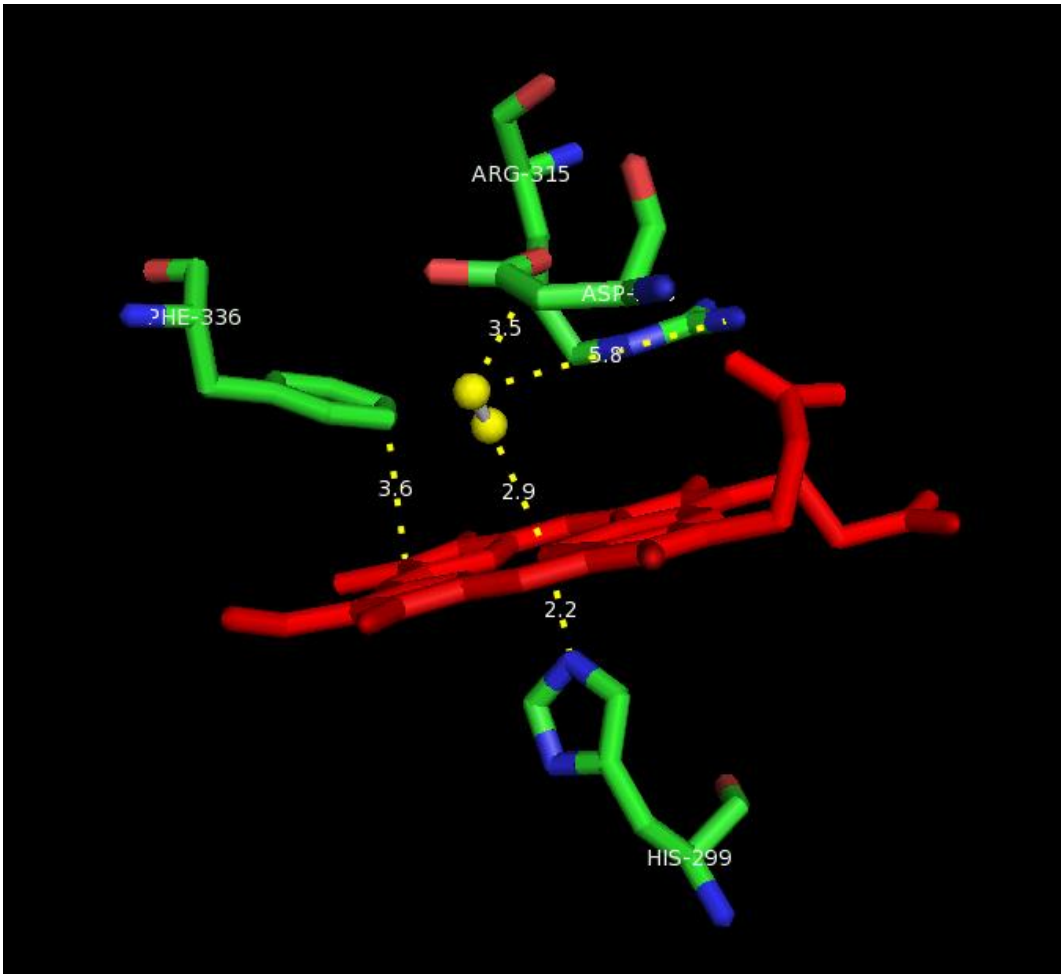

Figure 3.19- Distances between conserved catalytic residues and a molecular oxygen molecule present in heme distal area.The picture was generated by PyMOL [105].

The crystal structure of heme-bound TfuDyP displays a diatomic molecule acting as the distal ligand. Since the heme iron atom can be photoreduced to the ferrous state because of the prolonged x-ray exposure [107–109], therefore, it is most likely that the iron was in the ferrous form and coordinated by an oxygen molecule.

In all DyP structures solved so far, the presence of a phenylalanine residure in the distal area and above one of the pyrrole rings of heme is conserved. TfuDyP also possesses a phenylalanine residue in same position as Phe-336. So far no role has been assigned to this residue, therefore, in our site directed mutagenesis study we also planned to mutate this particular residue along with other selected residues present in the heme pocket.

Fig. 3.20 and Fig. 3.21 show the surface representation of TfuDyP structure and presence of two entrances for accessing of substrates to the heme pocket. The small entrance shown in Fig. 3.20 might be a passage for the hydrogen peroxide to access the distal heme area.

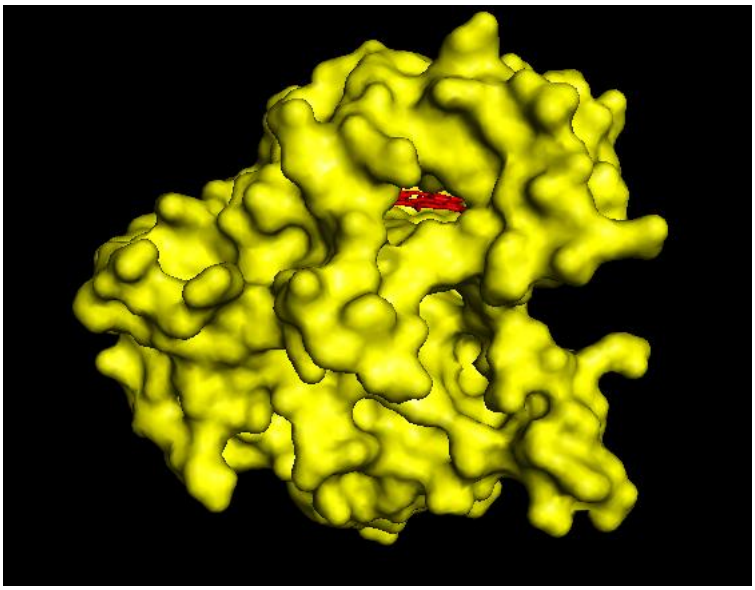

Figure 3.20-Surface representation of TfuDyP structure and the main entrance to the heme. The picture was generated by PyMOL [105].

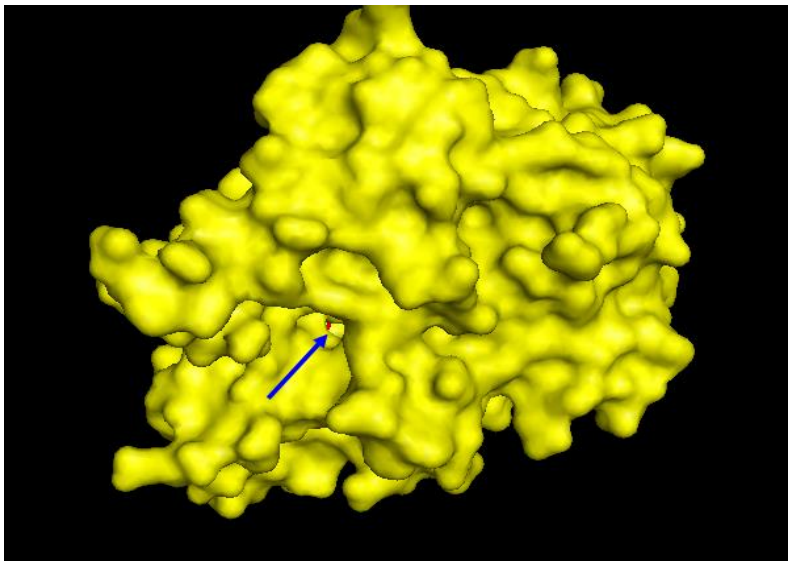

Figure 3.21-Surface representation of TfuDyP structure and position of the small entrance to the heme. The picture was generated by PyMOL [105].

Further anlysis of the structure by MOLE 2.0 software also revealed the presence of two tunnels for substrate to access the heme cavity. The main tunnel (Fig. 3.22) provides access to distal area and it is consisted of Asp-203, Gly-317, Ser-319, Leu-334, Phe-336, Arg-196, Tyr-318, Phe-181, Arg-183, Pro-195, Arg-315, Arg-316 and Ala-39.

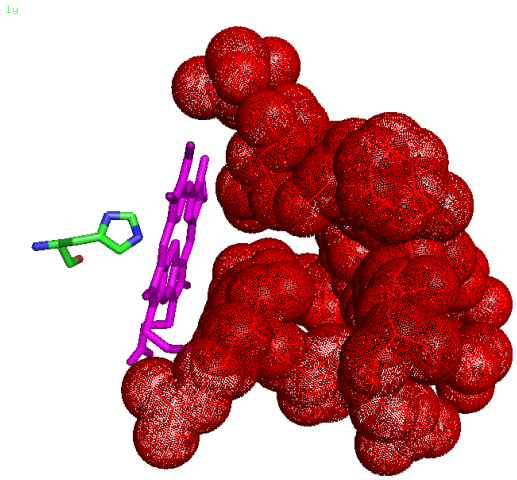

Figure 3.22-Dot representation of the tunnel that connects bulk medium to distal area in TfuDyP structure along with proximal histidine 299. The picture was generated by PyMOL [105].

The other tunnel provides access to heme pocket through proximal area; it is smaller tunnel than the above mentioned main tunnel. It is consisted of Ile-243, His-367, Ile-365, Gln-351, Leu-354, Asn-362, Thr-133, Ile-362 and Arg-366. Fig. 3.23 depicts the proximal tunnel.

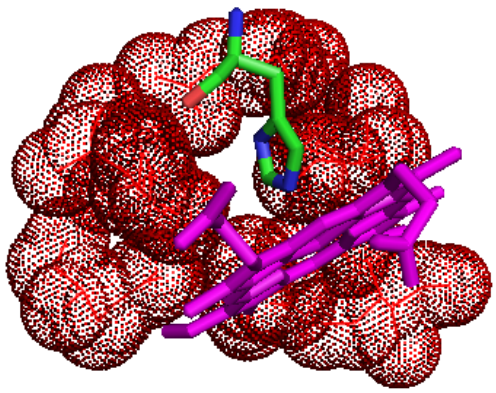

Figure 3.23-Dot representation of the tunnel that connects bulk medium to proximal area in TfuDyP structure along with proximal histidine 299. The picture was generated by PyMOL [105].

3.10 Mutational studies

In order to investigate the role of amino acids present in the distal area of heme pocket of TfuDyP, we aimed to mutate Asp-203, Arg-315 and Phe-336 to alanine, glutamine and alanine respectively. Mutations were carried on by QuikChange II XL Site-Directed Mutagenesis Kit as it explained in experimental sections. Expressing, purification and heme reconstition of mutant enzymes were performed as described in sections 3.2 and 3.3. Fig. 3.24, Fig. 3.25 and Fig. 3.26 show the gel pictures of purification of TfuDyP D203A, TfuDyP R315Q and TfuDyP F336A mutant enzyme respectively.

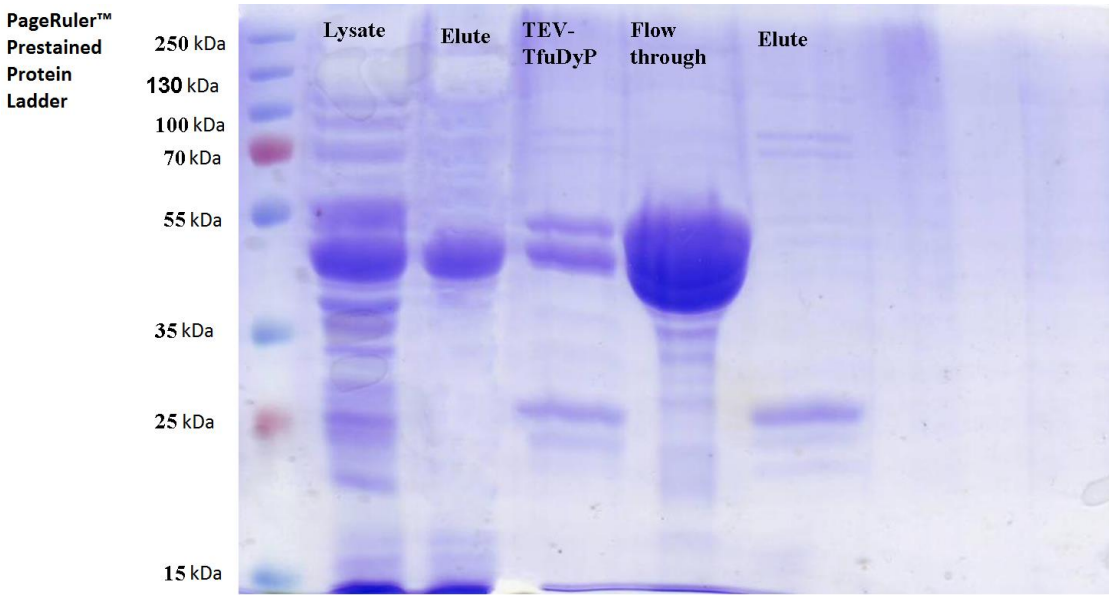

Figure 3.24 - SDS PAGE of TfuDyP D203A mutant purification steps

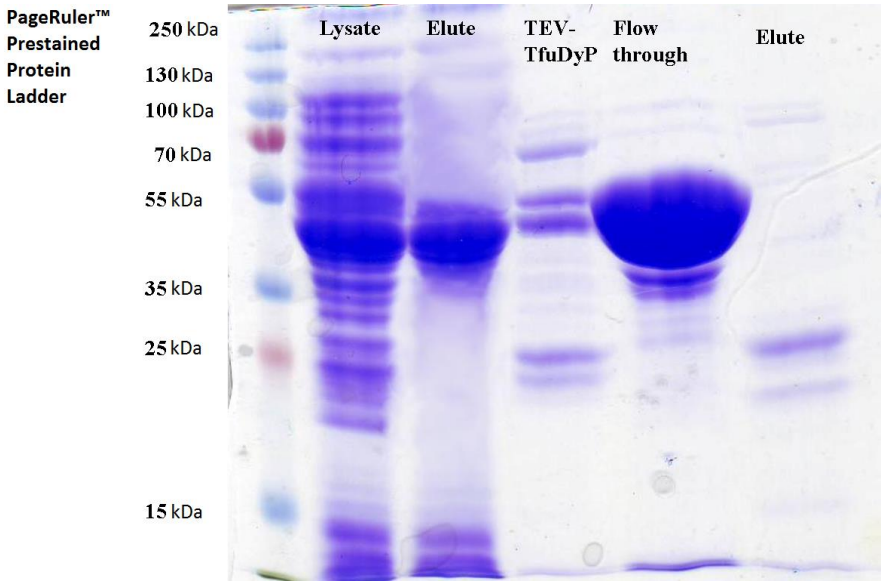

Figure 3.25 - SDS PAGE of TfuDyP R315Q mutant purification steps

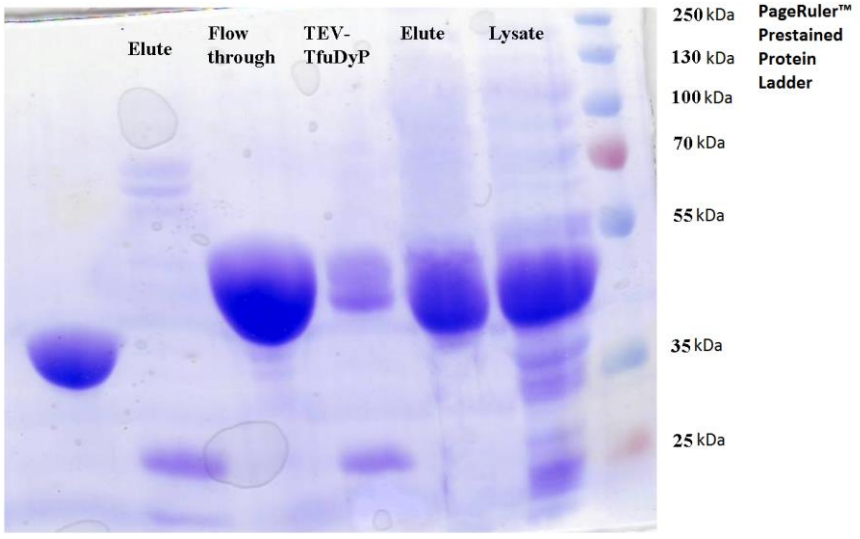

Figure 3.26 - SDS PAGE of TfuDyP F336A mutant purification steps

3.11 Kinetic parameters of TfuDyP mutants

TfuDyP mutant enzymes were characterised using two substrates, ABTS and Phenol, by UV-vis kinetic assays, and K_M and k_{cat} values measured, as shown in Table 3.3. For each parameter, standard errors were determined by statistical methods and represented along with the reported data. Fig. 3.27, Fig. 3.28 and Fig. 3.29 show steady state kinetic plots for TfuDyP D203A, TfuDyP R315Q and TfuDyP F336A, fitted by non-linear regression method.

Table 3.3 - Steady-state kinetic data for TfuDyP mutants

Enzyme	**ABTS**			**H_2O_2**			**Phenol**		
Unit	**K_M (mM)**	**k_{cat} (s^{-1})**	**k_{cat}/K_M (M^{-1} s^{-1})**	**K_M (mM)**	**k_{cat} (s^{-1})**	**k_{cat}/K_M (M^{-1} s^{-1})**	**K_M (mM)**	**k_{cat} (s^{-1})**	**k_{cat}/K_M (M^{-1} s^{-1})**
TfuDyP_WT	0.86±0.07	28.1±1	3.26×10^4	0.082±0.01	36.3±0.39	4.40×10^5	0.126±0.01	0.136±0.0	1077
TfuDyP_D203A	0.122±0.01	1.01±0.01	8.27×10^3	0.066±0.00	1.3±0.02	1.9×10^4	No activity	No activity	No activity
TfuDyP_R315Q	No Activity [a]	No activity	No activity	8.6±0.82 [b]	8.26±0.39	960.46	No activity	No activity	No activity
TfuDyP_F336A	1.13±0.12	66.5±3.5	5.88×10^4	0.053±0.00	30.51±0.48	5.72×10^5	0.118±0.01	0.137±0.0	1158

[a] No activity at 1mM hydrogen peroxide
[b] Activity measured at above 1mM hydrogen peroxide

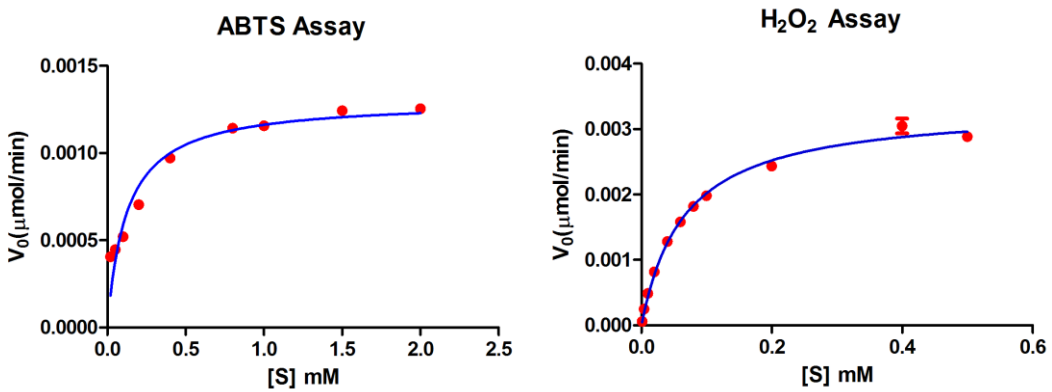

Figure 3.27 - Steady state kinetic plots of TfuDyP_ D203A

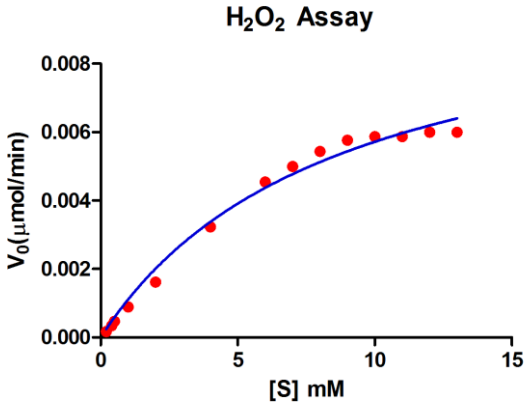

Figure 3.28 - Steady state kinetic plots of TfuDyP_ R315Q

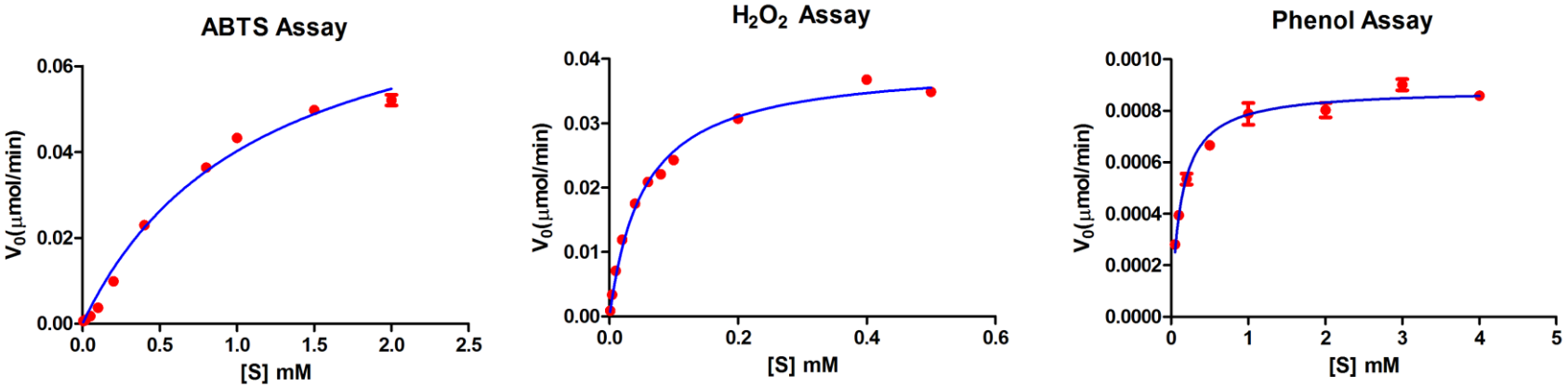

Figure 3.29 - Steady state kinetic plots of TfuDyP_ F336A

By comparing the obtained results from these three mutants with wild type TfuDyP, it seems that Arg 315 is involved in stabilizing bound hydrogen peroxide to the heme molecule [97]. The Michaelis constant of TfuDyP R315Q for hydrogen peroxide has increased 100-fold, accompanied by a 4-fold decrease in k_{cat}, whereas TfuDyP D203A variant shows a 36-fold decrease in k_{cat} for hydrogen peroxide and a small decrease in the Michaelis constant of hydrogen peroxide. Therefore, the obtained results indicate that the arginine residue in distal area of heme pocket of TfuDyP is involved in stabilizing of either bound hydrogen peroxide or the oxo-ferryl intermediate (compound **I**). TfuDyP R315Q did not show any activity for oxidation of ABTS, since the concentration of hydrogen peroxide was 1 mM in all of different concentrations of ABTS for enzyme activities that is much lower than the obtained Michaelis constant of TfuDyP R315Q for hydrogen peroxide. In case of oxidation of phenol by TfuDyP R315Q mutant, it did not show observable activity. This could be explained by drastic increase in Michaelis constant of TfuDyP R315Q that leads to its insensivity for hydrogen peroxide in its constant concentartion of 1 mM in enzyme activity assays and the enzyme behaves in similar fashion that acted for ABTS oxidation reaction.

The accepted view for the functional role of the catalytic aspartate residue in the distal area of heme in DyP peroxidases is involvment in the catalytic cycle of compound **I** formation by protonation of hydrogen peroxide and subsequent heterolytic cleavage of hydrogen peroxide [56,79]. This is in agreement with kinetic data obtained for oxidation of ABTS and hydrogen peroxide by TfuDyP D203A. Since aspartate reside might be involved in heterolytic cleavage of hydrogen peroxide, followed by compound **I** formation, the k_{cat} oxidation of ABTS and hydrogen peroxide have decreased 28 and 36-fold respectively. There is also 8-fold decrease for Michaelis constant of TfuDyP D203A for ABTS that might be the result of removing electrostatic clashes between aspartate residue and two sulfonic groups present in ABTS molecule that might improve binding of ABTS to heme pocket. In case of oxidation of phenol by TfuDyP D203A mutant, it did not show observable activity. It might be because of inherent low activity of TfuDyP toward oxidation of phenol and drastic

decrease in k_{cat} for hydrogen peroxide. Therfore, it is reasonable that no sign of activity was observed.

For oxidation of phenol TfuDyP F336A showed nearly similar trend to wild type TfuDyP but in cases of hydrogen peroxide and ABTS, it showed nearly different behaviour. Its reactivity toward hydrogen peroxide is accompanied with a 1.2 and 1.5-fold decrease in k_{cat} and Michaelis constant respectively compared with wild type enzyme. Interestingly, TfuDyP F336A showd a 2.3-fold increase in k_{cat} for oxidation of ABTS along with a 1.31-fold increase in the Michaelis constant. Probably the minor increase in k_{cat} for oxidation of ABTS is because of removing some steric effects or hindrance between the bulky molecule of ABTS and benzene ring of phenylalanine that leads to providing more space and improved orientation for ABTS to be oxidized in heme pocket. In contrast, the minor increase in the Michaelis constant for oxidation of ABTS might be also the result of participation of Phe-336 in formation of the main tunnel (Fig. 3.22) that provides access to distal area of heme pocket.

The obtained steady state kinetic results of these three mutants, specifically results of TfuDyP D203A and TfuDyP R315Q, support the view that Asp-203 is involved in protonation of hydrogen peroxide and subseqeunt compound **I** formation not Arg-315 [56,79]. This is in disagreement with results obtained for DyPB from *R. jostii* RHA1 that suggests the arginine residue in distal area of heme protonates the hydrogen peroxide and has the main role in formation of compound **I** [67]. However, the steady state kinetic results of the TfuDyP mutants represent a good agreement with data reported for Dec1 from fungus *B. adusta* [56] in which replacement of Asp-171 in *B. adusta* Dec1 by Asn leads to a 3,000-fold loss in catalytic activity, consistent with a catalytic role in protonation of the bound peroxide [56]. in addition, the crystal structure of the D171N *B. adusta* Dec1 mutant and wild-type enzymes shows considerable movement of the Asp/Asn residue, with high measured RMSD values, suggesting that the movement of Asp-171 within the active site is needed for protonation of

peroxide [79]. Table 3.4 shows compared kinetic constants of TfuDyP mutants, DyPB mutant from *R. jostii* RHA1 and DyP mutant from *B. adusta* Dec1.

Table 3.4 - Steady-state kinetic data of hydrogen peroxide for TfuDyP mutants, DyPB mutants from *R. jostii* RHA1 and DyP mutant from *B. adusta* Dec1 by using ABTS as a second substrate

Enzyme	**H_2O_2**		
	K_M (mM)	**k_{cat} (s^{-1})**	**k_{cat}/K_M (M^{-1} s^{-1})**
TfuDyP_WT	0.082±0.01	36.3±0.39	4.40×10^5
TfuDyP_D203A	0.066±0.00	1.3±0.02	1.9×10^4
TfuDyP_R315Q	8.6±0.82 [a]	8.26±0.39	960.46
DyPB_WT	0.027± 0.0	3.2±0.03	1.20×10^5
DyPB_ D153A	0.46±0.03	51±3	1.10×10^5
DyPB_R244L	No Activity	No activity	No activity
DyP_D171N	No Activity	No activity	No activity

[a] Activity measured at above 1 mM hydrogen peroxide

3.11 Conclusion

This study showed that TfuDyP from Gram-positive bacterium *T. fusca* is able to oxidize lignin model compound, Guicylglycerol-beta-guiacyl ether, and shows comparable activty toward Kraft lignin similar to DyP1B from Gram-negative bacterium *P. fluorescens* and DyP1B from Gram-positive bacterium *R. jostii*.

The enzyme was characterised using a range of peroxidase and K_M and k_{cat} values was measured. TfuDyP enzymes showed catalytic activity with peroxidase substrate ABTS, with k_{cat} values of 28.1 $s^{-1}$and it was active with dye substrate Reactive Blue 4, characteristic

of the DyP family of peroxidases [46, 55, 57, 62, 63, 70]. Similar to DyPA from *R. jostii* and *P. fluorescens*, TfuDyP showed no activity for Mn^{2+} oxidation and the enzyme was able to oxidise some phenolic substrates, less efficiently than ABTS.

By pre-steady-state kinetic charecterisation of TfuDyP, the second order rate constant of compound **I** formation was calculated (0.55 $x10^5$ M^{-1} s^{-1}) that was nearly half of the value obtained for DyP1B from *P. fluorescens* (1.22 $x10^5$ M^{-1} s^{-1}) and much smaller the observed value for *R. jostii RHA1* DyPB (1.79 $x10^5$ M^{-1} s^{-1}) [65]. It is indicative of less activity of DyP-type As compared with DyP-type Bs.

The structure of TfuDyP was solved at 1.7 Å and it showed general structural aspects of DyP-type peroxidases such as containing four-stranded antiparallel β-sheets fold and the presence of a βαββαβ motif in the secondary structure of TfuDyP that is indicative of a ferredoxin- like fold [45, 56, 57]. Similar to other DyPs, TfuDyP possesses GXXDG motif, which contains Asp-203 that is involved in the formation of compound **I** [45, 56, 57].

Based on the structural data of TfuDyP provided by X-ray crystallography, three amino acids in the distal area of heme pocket of TfuDyP were targeted for site directed mutation studies. The kinetic parametres for these three mutant enzyme showed that probably Asp-203 initiates the catalytic activity of TfuDyP by protonating of the hydrogen peroxide followed by heterolytic cleavage of hydrogen peroxide and formation of a oxo-ferryl intermediate, known as compound **I**. The mutational study suggests that the arginine residue present in the distal area of TfuDyP, contrary to DyPB from *R. jostii*, is involved in binding phenomena and stabilizing of bound hydrogen peroxide to the heme molecule rather than compound **I** formation.

Some of the results from next chapter have been published in FEBS Journal

Rahman Rahmanpour and *Timothy DH Bugg.* Assembly in vitro of *Rhodococcus jostii RHA1* encapsulin and peroxidase DyPB to form a nano compartment

FEBS J. 2013 May; 280(9):2097-104. doi: 10.1111/febs.12234.

Chapter Four

Assembly in vitro of *Rhodococcus jostii* RHA1 encapsulin and peroxidase DyPB to form a nanocompartment

4.1 Introduction

Compartmentalizing materials and enzymatic reactions for increasing metabolic efficiency is one of the outstanding characteristics of living cells. The accepted view has been that prokaryotic cells are inherently unstructured sacks of cytoplasm and the compartmentalization processes take place only in the eukaryotes. However, recent research utilizing electron microscopy, structural and biochemical techniques have changed this view.

Eukaryotes use membrane-bound organelles for compartmentalization whereas bacteria and archaea have been recently discovered to utilize protein-based compartments, thin polyhedral protein shells that accommodate enzymes that catalyze essential steps in bacterial metabolism. In other word, bacteria sequester key metabolic steps into polyhedral protein compartments [116]. These complex macromolecular assemblies allow bacteria to inhabit certain metabolic and/or geophysical niches [116]. Genes encoding the proteinous

compartment are present in all the main bacterial lineages, except the γ-proteobacteria [116] that is indicative of exploiting the compartmentalization approach in prokaryotes as a common strategy for sequestering of critical metabolic steps [116].

Protein-based organelles or so-called microcompartments have been recently identified in bacteria. They consist of polyhedron-shaped arrays of protein monomers that accommodate particular enzymes/proteins in their inside that catalyse a specific biochemical pathway [101]. The carboxysome, an icosahedral protein complex 80–150 nm in diameter, has been found in cyanobacteria and chemoautotrophic bacteria. It contains enzymes for CO_2 fixation, by sequestering ribulose 1, 5-bisphosphate carboxylase/oxygenase (RubisCO) enzyme along with a carbonic anhydrase (Fig. 4.1). The carboxysome makes available a compartment with elevated CO_2 levels that increase the kinetic competency of RubisCO [102, 77].

Salmonella enterica produces the polyhedral Pdu microcompartment that contains enzymes for 1,2-propanediol utilization [103]. Enteric bacteria such as *Escherichia coli, and S. enterica* possess the Eut microcompartment that contains enzymes for ethanolamine utilization [104].

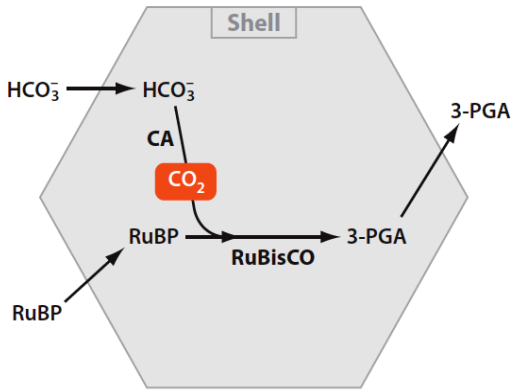

Figure 4.1 - Schematic picture of carboxysome that contains enzymes for efficient CO_2 fixation [101]. The picture was taken from Bacterial Microcompartment Organelles: Protein Shell Structure and Evolution. Todd O. Yeates *et al.*, Annu. Rev. Biophys., 2010, 39, 185

By sequestering the required enzymes for 1,2-propanediol and ethanolamine utilization in the Pdu and Eut protein shells respectively, the risk of diffusion and subsequent loss of volatile aldehyde intermediates, formed in the course of the pathway, that might damage cellular structures is prevented [117].

A short peptide signal was discovered on the N-terminus of those enzymes that are contained within the Pdu polyhedral shell of *S. enterica*. This short peptide signal acts as a leader sequence for the targeting of these enzymes into the proteinous compartment [118].

The shell proteins of microcompartment that have been purified and characterized so far are composed of several component polypeptides, each containing a Bacterial Microcompartment (BMC) domain (Pfam 00936). The BMC domain usually is made of about 90 amino acid residues. It shows β-α-β motif architecture that joined by a β-hairpin (Fig. 4.2). Most of the shell proteins comprise of a single BMC domain in their constituent subunits. Crystallographic studies have shown that the shell constituent monomers are organized into thin hexamers that actively interact in an edge-on fashion to form the flat facets of the polyhedral compartments (Fig. 4.3) [109, 117].

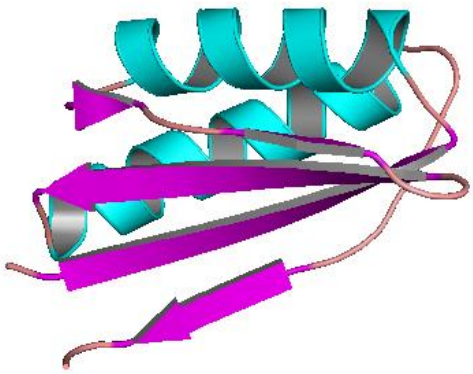

Figure 4.2 - Ribbon representation of the BMC domain that shows β-α-β motif architecture, joined by β-hairpin. The picture was generated by PyMOL [105].

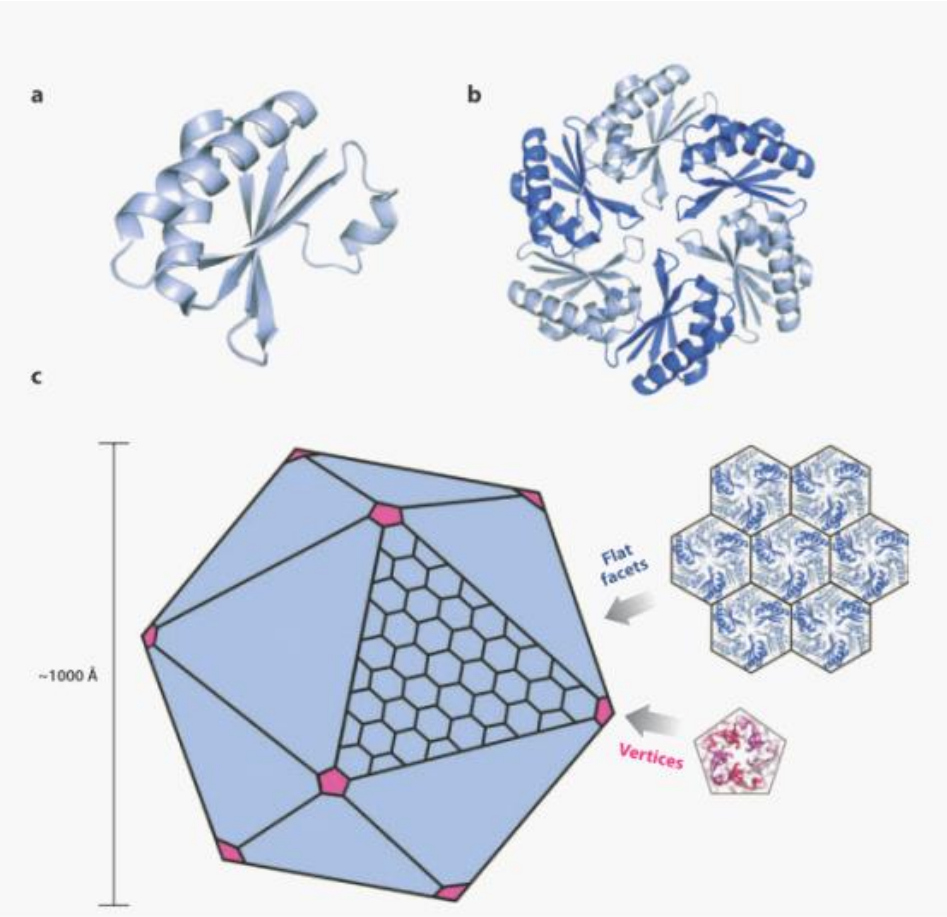

Figure 4.3 - Schematic model for assembly of the carboxysome and other bacterial microcompartments [101]. The ribbon representation of BMC fold (A). A hexameric assembly of a BMC protein in a ribbon diagram (B). Assembly of hexameric building blocks of the BMC proteins into a molecular layer (right), which constitutes flat facets of the polyhedral shells of bacterial microcompartments (C). The pentameric proteins (CcmL or CsoS4A) from the carboxysome (bottom, right) that are believed to form vertices of the icosahedral carboxysome (left) [101]. The pictures was taken from Bacterial Microcompartment Organelles: Protein Shell Structure and Evolution. Todd O. Yeates *et al*., Annu. Rev. Biophys., 2010, 39, 185

A smaller 240 Å icosahedral nanocompartment has been characterized in hyperthermophilic bacterium *Thermotoga maritima*, whose shell-forming protein is called encapsulin [76, 77]. Homologues of the encapsulin monomer has been characterized in *Brevibacterium linens*, where they show antibacterial activity as an extracellular 29-kDa protein, linocin [77, 120] and in *Mycobacterium tuberculosis* [77, 121]. The encapsulin from *T. maritima* is only 20-25% the diameter of most microcompartments [116]. Encapsulins are a

class of nanocompartments widespread in bacteria and archaea whose functions are still unclear [122].

The crystal structure of an encapsulin protein from *T. maritima* was determined at 3.1 Å [76]. Studies on the structure revealed that the icosahedral shell with diameter 240 Å is formed by assembly of 60 copies of a monomer [76] (Fig. 4.4).

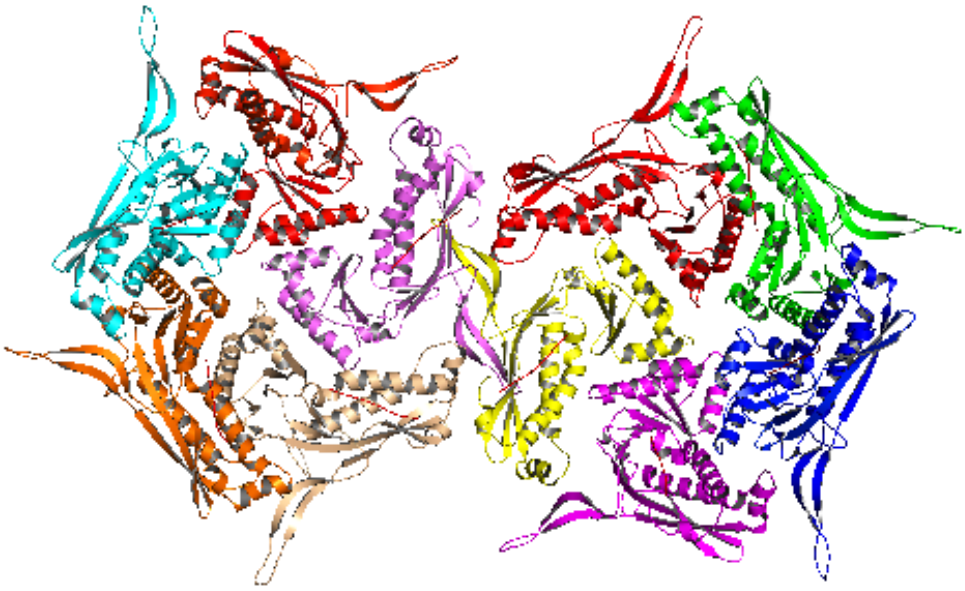

Figure 4.4 - Ribbon representation of two pentamers of encapsulin protein from *T. maritima* solved by X-ray crystallography at 3.1 Å. The Picture was generated by PyMOL [105].

The encapsulin forms 12 pentamers, each one with a central pore, which is uncharged. There are also some other small pores between neighbouring pentamers that are lined with charged residues and collectively providing several possibilities for selective entry and exit of ions and substances (Fig. 4.5), the size of these holes is nearly around 5 Å [76].

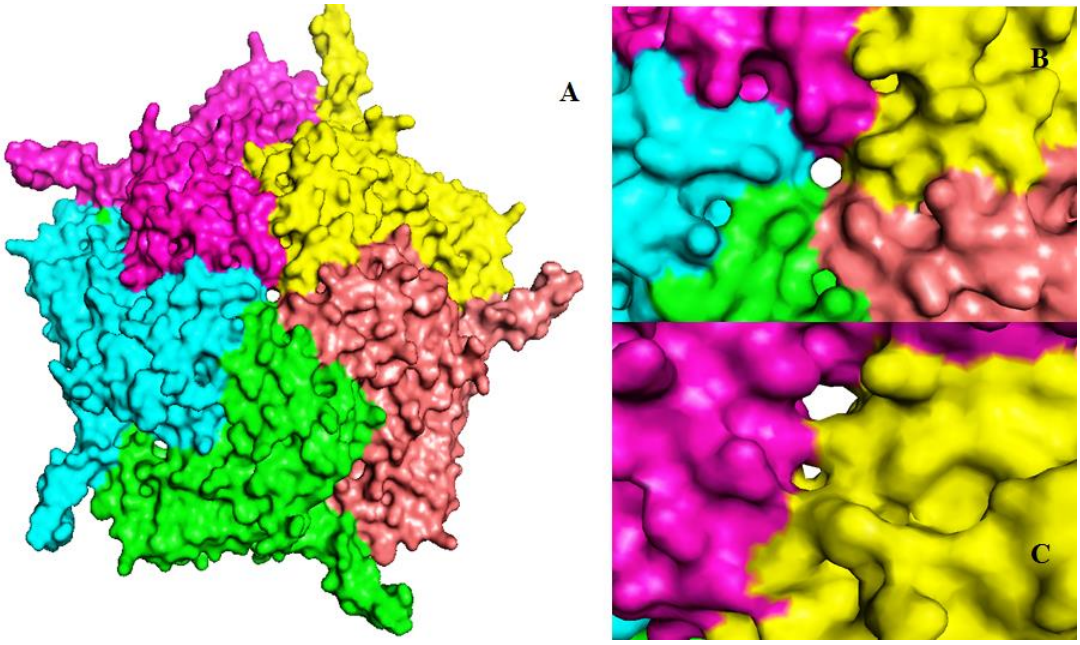

Figure 4.5 - Surface representation of the holes in the shell of *T. maritima* encapsulin; central hole in each pentamer (A&B), holes between adjacent monomer (C). The picture was generated by PyMOL [105].

The structure of the 31-kDa monomer of encapsulin from *T. maritima* (Fig. 4.6) is very similar to the viral capsid protein monomer but the sequence homology is weak [76].

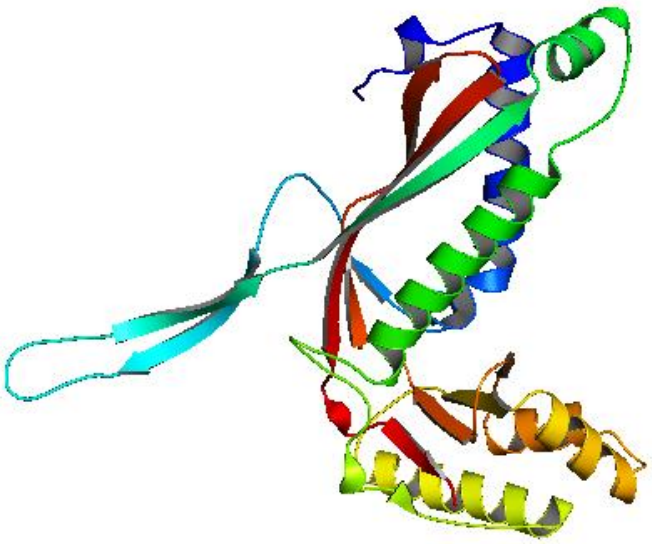

Figure 4.6 - Structure of encapsulin monomer of *T. maritima*. The picture was generated by PyMOL [105].

In the interior of this nanocompartment, there are conserved binding sites for short, specific sequences at the C-terminal of enzymes that are targeted to the encapsulin [76]. A C-terminal peptide extension has been identified by Sutter *et al*. [76] that acts to target two different types of protein to the interior of encapsulin in different bacteria: a DyP-type peroxidase and a ferritin-like protein. Bioinformatics studies also indicate when a BLAST search for the *T. maritima* encapsulin was performed, 49 homologous proteins appeared [76]. By checking the genomic context of these homologous, almost all of them can be categorized as a constituent of those operons that code for DyP- type peroxidase or ferritin-like protein [76]. The presence of Flp and of iron in encapsulin from *T. maritima* was confirmed by mass spectrometry and X-ray fluorescence techniques, respectively [76]. In the study of the *T. maritima* encapsulin, a 10-residue peptide sequence (GSLxIGSLKG) at the C-terminus of the associated DyP-type peroxidase or ferritin protein was identified [76]. The study suggested that the peptide sequence might be responsible for targeting of the protein to the nanocompartment [76, 77]. As shown in Table 4.1, this C-terminal peptide sequence also exists in DyPB enzyme from *Rhodococcus jostii* RHA1.

In this study we examined a number of bacterial DyPB homologues, and their C-terminal amino acid sequences, the results are represented in Table 4.1 [77].

Table 4.1 - Alignment of C-terminal amino acid sequences of bacterial DyPB homologues. Sequences are listed in order of sequence similarity to the R. jostii RHA1 DyPB sequence.

Bacterial strain	Accession number of DyPB homologue	C-terminal protein sequence (encapsulin-targeting sequence underlined)	Size (amino acids)	Downstream encapsulin family[a] gene (accession number)
Rhodococcus jostii RHA1	Q0SE24	ESLGDEPAGAES- - - - - -APEDPVEPAAAGPYDLSLKIGGLKGVSQ	350	Yes (Q0SE23)
Rhodococcus opacus B4	C1B1V7	ESLGDAPAAAEP- - - - - -APEDP-APAGASPYELSLKIGGLKGVSQ	349	Yes (C1B1V8)
Rhodococcus erythropolis	C0ZVK5	DDPPDAPTR- - - - - - - -LVPEATFTAPISDGSLGIGSLKRSAQQ	341	Yes (C0ZVK4)
Burkholderia phymatum	B2JNZ7	EALADREPQPASAS-- ---AAASADTFACAEPGHDGSLNIGSLKGTAQYE	352	Yes (B2JNZ6)
Burkholderia multivorans	A9ATN5	DALPDRAAPAEAAA- - - -PAPSSN- - -EPHRDGSLKIGSLKGVKSV	353	Yes (A9ATN4)
Mycobacterium tuberculosis	O07180	DHPP- - - - - - - - - -PLPQAATPTLAA- -GSLSIGSLKGSPR	335	Yes (O07181)
Nocardia cyriacigeorgica	H6R1G4	DDLPDPPG- - - - - - ASPADDATPAAPAADGSLGIGTLKRSS	341	Yes (H6R1G5)
Streptomyces coelicolor	Q9FBY9	EDLPARP	316	No
Streptomyces lividans	D6EC39	EDLSARP	329	No
Streptomyces hygroscopicus	H2JMY8	EDLPEPPAAG- - - - - - -AVAAVTPTDSQVRSSGSSLGIGSMKRSMSR	349	Yes (H2JMY9)
Streptomyces griseus	B1VSP6	DAPPPPPAPARTGNLPEPVPAPVRQEPPAAGADHGSLRIGSLQESAQ	357	Yes (B1VSP6)
Acetobacter pasteurianus	C7JE82	DDAPNMSTENTQ- - - - -ASPEPVTAPPLPKALHGSLGIGSLNNKDA	379	Yes (C7JE83)
Pseudomonas fluorescens	Q4KA97	EDLAERAPTGL	328	No
Pseudomonas fluorescens	I2BZP5	EALPDREPVA	320	No
		Sequence motif GSLxIGSLKG		

[a] Gene annotated as bacteriocin or linocin.

M. tuberculosis, R. jostii, *Rhodococcus erythropolis*, *Rhodococcus opacus*, *Burkholderia phymatum*, *Burkholderia multivorans*, *Nocardia cyriacigeorgica*, *Acetobacter pasteuranius*, *Streptomyces hygroscopicus* and *Streptomyces griseus* each possesses a DyPB homologue with 20–30 residue peptide sequence in the C-terminal that shows presence of the 10-residue sequence motif. In addition, in all of the mentioned organisms in their respective genome sequences, the *dypB* and *encapsulin* genes were found immediately adjacent [77]. However, homologues of DyPB from *Streptomyces lividans*, *Streptomyces coelicolor* and *Pseudomonas fluorescens* did not show the presence of the aforementioned C-terminal peptide sequence, and also in these organisms, there is no neighbouring encapsulin gene [77]. Despite the lack of signal sequence in all of DyPB sequences, a strong correlation between the presence of a downstream encapsulin gene and the existence of the C-terminal amino acid sequence motif exists [77].

The physiological advantage that bacteria obtain by sequestering certain enzymes into protein compartments is still unclear [116]. Sutter *et al*. [76] suggested that restraining of Flp iron oxidation products may have a role in protecting *T. maritima* from oxidative damage. The peroxidase activity of encapsulin-sequestered DyP may help the survival of pathogenic bacteria such as *M. tuberculosis* when they encounter a burst of reactive oxygen species as part of their host's defense system [116, 123].

Recently has been reported that DyPB from *R. jostii* RHA1shows lignin peroxidase activity and is able to oxidize β-aryl ether lignin model compound, manganese ions, and Kraft lignin [64, 123]. Gene deletion studies showed that *dypB* gene deletion reverse the lignin degradation activity of *R. jostii* RHA1 [64, 123] *in vivo* as determined by a recently developed colorimetric assay utilizing nitrated lignin molecule as a substrate [64, 92].The obtained results highlights that DyPB enzyme seems to be essential for the characterized lignin degradation feature shown by *R. jostii* RHA1.

Analysis of the genome sequnce of *R. jostii* RHA1, a potent organism in degradation of polychlorinated biphenyl, [41, 92], showed that immediately downstream of the *R. jostii dypB* gene (ro2407) is a 807-bp *encapsulin* gene (ro2408), as depicted in (Fig. 4.7).

Figure 4.7 - Genomic context of *R. jostii* RHA1 *dypB* and *encapsulin* genes.

We wished to investigate whether DyPB is packaged within the encapsulin nanocompartment, and examine what effect the nanocompartment has on lignin degradation activity. In this chapter the reconstitution of purified recombinant *R. jostii* encapsulin with *R. jostii* DyPB to form a packaged nanocompartment is discussed.

4.2 Expression and purification of *R. jostii* RHA1 encapsulin nanocompartments

For purification of encapsulin, cloning and expressing of the encapsulin gene in *E. coli* first was tried. Genomic DNA of *R. jostii* RHA1 was extracted using Wizard® Genomic DNA Purification Kit from Promega, from a total 1ml of overnight culture of *R. jostii* RHA1 in Luria-Bertani broth. Forward and reverse primers were designed for the *encapsulin* gene and a CACC overhang was added to the forward primers in 5' for purpose of performing TOPO cloning method, designed primers for isolation of *encapsulin* gene are as following:

$_{5'}$CACCATGAGTGATTCGAGCAATC$_{3'}$ and $_{5'}$TCAGCGTGCGAGGACGACC$_{3'}$. PCR reactions were carried by using Platinum Pfx-DNA polymerase from Invitrogen, following

the manufacturer's instructions. Fig. 4.8 shows the agarose gel picture for cloning of the encapsulin gene.

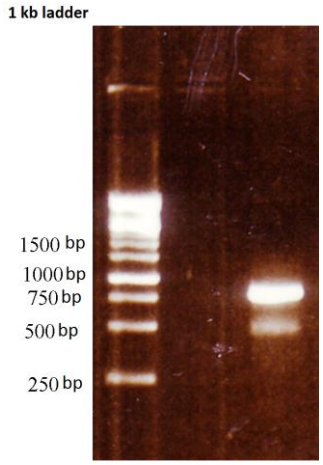

Figure 4.8 - Agarose gel of PCR products of *encapsulin* gene.

The amplified gene was cloned using the Champion™ pET 151 Directional TOPO® Expression Kit (Invitrogen) into expression vector pET151, and transformed into *E. coli* TOP10 competent cells (Invitrogen). The extracted plasmids from the obtained colonies were sent for sequencing, to confirm the accuracy of the sequence and the ligation respectively. The sequencing results showed that the amplified gene did not contain any mutations, and the ligated gene was in the correct orientation in the vector. The recombinant plasmid was then transformed into BL21 *E. coli* BL21 (Invitrogen), for protein expression.

For expression of the encapsulin recombinant gene, a 20 ml starter culture was grown in Luria-Bertani broth in the presence of 100 mg/ml ampicillin for 5 hour at 37 °C, then added to 2 litre Luria-Bertani broth for 3 hours at 37 °C, and finally the cells were induced by adding 0.5 mM final concentration of IPTG and shaken overnight at 15 °C. Cell pellets were harvested by centrifugation at 4000 × g.

Protein purification was performed by metal affinity chromatography. The harvested cells from a 2-litre culture described above were suspended in 20 ml lysis buffer in the

presence of 1 mM final concentration of PMSF. Cell lysis was carried out using a constant system cell disrupter, followed by centrifugation at 10000 × g for 30 minute. The clear supernatant was loaded onto a Ni-NTA resin FPLC column (HisTrap HP, 1 ml volume) equilibrated with lysis buffer followed by 100 ml of wash buffer, and the recombinant protein was eluted by 7 ml elution buffer, eluting at a flow rate of 0.5 ml min^{-1}. A sample of eluted protein was taken for SDS PAGE, the remainder of solution was subjected to buffer exchange through a PD-10 column into 10 ml MOPS buffer.

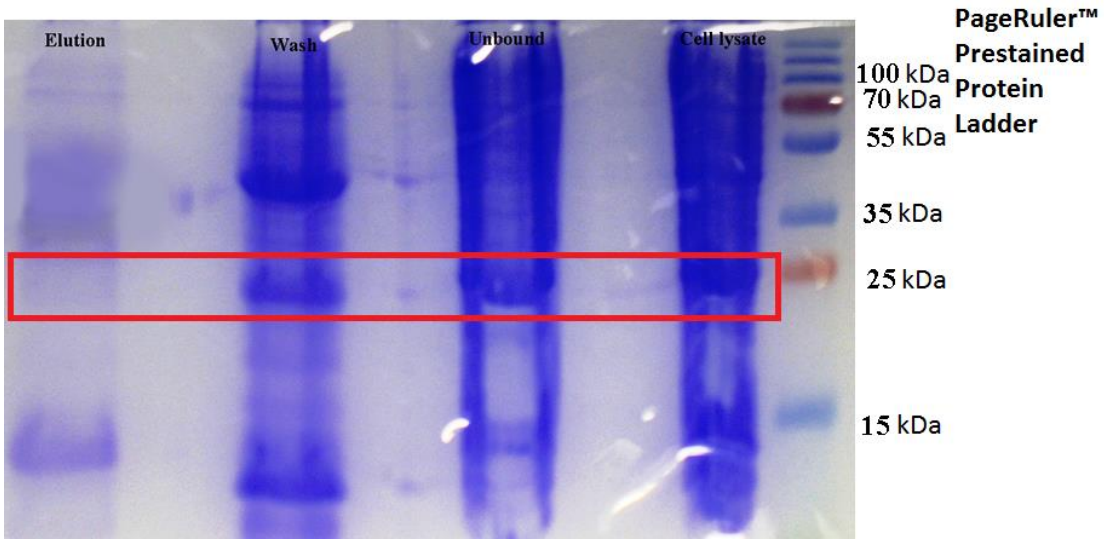

Figure 4.9 - SDS PAGE of purification of recombinant encapsulin in *E.coli* by batch method.

The SDS PAGE gel in Fig. 4.9 showed that encapsulin did not bind to HIS Tag affinity resin and nearly most of it remained unbound in cell lysate or wash fractions. After checking the structure of the monomer, we concluded maybe N-terminus may be buried in the protein and hence it could not bind to resin efficiently. Then we tried to purify recombinant protein with gel filtration, since the encapsulin molecular weight is very high. Interestingly,

again results showed that the recombinant encapsulin in *E.coli* did not form the assembled encapsulin and all of the protein was in the form of monomer as shown in Fig. 4.10. Either the the HIS tag tail interferes in the assemblly process or some special accessory proteins requires the encapsulin to proper assemblly *in vivo*, might be the causing effect of these observations [77]. Therefore, we decided to purify encapsulin from *R. jostii* RHA1.

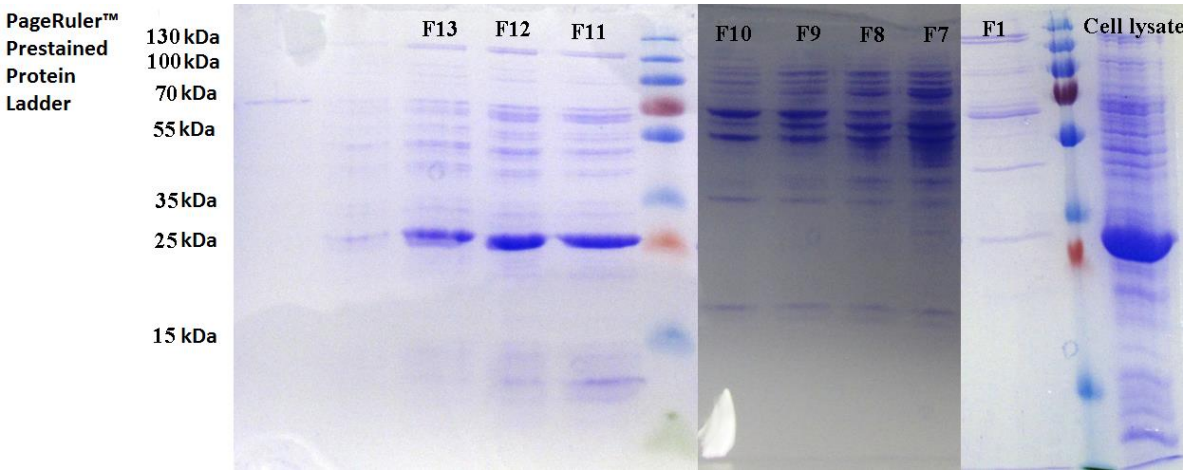

Figure 4.10 - SDS PAGE of purification of recombinant encapsulin in *E.coli* by gel filtration chromatography.

4.2.1 Strains

The gene deletion for strain *R. jostii* RHA1 Δ encapsulin, in which the encapsulin gene ro2408 is deleted, was made by R. Singh and L. Eltis (Department of Microbiology and Immunology, University of British Columbia), by using the method of van der Geize *et al.* [124]. The *R. jostii* RHA1 encapsulin gene was expressed on an inducible expression vector, pTipQC2 [125], allowing inducible expression of encapsulin in *R. jostii* RHA1.

4.2.2 Expression and purification of *R. jostii* encapsulin

A culture of *R. jostii* RHA1 Δencapsulin/pTipQC2 was grown in the presence of 35 μM chloramphenicol. The culture was induced by adding of thiostrepton (final concentration of 1 μg-mL^{-1}), the culture was grown for a overnight, and cells were then harvested by centrifugation. Cell lysis was carried out by sonication in lysis buffer. After centrifugation, the clear supernatant was concentrated and the concentrated cell lysate was applied to a Superdex 200 gel filtration column. Fig. 4.11 illustrates the chromatogram of gel filtration step in encapsulin purification.

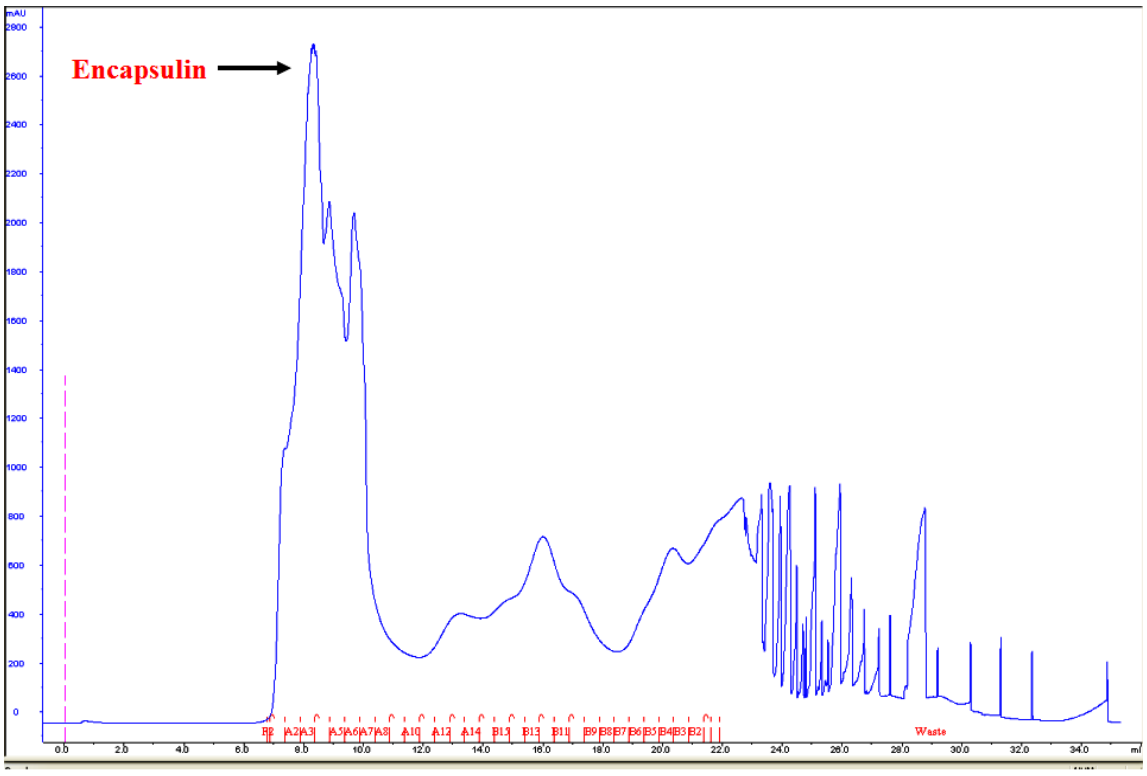

Figure 4.11 - Gel filtration superdex 200 chromatogram of cell lysate of *R. jostii* RHA1 containing an overexpressed encapsulin gene.

Starting purification with the cell lysate by Superdex 200 column, gel filtration chromatography, resulted a major peak at a short retention time, related to a very high molecular mass protein, consistent with a high molecular mass of nanocompartment. Fractions showing a 29-kDa band for encapsulin by SDS PAGE (Fig. 4.12) were pooled.

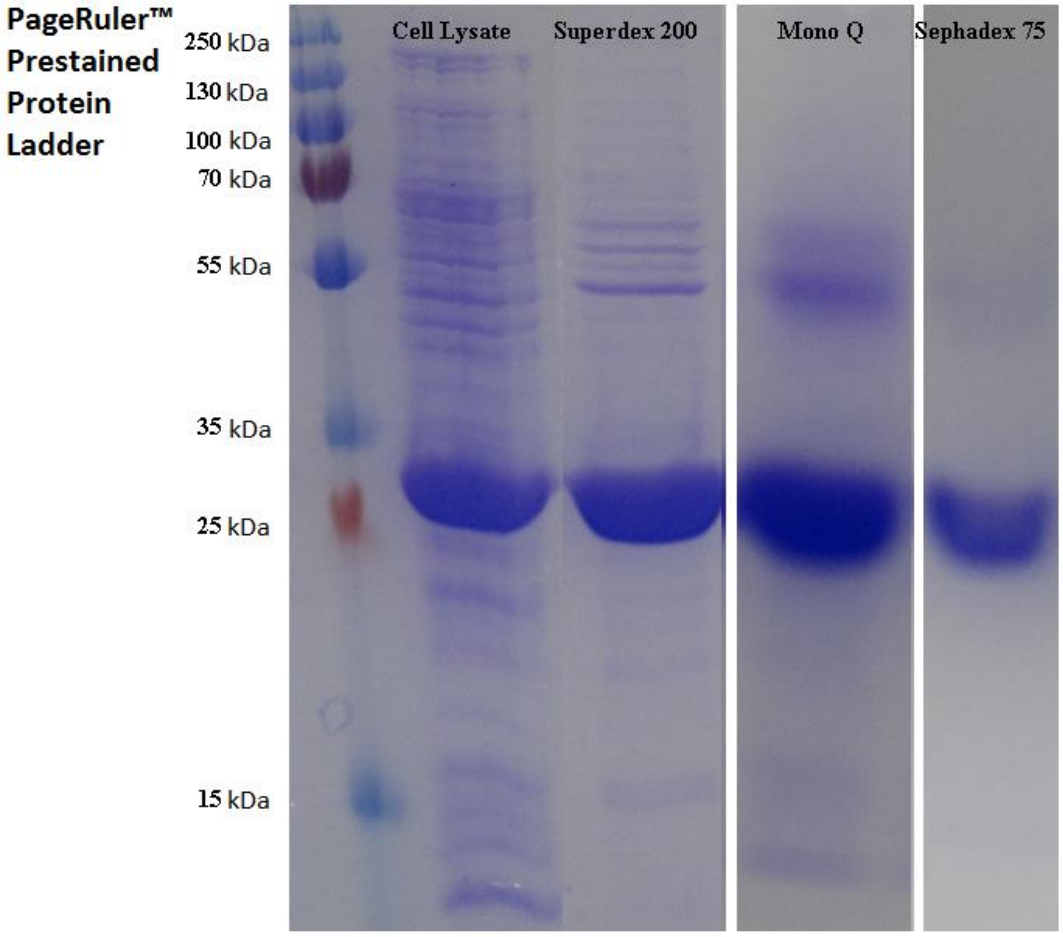

Figure 4.12 - SDS PAGE of purification steps of the encapsulin from *R. jostii* RHA1.

The resultant solution was applied to a Mono Q HR 5/5 anion exchange FPLC column, and protein was eluted with a gradient of 0–1 M NaCl in 20 mM Tris/HCl, pH 8.0. Fig. 4.13 illustrates the chromatogram of anion exchange chromatography step in encapsulin purification. Fractions containing the 29-kDa encapsulin band, which eluted at ~ 700 mM NaCl, were pooled (Fig. 4.12).

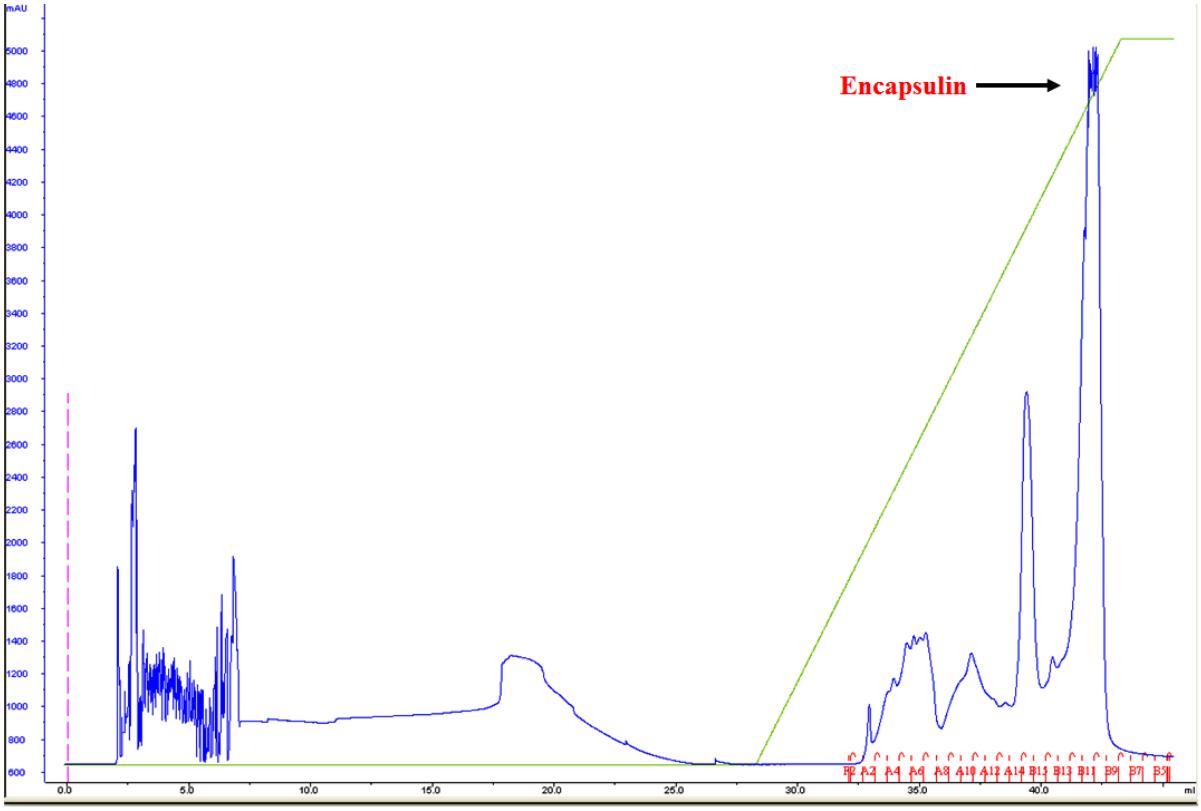

Figure 4.13 - Anion exchange chromatograms of encapsulin purification by Mono Q column.

Further purification was achieved by elution from a Sephadex G-75 column. Three peaks appeared and the fractions were collected for each of them. Fig. 4.14 shows the chromatogram of final gel filtration step by Sephadex G-75 column. Elution of the protein complex by Sephadex 75 gel filtration was found to give three peaks, each of which was shown to contain the encapsulin monomer by SDS PAGE, indicating the presence of three different multimeric forms in solution. Collected fractions containing pure encapsulin (yield: 2.5 mg of protein) were pooled (Fig. 4.12) for further analysis.

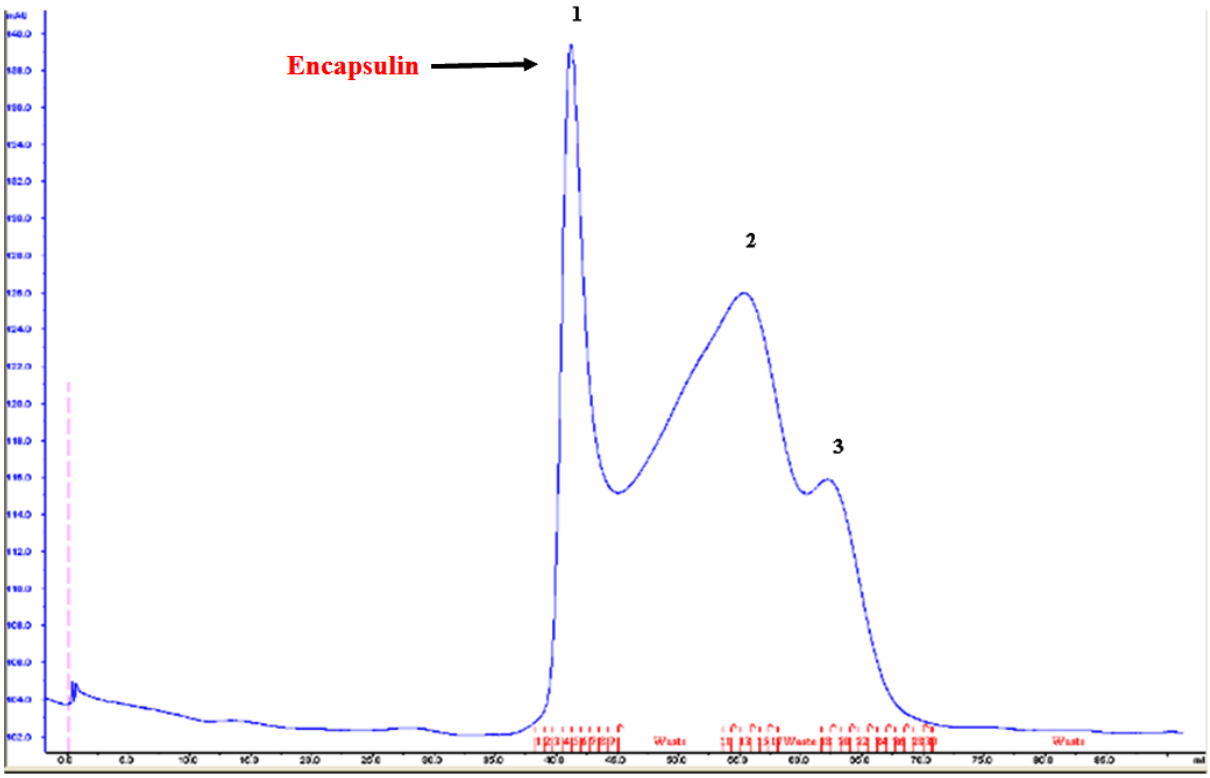

Figure 4.14 - Gel filtration chromatograms of encapsulin purification by Sephadex 75 column.

4.3 Disassembly and *in vitro* reassembly of encapsulin

Native gel electrophoresis and dynamic light scattering techniques were used to perform this experiment. The aim of this experiment was to show the possibility of reassembly of encapsulin after disassembly and denaturation. Since the encapsulin monomer is a small protein molecule, composed of just one domain and also because there are no cysteine amino acids and hence no disulfide bond in its structure, therefore if denaturation happens, the probability of gaining native structure after removing denaturant is high. Purified encapsulin was incubated in different pH ranges to determine which pH causes protein to be disassembled to its monomer constituents; native PAGE gel and dynamic light scattering were used for assay of this experiment.

Acidic pH was used as a denaturant. Firstly, protein samples were incubated in different pH ranging from pH 1 to 5. The pH of the incubated samples was then raised to pH 7 as explained in the Experimental Section. The native PAGE gel result revealed that renaturation and reassembly did not happen in pH 1 and pH 2, probably because of breaking of peptide bonds or side chain covalent modifications. In pH 4 and pH 5, denaturation did not happen and the protein remained in its native state. Only 50 mM in acetate buffer pH 3.0 did the reversible denaturation/renaturation occur as shown in Fig. 4.15.

In the Fig. 4.15, the first lane after the marker is purified native encapsulin, the second lane is denatured encapsulin in pH 3 and finally third lane is reassembled encapsulin at pH 7. As it is apparent in the lane 1, protein band resides in the top of the gel, right above the separating part of gel that indicates the presence of very high molecular weight protein. In the second lane, in addition to the high molecular weight band there is a distinct band nearly above the 55 kDa position, which might indicate a dimer species of building block, and some pale, thin bands distributed between 130 kDa and 250 kDa which might include trimer, tetramer and pentamer species. The third lane relates to treated encapsulin in pH 7 buffer after incubation in pH 3. As it is apparent, the distinct high molecular band at the top of the gel

again reappears, that indicate encapsulin reassembles after dissociation and disassembly of its monomers.

For further investigation of the disassembly/reassembly and the size of encapsulin in different states of experiment, dynamic light scattering (DLS) was used, a technique which has been used to measure the dynamic radius of protein aggregates in solution [126].

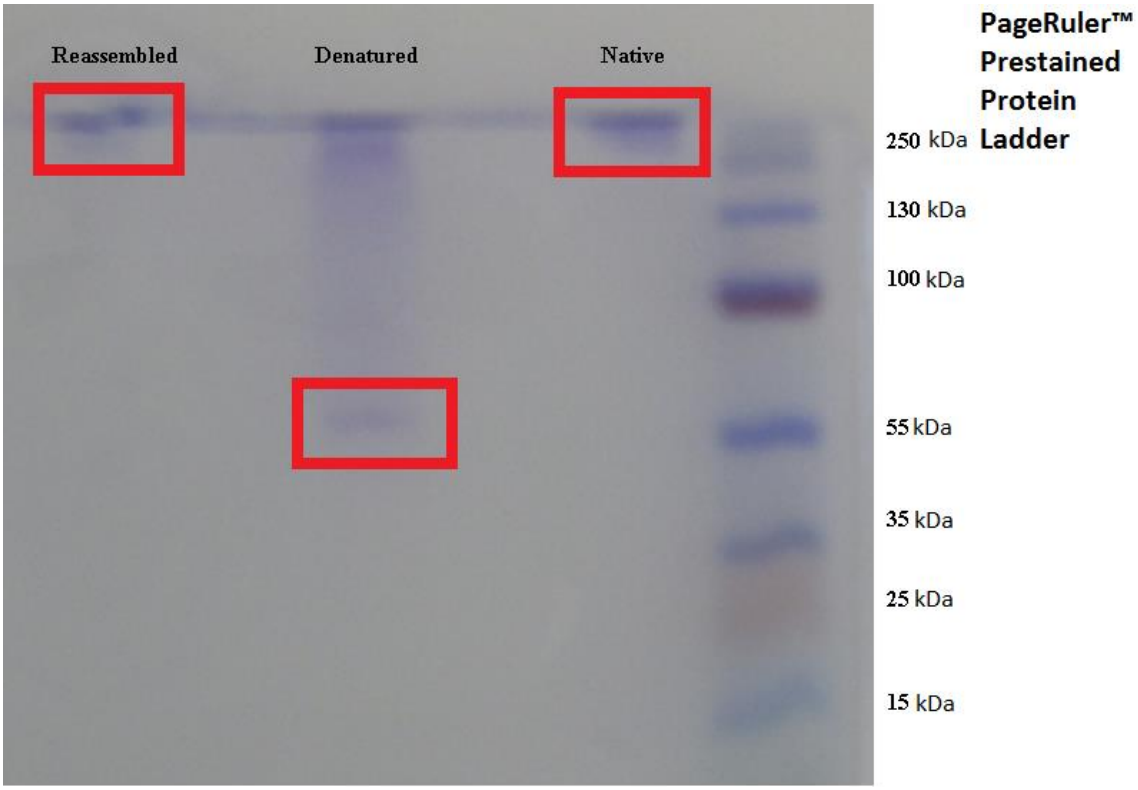

Figure 4.15 - Native PAGE gel for native denatured at pH 3.0 and reassembled Encapsulin.

Fig. 4.16 shows the DLS results for native, denatured and reassembled encapsulin. The determined sizes for native, denatured and reassembled encapsulin are 22 nm, 32nm and 1.69 nm respectively. The native purified nanocompartment produced a single peak related to a radius of 22 nm, which matched with the 240-Å diameter of the *T. maritima* nanocompartment, determined by X-ray crystallography [76]. A sample of protein treated at pH 3.0 resulted a major peak at a much smaller size, corresponding to a radius of 1.69 nm.

The thickness of the *T. maritima* nanocompartment was found to be 20–25 Å [76]. Therefore, the observed dynamic radius is consistent with the dimeric form of encapsulin. Analysis of the reassembled nanocompartment by dynamic light scattering exhibited that the reassembled encapsulin nancompartment had a dynamic radius of 31 nm, that was similar to but slightly larger than that of the native nanocompartment, indicating a slightly expanded structure.

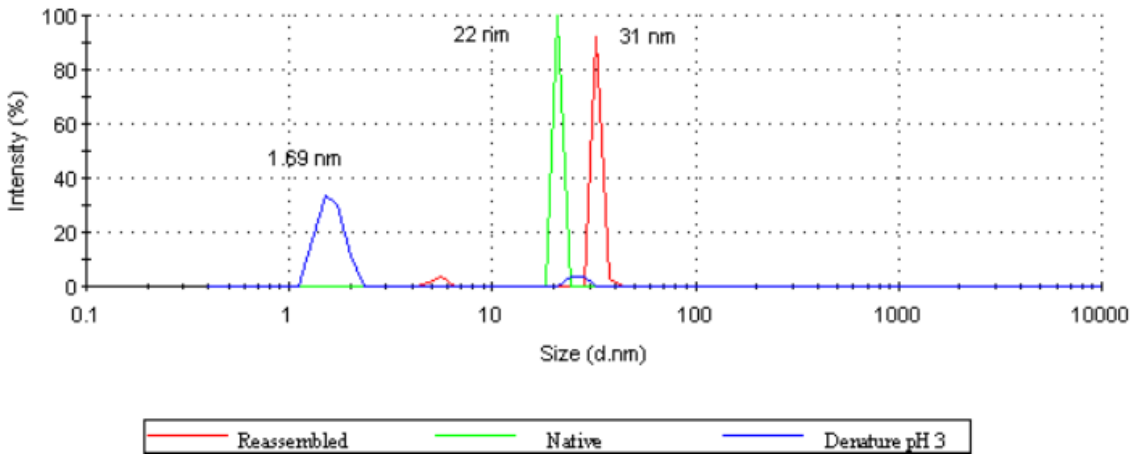

Figure 4.16 - Dynamic light scattering for native, denatured in acidic pH and reassembled encapsulin.

4.4 Disassembly/Reassembly of encapsulin in presence of DyPB

Since one of the functional roles that is considered for encapsulin is enclosing or encapsulating of B-type DyP peroxidases that possessing a C-terminal signal in their sequences, we decided to check this property with the purified encapsulin and a DyPB type peroxidase from *R .jostii* RHA1 that has a C-terminal signal. Previous research has shown that encapsulin from *T. maritima* could accommodate 3 dimers of DyPB [76].

In order to study reassembly with DyPB, the disassembled encapsulin was mixed with purified *R. jostii* RHA1 DyPB. In this experiment, 0.6 mg/ml of encapsulin and 0.2

mg/ml of DyPB were used, to prevent the probability of aggregation and unwanted interactions between encapsulin monomers and DyPB molecules and also reducing the possibility of macromolecular crowding in the denatured state. A low concentration of DyP B was used for increasing the efficiency of encapsulin reassembly.

The mixture was incubated in 100 mM phosphate buffer pH 7.4 containing 100 mM NaCl for 30 min, and then loaded to a Superdex 200 gel filtration column. Two major peaks were observed (Fig. 4.17): the first, a peak whose retention time of 9.5 min matched well with the retention time of the originally encapsulin.

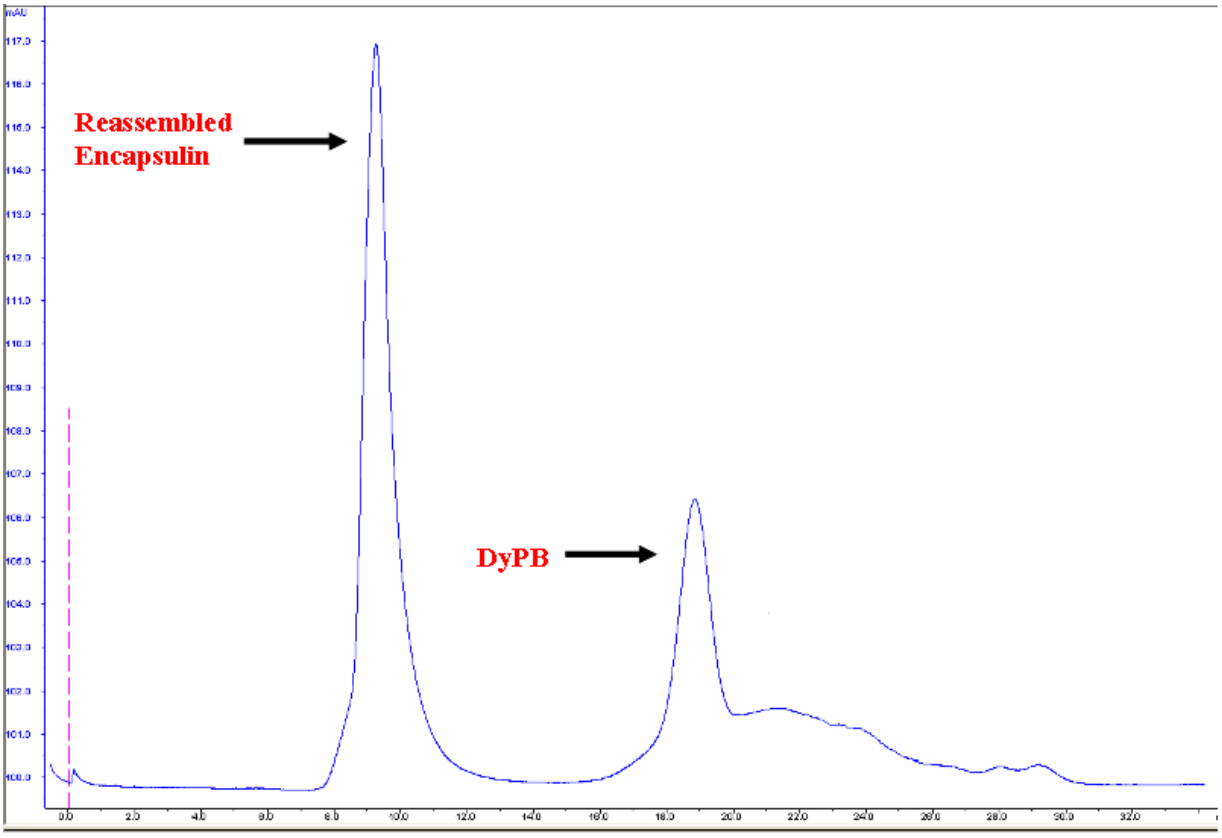

Figure 4.17 - Gel filtration chromatogram of the reassembled encapsulin in the presence of DyPB by superdex 200 column.

The second peak belongs to the DyPB dimer, 70 kDa. The proteins in the collected fractions analysed by SDS PAGE (Fig. 4.18).

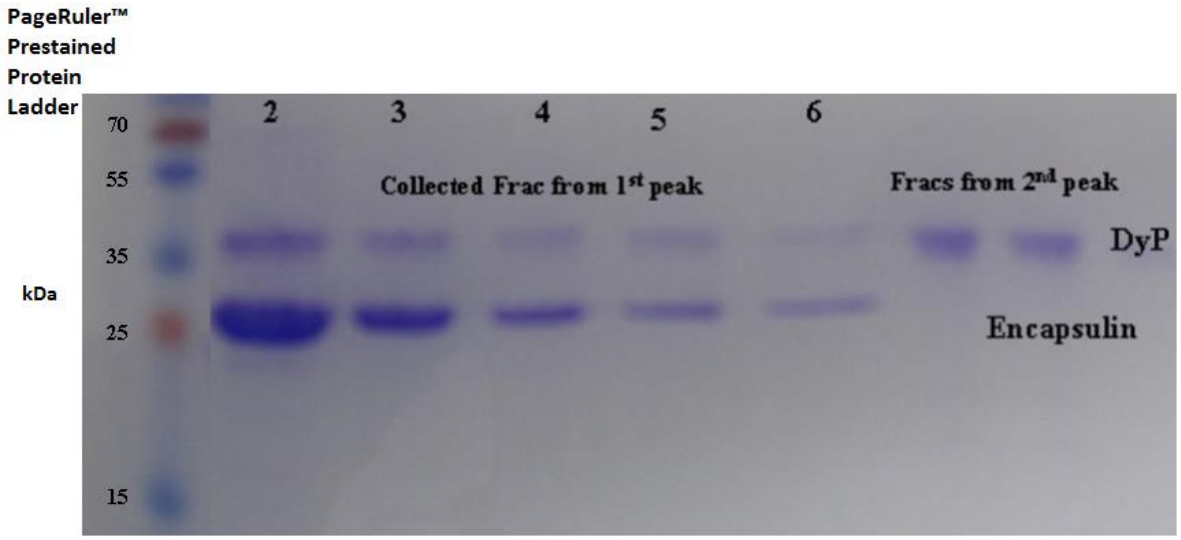

Figure 4.18 - SDS PAGE of the collected fractions from gel filtration Superdex 200.

The protein bands in first peak correspond to encapsulin and DyPB, whereas the second peak at retention time 19.0 min consisted only of DyPB, as shown in Fig. 4.18 that illustrate how these two proteins were distributed among fractions. Lane 2 contains the reassembled encapsulin before injecting to the column, and other four lanes after that relate to the collected fractions of the first peak. The rest of the lanes belong to the second peak. As is apparent from the SDS PAGE gel, in the lanes of 3, 4, 5 and 6 which belong to collected fractions of the first peak, the DyPB specific band associates with the encapsulin band. By considering the large difference between the molecular weight of encapsulin (1.8 MDa) and DyPB dimer (70 kDa) and using the Superdex 200 gel filtration column which has very high resolution in separating molecules from molecular weight ranges of 10 kDa to 600 kDa, the presence of the DyPB specific band along with encapsulin band in SDS PAGE gel, strongly indicates that DyPB is encapsulated in the reassembled encapsulin *in vitro*.

These data indicate that reassembly of DyPB with encapsulin has been achieved, to form a high molecular mass assembly. The reassembled encapsulin–DyPB complex exhibits a similar gel filtration retention time to the originally expressed nanocompartment, but contains DyPB, so we could conclude that the DyPB protein has been packaged within the encapsulin nanocompartment. It is noteworthy to mention that, the possibility of formation of a nonspecific aggregate in the reassembled DyPB–encapsulin complex is unlikely, as a sharp peak was observed for the complex by gel filtration (Fig. 4.17), whereas one would expect to see multiple species formed in the case of a nonspecific aggregate. Also, the reassembled complex is enzymatically active (see section 4.6), which would not be expected in the case of an aggregate. In addition, *R. jostii* RHA1 encapsulin contains no cysteines, so the formation of disulfide linkages is not feasible.

4.5 Determining the ratio of encapsulin to DyPB protein

In the reassembled complex, the ratio of encapsulin to DyPB proteins was studied. Firstly, reassembled encapsulin–DyPB complex was heated at 50 °C for 5 min, then sonicated for 3 min, and finally total protein was determined with the Bradford assay in triplicate. DyPB content was assessed by measurement of haem content at 404 nm, and comparison with a DyPB standard curve (Fig. 4.19). The total protein was 0.72 mg/ml, and concentration of the used encapsulin in reassembly experiment was 0.6 mg/ml that is nearly 21 micro mole. Therefore, the concentration of DyPB in encapsulin is around 0.12 mg/ml, which accounts for nearly 2.5 micromoles. The molar ratio of encapsulin to DyPB was found to be 8.6 μmol.encapsulin. μmol^{-1} DyPB. The calculated stoichiometry of 8.6 mol encapsulin/mol DyPB is compatibale with the sugessted stoichiometry of 10 mol encapsulin per mol DyPB predicted from the crystal structure, where one nanocompartment containing 60 subunits of encapsulin was predicted to contain six subunits of DyPB [76].

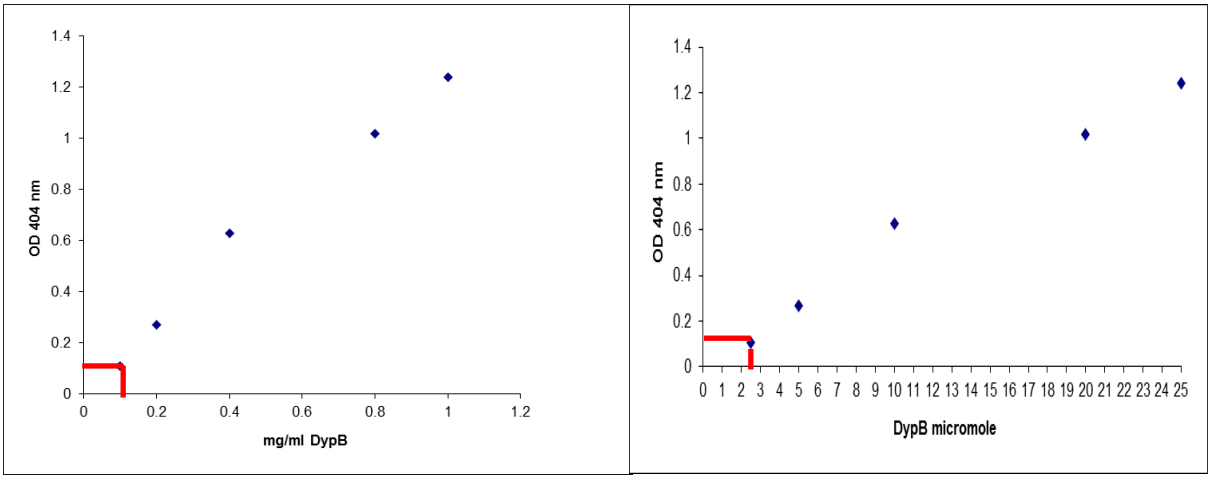

Figure 4.19- Standard curve of DyPB content obtained by measuring absorbance of different DyPB concentrations at 404 nm (haem content).

4.6 Peroxidase activity of the encapsulin–DyPB complex

The collected fractions from the first peak were pooled and two different peroxidase assay methods, ABTS and nitrated lignin, were used for monitoring activity of DyPB in the encapsulated form. The peroxidase activity of the reassembled DyPB–encapsulin complex was assessed with kinetic assays. For each assay, positive and negative controls were included; assay of free DyPB as positive and assay of reaction mixture without the enzyme as negative. DyPB from *R. jostii* RHA1 has shown activity toward the dye 2,2′-azinobis(3-ethylbenzo-6-thiazolinesulfonic acid) (ABTS), which can be assayed colorimetrically at 420 nm, and with nitrated milled wood lignin, which can be assayed colorimetrically at 430 nm [64].

Fig. 4.20 shows the result of the peroxidase activity of DyPB with ABTS as a common substrate for assaying peroxidase activity in two different concentrations of protein; 0.2 mg/ml and 0.4 mg/ml. The reassembled encapsulin in the presence of DyPB shows activity with ABTS and its activity changes in response to increasing the encapsulin concentration but its activity profile is still very low in comparison with free DyPB enzyme. Fig. 4.21 shows activity profiles of the reassembled encapsulin in the presence of DyPB and

free DyPB for nitrated lignin, a method developed in our laboratory for qualitative screening of peroxidases to check their potential for degrading and breaking lignin compounds by utilizing the hydrogen peroxide oxidation potency. Despite its qualitative nature and showing high background, the values of activity for the reassembled encapsulin and free DyPB are still twice that of the negative control. These activity results indicate DyPB peroxidase is active in its encapsulated form, which raises some ideas about potential applications of encapsulated enzymes.

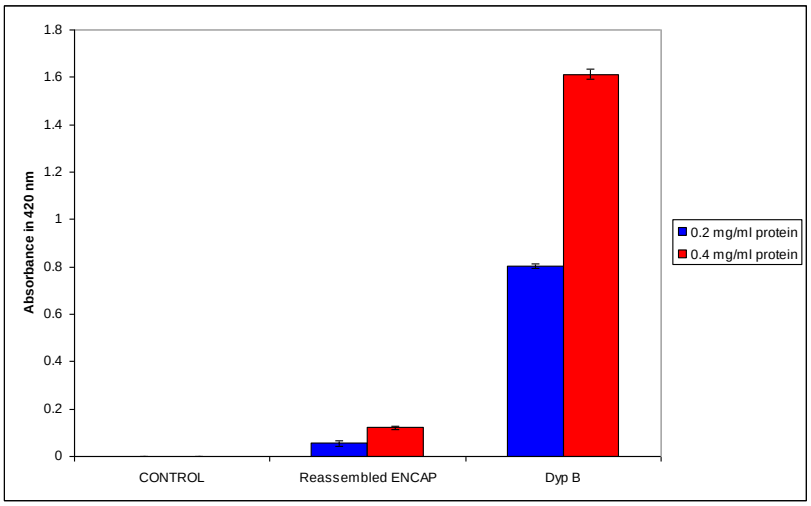

Figure 4.20- Results of the peroxidase activity of the reassembled encapsulin in the presence of DyPB and free DyPB with ABTS using two different protein concentrations: 0.2 and 0.4 mg/ml.

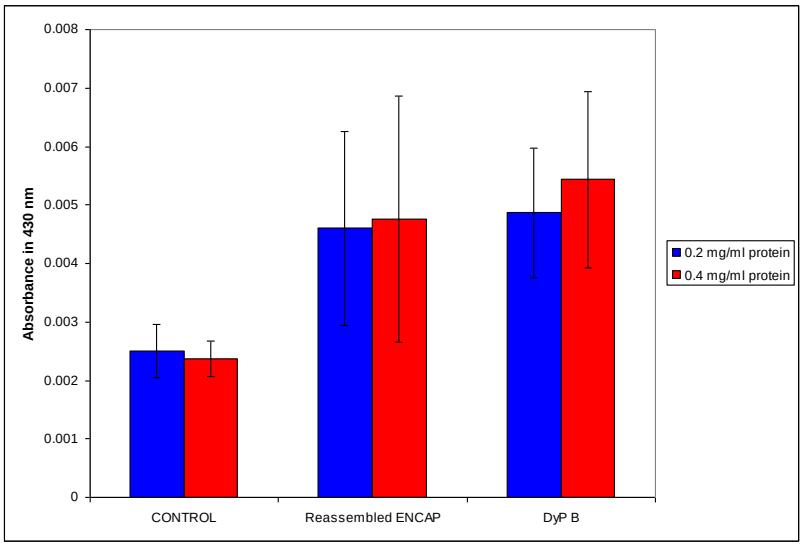

Figure 4.21- Results of peroxidase activity of the reassembled encapsulin in presence of DyPB and free DyPB for nitrated lignin using two different protein concentrations: 0.2 and 0.4 mg/ml.

As shown in Table 4.2, the activity per milligram of protein of the reassembled DyPB–encapsulin complex was ~ 10-fold lower with ABTS than with pure DyPB, but, when corrected for the proportion of the complex present as DyPB (8.6 mol encapsulin complex per mol DyPB), the peroxidase activity of the DyPB enzyme in the complex with ABTS was 70–75% of that of native DyPB. In the nitrated lignin assay [92], the activity of the reassembled DyPB–encapsulin complex was similar to that of DyPB alone, but, when corrected for the proportion of the complex present as DyPB, the activity per milligram of DyPB was eightfold higher than that of DyPB alone, indicating that assembly in the encapsulin somehow enhances the lignin degradation activity of DyPB [77].

Table 4.2 - Peroxidase activity of the reassembled DyPB–encapsulin complex. Assays were carried out with 0.2 mg of protein (either purified DyPB or reassembled encapsulin–DyPB complex).

	DyPB only		DyPB–encapsulin assembly	
Substrate	Activity per mg of protein	Activity per μmole of DyPB	Activity per mg of protein	Activity per μmole of DyPB
ABTS	4.05 ±0.05 AU.min^{-1}	4.24 ±0.05 AU.min^{-1}	0.275 ±0.5AU.min^{-1}	2.43 ±0.5 μmol.min^{-1}
Nitrated lignin	0.025 ±0.005 AU.min^{-1}	0.92 ±0.005 AU.min^{-1}	0.023 ±0.008AU.min^{-1}	7.4 ±2.5 AU.min^{-1}

The peroxidase activity of the reassembled encapsulin–DyPB complex provides some interesting clues as to the possible functional role of the encapsulin–DyPB complex. With ABTS as substrate, the peroxidase activity of the complex is similar to that of DyPB alone, which is surprising, as the pores in the encapsulin nancompartment structure are < 5 Å wide, large enough to allow hydrogen peroxide to enter, but not a large dye molecule such as ABTS. It is conceivable that some subunits of DyPB might be attached to the exterior of the nanocompartment, but all of the binding sites for the C-terminal targeting peptide are located on the inside of the nanocompartment [76, 77]. The other possibility is that the nanocompartment is a flexible, dynamic structure that is able to open and close to take up

substrate molecules [77]. This explanation seems consistent with the observation of other assemblies by the use of gel filtration chromatography [77] (Fig. 4.13).

The observation that the reassembled encapsulin–DyPB complex shows eight-fold higher activity in the nitrated lignin assay (per milligram of DyPB) than DyPB alone implies that the encapsulin nanocompartment somehow increases the activity with polymeric lignin. One possible explanation is that it may assist in localizing DyPB to the hydrophobic surface of lignin. The nonspecific binding of cellulase enzymes to the hydrophobic surface of lignin is thought to slow down the rate of lignocellulose breakdown by cellulases [77,127], which can be alleviated by addition of nonionic detergents that preferentially bind to lignin [128]. Furthermore, lignin peroxidase from *Phanerochaete chrysosporium* has been shown to directly adsorb to the surface of synthetic lignin [129], thereby assisting in lignin breakdown. If the encapsulin nanocompartment is a dynamic structure, then it seems possible that it could disassemble on the surface of lignin or lignocellulose, and therefore localize DyPB to the surface of lignin or lignocellulose. The close proximity of DyPB to the surface may increase its activity, owing to the generation of short-lived oxidants (e.g. Mn^{2+} or phenolic radicals) used for lignin oxidation [77].

4.7 Examining the probability of considering encapsulin as a extracellular protein candidate

One issue that is unresolved is the cellular location of the DyPB–encapsulin complex. The lignin degradation activity of *R. jostii* RHA1 was measured with extracellular extract [64, 77, 92], implying that DyPB is exported from the cell. The encapsulin-related linocins from *B. linens* and *M. tuberculosis* have also been detected extracellularly [77, 120, 121], and we have also observed a protein band corresponding to encapsulin in extracellular fractions of *R. jostii* RHA1; however, the encapsulin nanocompartment has only been observed intracellularly [76].

Both wild type and overexpressed strain's liquid culture fractions were checked for probable presence of encapsulin in extracellular medium by concentrating harvested bacterial extracellular medium at early stage of bacterium growth (OD= 0.6) through a 50-kDa centricon device followed by SDS PAGE. Fig. 4.22 shows the SDS PAGE gel picture of concentrated *R. jostii* RHA1 liquid culture.

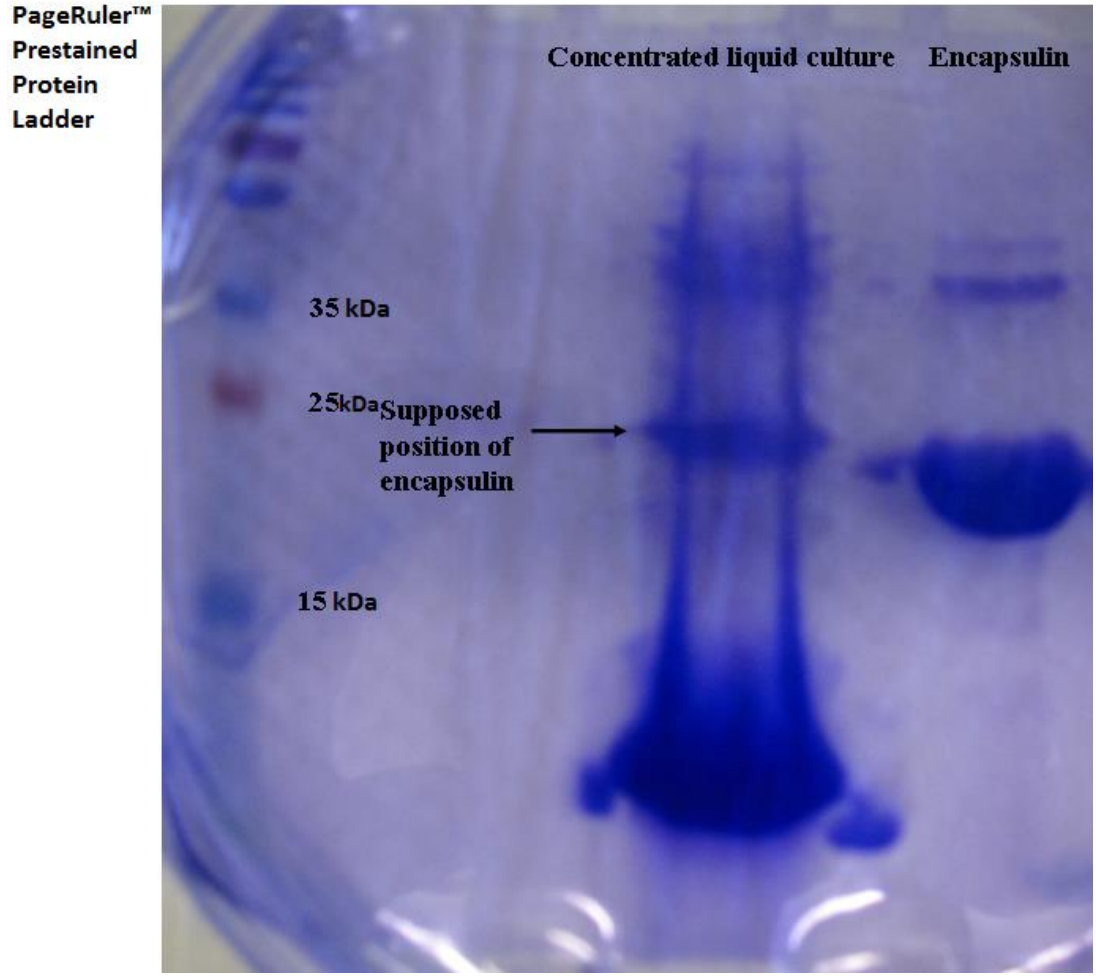

Figure 4.22- SDS PAGE gel picture of concentrated *R. jostii* RHA1 liquid culture.

The observed protein band in SDS PAGE gel at the expected position of encapsulin was cut and sent for protein identification by means of tryptic digest and nanoLC-ESI-MS/MS. Proteomic analysis showed presence of encapsulin in both wild type and overexpressed strain in extracellular fraction. As Table 4.3 indicates, the highest coverage

(36%) in proteomic analysis of excised band from the concentrated liquid culture fraction of overexpressed strain belongs to Uniprot accession number of encapsulin (Q0SE23).

Table 4.3 - Proteomic analysis on obtained peptides from the incised SDS PAGE gel band of concentrated liquid culture fraction of overexpressed strain.

Accession	Entry	Description	mM(Da)	Peptides	Coverage(%)
Q0SE23	Q0SE23_ RHOSR	Possible bacteriocin protein OS Rhodococcus sp strain RHA1 ro02408	28784	8	36.19
Q0S9D1	Q0S9D1_ RHOSR	Probable mycolyltransferase protein OS Rhodococcus sp strain RHA1 ro04058	36308	6	23.81
Q0S9D0	Q0S9D0_ RHOSR	Probable antigen 85 complex protein OS Rhodococcus sp strain RHA1 ro04059	35484	2	5.74

Table 4.4 shows the proteomic analysis of excised band from the concentrated liquid culture fraction of wild type and the highest coverage (10%) is also represented for encapsulin accession number.

Table 4.4 - Proteomic analysis on obtained peptides from the incised SDS PAGE gel band of concentrated liquid culture fraction of wild type strain.

Accession	Entry	Description	mM(Da)	Peptides	Coverage(%)
Q0SE23	Q0SE23_RHOSR	Possible bacteriocin protein OS Rhodococcus sp strain RHA1 GN RHA1 ro02408	28784	3	10.45
Q0S9D1	Q0S9D1_ RHOSR	Probable mycolyltransferase protein OS Rhodococcus sp strain RHA1 GN RHA1 ro04058	36308	3	10.42
Q0SlG0	PAS_ RHOSR	Proteasome subunit alpha OS Rhodococcus sp strain RHA1 GN prcA	35484	2	5.41
Q0SHS9	Q0SHS9_RHOSR	Cell division initiation protein OS Rhodococcus sp strain RHA1 GN RHA1 ro01080	30370	1	3.91
Q0S1P5	Q0S1P5_RHOSR	Glutamate binding protein OS Rhodococcus sp strain RHA1 GN gluB1	29252	1	3.97

The mechanism for cell export of encapsulin and DyPB is unknown, and would seem not to follow known protein export mechanisms. In summary, the ability to package proteins into the cavity of such a nanocompartment, using a specific targeting sequence, offers

interesting possible applications for biotechnology, and may have specific application for biomass deconstruction.

4.8 Conclusion

The obtained results from this study indicate that in vitro disassembly/reassembly of encapsulin from *R. jostii* RHA1 is reversible. It was shown experimentally that DyPB from *R. jostii* RHA1 is encapsulated by encapsulin and the encapsulated DyPB is active and able to show peroxidase functionality.

Efforts to overexpress encapsulin in *E.coli* failed, either because hexa His-tag tail interferes in the assembly process or some special accessory proteins are required for the encapsulin to assemble *in vivo* correctly. It was demonstrated here that encapsulin protein from *R. jostii* RHA1 could be purified as a wholly assembled nano-compartment and its disassembly/reassembly process is reversible in pH 3. Analysis by DLS of purified encapsulin, after treatment by acid, and reassembled encapsulin indicated that the nano-compartment forms a more expanded structure than untreated encapsulin. The ratio of encapsulin to DyPB proteins was studied. The molar ratio of encapsulin to DyPB was found to be 8.6 μmol.encapsulin. μmol^{-1} DyPB, which is compatible with the suggested stoichiometry of 10 mol encapsulin per mol DyPB predicted from the crystal structure, where one nano-compartment containing 60 subunits of encapsulin is seem to contain six subunits of DyPB.

The proteomic analysis of concentrated *R. jostii* RHA1 liquid culture showed the presence of encapsulin protein in the extracellular fluid that might be indicative of the possibility of physiological presence of encapsulin as an extracellular protein outside the cell. This certainly warrants more comprehensive cellular and biochemical investigations.

4.9 Thesis summary

In overall summary the study of three DyP-type peroxidases from the Gram-negative bacterium, *Pseudomonas fluorescens*, showed that one of them, DyP1B, can oxidise lignin. Each enzyme was characterised using UV-vis kinetic assays, in order to measure K_M and k_{cat} values with a range of peroxidase and lignin substrates. DyP1B and DyPA were active with dye substrate Reactive Blue 4, characteristic of the DyP family of peroxidases. DyP1B and DyP2B showed catalytic activity for Mn^{2+} oxidation (k_{cat} 2.4-3.6 s^{-1}, k_{cat}/K_M 330-2100 $M^{-1}s^{-1}$), whereas DyPA showed no activity for Mn^{2+} oxidation. All three enzymes were able to oxidise some phenolic substrates, less efficiently than ABTS, and only DyP1B showed activity towards guaiacol.

By expressing and characterising the three *P. fluorescens* DyP enzymes, *P. fluorescens* DyP1B was found to be a lignin-oxidising enzyme. Both *R. jostii* DyPB and *P. fluorescens* DyP1B show time-dependent changes by HPLC when incubated with wheat straw lignocellulose, but uniquely, the *P. fluorescens* DyP1B liberates a low molecular weight aromatic product from wheat straw lignocellulose. The molecular structure of this lignin fragment was identified, which contains a G unit linked via a β-aryl ether linkage to an H unit, which contains a benzylic ketone. The catalytic activities of these bacterial DyP-type peroxidases towards lignin, Mn (II) and a range of aromatic substrates further demonstrates the potential of DyP peroxidases for biotechnological applications including lignin valorisation, and the potential of pseudomonads for conversion of lignin to aromatic products.

The study on TfuDyP from Gram-positive bacterium *T. fusca* showed that it is able to oxidize lignin model compound, Guicylglycerol-β-guiacyl ether, and shows comparable activity toward Kraft lignin similar to DyP1B from Gram-negative bacterium *P. fluorescens*.

The enzyme was characterised using a range of substrates and K_M and k_{cat} values was measured. Similarly to DyPA from *R. jostii* and *P. fluorescens*, TfuDyP showed no activity

for Mn^{2+} oxidation and the enzyme was able to oxidise some phenolic substrates. By pre-steady-state kinetic charecterisation of TfuDyP, the second order rate constant of compound I formation was calculated (0.55×10^5 M^{-1} s^{-1}) that was nearly half the value obtained for DyP1B from *P. fluorescens* (1.22×10^5 M^{-1} s^{-1}) and much smaller than the value observed for *R. jostii* RHA1 DyPB (1.79 x 105 M^{-1} s^{-1}).

The structure of TfuDyP was solved at 1.7 Å resolution and it showed general structural aspects of DyP-type peroxidases such as containing a four-stranded antiparallel β-sheet fold and the presence of a βαββαβ motif in the secondary structure of TfuDyP that is indicative of a ferredoxin-like fold. Similarly to other DyPs, TfuDyP possesses a GXXDG motif, which contains Asp-203 that is involved in the formation of compound **I**.

Three amino acids in the distal area of the heme pocket of TfuDyP were targeted for site directed mutation studies. The kinetic parametres for these three mutant enzyme showed that Asp-203 probably initiates the catalytic activity of TfuDyP by protonating hydrogen peroxide, followed by heterolytic cleavage of hydrogen peroxide and formation of an oxo-ferryl intermediate, known as compound **I**. This mutational study suggests that, contrary to DyPB from *R. jostii*, the arginine residue present in the distal area of TfuDyP is involved in thebinding and stabilization of hydrogen peroxide to the heme molecule rather than compound **I** formation.

The studies of three DyPs from *Pseudomonas fluorescens* have shed light on their kinetic parameters and their catalytic activities against lignin substrates and dyes. Showing activity for Mn^{2+}, oxidising and subsequently releasing a lignin dimer fragment by DyP1B, are indicatives of possibility of utilizing this enzyme in bio-technology and bio-catalysis processes of lignocelluloses.

Steady state and fast kinetic characterization of TfuDyP from *T. fusca* along with solving its molecular X-ray structure and site directed mutagenesis of three residues in the active site elucidated in detail role of the amino acid residues involved in catalysis. Having the molecular X-ray structure of TfuDyP provides us valuable information for rational engineering and optimization of this thermophile DyP-type peroxidase.

The studies of encapsulin protein from *R.Josti* RHA1 showed the possibility of its reversible disassembly/reassembly *in vitro*, encapsulation of *R. jostii* RHA1 DyPB, and functionality of the encapsulated DyPB. This study also for the first time, as we are aware of, presented some preliminary evidences in supporting considering of encapsulin as an extracellular protein.

Chapter Five

Experiments

5.1 General Experimental Information

All reagents and solvents were, unless otherwise stated, used and purchased from VWR, Sigma-Aldrich UK, Fischer Scientific or Invitrogen. All procedures were conducted at room temperature (≈ 23° C) unless otherwise stated, all biological procedures were conducted under sterile conditions and all solvents used for HPLC were of HPLC grade. All Bioinformatics analysis were performed by CLC Main Workbench 6 software equipped with BLOSUM62 scoring matrix for sequnces allignments.

5.2 Instruments and Equipment

Sterilisation of media and equipment for the growth of bacterial strains was performed in a Prioclave autoclave according to standard proceedures.

For large volumes, centrifugation was performed by a Sorval Rc 6 Plus centrifuge with an SLA-3000 or SS-34 rotor. For small volumes, centrifugation was performed by an

Eppendorf 5810R or 5804R and either a Thermo AccuSpin micro or an Eppendorf Centrifuge 5415R (for samples less than 2 mL).

PCR was performed using an Eppendorf Mastercycler Personal. Agarose gel electrophoresis was performed using a BioRad Mini-Sub Cell GT system and visualised at 260 nm by a UVP Ultraviolet (UV) transilluminator. Low range ladder from Fermentas FastRuler was used to estimate DNA fragment sizes.

Innova 44 or an Innova 4300 shaker were used for growth of overnight cultures. The optical density (OD) at 600 nm was measured by a BioMate3 ultraviolet-visible (UV-Vis) spectrometer. Cell lysis was performed by a Constant Systems pneumatic cell disruptor at 20.1 kilo-pound per square inch (kpsi).

A GE Healthcare AKTA design fast protein liquid chromatograph (FPLC) was used for protein purification, equipped with a P-920 pump and UPC-900 UV monitor. Sodium-dodecyl sulfate polyacrylamide gel electrophoresis (SDS-PAGE) was performed using a BioRad Mini Protean II electrophoresis system and visualised using bromophenol blue G-250. PageRuler Plus prestained protein ladder from Thermo Scientific was used for all SDS-PAGE gels.

High-performance liquid chromatography (HPLC) was performed with an Agilent 1100 Series liquid chromatograph (Agilent Technologies, Santa Clara, USA) equipped with a G1311A quaternary pump and a G1315A photodiode array detector (1100). Liquid-chromatography mass spectrometry (LC-MS) was performed with an Agilent 1200 HPLC system equipped with a G1315A photodiode array detector coupled to a Bruker HTC-Ultra electrospray ionisation (ESI) mass spectrometer. Data analysis was performed with either Bruker Data Analysis post-processing software or Agilent ChemStation (B.01.03). Low resolution ESI was performed using an Agilent 6130B single Quad mass spectrometer. High-resolution mass spectra were obtained via the departmental Mass Spectrometry Service using a Bruker MaXis mass spectrometer.

UV-Vis measurements were obtained using either a Varian Cary 1 or Varian Cary50 Bio UV-Vis spectrometer.

5.3. General Buffers and Solutions

5.3.1 Luria Bertani (LB)

1% yeast extract (w/v), 1% tryptone, (w/v), 1% sodium chloride (w/v). For LB agar: additional 2% agar (w/v).

5.3.2 SDS-PAGE Loading Dye

60 mM Tris-HCl pH 6.8, 10% glycerol (v/v), 2% sodium dodecyl sulfate (w/v), 0.1% bromophenol blue (w/v), 1% 2-mercaptoethanol (v/v).

5.3.3 SDS-PAGE running buffer

150 mM glycine, 20 mM tris base, 0.8% sodium dodecyl sulfate (w/v), pH 8.0

5.3.4 SDS-PAGE Staining Solution

50% distilled water (v/v), 40% methanol (v/v), 10% acetic acid (v/v), 1% Coomassie R250 (w/v).

5.3.5 SDS-PAGE Destaining Solution

70% distilled water (v/v), 20% methanol (v/v), 10% acetic acid (v/v).

5.3.6 Tris Buffer pH 8.8

1.5 M Tris-HCl, pH 8.8.

5.3.7 Tris Buffer pH 6.8

500 mM Tris-HCl, pH 6.8.

5.3.8 Phosphate Buffered Saline (PBS)

140 mM sodium chloride, 2.7 mM potassium chloride, 10 mM disodium hydrogen phosphate, 1.8 mM potassium dihydrogen phosphate, pH 7.3.

5.3.9 N-His_6 Wash Buffer

50 mM sodium hydrogen phosphate, 300 mM sodium chloride, 20 mM imidazole, pH 8.0.

5.3.10 N-His_6 Elution Buffer

50 mM sodium hydrogen phosphate, 300 mM sodium chloride, 250 mM imidazole, pH 8.0.

5.3.11 MOPS Buffer

20 mM MOPS, 80 mM sodium chloride, pH 7.5.

5.3.12. Tris-Borate EDTA (TBE) Buffer

70 mM Tris-base, 90 mM boric acid, 8 mM ethylenediaminetetraacetic acid, pH 8.0.

5.3.13 Britton–Robinson buffer

Boric acid 50 mM, sodium acetate 50 mM, and potassium phosphate 50 mM. The pHs were then adjusted to the desired pH at 0.5 pH unit intervals between 3.5 and 9.0.

5.3.14 Phosphate Buffered Saline (PBS)

100 mM sodium chloride, 10 mM disodium hydrogen phosphate, 1.8 mM potassium dihydrogen phosphate, pH 7.4

5.4 General Procedures

5.4.1 Transformation of chemically competent *E. coli* BL21 and *E. coli* DH5α

Chemically competent Top10 or BL21, 100 µL was defrosted on ice. Plasmid DNA or ligation mixture (3 µL, approximately 50–100 ng) was added and mixed gently. Cells were incubated on ice for 30 minutes then were heat shocked at 42º C for 30 seconds and immediately placed on ice. Room temperature LB media was added (250 µL) to cells and they were incubated at 37º C, 180 rpm for 60 minutes. Cells (2 x 150 µL) was then plated onto LB agar containing appropriate antibiotic before being incubated at overnight at 37º C.

5.4.2 PCR Screening of Transformants

To a single colony of transformed *E. coli* was added distilled sterile water (3 µL). PCR was performed according to the procedure detailed for the particular protein with appropriate primers. PCR product was analysed via agarose gel electrophoresis. PCR reactions consisted of water (39.1 µL),10 X *pfx* buffer (Invitrogen) (5.0 µL), 50 mM magnesium sulfate (1.0 µL), 10 mM deoxynucleotide triphosphates (dNTPs) (1.5 µL), 10 µM forward primer (1.5 µL), 10 µM reverse primer (1.5 µL), *pfx* tag polymerase (1.0 µL from 2.5 unit/µL) and *E. coli* colony solution (1.0 µL).

5.4.3 Agarose Gel Electrophoresis

Agarose (1 g) was dissolved in TBE buffer (100 mL) by heating in a microwave until the solution became transparent. GelRed (Cambridge Bioscience) (5 µL) was added and the molten agarose was added to an appropriate cast with comb. Gels were run at 100 V for 60 minutes. DNA was visualised at 260 nm.

5.4.4 Overproduction of proteins in *E. coli* BL21

LB media, 10 mL containing appropriate antibiotic was inoculated with a single colony of *E. coli* BL21 and grown overnight at 37º C, 180 rpm. LB media (1000 mL) containing appropriate antibiotics was inoculated with the overnight culture and grown at 37º C, 180 rpm until the OD at 600 nm reached 0.6 AU. Isopropyl *β*-d-1-thiogalactopyranoside (IPTG) was added to a final concentration of 0.5 mM. Cultures were incubated overnight at 15 º C, 180 rpm. Cells were harvested at 5000 × g at 4º C for 15 minutes.

5.4.5 Sodium Dodecyl Sulfate Polyacrylamide Gel Electrophoresis

Protein samples were analysed using 12% SDS-PAGE gels unless otherwise stated. SDS-PAGE loading dye (5 µL) was added to protein samples (15 µl) and samples were boiled for 7 minutes at 100° C. Gels were made based on the recipe in Table 8.3 and run at 200 V for one hour at cold room. Gels were stained for one hour using SDS-PAGE staining solution and destained for 30 minutes with SDS-PAGE destaining solution.

Table 5.1– Recipes for SDS-PAGE gels used.

Gel Percentage	12%	Stacking Gel
Water (mL)	1.89	1.63
30% Acrylamide Mix (mL)	2.82	0.25
Tris Buffer pH 8.8 (mL)	1.41	-
Tris Buffer pH 6.8 (mL)	-	0.63
10% (w/v) Sodium dodecyl sulfate (SDS) (mL)	0.058	0.025
10% (w/v) ammonium persulfate (APS) (mL)	0.058	0.025
Tetramethylethylenediamine (TEMED) (mL)	0.005	0.003

5.5 Genomic DNA extraction from *P. fluorescens*, *R. jostii* RHA1 and *T.fusca*

Genomic DNA was extracted using Wizard® Genomic DNA Purification Kit from Promega, briefly as follow:

1) A total 1ml of overnight culture was centrifuged for 2 minutes at 13,000–16,000 × g.

2) Cells was lysed with Nuclei Lysis Solution and RNA was degraded by adding RNase Solution

3) Proteins were precipitated with Protein Precipitation Solution and centrifuged at 13,000–16,000 × g for 3 minutes

4) DNA was precipitated and rehydrated by addition of isopropanol to supernatant, centrifuged, 70% ethanol was added to pellet, centrifuged, ethanol was discarded, the pellet was air-dried and the DNA pellet was rehydrated by rehydration solution

5.6 Primer Design and PCR reaction conditions for *dyp* genes from *P. fluorescens* and *T.fusca*

Primers were designed by oligo calc: Oligonucleotide Properties Calculator website (http://www.basic.northwestern.edu/biotools/oligocalc.html), their properties and sequences of each is as following:

dyp1b:

FW: 5′ ATG AG T TA C TA C CA G CC C GGC ATC 3′ Tm: 73, Length=28, GC %:54

RV: 5′ TCA TTT CGA CGC TTG CAG CGC G 3′ Tm: 71, Length= 22, GC %:59

dyp2b:

FW: 5′ ATG ACC CAG CCG TCC TCC 3′ Tm: 60, Length=18, GC %:67

RV: 5′ CTA CAG GCC GGT GGG CGC 3′ Tm: 65, Length= 18, GC %:78

dypa:

FW: 5′ ATG AAC GAT TCA GAT CAG CCC 3′ Tm: 59, Length=21, GC %:48

RV: 5′ TCA GGC AGT GCT TTT AGG TCG 3′ Tm: 61, Length= 21, GC %:52

Tfudyp:

FW: $_{5'}$ ATG ACC GAA CCA GAC ACG G $_{3'}$ Tm: 59.5, Length=19, GC %:58

RV: $_{5'}$ TCA TCC TTC GAT CAG GTC CTG $_{3'}$ Tm: 61.2, Length= 21, GC %:52

PCR: 1 cycle of 94 °C for 300 seconds; 35 cycles of 94 °C for 30 seconds, 58 °C for 30 seconds, 72° C for 60 seconds; 1 cycle of 72° C for 120 seconds. PCR reactions were carried by using Platinum Pfx-DNA polymerase from Invitrogen by using an Eppendorf Mastercycler. PCR reactions consisted of water (39.1 µL), 10 X pfx buffer (Invitrogen) (5.0 µL), 50 mM magnesium sulfate (1.0 µL), 10 mM deoxynucleotide. triphosphates (dNTPs) (1.5 µL), 10 µM forward primer (1.5 µL), 10 µM reverse primer (1.5 µL), pfx tag polymerase (1.0 µL from 2.5 unit/µL) and genomic DNA (1.0 µL). After performing 35 cycles of reaction, 5 µL of each tube mixed with 1 µL of loading dye and electrophoresis was carried out using 1% (w/v) agarose mixed with 5 µL of gel red dye for visualising and checking the bands out on agarose gel. Amplified PCR products were isolated from 1% of agarose gel and DNA was purified by Wizard® SV Gel and PCR Clean-Up System kit from Promega.

5.7 Cloning and transformation of amplified *dyp* genes in to *E.coli*

Cloning of *dyp* genes were performed using the TOPO cloning strategy provided by a kit from Invitrogen, Champion™ pET Directional TOPO® Expression Kits, which is a Ligation-independent cloning (LIC) method, a form of molecular cloning that is able to be performed without the use of restriction endonucleases and DNA ligase. Designed primers for the encapsulin gene incorporated a CACC overhang on the 5' terminus for ligation into the D-TOPO vector. Briefly, the recommended amount of purified PCR product based on the kit's protocol is added to linearised and activated plasmid in the presence of water and salt solution for performing ligation reactions. The plasmid that was used in this study was TOPO 151 that confers ampicillin resistance to transformed cells and provide a cleavage site of HIS tag by TEV protease. The proper amount of ligation reaction was then added to TOP10 competent

cells and then transformation was carried out by chemical transformation and heat shock method.

TOP 10 transformed cells were grown on ampicillin plates overnight, and 10 of resultant colonies were picked and colony PCR was performed. The positive colonies were grown in liquid culture to extract plasmid DNA for sequencing and also transforming BL21 strain cell for expression under control of IPTG. For both Top10 and BL21 cells containing plasmid for each *dyp* genes, glycerol stocks were produced and stored at -80 °C.

5.8 Purification of DyP enzymes

Protein purification was performed by metal affinity chromatography followed by TEV protease cleavage of the $(His)_6$ fusion tag. The harvested cells from a 2-litre culture described above were suspended in 20 ml lysis buffer (50 mM NaH_2PO_4, 300 mM NaCl, 10 mM imidazole, pH 8.0) in the presence of 1 mM final concentration of PMSF. Cell lysis was carried out using a constant system cell disrupter, followed by centrifugation at 10000 × g for 30 minute. The clear supernatant was loaded onto a Ni-NTA resin FPLC column (HisTrap HP, 1 ml volume) equilibrated with lysis buffer followed by 100 ml of wash buffer (50 mM NaH_2PO_4, 20 mM imidazole, 300 mM NaCl, pH 8.0), and the recombinant protein was eluted by 7 ml elution buffer (50 mM NaH_2PO_4, 250 mM imidazole, 300 mM NaCl, pH 8.0), eluting at a flow rate of 0.5 ml min^{-1}. The solution was subjected to buffer exchange through a PD-10 column into 10 ml wash buffer (50 mM NaH_2PO_4, 20 mM imidazole, 300 mM NaCl, pH 8.0). After buffer exchange, the protein solution was mixed with previously purified TEV protease in equal molar ratio overnight in room temperature, then applied again to a Ni-NTA FPLC column, and eluted in elution buffer (50 mM NaH_2PO_4, 250 mM imidazole, 300 mM NaCl, pH 8.0). The flow-through fraction (25 ml) containing untagged recombinant DyP enzyme

was collected. The purified enzyme was buffer exchanged by a PD-10 column to 20 mM MOPS 80 mM NaCl buffer pH 7.0.

5.9 Heme reconstitution

Dissolved hemin in DMSO (25 mg ml^{-1}) was added to the protein solution in a ratio of 2:1 molar respectively. The mixture was incubated at room temperature for two hours and then it was centrifuged at high speed to remove excess heme. The sample was subsequently passed through a PD-10 column equilibrated with MOPS 20 mM, 80 mM NaCl pH 7.0 and dialysed in the same buffer at 4 °C for overnight. The protein solution then was concentrated by a 10 kDa Amicon centricon device, and after flash freezing using liquid nitrogen, it was stored at -80 ^{o}C for further kinetic analysis.

5.10 pH-rate profile

The pH-rate profile for the peroxidase activity of all purified enzyme was determined at 25°C using the 2,4-DCP oxidation assay with a variation of pH buffers. For all samples, the buffer system contained boric acid (50 mM), sodium acetate (50 mM), and potassium phosphate (50 mM) and were then adjusted to the desired pH every half pH unit between 3.5 and 10.5. The final assay contained H_2O_2 (1 mM), 2,4-DCP (3 mM), and 4-AAP (0.32mM) in a total assay volume of 1 mL.

5.11 Temperature-rate profile

The temperature-rate profile for the peroxidase activity was determined by performing 2,4-DCP oxidation assay in optimum pH of each purified enzyme. Enzymatic reaction was started in each temperature point by adding purified enzyme and hydrogen peroxide to the temperature equilibrated state of substrates solution. Desired temperatures were attained by using temperature controlled water bath. The final assay contained H_2O_2 (1 mM), 2,4-DCP (3 mM), and 4-AAP (0.32 mM) in a total assay volume of 1 mL.

5.12 Steady-state kinetic assays

All assays were performed at 25°C in 100 mM Sodium acetate buffer, in optimum pH of each enzyme using a Cary spectrophotometer. Kinetic parameters (k_{cat} and K_M) were determined by nonlinear curve fitting to the obtained enzyme activity, through Graphpad prism 5 software, using the Michaelis-Menten equation: $v_0 = v_{max}$ [S]/ K_M + [S] where v_0 is the initial rate and [S] is the substrate concentration. All assays were performed in triplicate, and standard error determined from curve fitting.

5.12.1 2,4-dichlorophenol assay

Oxidation of DCP (2,4-dichlorophenol, concentration 10µM-6mM) was performed with 1 mM hydrogen peroxide, monitoring at 510 nm (ε_{510} = 18,000 $M^{-1}cm^{-1}$) [7].

5.12.2. ABTS assay

Oxidation of ABTS (2,2'-azino-bis(3-ethylbenzothiazoline-6-sulphonic acid, concentration 25 µM-6 mM) was performed with 1 mM hydrogen peroxide, monitoring at 420 nm (ε_{420} = 36,000 $M^{-1}cm^{-1}$) [14].

5.12.3 Mn^{2}+oxidation

Oxidation of Mn^{2+} was carried out using $MnCl_2$ (concentration 100 µM-6 mM) in 100 mM sodium tartrate buffer (pH 5.5) with 1 mM hydrogen peroxide, monitoring at 238nm (ε_{238}= 6,500 M^{-1} cm^{-1}) [15].

5.12.4 Pyrogallol assay

Oxidation of pyrogallol (concentration 25 µM-60 mM) was performed with 1 mM hydrogen peroxide, monitoring at 430 nm (ε_{430}=2,470 M^{-1} cm^{-1}) [14].

5.12.5 Guaiacol assay

Oxidation of guaiacol (concentration 2 µM-1 mM) was performed with 1 mM hydrogen peroxide, monitoring at 465nm (ε_{465}=26,600 M^{-1} cm^{-1}) [8].

5.12.6 Phenol assay

Oxidation of phenol (concentration 100 µM-15 mM) was performed with 1 mM hydrogen peroxide, monitoring at 505 nm (ε_{510}=7100 M^{-1} cm^{-1}) [16].

5.12.7 Reactive blue 4

Decolourization of Reactive blue 4 (concentration 25 µM-600 µM) was performed with 1 mM hydrogen peroxide, monitoring at 610 nm (ε_{610}=4,200 M^{-1} cm^{-1}) [14].

5.12.8 Kraft lignin assay

Oxidation of alkali Kraft lignin (Sigma-Aldrich, concentration 2 µM-50 µM) was performed with 1 mM hydrogen peroxide, monitoring at 465 nm [5]. The molar concentration of Kraft lignin was calculated using an average molecular mass of 10000 Da.

5.12.9 Hydrogen peroxide assay

The kinetic constants for hydrogen peroxide were determined using the ABTS assay, at 5 mM ABTS concentration, using 12 µM-1 mM concentration of hydrogen peroxide.

5.13 Pre-steady state kinetic analysis

Stopped flow experiments were performed on an Applied Photophysics SX.18MV machine, at 25 °C in 100 mM Sodium acetate buffer pH 5.5. For obtaining the soret band decay curve, equimolar mixing of enzyme and hydrogen peroxide was performed (having 5 µM enzyme and 5 µM of hydrogen peroxide in cuvette). For calculating the second order rate constant of formation of compound **I** enzyme in constant concentration of 5 µM was titrated with varying concentrations of hydrogen peroxide ranged from 25 µM to 250 µM.

Measurement and fitting of obtained apparent rate constants was performed by pro-data viewer software.

5.14 Oxidation of wheat straw lignocellulose and HPLC analysis

Powdered wheat straw lignocellulose (5 mg) was added to succinate buffer (3 mL, 50 mM, pH 5.5), and then DyP1B (100 µL, 1 mg/mL) was added, followed by H_2O_2 (1 mM) and $MnCl_2$ (1 mM). The resulting solution was incubated at 30 ºC for 1 h. Aliquot (500 µL) was taken and reaction was stopped by adding CCl_3COOH (100%, w/v, 50 µL) and the solution was then centrifuged for 5 min at 10000 rpm. HPLC analysis was conducted using a Phenomenex Luna 5 µm C_{18} reverse phase column (100 Å, 50 mm, 4.6 mm) on a Hewlett-Packard Series 1100 analyzer, at a flow rate of 0.5 mL/min, with monitoring at 310 nm. The gradient was as follows: 20 to 30% MeOH/H_2O over 5 min, 30 to 50% MeOH/H_2O from 5 to 12 min, and 50 to 80% MeOH/H_2O from 12 to 26 min.

5.15 Treatment of collected peak with $NaBH_4$

Solution of $NaBH_4$ in dilute sodium hydroxide solution was made up by dissolving 5 mg $NaBH_4$ in 100 µL 100 mM NaOH, the pH was adjusted to 7. A10 µl of this solution was added to collected solution from HPLC for 30 minutes. Then sample was reanalysed by HPLC.

5.16 Oxidation of Beta-Aryl ether lignin model compound (Guicylglycerol-beta-guiacyl ether) and HPLC analysis

Model compound (5 mg) was dissolved in acetone 200 µL and the volume was increased to 3 ml by sodium acetate buffer (100 mM, pH 6) and then TfuDyP (100 µL, 1 mg/mL) was added, followed by H_2O_2 (1mM). The resulting solution was incubated at 30 ºC for 1 h. Aliquot (500 µL) was taken and reaction was stopped by adding CCl_3COOH (100%, w/v, 50 µL) and the solution was then centrifuged for 5 min at 10000 rpm. HPLC analysis was conducted using a Phenomenex Luna 5 µm C_{18} reverse phase column (100 Å, 50 mm, 4.6 mm) on a Hewlett-Packard Series 1100 analyzer, at a flow rate of 0.5 mL/min, with monitoring at 310 nm. The gradient was as follows: 20 to 30% MeOH/H_2O over 5 min, 30 to 50% MeOH/H_2O from 5 to 12 min, and 50 to 80% MeOH/H_2O from 12 to 26 min.

5.17 TfuDyP Crystallization

Pure recombinant TfDyP (15 mg/ml) in 20 mM MOPS buffer pH 7.5 was subjected to crystallization screening using a Cartesian Honeybee liquid handling robot. Protein 200 nL was mixed with 200 nL of crystallization solution from commercially available screens in MRC 96-well 2-drop MRC crystallization plates (Molecular Dimensions). Plates were sealed with sealing films (Sigma) and incubated at 18 °C. Large red shard and pink rod protein crystals grew within 3-4 weeks in conditions H2-H5 of the PACT Premier HT-96 crystallization screen (Molecular Dimensions) containing 20% (w/v) PEG 3350, 0.1 M Bis Tris propane pH 8.5, and 0.2 M sodium bromide, sodium iodide, potassium thiocyanate, or sodium nitrate. Following optimisation, crystals of approximately 250 x 250 µm were grown using the hanging drop method in 20-22.5% PEG 3350, 0.2 M sodium bromide or potassium thiocyanate, and 0.1 M Bis Tris propane pH 8.5. The best crystals were obtained by

microseeding fresh drops 4-24 h after set-up with crushed crystals from the initial screens using an acupuncture needle. Crystals were removed from drops using a nylon loop, cryoprotected using LV cryo oil (MiTeGen), and flash-frozen in liquid nitrogen.

5.18 X-ray data collection, structure determination and refinement

X-ray diffraction data were collected to 1.7 Å at beam line I24 at Diamond Light Source using a Pilatus 6M-F detector and an X-ray wavelength of 0.97903 Å. Data were indexed and scaled using XDS [110]. Further data handling was carried out using the CCP4 software package [111]. Molecular replacement was carried out using the Thermobifida cellulosilytica DyP-type peroxidase (PDB code 4GS1) as a search model with PHASER [112]. Refinement of the structure was carried out by alternate cycles of REFMAC5 [113] and manual refitting using O [114]. Water molecules were added to the atomic model automatically using ARP [115] at positions of large positive peaks in the difference electron density, only at places where the resulting water molecule fell into an appropriate hydrogen-bonding environment. Refinement of the structure was carried out using non-crystallographic symmetry restraints and in the last steps of refinement all the non-crystallographic symmetry restraints were released. The crystallographic asymmetric unit contains a homodimer and the polypeptide chain could be unambiguously traced in between residues 10-278 and 293-391 for each chain.

5.19 Site directed mutagenesis and purification of TfuDyP mutants

Site directe mutagenesis was performed for selected aminoacids by using QuikChange II XL Site-Directed Mutagenesis Kit from Agilent technologies. For each target aminoacid, pair of primer, contained flanking areas of mutation point and a codon for desired

aminoacid were designed by Agilent technologies primer design software. The list of primers is as follow:

TfuDyP D203A:

Fw: $_{5'}$TGGCGGTGCCGGCGATCTGCCCC$_{3'}$

RV: $_{5'}$ GGGGCAGATCGCCGGCACCGCCA$_{3'}$

TfuDyP R315Q:

FW: $_{5'}$ AGCTGTAGCCGCGCTGGAACATGCGGGC$_{3'}$

RV: $_{5'}$ GCCCGCATGTTCCAGCGCGGCTACAGCT$_{3'}$

TfuDyP F336A:

FW: $_{5'}$ CTTGCCAGGCCATGGCGAGCAGTCCGGCGT$_{3'}$

RV: $_{5'}$ ACGCCGGACTGCTCGCCATGGCCTGGCAAG$_{3'}$

Mutations procedure was followed exactly based on protocole and materials provided by Agilent technologies. Berifly, mutant strand synthesis was performed by using PfuUltra DNA polymerase and designed primer in thermal cycling reaction, then the PCR reaction was treated by Dpn I enzyme for digestion of template followed by transformation of mutated molecule into competent cells for nick repair and selection on ampicillin plate.The plasmid contained mutated insert was extracted from selected grown colonies and sent for sequencing for checking presence of the desired mutation in right place. Expression and purification of the each mutant protein was performed as explained in section 5.18 for purification of DyPs enzymes.

5.20 Primer Design and PCR reaction conditions for *encapsulin* gene

Primers were designed by oligo calc: Oligonucleotide Properties Calculator website (http://www.basic.northwestern.edu/biotools/oligocalc.html), their properties and sequences of each is as following:

FW: $_{5'}$ATGAGTGATTCGAGCAATC$_{3'}$ Tm: 53, Length=19, GC %:42

RV: $_{5'}$TCAGCGTGCGAGGACGACC$_{3'}$ Tm: 63, Length= 19, GC %:68

PCR: 1 cycle of 94° C for 300 seconds; 35° C cycles of 94° C for 30 seconds, 55° C for 30 seconds, 72° C for 60 seconds; 1 cycle of 72° C for 120 seconds. PCR reactions were carried by using Platinum Pfx-DNA polymerase from Invitrogen by using an Eppendorf Mastercycler. PCR reactions consisted of water (39.1 µL), 10 X pfx buffer (Invitrogen) (5.0 µL), 50 mM magnesium sulfate (1.0 µL), 10 mM deoxynucleotide. Triphosphates (dNTPs) (1.5 µL), 10 µM forward primer (1.5 µL), 10 µM reverse primer (1.5 µL), pfx tag polymerase (1.0 µL) and *R. jostii* RHA1 genomic DNA (1.0 µL). After performing 35 cycles of reaction, 5 µL of each tube mixed with 1 µL of loading dye and electrophoresis was carried out using 1% (w/v) agarose mixed with 5 µL of gel red dye for visualising and checking the bands out on agarose gel. Amplified PCR products were isolated from 1% of agarose gel and DNA was purified by Wizard® SV Gel and PCR Clean-Up System kit from Promega.

5.21 Cloning and transformation of amplified *encapsulin* gene in to *E.coli*

Cloning of *encapsulin* was performed using the TOPO cloning strategy provided by a kit from Invitrogen, Champion™ pET Directional TOPO® Expression Kits, which is a Ligation-independent cloning (LIC) method, a form of molecular cloning that is able to be performed without the use of restriction endonucleases and DNA ligase. Designed primers for

the *encapsulin* incorporated a CACC overhang on the 5' terminus for ligation into the D-TOPO vector. Briefly, the recommended amount of purified PCR product based on the kit's protocol is added to linearised and activated plasmid in the presence of water and salt solution for performing ligation reactions. The plasmid that was used in this study was TOPO 200 that confers kanamycin resistance to transformed cells. The proper amount of ligation reaction was then added to TOP10 competent cells and then transformation was carried out by chemical transformation and heat shock method.

TOP10 transformed cells were grown on kanamycin plates overnight, and 10 of resultant colonies were picked and colony PCR was performed. The positive colonies were grown in liquid culture to extrac plasmid DNA for sequencing and also transforming BL21 strain cell for expression under control of IPTG. For both Top10 and BL21 cells containing plasmid for each DyP genes, glycerol stocks were produced and stored in -80 °C.

5.22 Expression and purification of *R. jostii* encapsulin

A 1-L culture of *R. jostii* RHA1 Δencapsulin/pTipQC2 (knockout for the genomic encapsulin gene but complemented for the encapsulin gene with plasmid pTipQC2) was grown in the presence of 35 μg/mL chloramphenicol for 36 h at 30 °C, with shaking at 180 r.p.m. At a A600 nm of 0.6, the culture was induced by addition of thiostrepton (final concentration of 1 μg-mL^{-1}), the culture was grown for a further 16 h at 30 °C overnight, and cells were then harvested by centrifugation at 13000 × g (10 min). The cell pellets were resuspended in 10 mL of lysis buffer in the presence of 1 mM phenylmethanesulfonyl fluoride, and then lysozyme (1 mg-mL^{-1}) and DNase (2 U-g^{-1} of cells) were added, and the mixture was left at room temperature for 30 min. Cell lysis was carried out by sonication (3 ×1 min, 0 °C). After centrifugation at 13000 × g (30 min), the clear supernatant was filtered (20 mL) and concentrated to 1 mL with a 50-kDa Amicon centricon device. The concentrated

cell lysate was applied to a Superdex 200 gel filtration column (GE Healthcare, Little Chalfont, UK), and eluted with 50 mM phosphate buffer and 100 mM NaCl, pH 7.4 at a flow rate of 0.5 mL/min. Fractions (0.5 mL) showing a 29-kDa band for encapsulin by SDS PAGE were pooled and the buffer was exchanged for 20 mM Tris/HCl, pH 8.0 with a PD-10 column. The resultant solution was applied to a Mono Q HR 5/5 anion exchange FPLC column, and protein was eluted with a gradient of 0–1 M NaCl in 20 mM Tris/HCl, pH 8.0. Fractions containing the 29-kDa encapsulin band, which eluted at ~ 700 mM NaCl, were pooled. Further purification was achieved by elution from a Sephadex G-75 column (Sigma-Aldrich, St Louis, MO, USA), equilibrated with 50 mM phosphate buffer and 100 mM NaCl, pH 7.4, at a flow rate of 0.75 mL-min $^{-1}$. Three peaks appeared and the fractions were collected for each of them. Collected fractions containing pure encapsulin were pooled for further analysis.

5.23 Disassembly and reassembly of encapsulin

Purified encapsulin (0.6 mg) was placed in 100 mM acetate buffer (pH 3.0) (1 mL) on ice for 15 min, and a sample (100 μL) was taken for native PAGE and dynamic light scattering. Then, 100 mM phosphate buffer and 100 mM NaCl (pH 7.4) (2 mL) was added to the solution, which was incubated for 30 min on ice. Buffer was exchanged with 50 mM phosphate buffer and 100 mM NaCl (pH 7.4) by two passages through a 10-kDa Centricon device. A sample (100 μL) was taken for native PAGE and dynamic light scattering.

5.24 Disassembly/reassembly in the presence of DyPB

Purified encapsulin (0.6 mg, 21 nmol) was placed in 100 mM acetate buffer (pH 3.0) (1 mL) on ice for 15 min in the presence of DyPB (0.2 mg, 5.3 nmol). DyPB has been shown

to be highly active at pH 3, and does not lose activity for this period of time at this pH. Reassembly was carried out as described above, and the solution was then injected onto a Superdex 200 column equilibrated with 50 mM phosphate buffer and 100 mM NaCl (pH 7.4), and eluted with this buffer at a flow rate of 0.5 mL/min. Samples from each fraction were analysed by SDSPAGE.

5.25 Analysis by dynamic light scattering

Analysis of dynamic radius was carried out by dynamic light scattering with a Malvern Zetasizer instrument (Malvern Instruments, Malvern, UK) with a laser wavelength of 633 nm, and a 0.1 mg-mL $^{-1}$ solution (45 μL) in 50 mM phosphate buffer and 100 mM NaCl (pH 7.4) buffer, except for disassembled protein, which was in 100 mM acetate buffer (pH 3.0). Three measurements were performed at 20 °C, each cycle lasting for 60 s. Data were analysed and presented with ZETASIZER NANOSERIES software, and the average size for each measurement was calculated and recorded.

5.26 Assays for peroxidase activity

The reassembled encapsulin–DyPB complex, purified by gel filtration as described above, was assayed with ABTS [15] and nitrated lignin [16] procedures. Assays were carried out at 0.2 mg/mL total protein, and the results were compared with those obtained with pure *R. jostii* RHA1 DyPB and a buffer-only control. ABTS assay: assays were carried out with enzyme (0.2 mg) in 100 mM acetate buffer (pH 5), to which was added ABTS (10 mM final concentration) and 1 mM H_2O_2, in a final volume of 1 mL. Reactions were initiated by the addition of H_2O_2, and initial rates were monitored at 420 nm. Nitrated lignin assay: assays were carried out with a stock solution of nitrated milled wood lignin (0.015 mM, 800 μL)

[16], in 750 mM Tris buffer (pH 7.4) containing 50 mM NaCl, to which was added 0.2 mg of enzyme and 40 mM H_2O_2 (50 μL), in a total volume of 1.0 mL. Reactions were initiated by the addition of H_2O_2, and initial rates were monitored at 430 nm over a period of 20 min. Control assays were carried out in which protein solution was replaced with 750 mM Tris (pH 7.4) and 50 mM NaCl.

Chapter Six

Bibliography

1. A. C. O'Sullivan, *Cellulose*, 1997, **4**, 173–207
2. D. Crawford, M.J. Barder, A.L. Pometto, and R.L. Crawford, *Arch. Microbiol*., 1982, **131**, 140
3. R.L. Crawford, *Appl. Environ. Microbiol*., 1976, **31**, 714
4. J. M. Humphreys and C. Chapple, *Curr. Opin. Plant Biol.*, 2002, **3**, 224
5. L. B. Davin and N. G. Lewis, *Curr. Opin. Biotechnol.*, 2005, **4**, 407
6. G. Brunow, O. Karlsson, and K. Lundquist, *Wood Sci. Technol.*, 1993, **4**, 281
7. F. S. Chakar and A. J. Ragauskas, *Ind. Crops Prod*., 2004, **2**, 131
8. J. O. Sánchez, R.Sierra, and C.J. Alméciga-Díaz, *Delignification Process of Agro-Industrial Wastes an Alternative to Obtain Fermentable Carbohydrates for Producing Fuel*,ed. M. Manzanera, InTech, 2011, 111-154

9. Y. Kim, R. Hendrickson, N. S. Mosier, and M. R. Ladisch, *Methods Mol. Biol.*, 2009, **581**, 93

10. X. Zhao, K. Cheng, and D. Liu, *Appl. Microbiol. Biotechnol.*, 2009, **5**, 815

11. A. Hatakka, *Biodegradation of lignin, Biopolymers*, ed. M. Hofrichter, and A. Steinbüchel, Wiley- VCH, Germany, 2001, 129-180

12. T.K. Kirk, and R.L. Farrell, *Ann. Rev. Microbiol.*, 1987, **41**, 465

13. AT. Martínez, M. Speranza, F.J. Ruiz-Dueñas, P. Ferreira, S. Camarero, F. Guillén, M.J. Martínez, Gutiérrez A, and J.C. Del Río, *Int Microbiol.*, 2005, **8**, 195

14. S. Dey, T.K. Maiti, and B.C. Bhattacharyya, *Appl. Environ. Microbiol.*, 1994 , **60**, 4216

15. J.A. Bumpus and D.A. Steven, *Bioessays*, 1987, **6**, 166

16. T. D. H. Bugg, M. Ahmad, E. M. Hardiman, and R. Rahmanpour, *Nat. Prod. Rep.*, 2011, **12**, 1883

17. A. Levasseur, F. Piumi, P.M. Coutinho, C. Rancurel, M. Asther, M. Delattre, B. Henrissat, P. Pontarotti, M. Asther, and E. Record, *Fungal Genet Biol*., 2008, **45**, 638

18. S. Macarena, L.L. Fernando, V. Mónica, V. Rafael, G. Bernardo, *FEMS Microbiol Lett.*, 2005, **242**, 37

19. S. L. Edwards, R. Raag, H. Wariishi, M. H. Gold, and T. L. Poulos, *Proc. Natl. Acad. Sci. U.S.A.*, 1993, **90**, 750

20. M. Sundaramoorthy, K. Kishi, M. H. Gold, and T.L. Poulos, () *J. Biol. Chem.*, 1994, **269**, 32759

21. L. Banci, S. Ciofi-Baffoni, and M.Tien, *Biochemistry*,1999, **10**, 3205

22. A. T. Martínez**,** *Enzyme Microb. Technol.*, 2002, **30**, 425

23. M. Hofrichter, *Enzyme Microb. Technol.*, 2002, **30**, 454

24. D. Cai, and M. Tien, *J. Biotechnol.*, 1993, **30**, 79

25. M. Tien, T.K. Kirk, C. Bull, and J.A.Fee, *J. Biol. Chem.*, 1986, **26**, 1687

26. W.A. Doyle, W. Blodig, N.C. Veitch, K. Piontek, and A.T. Smith, *Biochemistry*, 1998, **37**, 15097

27. A. Khindaria, I. Yamazaki, and S.D. Aust, *Biochemistry*, 1996, **35**, 6418

28. L.P. Candeias and P.J. Harvey, *J. Biol. Chem.*, 1995, **270**, 16745

29. D.J. O'Sullivan and F. O'Gara, *Microbiol. Mol. Biol. Rev.*,1992, **56**, 662

30. E. A. Robleto, I. L. Hernandez, M. W. Silby, and S. B. Levy, *J. Bacteriol*, 2003, **185**, 453

31. L. S. Thomashow and D. M. Weller, *J. Bacteriol*, 1988, **170**, 3499

32. S. Capdevila, F. M. Martınez-Granero, M. S. Contreras, R. Rivilla, and M. Martin, *Microbiology*, 2004, **150**, 3889

33. S. R. Giddens, R. W. Jackson, C. D. Moon, M. A. Jacobs, X. X. Zhang, S. M. Gehrig, and P.B. Rainey, *Proc Natl Acad Sci USA*, 2007, **104**, 18247

34. U. F. Walsh, J. P. Morrissey, and F. O'Gara, *Curr. Opin. Biotechnol.*, 2001, **12**, 289

35. I.T. Paulsen, C.M. Press, and J. Ravel, *Nat. Biotechnol.*, 2005, **23**, 873

36. http://www.ncbi.nlm.nih.gov/entrez/query.fcgi?db=genomeprj&cmd=Retrieve&dopt=Overview&list_uids=12300

37. T.C. Montie, Pseudomonas, Springer, 1998

38. DOE Joint Genome Institute, Thermobifida fusca YX project: http://www.ncbi.nlm.nih.gov/entrez/query.fcgi?db=genomeprj&cmd=Retrieve&dopt=Overview&list_uids=94

39. A. Lykidis, K. Mavromatis, N. Ivanova, I. Anderson, M. Land, G. D. Bartolo, M. Martinez, A. Lapidus, S. Lucas, A. Copeland, P. Richardson, D.B. Wilson, and N. Kyrpides, *J Bacteriol*, 2007, **189**, 2477

40. K. C. Yam, S. Okamoto, J. N. Roberts, and L. D. Eltis, *Can j Microbiol*, 2011, **57**,155

41. M.P. McLeod, R. L. Warren, W. W. L. Hsiao, N. Araki, M. Myhre, C. Fernandes, D. Miyazawa, W. Wong, A. L. Lillquist, D. Wang, M. Dosanjh, H. Hara, A. Petrescu, R. D. Morin, G. Yang, J. M. Stott, J. E. Schein, H. Shin, D. Smailus, A.S. Siddiqui, M. A. Marra, S. J. M. Jones, R. Holt, F. S. L. Brinkman, K. Miyauchi, M. Fukuda, J. E. Davies, W. W. Mohn, and L. D. Eltis, *Proc. Natl. Acad. Sci. U.S.A*, 2006, **103**, 15582

42. T. Lichtinger, G. Reiss, and R. Benz, *J Bacteriol*, 2000, **182**, 764

43. T.L. Poulos, *Arch. Biochem. Biophys.*, 2010, **500,** 3

44. P.J. O'Brien, *Chem.-Biol. Interact.*, 2000, **129,** 113

45. K. G. Welinder, *Curr. Opin. Struct. Biol.*, 1992, **2**, 388

46. Y. Sugano, *Cell. Mol. Life Sci.*, 2009, **66**,1387

47. M. J. Davies, C. L. Hawkins, D. I. Pattison, and M. D. Rees, *Antioxid. Redox Signaling*, 2008, **10**, 1199

48. F. Passardi, C. Cosio, C. Penel, and C. Dunand, *Plant Cell Rep.*, 2005, **24**, 255

49. C. Regalado, B.E. García-Almendárez, and M.A. Duarte-Vázquez, *Phytochem Rev.*, 2004, **3**, 243

50. M. Za´mocky and C. Obinger, *Biocatalysis Based on Heme Peroxidases*, ed. E.Torres and M. Ayala, Springer Verlag, Berlin, Germany, 2010, 7–35

51. S. J. Kim, K. Ishikawa, M. Hirai, and M. Shoda, *J. Ferment. Bioeng.*, 1995, **79**, 601

52. S. J. Kim, and M. Shoda, *Biotechnol. Tech.*, 1998, **12**, 497

53. S. J. Kim, and M. Shoda, *Biotechnol. Bioeng.*, 1999a, **62**, 114

54. S. Shintani, Y. Sugano, and M. Shoda, *J.Wood Sci.*, 2002, **48**, 402

55. S. J. Kim, and M. Shoda, *Appl. Environ. Microbiol.*, 1999, **65**, 1029

56. Y. Sugano, R. Muramatsu, A. Ichiyanagi, T. Sato, and M. Shoda, *J. Biol. Chem.*, 2007, **282**, 36652

57. C. Zubieta, S. S. Krishna, M. Kapoor, P. Kozbiel, D. McMullan, H. L. Axelrod, M. D. Miller, P. Abdubek, E. Ambing, T. Astakhova, D.Carlton, H. J. Chiu, T. Clayton, M. C. Deller, L. Duan, M.A. Elsliger, J. Feuerhelm, S. K. Grzechnik, J. Hale, E. Hampton, G.W. Han, L. Jaroszewski, K. K. Jin, H. E. Klock, M. W. Knuth, A. Kumar, D. Marciano, A. T. Morse, E. Nigoghossian, L.Okach, S. Oommachen, R. Reyes, C. L. Rife, P. Schimmel, H. van den Bedem, D. Weekes, A. White, Q. Xu, K. O. Hodgson, J. Wooley, A. M. Deacon, A. Godzik, S. A. Lesley, and I. A. Wilson, *Proteins.*, 2007, **69**, 223

58. C. Zubieta, R. Joseph, S. S. Krishna, D. McMullan, M. Kapoor, H. L. Axelrod, M. D. Miller, P. Abdubek, C. Acosta, T. Astakhova, D.Carlton, H. J. Chiu, T. Clayton, M. C. Deller, L. Duan, Y.Elias, M.A. Elsliger, J. Feuerhelm, S. K. Grzechnik, J. Hale, G. W. Han, L. Jaroszewski, K. K. Jin, H. E. Klock, M. W. Knuth, P. Kozbial, A. Kumar,

D. Marciano, A. T. Morse, K.D.Murphy, E. Nigoghossian, L.Okach, S. Oommachen, R. Reyes, C. L. Rife, P. Schimmel, C. V.Trout, H. van den Bedem, D. Weekes, A. White, Q. Xu, K. O. Hodgson, J. Wooley, A. M. Deacon, A. Godzik, S. A. Lesley and I. A. Wilson, *Proteins.*, 2007, **69**, 234

59. M. Hofrichter, R. Ullrich, M.J. Pecyna, C. Liers, and T. Lundell, *Appl. Microbiol.Biotechnol.*, 2010, **87**, 871

60. C. Liers, E. Aranda, E. Strittmatter, K. Piontek, D. A. Plattner, H. Zorn, R.Ullrich, and M. Hofrichter, *J. Mol. Catal. B: Enzym.*, 2014, **103**, 41

61. A. Sturm, A. Schierhorn, U. Lindenstrauss, H. Lilie, and T. Bruser, *J. Biol. Chem.*, 2006, **281**, 13972

62. H.J. Ogola, T. Kamiike, N. Hashimoto, H. Ashida, T. Ishikawa, H. Shibata, and Y. Sawa, *Appl. Environ. Microbiol.*, 2009, **75**, 7509

63. E. V. Bloois, D.E. Torres Pazmino, R.T. Winter, and M.W. Fraaije, *Appl. Microbiol. Biotechnol.*, 2010, **86**, 1419

64. M. Ahmad, J.N. Roberts, E.M. Hardiman, R. Singh, L.D. Eltis and T.D.H. Bugg, *Biochemistry*, 2011, **50**, 5096

65. J. N. Roberts, R. Singh, J.C. Grigg, M.E.P. Murphy, T.D.H. Bugg, and L.D. Eltis, *Biochemistry*, 2011, **50**, 5108

66. R. Singh, J.C. Grigg, W. Qin, J.F. Kadla, M.E.P. Murphy, and L.D. Eltis, *ACS Chem. Biol.*, 2013, **8**, 700

67. R. Singh, J.C. Grigg, Z. Armstrong, M.E.P. Murphy, and L.D. Eltis, *J. Biol. Chem.*, 2012, **287**, 10623

68. M.E. Brown, T. Barros, and M.C.Y. Chang, *ACS Chem. Biol.*, 2012, **7**, 2074

69. A. Santos, S. Mendes, V. Brissos, and L.O. Martins, *Appl. Microbiol. Biotechnol.*, 2014, **98**, 2053

70. C. Liers, C. Bobeth, M. Pecyna, R. Ullrich, and M. Hofrichter, *Appl. Microbiol. Biotechnol.*, 2010, **85**,1869

71. E. Strittmatter, C. Liers, R. Ullrich, S. Wachter, M. Hofrichter, D.A. Plattner, and K. J. Piontek, *Biol. Chem.*, 2013, **288**, 4095

72. A.Kaur, P. T.Van, C. R. Busch, C. K. Robinson, M. Pan, W. L. Pang, D. J. Reiss, J. Diruggiero, and N. S. Baliga, *Mol. Syst. Biol.*, 2010, **6**, 393

73. L. Kong, D. Guo, S. Zhou, X. Yu, G. Hou, R. Li, and B. Zhao, *Arch. Microbiol.*, 2010, **192**, 585

74. S. Létoffé, G. Heuck, P. Delepelaire, N. Lange, and C. Wandersman, *Proc. Natl. Acad. Sci.*, 2009, **106**, 11719

75. H. A. Dailey, A. N. Septer, L. Daugherty, D. Thames, S. Gerdes, E. V. Stabb, A. K. Dunn, T. A. Dailey, and J. D. Phillips, *Mbio*., 2011, **2**, 248

76. M. Sutter, D. Boehringer, S. Gutmann, S. Gunther, D. Prangishvili, M. J. Loessner, K. O. Stetter, E. W. Ban, and N. Ban, *Nat. Struct. Mol. Biol.*, 2008, **15**, 939

77. R. Rahmanpour and T. D. H. Bugg, *FEBS J*., 2013, **280**, 2097

78. B. Goblirsch, R. C. Kurker, B. R. Streit, C. M. Wilmot, and J. L. DuBois, *J. Mol. Biol.*, 2011, **408**, 379

79. T. Yoshida, H. Tsuge, H. Konno, T. Hisabori, and Y. Sugano, *FEBS J.*, 2011, **278**, 2387

80. W. Blodig, W. A. Doyle, A. T. Smith, K. Winterhalter, T. Choinowski, and K. Piontek, *Biochemistry*, 1998, **37**, 8832

81. W. Blodig, A. T. Smith, K. Winterhalter, and K. Piontek, *Arch. Biochem. Biophys.*, 1999, **370**, 86

82. X. Liu, Q. Du, Z. Wang, D. Zhu,Y. Huang, N. Li, T. Wei, S. Xu, and L. Gu, *J. Biol. Chem.*, 2011, **286**, 14922

83. J. Cao, M. R.Woodhall, J. Alvarez, M. L. Cartron, and S. C. Andrews, *Mol. Microbiol.*, 2007, **65**, 857

84. M. B. Rajasekaran, S. Nilapwar, S. C. Andrews, and K. A. Watson, *BioMetals*., 2010, **23**, 1

85. M. L. Cartron, S. A. Mitchell, M. R. Woodhall, S. C. Andrews, and K. A. Watson, *Acta Crystallogr., Sect. F: Struct. Biol. Cryst. Commun*., 2007, **63**, 37

86. Y. Sugano, R. Nakano, K. Sasaki, M. Shoda, *Appl. Environ. Microbiol.*, 2000, **66**, 1754

87. Y. Sugano, Y. Matsushima, K. Tsuchiya, H. Aoki, M. Hirai, M. Shoda, *Biodegradation*, 2009, **20**, 433

88. E. Adler, *Wood Sci. Technol*., 1977, **11**, 169

89. T.K. Kirk, M. Tien, P.J. Kersten, M.D. Mozuch, and B. Kalyanaraman, *Biochem. J.*, 1986, **236**, 279

90. C. Bohlin, P. Persson, L. Gorton, K. Lundquist, and L.J. Jönsson, *J. Mol. Catal. B: Enzym.*, 2005, **35**, 100

91. K. Kishi, M. Kusters-van Someren, M. B. Mayfield, J. Sun, T.M. Loehr, and M. H. Gold, *Biochemistry*, 1996, **35**, 8986

92. M. Ahmad, C. R. Taylor, D. Pink, K. Burton, D. Eastwood, G. D. Bending, and T. D. H. Bugg, *Mol. BioSyst.*, 2010, **6**, 815

93. G. Battistuzzi, M. Bellei, C. A. Bortolotti, and M. Sola, *Arch. Biochem. Biophys.*, 2010, **500**, 21

94. T.L. Poulos and J. Kraut, *J. Biol. Chem.*, 1980, **255**, 8199

95. P. Jones and H.B. Dunford, *J. Inorg. Biochem.*, 2005, **99**, 2292

96. E.L. Raven, *Nat. Prod. Rep.*, 2003, **20**, 367

97. A. N. P. Hiner, E. L. Raven, R. N. F. Thorneley, F. Garcia-Canovas, and J. N. Rodriguez-Lopez, J. *Inorg. Biochem.*, 2002, **91**, 27

98. Y.V. Guillen Schlippe and L. Hedstrom, *Arch. Biochem. Biophys.*, 2005, **433**, 266

99. M. Xin and T.D.H. Bugg, *J. Am. Chem. Soc.*, 2008, **130**, 10422

100. C. R.Taylor, E. M. Hardiman, M. Ahmad, P. D. Sainsbury, P. R. Norris, and T. D. H. Bugg, *J. Appl. Microbiol.*, 2012, **113**, 521

101. T. O. Yeates, C. S. Crowley, and S. Tanaka, *Annu. Rev. Biophys.*, 2010, **39**, 185

102. S. Tanaka, C. A. Kerfeld, M. R. Sawaya, F. Cai, S. Heinhorst, G.C. Cannon, and T. O. Yeates, *Science*, 2008, **319**, 1083

103. G.D. Havemann, E.M. Sampson, and T.A. Bobik, *J. Bacteriol.*, 2002, **184**, 1253

104. S. Tanaka, M.R. Sawaya, and T. O. Yeates, *Science*, 2010, **327**, 81

105. W.L. DeLano, *The PyMOL User's Manual*, DeLano Scientific, Palo Alto, CA, 2002

106. D.W. Cruickshank, *Acta Cryst. D*, 1999, **55**, 583

107. L. M. Podust, A. Ioanoviciu, and P. R. Ortiz de Montellano, *Biochemistry*, 2008, **47**, 12523

108. A. Arcovito, T. Moschetti, P. D'Angelo, G. Mancini, B.Vallone, M. Brunori, and S. Della Longa, *Arch. Biochem. Biophys*., 2008, **475**, 7

109. T. Beitlich, K. Kühnel, C. Schulze-Briese, R. L. Shoeman, and I. Schlichting, *J Synchrotron Radiat*., 2007, **14**, 11

110. W. Kabsch, *Acta cryst. D*, 2010, **66**, 125

111. Collaborative Computational Project Number 4, *Acta cryst. D*, 1994, **50**, 760

112. A.J. McCoy, R. W. Grosse-Kunstleve, P. D. Adams, M. D. Winn, L. C Storoni, and R. J. Read, *J. Appl. Cryst.*, 2007 **40**, 658

113. G. N. Murshudov, P. Skubak, A. A. Lebedev, N. S. Pannu, R. A. Steiner, R. A. Nicholls, M. D. Winn, F. Long, and A. A. Vagin, *Acta cryst. D.*, 2011, **67**, 355

114. T. A. Jones, J. Y. Zou, S. W. Cowan, and M. Kjeldgaard, *Acta Cryst. A*.,1991, **47**, 110

115. A. Perrakis, R. Morris, and V. S. Lamzin, *Nat. Struct. Biol.*, 1999, **6**, 458

116. S. Heinhorst, and G. C. Cannon, *Nat. Struct. Mol. Biol*, 2008, **15**, 897

117. S. Heinhorst, and G. C. Cannon, *Proc. Natl. Acad. Sci.*, 2010, **107**, 7627

118. C. Fana, S. Chenga, Y. Liua, C. M. Escobara, C. S. Crowleyb, R. E. Jeffersonc, T. O. Yeates, and T. A. Bobika, *Proc. Natl. Acad. Sci.*, 2010, **107**, 7509

119. C. A. Kerfeld, M. R. Sawaya, S. Tanaka, C. V. Nguyen, M. Phillips, M. Beeby, and T. O. Yeates, *Science*, 2005, **309**, 936

120. N. Valdes-Stauber and S. Scherer, *Appl. Environ. Microbiol.* **60**, 3809

121. L. Rosenkrands, P. B. Rasmussen, M. Carnio, S. Jacobsen, M. Theisen, and P. Andersen, *Infect. Immun.*,1998, **66**, 2728

122. C. A. McHugh, J. Fontana, D. Nemecek, N. Cheng, A. A. Aksyuk, J.B. Heymann, D. C. Winkler, A.S. Lam, J. S. Wall, A. C. Steven, E. Hoiczyk, *EMBO J*, 2014, **33**, 1896

123. H. Contreras, M. S. Joens, L. M. McMath, V. P. Le, M. V. Tullius, J. M. Kimmey, N. Bionghi, M. A. Horwitz, J. A. Fitzpatrick, C. W. Goulding, *J. Biol. Chem.*, 2014, **289**, 18279

124. R. van der Geize, Hessels GI, R. van Gerwen, P. van der Meijden, and L. Dijkhuizen, *FEMS Microbiol Lett*, 2001, **205**, 197

125. N. Nakashima and T. Tamura, *Appl. Environ. Microbiol.*, 2004, **70**, 5557

126. J. Moradian-Oldak, M. L. Paine, Y. P. Lei, A. G. Fincham, and M. L. Snead, *J. Struct. Biol.*, 2000, **131**, 27

127. H. Palonen, F. Tjerneld, G. Zacchi, and M. Tenkanen, *J. Biotechnol*., 2004, **107**, 65

128. T. Eriksson, J. BÖrjesson, and F. Tjerneld, *Enzyme Microb. Technol.*, 2002, **31**, 353

129. T. Johjima, N. Itoh, M. Kabuto, F. Tokimura, T. Nakagawa, H. Warishi, and H. Tanaka, *Proc. Natl. Acad. Sci.*,1999, **96**, 1989

Chapter Seven

Appendix

the FEBS Journal

Assembly *in vitro* of *Rhodococcus jostii* RHA1 encapsulin and peroxidase DypB to form a nanocompartment

Rahman Rahmanpour and Timothy D. H. Bugg

Department of Chemistry, University of Warwick, Coventry, UK

Keywords
encapsulin; lignin; nanocompartment; peroxidase DypB

Correspondence
T. D. H. Bugg, Department of Chemistry, University of Warwick, Coventry CV4 7AL, UK
Fax: +44 2476 524112
Tel: +44 2476 573018
E-mail: T.D.Bugg@warwick.ac.uk

(Received 8 January 2013, revised 18 February 2013, accepted 4 March 2013)

doi:10.1111/febs.12234

Rhodococcus jostii RHA1 peroxidase DypB has been recently identified as a bacterial lignin peroxidase. The *dypB* gene is cotranscribed with a gene encoding an encapsulin protein, which has been shown in *Thermotoga maritima* to assemble to form a 60-subunit nanocompartment, and DypB contains a C-terminal sequence motif that is thought to target the protein to the encapsulin nanocompartment. *R. jostii* RHA1 encapsulin protein was overexpressed in *R. jostii* RHA1, and purified as a high-M_r assembly ($M_r > 10^6$). The purified nanocompartment could be disassembled to form a low-M_r species by treatment at pH 3.0, and reassembled to form an assembly of similar size and shape, as assessed by dynamic light scattering. Recombinant DypB could be assembled *in vitro* with monomeric encapsulin to form an assembly of similar size to the encapsulin-only nanocompartment, as assessed by gel filtration. The assembled complex showed enhanced lignin degradation activity per milligram of DypB present as compared with native DypB, as determined with a nitrated lignin UV–visible assay method. The measured stoichiometry of 8.6 μmol encapsulin/μmol DypB in the complex was similar to the value of 10 predicted from the crystal structure.

Structured digital abstract

- encapsulin and encapsulin bind by blue native page (View interaction)
- encapsulin and encapsulin bind by dynamic light scattering (View interaction)

Introduction

Several types of bacterial protein-based organelles, or microcompartments, have been characterized in recent years, and consist of polyhedron-shaped arrays of protein subunits, containing enzymes in their interior that typically catalyse a particular biochemical pathway [1]. Cyanobacteria and chemoautotrophic bacteria contain the carboxysome, an icosahedral complex 80–150 nm in diameter that contains enzymes for CO_2 fixation [2]; the polyhedral Pdu microcompartment in *Salmonella enterica* contains enzymes for 1,2-propanediol utilization [3]; and the Eut microcompartment in the enteric bacteria *Escherichia coli* and *S. enterica* contains enzymes for ethanolamine utilization [4]. A smaller 240-Å icosahedral nanocompartment has been characterized in *Thermotoga maritima*, whose shell-forming protein is called an encapsulin [5]. Homologues of the encapsulin protein are found in *Brevibacterium linens*, where they show antibacterial activity as an extracellular 29-kDa linocin [6], and in *Mycobacterium tuberculosis* [7]. The crystal structure of the *T. maritima* nanocompartment has been determined, and it contains 60 subunits of encapsulin, enclosing a large central cavity [5]. Sutter *et al.* [5] have identified a C-terminal peptide extension that

Abbreviation
ABTS, 2,2′-azinobis(3-ethylbenzo-6-thiazolinesulfonic acid).

appears to target two types of protein to the nanocompartment in different bacteria: a DyP-type peroxidase, and a ferritin-like protein.

We have recently reported that DypB from *Rhodococcus jostii* RHA1 shows activity as a lignin peroxidase, oxidizing a β-aryl ether lignin model compound, manganese ions, or polymeric Kraft lignin [8]. Deletion of the *dypB* gene abolishes the lignin degradation activity of *R. jostii* RHA1 [8], as determined with a colorimetric assay involving nitrated milled wood lignin [9]; therefore, DypB appears to be important for the lignin degradation activity of this microorganism. The genome sequence of *R. jostii* RHA1, a powerful polychlorinated biphenyl-degrading organism, has been determined [10]. Immediately downstream of the *R. jostii dypB* gene (ro2407) is a 807-bp encapsulin gene (ro2408), as shown in Fig. 1. We therefore wished to investigate whether DypB is packaged within the encapsulin nanocompartment, and examine what effect the nanocompartment has on lignin degradation activity. Here, we report the reconstitution of purified recombinant *R. jostii* encapsulin with *R. jostii* DypB to form a packaged nanocompartment.

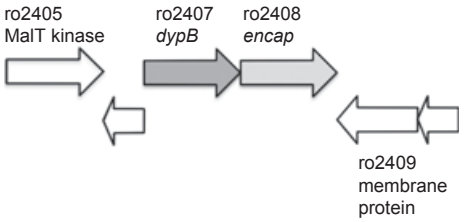

Fig. 1. Genomic context of *R. jostii* RHA1 *dypB* and encapsulin genes.

Results

Sequence analysis

In their study of the *T. maritima* encapsulin, Sutter *et al.* [5] identified a 10-residue peptide sequence (GSLxIGSLKG) found at the C-terminus of the associated Dyp-type peroxidase or ferritin protein that appears to be responsible for targeting of the protein to the nanocompartment. As shown in Table 1, this C-terminal peptide sequence is present in *R. jostii* RHA1 DypB. A number of bacterial DypB homologues were examined, and their C-terminal amino acid sequences are shown in Table 1. DypB sequences from *R. jostii*, *Rhodococcus opacus*, *Rhodococcus erythropolis*, *Nocardia cyriacigeorgica*, *Burkholderia phymatum*, *Burkholderia multivorans*, *M. tuberculosis*, *Acetobacter pasteuranius*, *Streptomyces hygroscopicus* and *Streptomyces griseus* each show a 20–30-residue extension containing the 10-residue sequence motif, and, in each of these organisms, the *dypB* and encapsulin genes were found immediately adjacent in the respective genome sequences (Fig. 2). However, DypB homologues from *Pseudomonas fluorescens*, *Streptomyces coelicolor* and

Table 1. Alignment of C-terminal amino acid sequences of bacterial DypB homologues. Sequences are listed in order of sequence similarity to the *R. jostii* RHA1 DypB sequence.

Bacterial strain	Accession number of DypB homologue	C-terminal protein sequence (encapsulin-targeting sequence underlined)	Size (amino acids)	Downstream encapsulin family[a] gene? (accession number)
Rhodococcus jostii RHA1	Q0SE24	ESLGDEPAGAES------APEDPVEPAAAGPYDLSLKIGGLKGVSQ	350	Yes (Q0SE23)
Rhodococcus opacus B4	C1B1V7	ESLGDAPAAAEP------APEDP-APAGASPYELSLKIGGLKGVSQ	349	Yes (C1B1V8)
Rhodococcus erythropolis	C0ZVK5	DDPPDAPTR---------LVPEATFTAPIS—DGSLGIGSLKRSAQQ	341	Yes (C0ZVK4)
Burkholderia phymatum	B2JNZ7	EALADREPQPASAS----AAASADTFACAEPGHDGSLNIGSLKGTAQYE	352	Yes (B2JNZ6)
Burkholderia multivorans	A9ATN5	DALPDRAAPAEAAA----PAPSSN----EPHRDGSLKIGSLKGVKSV	353	Yes (A9ATN4)
Mycobacterium tuberculosis	O07180	DHPP----------PLPQAATPTLAA----GSLSIGSLKGSPR	335	Yes (O07181)
Nocardia cyriacigeorgica	H6R1G4	DDLPDPPG---------ASPADDATPAAPAADGSLGIGTLKRSS	341	Yes (H6R1G5)
Streptomyces coelicolor	Q9FBY9	EDLPARP	316	No
Streptomyces lividans	D6EC39	EDLSARP	329	No
Streptomyces hygroscopicus	H2JMY8	EDLPEPPAAG-------AVAAVTPTDSQVRSSGSSLGIGSMKRSMSR	349	Yes (H2JMY9)
Streptomyces griseus	B1VSP6	DAPPPPPAPARTGNLPEPVPAPVRQEPPAAGADHGSLRIGSLQESAQ	357	Yes (B1VSP6)
Acetobacter pasteurianus	C7JE82	DDAPNMSTENTQ-----ASPEPVTAPPLPKALHGSLGIGSLNNKDA	379	Yes (C7JE83)
Pseudomonas fluorescens	Q4KA97	EDLAERAPTGL	328	No
Pseudomonas fluorescens	I2BZP5	EALPDREPVA	320	No
		Sequence motif GSLxIGSLKG		

[a] Gene annotated as bacteriocin or linocin.

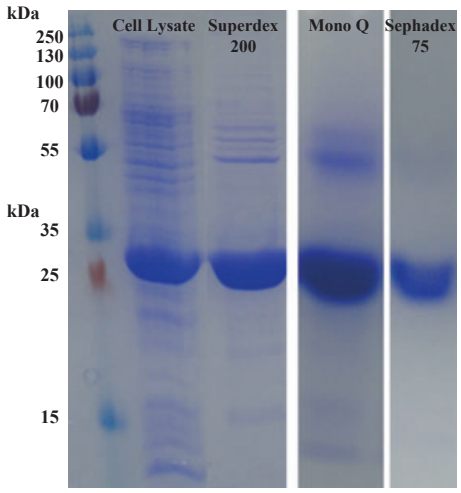

Fig. 2. Purification of *R. jostii* RHA1 encapsulin: SDS/PAGE analysis of pooled fractions from cell extract, Superdex 200 gel filtration chromatography, Mono Q anion exchange, and Sephadex 75 gel filtration.

Streptomyces lividans lack the C-terminal peptide sequence, and, in these organisms, there is no adjacent encapsulin gene. Although the targeting sequence is not always present, there is a clear correlation between the presence of the C-terminal amino acid sequence motif and the presence of a downstream encapsulin gene.

Expression and purification of *R. jostii* RHA1 encapsulin nanocompartments

Overexpression of the *R. jostii* RHA1 encapsulin gene in a pET200 expression vector in *E. coli* was found to give rather weak expression of a 29-kDa protein band (data not shown) that, upon analytical gel filtration, eluted as a low molecular mass protein, suggesting that the assembly to form a nanocompartment had not occurred. Overexpression of the *R. jostii* encapsulin gene in the pTipQC2 expression vector in an *R. jostii* RHA1 Δencapsulin strain, however, was found to give high expression of a 29-kDa protein band by SDS/PAGE (Fig. 2, lane 2). Purification of the cell lysate by Superdex 200 gel filtration chromatography gave a major peak at a short retention time (Fig. S1), corresponding to a very high molecular mass protein (predicted molecular mass of 1.8 MDa by calibration with protein standards), consistent with a high molecular mass nanocompartment. Purification to homogeneity was achieved by Mono Q anion exchange, followed by Sephadex 75 gel filtration chromatography (Fig. 2). Elution of the protein complex by Sephadex 75 gel filtration was found to give three

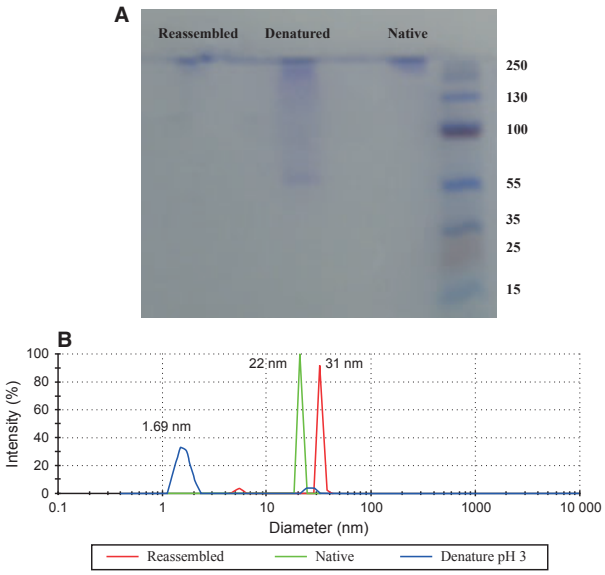

Fig. 3. Disassembly and reassembly of the encapsulin nanocompartment. (A) Native SDS/PAGE analysis of: native encapsulin nanocompartment; treatment at pH 3.0 leading to disassembly; and reassembly at pH 7.0. (B) Analysis of the same samples by dynamic light scattering, showing the predicted particle diameter.

peaks, each of which was shown to contain the encapsulin monomer by SDS/PAGE, indicating the presence of three different multimeric forms in solution (Fig. S2).

Disassembly and *in vitro* reassembly of the nanocompartment

Using the purified *R. jostii* RHA1 encapulin nanocompartment, we investigated methods to disassemble the nanocompartment, using native SDS/PAGE to monitor changes in native molecular mass. The native nanocompartment appeared as a very high molecular mass band on native SDS/PAGE, as shown in Fig. 3. Treatment with acetate buffer at pH 3 was found to give a low molecular mass band, eluting at ~ 60 kDa on native PAGE (Fig. 3A), consistent with a dimeric species. When the species obtained by treatment at pH 3.0 was subsequently incubated in 50 mM phosphate buffer (pH 7.0) for 30 min, analysis by native PAGE revealed once again the high molecular mass band corresponding to the reassembled nanocompartment.

For further characterization of the disassembled and reassembled protein fractions, they were analysed with dynamic light scattering, which has been used to measure the dynamic radius of protein aggregates in solution [11]. The native purified nanocompartment gave a

single peak corresponding to a radius of 22 nm, which matched quite well with the 240-Å diameter of the *T. maritima* nanocompartment, determined by X-ray crystallography [5]. A sample of protein treated at pH 3.0 gave a major peak at a much smaller size, corresponding to a radius of 1.69 nm. The thickness of the *T. maritima* nanocompartment was found to be 20–25 Å [5], so the observed dynamic radius is consistent with the dimeric form of encapsulin. Analysis of the reassembled nanocompartment by dynamic light scattering showed that the reassembled encapsulin nancompartment had a dynamic radius of 31 nm, which was similar to but slightly larger than that of the native nanocompartment, perhaps indicating a slightly expanded structure.

In order to investigate reassembly with DypB, the 'disassembled' encapsulin (21 nmol) was mixed with purified *R. jostii* RHA1 DypB (5.3 nmol) [8]. In this experiment, a protein concentration of 0.8 mg/mL was used, to prevent the possibility of aggregation and unwanted interactions between encapsulin monomers and DypB molecules, and to reduce the possibility of macromolecular crowding in the disassembled state; also, a low concentration of DypB was considered to increase the efficiency of encapsulin reassembly. The mixture was incubated in 100 mM phosphate buffer and 100 mM NaCl (pH 7.4) for 30 min, and then passed through a Superdex 200 gel filtration column; two major peaks were observed (Fig. S3). The first was a well-defined peak whose retention time of 9.5 min matched the retention time of the material originally purified (Fig. S1; retention time of 8.5–10 min). Analysis of this peak by denaturing SDS/PAGE revealed two protein bands, corresponding to encapsulin and DypB, whereas the second peak at retention time 19.0 min consisted only of DypB, as shown in Fig. 4. These data indicate that reassembly of DypB with encapsulin had been achieved, to form a high molecular mass assembly.

The ratio of encapsulin to DypB proteins in the reassembled complex was investigated. Reassembled encapsulin–DypB complex was heated to 50 °C for 5 min, and sonicated for 3 min, and total protein was then determined with the Bradford assay in triplicate. DypB content was assessed by measurement of haem content at 404 nm, and comparison with a DypB standard curve. The molar ratio of encapsulin to DypB was found to be 8.6 μmol·encapsulin·μmol^{-1} DypB.

Peroxidase activity of the encapsulin–DypB complex

The peroxidase activity of the reassembled DypB–encapsulin complex was assessed with kinetic assays. *R. jostii* RHA1 DypB has been shown to be active with the dye 2,2′-azinobis(3-ethylbenzo-6-thiazoline-sulfonic acid) (ABTS), which can be assayed colorimetrically at 420 nm, and with nitrated milled wood lignin, which can be assayed colorimetrically at 430 nm [8]. As shown in Table 2, the activity per milligram of protein of the reassembled DypB–encapsulin complex was ~ 10-fold lower with ABTS than with pure DypB, but, when corrected for the proportion of the complex present as DypB (8.6 mol encapsulin complex per mol DypB), the peroxidase activity of the DypB enzyme in the complex with ABTS was 70–75% of that of native DypB. In the nitrated lignin assay [9], the activity of the reassembled DypB–encapsulin complex was similar to that of DypB alone, but, when corrected for the proportion of the complex present as DypB, the activity per milligram of DypB was eight-fold higher than that of DypB alone, indicating that assembly in the encapsulin somehow enhances the lignin degradation activity of DypB.

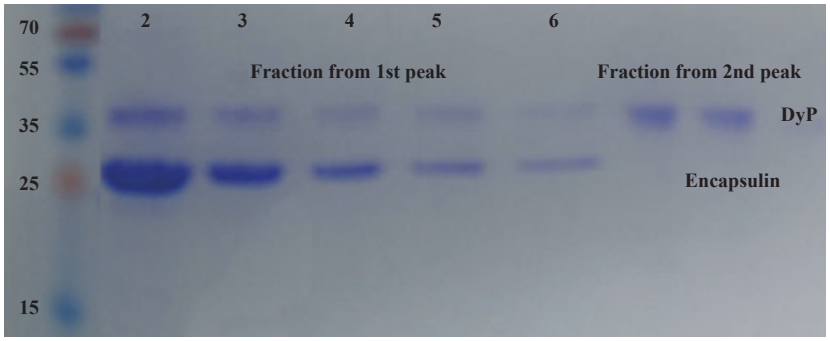

Fig. 4. Purification of reassembled encapsulin–DypB complex by Superdex 200 gel filtration. Analysis by SDS/PAGE shows the presence of encapsulin and DypB in the high molecular mass fraction (1st peak), and only DypB in the lower molecular mass fraction (2nd peak).

Table 2. Peroxidase activity of the reassembled DypB–encapsulin complex. Assays were carried out with 0.2 mg of protein (either purified DypB or reassembled encapsulin–DypB complex) as described in Experimental procedures. For DypB only, activity per μmole of DypB was calculated by using M_r 37 222 for *R. jostii* DypB, ε_{420} 36 000 $M^{-1}\cdot cm^{-1}$ for ABTS; no ε value was available for the nitrated lignin assay, as a mixture of products is formed [9]. For DypB–encapsulin assembly, activity per μmole of DypB was calculated by using a stoichiometry of 8.6 mol encapsulin complex/mol DypB.

	DypB only		DypB–encapsulin assembly	
Substrate	Activity per mg of protein	Activity per μmole of DypB	Activity per mg of protein	Activity per μmole of DypB
ABTS	4.05 ± 0.05 AU·min^{-1}	4.24 ± 0.05 μmol·min^{-1}	0.275 ± 0.5 AU·min^{-1}	2.43 ± 0.5 μmol·min^{-1}
Nitrated lignin	0.025 ± 0.005 AU·min^{-1}	0.92 ± 0.2 AU·min^{-1}	0.023 ± 0.008 AU·min^{-1}	7.4 ± 2.5 AU·min^{-1}

Discussion

This work has demonstrated that *R. jostii* DypB can be assembled *in vitro* with *R. jostii* encapsulin, which is consistent with the colocalization of the two genes on the genome, and the presence of the C-terminal targeting sequence in DypB. The work also provides procedures for *in vitro* disassembly of the nanocompartment and reassembly with 'cargo' proteins. The nanocompartment might prove to have useful applications for biotechnology, as these procedures could be used to load proteins into the nanocompartment *in vitro*. The data obtained with dynamic light scattering (Fig. 3B) show that the reassembled encapsulin nanocompartment is similar (although not identical) to the original nanocompartment, and the diameter of 22 nm agrees well with the diameter of 240 Å determined from the crystal structure of the *T. maritima* nanocompartment [5]. The reassembled encapsulin–DypB complex shows a similar gel filtration retention time to the originally expressed nanocompartment, but contains DypB, so our interpretation is that the DypB protein has been packaged within the encapsulin nanocompartment. (A referee has raised the possibility that the reassembled DypB–encapsulin complex may be a nonspecific aggregate. We consider this to be unlikely, as a sharp peak was observed for the complex by gel filtration (Fig. S3), whereas one would expect to see multiple species formed in the case of a nonspecific aggregate. Also, the reassembled complex is enzymatically active, which would not be expected in the case of an aggregate. We note that *R. jostii* RHA1 encapsulin contains no cysteines, so the formation of disulfide linkages is not feasible.) The stoichiometry of 8.6 mol encapsulin/mol DypB also agrees quite well with the stoichiometry of 10 mol encapsulin per mol DypB predicted from the crystal structure, where one nanocompartment containing 60 subunits of encapsulin was predicted to contain six subunits of DypB.

The peroxidase activity of the reassembled encapsulin–DypB complex provides some interesting clues as to the possible functional role of the encapsulin–DypB complex. With ABTS as substrate, the peroxidase activity of the complex is similar to that of DypB alone, which is surprising, as the pores in the encapsulin nancompartment structure are < 5 Å wide, large enough to allow hydrogen peroxide to enter, but not a large dye molecule such as ABTS. It is conceivable that some subunits of DypB might be attached to the exterior of the nanocompartment, but all of the binding sites for the C-terminal targeting peptide are located on the inside of the nanocompartment [5]. The other possibility is that the nanocompartment is a flexible, dynamic structure that is able to open and close to take up substrate molecules. This explanation seems consistent with the observation of other assemblies by the use of gel filtration chromatography (Fig. S2).

The observation that the reassembled encapsulin–DypB complex shows eight-fold higher activity in the nitrated lignin assay (per milligram of DypB) than DypB alone implies that the encapsulin nanocompartment somehow increases the activity with polymeric lignin. One possible explanation is that it may assist in localizing DypB to the hydrophobic surface of lignin. The nonspecific binding of cellulase enzymes to the hydrophobic surface of lignin is thought to slow down the rate of lignocellulose breakdown by cellulases [12], which can be alleviated by addition of nonionic detergents that preferentially bind to lignin [13]. Furthermore, lignin peroxidase from *Phanerochaete chrysosporium* has been shown to directly adsorb to the surface of synthetic lignin [14], thereby assisting in lignin breakdown. If the encapsulin nanocompartment is a dynamic structure, then it seems possible that it could disassemble on the surface of lignin or lignocellulose, and therefore localize DypB to the surface of lignin or lignocellulose, as illustrated in Fig. 5. The close proximity of DypB to the surface may increase its activity, owing to the generation of short-lived

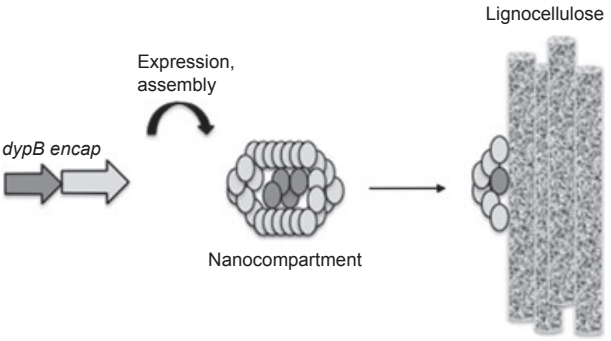

Fig. 5. Assembly of the nanocompartment, and hypothetical pathway for delivery to the surface of lignocellulose.

oxidants (e.g. Mn^{2+} or phenolic radicals) used for lignin oxidation.

One issue that is unresolved is the cellular location of the DypB–encapsulin complex. The lignin degradation activity of *R. jostii* RHA1 was measured with extracellular extract [8,9], implying that DypB is exported from the cell. The encapsulin-related linocins from *B. linens* and *M. tuberculosis* have also been detected extracellularly [6,7], and we have also observed a protein band corresponding to encapsulin in extracellular fractions of *R. jostii* RHA1 (data not shown); however, the encapsulin nanocompartment has only been observed intracellularly [5]. The mechanism for cell export of encapsulin and DypB is unknown, and would seem not to follow known protein export mechanisms. In summary, the ability to package proteins into the cavity of such a nanocompartment, using a specific targeting sequence, offers interesting possible applications for biotechnology, and may have specific application for biomass deconstruction.

Experimental procedures

Strains

The gene deletion strain *R. jostii* RHA1 Δencapsulin, in which the encapsulin gene ro2408 is deleted, was constructed by R. Singh and L. Eltis (Department of Microbiology and Immunology, University of British Columbia), using the method of van der Geize *et al.* [15], as described previously for construction of a ΔdypB strain [8]. The *R. jostii* RHA1 encapsulin gene was expressed on an inducible expression vector, pTipQC2 [16], by R. Singh, allowing inducible expression of encapsulin in *R. jostii* RHA1.

Expression and purification of *R. jostii* encapsulin

A 1-L culture of *R. jostii* RHA1 Δencapsulin/pTipQC2 (knockout for the genomic encapsulin gene but complemented for the encapsulin gene with plasmid pTipQC2) was grown in the presence of 35 μg/mL chloramphenicol for 36 h at 30 °C, with shaking at 180 r.p.m. At a $A_{600\ nm}$ of 0.6, the culture was induced by addition of thiostrepton (final concentration of 1 $\mu g \cdot mL^{-1}$), the culture was grown for a further 16 h at 30 °C overnight, and cells were then harvested by centrifugation at 13 000 ***g*** (10 min). The cell pellets were resuspended in 10 mL of lysis buffer (50 mM NaH_2PO_4, 10 mM imidazole, pH 8.0) in the presence of 1 mM phenylmethanesulfonyl fluoride, and then lysozyme (1 $mg \cdot mL^{-1}$) and DNase (2 $U \cdot g^{-1}$ of cells) were added, and the mixture was left at room temperature for 30 min. Cell lysis was carried out by sonication (3 × 1 min, 0 °C). After centrifugation at 13 000 ***g*** (30 min), the clear supernatant was filtered (20 μm) and concentrated to 1 mL with a 50-kDa Amicon centricon device.

The concentrated cell lysate was applied to a Superdex 200 gel filtration column (GE Healthcare, Little Chalfont, UK), and eluted with 50 mM phosphate buffer and 100 mM NaCl (pH 7.4) at a flow rate of 0.5 mL/min. Fractions (0.5 mL) showing a 29-kDa band for encapsulin by SDS/PAGE were pooled, and the buffer was exchanged for 20 mM Tris/HCl (pH 8.0) with a PD-10 column. The resultant solution was applied to a Mono Q HR 5/5 anion exchange FPLC column, and protein was eluted with a gradient of 0–1 M NaCl in 20 mM Tris/HCl (pH 8.0). Fractions containing the 29-kDa encapsulin band, which eluted at ~ 700 mM NaCl, were pooled. Further purification was achieved by elution from a Sephadex G-75 column (Sigma-Aldrich, St Louis, MO, USA), equilibrated with 50 mM phosphate buffer and 100 mM NaCl (pH 7.4), at a flow rate of 0.75 $mL \cdot min^{-1}$. Collected fractions containing pure encapsulin (yield: 2.5 mg of protein) were pooled for further analysis.

Disassembly and reassembly of encapsulin

Purified encapsulin (0.6 mg) was placed in 100 mM acetate buffer (pH 3.0) (1 mL) on ice for 15 min, and a sample (100 μL) was taken for native PAGE and dynamic light scattering. Then, 100 mM phosphate buffer and 100 mM NaCl (pH 7.4) (2 mL) was added to the solution, which was incubated for 30 min on ice. Buffer was exchanged with 50 mM phosphate buffer and 100 mM NaCl (pH 7.4) by two passages through a 10-kDa Centricon device. A sample (100 μL) was taken for native PAGE and dynamic light scattering.

Disassembly/reassembly in the presence of DypB

Purified encapsulin (0.6 mg, 21 nmol) was placed in 100 mM acetate buffer (pH 3.0) (1 mL) on ice for 15 min in the presence of DypB (0.2 mg, 5.3 nmol). DypB has been shown to be highly active at pH 3, and does not lose activity for this period of time at this pH. Reassembly was carried out as described above, and the solution

was then injected onto a Superdex 200 column equilibrated with 50 mM phosphate buffer and 100 mM NaCl (pH 7.4), and eluted with this buffer at a flow rate of 0.5 mL/min. Samples from each fraction were analysed by SDS/PAGE.

Analysis by dynamic light scattering

Analysis of dynamic radius was carried out by dynamic light scattering with a Malvern Zetasizer instrument (Malvern Instruments, Malvern, UK) with a laser wavelength of 633 nm, and a 0.1 $mg{\cdot}mL^{-1}$ solution (45 μL) in 50 mM phosphate buffer and 100 mM NaCl (pH 7.4) buffer, except for disassembled protein, which was in 100 mM acetate buffer (pH 3.0). Three measurements were performed at 20 °C, each cycle lasting for 60 s. Data were analysed and presented with ZETASIZER NANOSERIES software, and the average size for each measurement was calculated and recorded.

Assays for peroxidase activity

The reassembled encapsulin–DypB complex, purified by gel filtration as described above, was assayed with ABTS [8] and nitrated lignin [9] procedures. Assays were carried out at 0.2 mg/mL total protein, and the results were compared with those obtained with pure *R. jostii* RHA1 DyPB and a buffer-only control. ABTS assay: assays were carried out with enzyme (0.2 mg) in 100 mM acetate buffer (pH 5), to which was added ABTS (10 mM final concentration) and 1 mM H_2O_2, in a final volume of 1 mL. Reactions were initiated by the addition of H_2O_2, and initial rates were monitored at 420 nm. Nitrated lignin assay: assays were carried out with a stock solution of nitrated milled wood lignin (0.015 mM, 800 μL), prepared as previously described [9], in 750 mM Tris buffer (pH 7.4) containing 50 mM NaCl, to which was added 0.2 mg of enzyme and 40 mM H_2O_2 (50 μL), in a total volume of 1.0 mL. Reactions were initiated by the addition of H_2O_2, and initial rates were monitored at 430 nm over a period of 20 min. Control assays were carried out in which protein solution was replaced with 750 mM Tris (pH 7.4) and 50 mM NaCl.

Acknowledgements

We thank R. Singh and L. Eltis (Department of Microbiology and Immunology, University of British Columbia) for providing us with the gene deletion strain *R. jostii* RHA1 Δencapsulin and plasmid pTipQC2 containing the recombinant encapsulin gene. We thank the University of Warwick for provision of a Studentship (R. Rahmanpour), A. Rodger (University of Warwick) for advice on dynamic light scattering, and D. Braddick for practical assistance.

References

1 Yeates TO, Crowley CS & Tanaka S (2010) Bacterial microcompartment organelles: protein shell structure and evolution. *Annu Rev Biophys* **39**, 185–205.
2 Tanaka S, Kerfeld CA, Sawaya MR, Cai F, Heinhorst S, Cannon GC & Yeates TO (2008) Atomic-level models of the bacterial carboxysome shell. *Science* **319**, 1083–1086.
3 Havemann GD, Sampson EM & Bobik TA (2002) PduA is a shell protein of polyhedral organelles involved in coenzyme B_{12}-dependent degradation of 1,2-propanediol in *Salmonella enterica* serovar Typhimurium LT2. *J Bacteriol* **184**, 1253–1261.
4 Tanaka S, Sawaya MR & Yeates TO (2010) Structure and mechanisms of a protein-based organelle in *Escherichia coli*. *Science* **327**, 81–84.
5 Sutter M, Boehringer D, Gutmann S, Günther S, Prangishvili D, Loessner MJ, Stetter KO, Weber-Ban E & Ban N (2008) Structural basis of enzyme encapsulation into a bacterial nanocompartment. *Nat Struct Mol Biol* **15**, 939–947.
6 Valdes-Stauber N & Scherer S (1994) Isolation and characterization of linocin M18, a bacteriocin produced by *Brevibacterium linens*. *Appl Environ Microbiol* **60**, 3809–3814.
7 Rosenkrands L, Rasmussen PB, Carnio M, Jacobsen S, Theisen M & Andersen P (1998) Identification and characterization of a 29-kDa protein from Mycobacterium tuberculosis culture filtrate recognized by mouse memory effector cells. *Infect Immun* **66**, 2728–2735.
8 Ahmad M, Roberts JN, Hardiman EM, Singh R, Eltis LD & Bugg TDH (2011) Identification of DypB from *Rhodococcus jostii* RHA1 as a lignin peroxidase. *Biochemistry* **50**, 5096–5107.
9 Ahmad M, Taylor CR, Pink D, Burton K, Eastwood D, Bending GD & Bugg TDH (2010) Development of novel assays for lignin degradation: comparative analysis of bacterial and fungal lignin degraders. *Mol BioSyst* **6**, 815–821.
10 McLeod MP, Warren RL, Hsiao WWL, Araki N, Myhre M, Fernandes C, Miyazawa D, Wong W, Lillquist AL, Wang D *et al.* (2006) The complete genome of *Rhodococcus* sp. RHA1 provides insights into a catabolic powerhouse. *Proc Natl Acad Sci USA* **103**, 15582–15587.
11 Moradian-Oldak J, Paine ML, Lei YP, Fincham AG & Snead ML (2000) Self-assembly properties of recombinant engineered amelogenin proteins analysed by dynamic light scattering and atomic force microscopy. *J Struct Biol* **131**, 27–37.
12 Palonen H, Tjerneld F, Zacchi G & Tenkanen M (2004) Adsorption of *Trichoderma reesei* CBH1 and

EGII and their catalytic domains on steam-pretreated softwood and isolated lignin. *J Biotechnol* **107**, 65–72.
13 Eriksson T, Börjesson J & Tjerneld F (2002) Mechanism of surfactant effect in enzymatic hydrolysis of lignocellulose. *Enzyme Microb Technol* **31**, 353–364.
14 Johjima T, Itoh N, Kabuto M, Tokimura F, Nakagawa T, Wariishi H & Tanaka H (1999) Direct interaction of lignin and lignin peroxidase from *Phanerochaete chrysosporium*. *Proc Natl Acad Sci USA* **96**, 1989–1994.
15 van der Geize R, Hessels GI, van Gerwen R, van der Meijden P & Dijkhuizen L (2001) Unmarked gene deletion mutagenesis of *kstD*, encoding 3-ketosteroid Δ^1-dehydrogenase, in *Rhodococcus erythropolis* SQ1 using *sacB* as counter-selectable marker. *FEMS Microbiol Lett* **205**, 197–202.
16 Nakashima N & Tamura T (2004) Isolation and characterization of a rolling-circle-type plasmid from *Rhodococcus erythropolis* and application of the plasmid to multiple-recombinant-protein expression. *Appl Environ Microbiol* **70**, 5557–5568.

Supporting information

Additional supporting information may be found in the online version of this article at the publisher's web site:

Fig. S1. Purification of cell extract containing *R. jostii* RHA1 encapsulin by Superdex 200 gel filtration chromatography.

Fig. S2. Elution of purified *R. jostii* RHA1 encapsulin from a Sephadex G75 gel filtration column, showing three protein peaks.

Fig. S3. Elution of reassembled encapsulin–DypB mixture from a Superdex 200 gel filtration column.

WILEY Blackwell

the FEBS Journal

www.febsjournal.org

Assembly *in vitro* of *Rhodococcus jostii* RHA1 encapsulin and peroxidase DypB to form a nanocompartment

Rahman Rahmanpour and Timothy D. H. Bugg

DOI: 10.1111/febs.12234

Assembly *in vitro* of *Rhodococcus jostii* RHA1 Encapsulin and Peroxidase DypB to form a Nanocompartment

Rahman Rahmanpour and Timothy D.H. Bugg*

Department of Chemistry, University of Warwick, Coventry CV4 7AL, U.K.

Supporting Information

Figure S1. Purification of cell extract containing *R. jostii* RHA1 encapsulin by Superdex 200 gel filtration chromatography. Elution volume from left to right, absorbance at 280 nm.

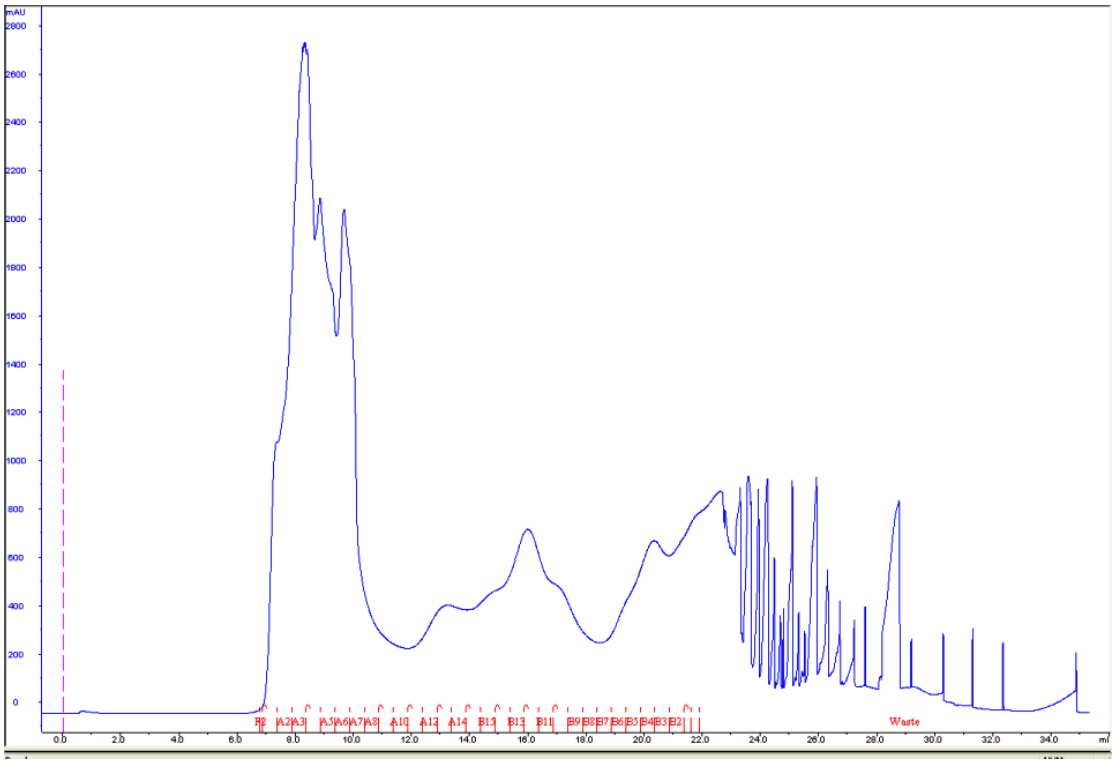

Figure S2. Elution of purified *R. jostii* RHA1 encapsulin from Sephadex 75 gel filtration column, showing three protein peaks. Elution volume from left to right, absorbance at 280 nm.

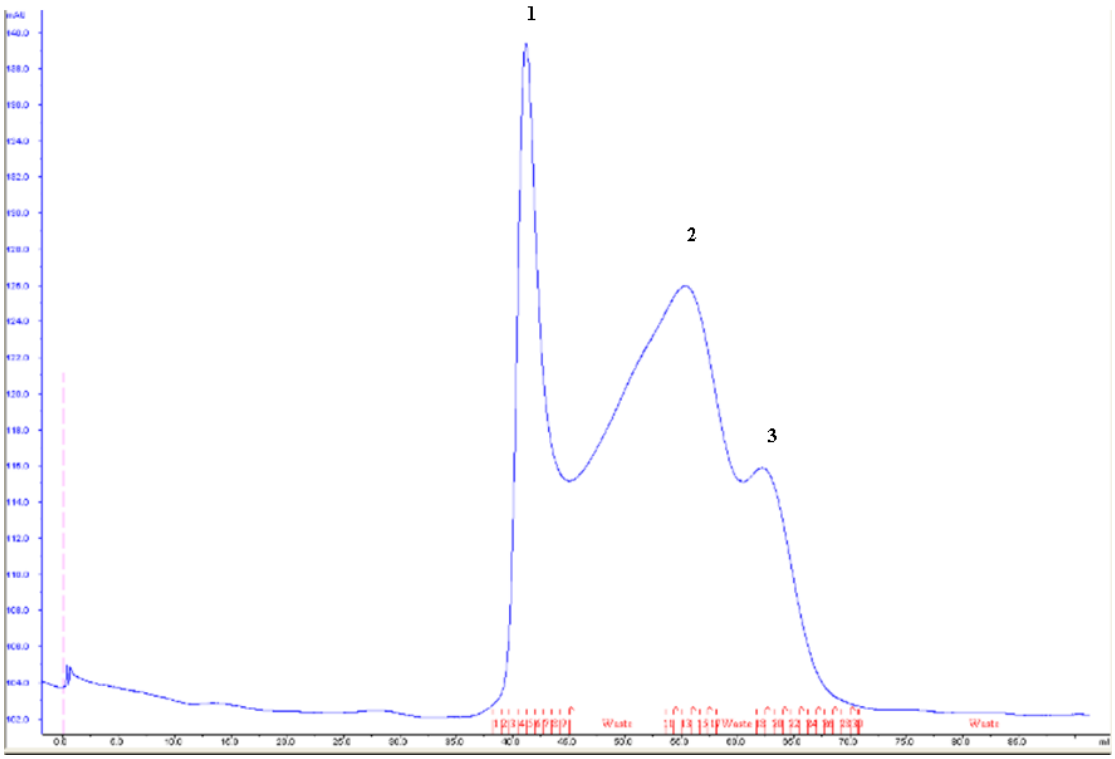

Figure S3. Elution of reassembled encapsulin/DypB mixture from Superdex 200 gel filtration. Elution volume from left to right, absorbance at 280 nm. Retention times: encapsulin/DypB complex, 9.5 min; DypB, 19.0 min.

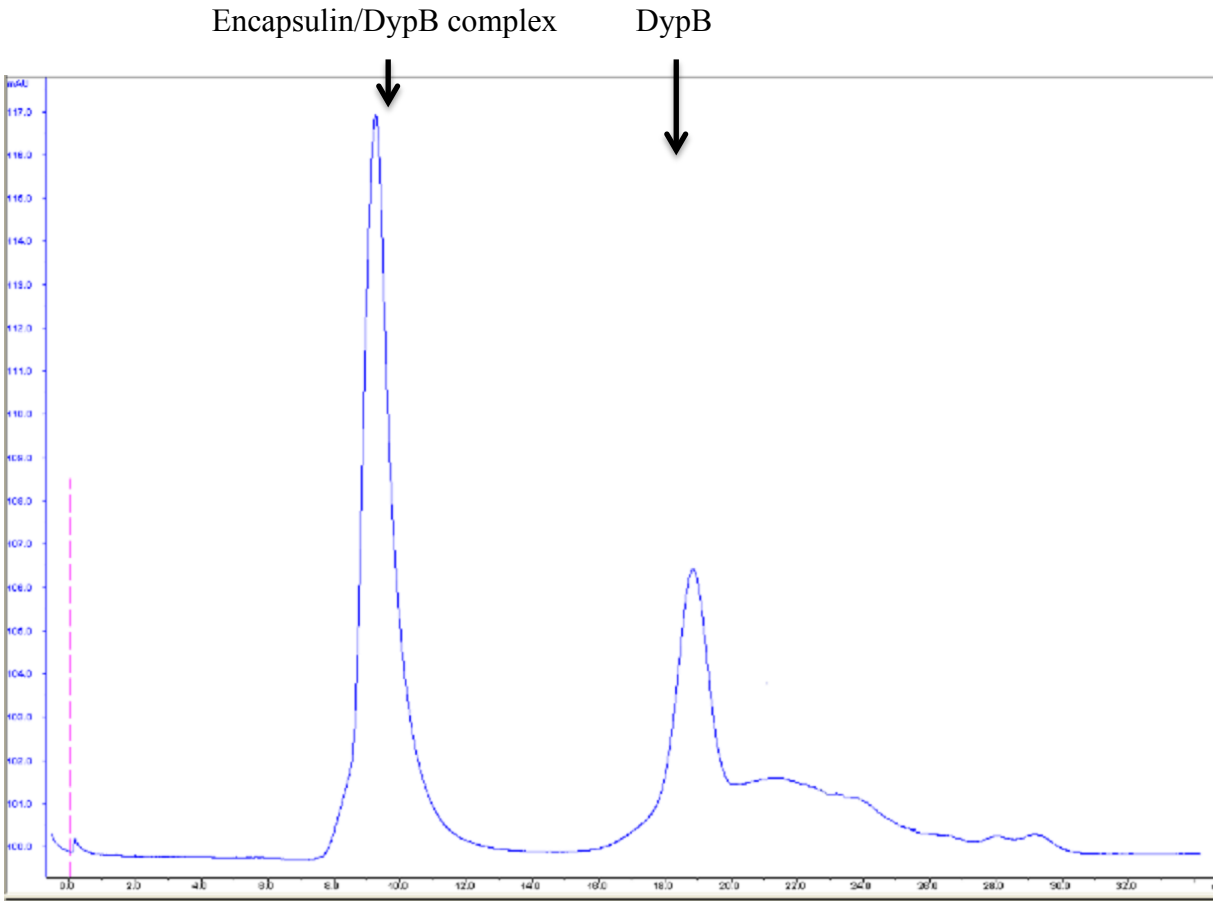

Archives of Biochemistry and Biophysics 574 (2015) 93–98

Contents lists available at ScienceDirect

Archives of Biochemistry and Biophysics

journal homepage: www.elsevier.com/locate/yabbi

Characterisation of Dyp-type peroxidases from *Pseudomonas fluorescens* Pf-5: Oxidation of Mn(II) and polymeric lignin by Dyp1B

Rahman Rahmanpour, Timothy D.H. Bugg *

Department of Chemistry, University of Warwick, Coventry CV4 7AL, UK

ARTICLE INFO

Article history:
Received 15 December 2014
and in revised form 19 December 2014
Available online 3 January 2015

Keywords:
Dye decolourising peroxidase
Lignin
Pseudomonas fluorescens

ABSTRACT

Members of the DyP family of peroxidases in Gram-positive bacteria have recently been shown to oxidise Mn(II) and lignin model compounds. Gram-negative pseudomonads, which also show activity for lignin oxidation, also contain dyp-type peroxidase genes. *Pseudomonas fluorescens* Pf-5 contains three dyp-type peroxidases (35, 40 and 55 kDa), each of which has been overexpressed in *Escherichia coli*, purified, and characterised. Each of the three enzymes shows activity for oxidation of phenol substrates, but the 35 kDa Dyp1B enzyme also shows activity for oxidation of Mn(II) and Kraft lignin. Treatment of powdered lignocellulose with Dyp1B in the presence of Mn(II) and hydrogen peroxide leads to the release of a low molecular weight lignin fragment, which has been identified by mass spectrometry as a β-aryl ether lignin dimer containing one G unit and one H unit bearing a benzylic ketone. A mechanism for release of this fragment from lignin oxidation is proposed.

Introduction

The aromatic heteropolymer lignin consists of 15–30% dry weight of the lignocellulose component of plant cell walls. Consisting of aryl-C3 units linked via carbon–oxygen ether and carbon–carbon bonds, lignin is not susceptible to hydrolytic breakdown, and is refractive towards degradation [1]. There is considerable interest in lignin valorisation to aromatic chemicals, since lignin represents a renewable and sustainable source of aromatic chemicals [2]. Microbial degradation of lignin has mainly been studied in basiodiomycete fungi such as *Phanerochaete chrysosporium*, which produces extracellular lignin peroxidase and manganese peroxidase enzymes that can attack lignin [1].

Although there were some reports that bacteria such as *Streptomyces viridosporus* could break down lignin [3], until recently the enzymology of bacterial lignin degradation was poorly understood [4]. A Dyp-type peroxidase enzyme DypB from *Rhodococcus jostii* RHA1 has been identified that can oxidise a β-aryl ether lignin model compound, and can attack Kraft lignin or wheat straw lignocellulose in the presence of Mn^{2+} [5]. The catalytic activity of *R. jostii* DypB has been enhanced by site-directed mutagenesis [6], and a further Dyp2 enzyme has been identified in *Amycolatopsis* sp. 75iv2 that has higher activity towards Mn^{2+} oxidation, and exhibits peroxidase activity against phenols, azo dyes, anthroquinone dyes [7].

A Dyp-type peroxidase enzyme, TfuDyP from *Thermobifida fusca*, a moderate thermophile bacteria, exhibits dye-decolourising activity and shows activity towards substrates such as guaiacol and 2,6-dimethoxyphenol [8]. TfuDyP can also catalyse enantioselective sulfoxidation, a type of reaction that had not been reported before for DyP-type peroxidases [8]. Recently two new-bacterial DyP-type peroxidases from *Bacillus subtilis* and *Pseudomonas putida MET94* were characterised kinetically and spectroscopically [9]. YfeX and EfeB, two *Escherichia coli* paralogs which belong to DyP-type peroxidase family, can catalyse the release of iron from heme without tetrapyrrole degradation, a reaction referred to as deferrochelation of the heme [10,11]. Kinetic data has shown that EfeB exhibits modest guaiacol peroxidase activity, so EfeB could be considered as a bi-functional enzyme [11]. The bacterial dye-decolourising peroxidase (Dyp)[1] family therefore represent an interesting class of enzymes for biotechnological application.

As well as Gram-positive actinobacteria such as *Rhodococcus* [12], *Streptomyces* [12], and *Microbacterium* [13], lignin degradation activity has been detected in Gram-negative aromatic degraders such as *P. putida* [12] and *Ochrobactrum* [13], but the enzymology of lignin oxidation in these organisms is unknown. In this paper we investigate three Dyp-type peroxidases from

* Corresponding author.
E-mail address: T.D.Bugg@warwick.ac.uk (T.D.H. Bugg).

[1] *Abbreviations used:* Dyp, dye-decolourising peroxidase; PMSF, phenylmethanesulfonylfluoride; DCP, 2,4-dichlorophenol; ABTS, 2,2′-azino-bis(3-ethylbenzothiazoline-6-sulphonic acid.

http://dx.doi.org/10.1016/j.abb.2014.12.022
0003-9861/

Gram-negative *P. fluorescens* Pf-5, and we identify a novel Dyp-type peroxidase as an enzyme capable of lignocellulose oxidation.

Materials and methods

Cloning and expression of Pseudomonas dyp peroxidases

Genomic DNA was extracted using the Wizard® Genomic DNA Purification Kit from Promega, from a total of 1 ml of overnight culture of *P. fluorescens* Pf-5 in Luria–Bertani broth. Forward and reverse primers were designed for the three dyp genes, and a CACC overhang was added to the forward primers at the 5′ end for the purpose of performing the TOPO cloning method. The designed primers for isolation of *dyp1B*, *dyp2B* and *dypA* are as following respectively: $_{5'}$C ACC ATG AGT TAC TAC CAG CCC GG$_{3'}$ and $_{5'}$TCA TTT CGA CGC TTG CAG CG$_{3'}$, $_{5'}$C ACC ATG ACC CAG CCG TCC TCC C$_{3'}$ and $_{5'}$CTA CAG GCC GGT GGG CGC$_{3'}$, $_{5'}$C ACC ATG AAC GAT TCA GAT CAG CCC$_{3'}$ and $_{5'}$TCA GGC AGT GCT TTT AGG TCG$_{3'}$. PCR reactions were carried using Platinum Pfx-DNA polymerase from Invitrogen, following the manufacturer's instructions. The amplified genes were cloned using the Champion™ pET 151 Directional TOPO® Expression Kit (Invitrogen) into expression vector pET151, and transformed into *E. coli* TOP10 competent cells (Invitrogen). The extracted plasmids from the obtained colonies were sent for sequencing in order to confirm the accuracy of the sequence and the ligation respectively. The sequencing results showed the amplified genes did not contain any mutations, and the ligated genes were in the correct orientation in the vector. The recombinant plasmids were then transformed into BL21 *E. coli* BL21 (Invitrogen), for protein expression. For expression of each recombinant gene, a 20 ml starter culture was grown in Luria–Bertani broth in the presence of 100 mg/ml ampicillin for 5 h at 37 °C, then added to 2 l Luria–Bertani broth for 3 h at 37 °C, and finally the cells were induced by adding 0.5 mM final concentration of IPTG and shaken overnight at 15 °C. Cell pellets were harvested by centrifugation at 4000*g*.

Enzyme purification

Protein purification was performed by metal affinity chromatography followed by TEV protease cleavage of the $(His)_6$ fusion tag. The harvested cells from a 2 l culture described above were suspended in 20 ml lysis buffer (50 mM NaH_2PO_4, 300 mM NaCl, 10 mM imidazole, pH 8.0) in the presence of 1 mM final concentration of PMSF (phenylmethanesulfonylfluoride). Cell lysis was carried out using a constant system cell disrupter, followed by centrifugation at 10,000*g* for 30 min. The clear supernatant was loaded onto a Ni-NTA resin FPLC column (HisTrap HP, 1 ml volume) equilibrated with lysis buffer, followed by 100 ml of wash buffer (50 mM NaH_2PO_4, 20 mM imidazole, 300 mM NaCl, pH 8.0), and the recombinant protein was eluted by 7 ml elution buffer (50 mM NaH_2PO_4, 250 mM imidazole, 300 mM NaCl, pH 8.0), eluting at a flow rate of 0.5 ml min^{-1}. A sample of eluted protein was taken for SDS PAGE and protein assay (using the BioRad Protein Assay kit), the remainder of solution was subjected to buffer exchange through a PD-10 column into 10 ml wash buffer (50 mM NaH_2PO_4, 20 mM imidazole, 300 mM NaCl, pH 8.0). After buffer exchange, the protein solution was mixed with previously purified TEV protease in equal molar ratio overnight in room temperature, then applied again to a Ni-NTA FPLC column, and eluted in elution buffer (50 mM NaH_2PO_4, 250 mM imidazole, 300 mM NaCl, pH 8.0). The flow-through fraction (25 ml) containing untagged recombinant DyP enzyme was collected. The purified enzyme was exchanged using a PD-10 column into 20 mM MOPS 80 mM NaCl buffer pH 7.0. 2.0 M equivalents of dissolved hemin in DMSO (25 mg ml^{-1}) were added to the protein solution. The mixture was incubated at room temperature for 2 h and then centrifuged at 10,000*g* to remove excess heme. The sample was subsequently passed through a PD-10 column equilibrated with MOPS 20 mM, 80 mM NaCl pH 7.0 and dialysed in the same buffer at 4 °C for overnight. The protein solution then was concentrated using a 10 kDa Amicon centricon device, and after flash freezing using liquid nitrogen, it was stored at −80 °C for further kinetic analysis.

Steady-state kinetic assays

All assays were performed at 25 °C in 100 mM acetate buffer pH 5.5 using a Cary spectrophotometer. Kinetic parameters (k_{cat} and K_M) were determined by nonlinear curve fitting to the obtained enzyme activity, using Graphpad prism 5 software, fitting to the Michaelis–Menten equation: $v_0 = v_{max}[S]/K_M + [S]$ where v_0 is the initial rate and [S] is the substrate concentration. All assays were performed in triplicate, and standard error determined from curve fitting.

Oxidation of DCP (2,4-dichlorophenol, concentration 10 μM–6 mM) was performed with 1 mM hydrogen peroxide, monitoring at 510 nm (ε_{510} = 18,000 M^{-1} cm^{-1}) [7]. Oxidation of ABTS (2,2′-azino-bis(3-ethylbenzothiazoline-6-sulphonic acid), concentration 25 μM–6 mM) was performed with 1 mM hydrogen peroxide, monitoring at 420 nm (ε_{420} = 36,000 M^{-1} cm^{-1}) [14]. Oxidation of Mn^{2+} was carried out using $MnCl_2$ (concentration 100 μM–6 mM) in 100 mM sodium tartrate buffer (pH 5.5) with 1 mM hydrogen peroxide, monitoring at 238 nm (ε_{238} = 6500 M^{-1} cm^{-1}) [15]. Oxidation of pyrogallol (concentration 25 μM-60 mM) was performed with 1 mM hydrogen peroxide, monitoring at 430 nm

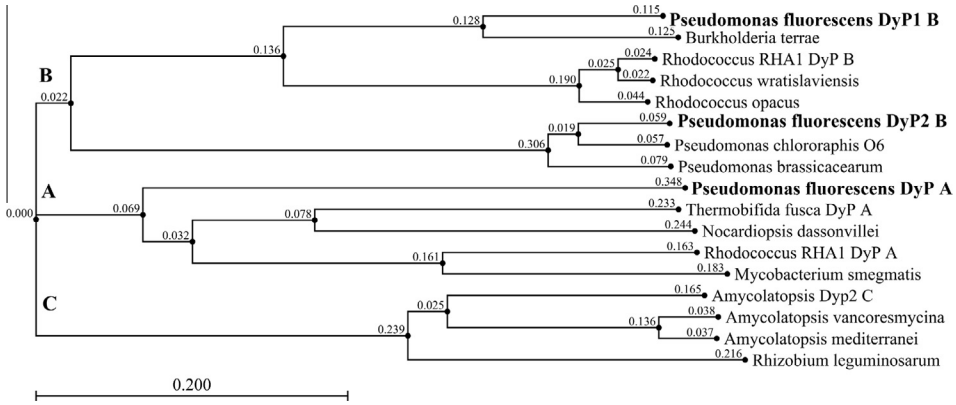

Fig. 1. Phylogenetic tree for *Pseudomonas fluorescens* Dyp sequences versus DypA, DypB and DypC enzymes, using CLC Main workbench 6.5 software.

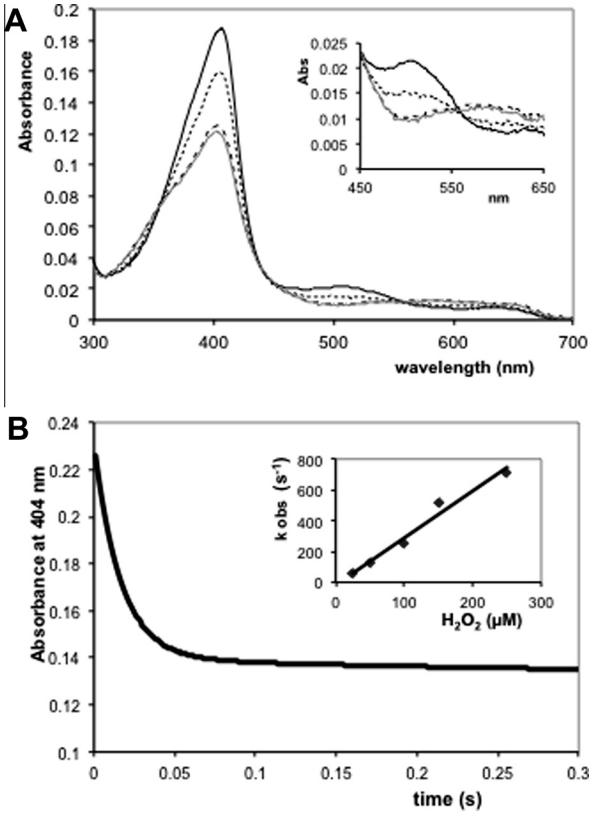

Fig. 2. Stopped flow kinetic data for *P. fluorescens* Dyp1B. (A) UV–visible spectrophotometric scans of reaction of Dyp1B with 1 mM hydrogen peroxide from 1 to 400 ms, showing Soret band at 406 nm (bold line, 1 ms), then transition after 4 ms (dotted line) and 40 ms (dashed line) to compound I peak at 402 nm (gray line, 400 ms). Inset shows new absorption at 550–600 nm. (B) Transient kinetic plot for absorbance at 404 nm. Inset shows plot of first order k_{obs} values for reaction with hydrogen peroxide against hydrogen peroxide concentration.

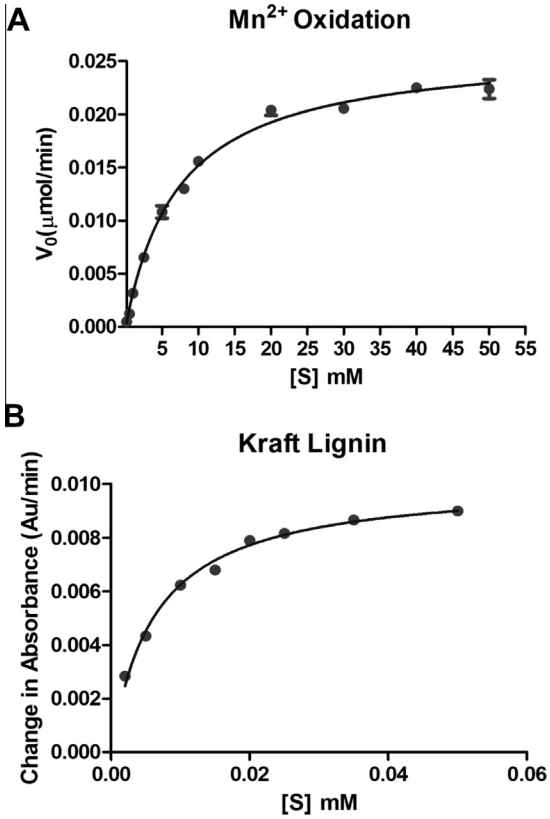

Fig. 3. Steady-state activity of *P. fluorescens* Dyp1B with (A) Mn^{2+} and (B) Kraft lignin.

(ε_{430} = 2470 M^{-1} cm^{-1}) [14]. Oxidation of guaiacol (concentration 2 μM–1 mM) was performed with 1 mM hydrogen peroxide, monitoring at 465 nm (ε_{465} = 26,600 M^{-1} cm^{-1}) [8]. Oxidation of phenol (concentration 100 μM–15 mM) was performed with 1 mM hydrogen peroxide, monitoring at 505 nm (ε_{510} = 7100 M^{-1} cm^{-1}) [16]. Decolourisation of Reactive Blue 4 (concentration 25–600 μM) was performed with 1 mM hydrogen peroxide, monitoring at 610 nm (ε_{610} = 4200 M^{-1} cm^{-1}) [14]. Oxidation of alkali Kraft lignin (Sigma–Aldrich, concentration 2–50 μM) was performed with 1 mM hydrogen peroxide, monitoring at 465 nm [5]. The molar concentration of Kraft lignin was calculated using an average molecular mass of 10,000 Da. The kinetic constants for hydrogen peroxide were determined using the ABTS assay, at 5 mM ABTS concentration, using 12 μM–1 mM concentration of hydrogen peroxide. All chemicals and biochemical were purchased from Sigma–Aldrich.

HPLC analysis

Powdered wheat straw lignocellulose (5 mg) was added to succinate buffer (3 ml, 50 mM, pH 5.5), and then DyP1B (100 μL, 1 mg/ml) was added, followed by H_2O_2 (1 mM) and $MnCl_2$ (1 mM). The resulting solution was incubated at 30 °C for 1 h. Aliquots (500 μL) were taken and reaction was stopped by adding

Table 1
Steady-state kinetic data for *P. fluorescens* Dyp peroxidase enzymes.

Substrate	Dyp1B			Dyp2B			DypA		
	K_M (mM)	k_{cat} (s^{-1})	k_{cat}/K_M (M^{-1} s^{-1})	K_M (mM)	k_{cat} (s^{-1})	k_{cat}/K_M (M^{-1} s^{-1})	K_M (mM)	k_{cat} (s^{-1})	k_{cat}/K_M (M^{-1} s^{-1})
ABTS	1.13 ± 0.1	13.5 ± 0.4	1.2×10^4	1.7 ± 0.2	10.2 ± 0.4	5.8×10^3	0.82 ± 0.1	23.1 ± 1.0	2.8×10^4
H_2O_2[a]	0.048 ± 0.02	23.3 ± 0.2	4.8×10^5	0.061 ± 0.005	9.2 ± 0.2	1.5×10^5	0.07 ± 0.003	35 ± 0.4	4.8×10^5
Mn^{2+}	7.3 ± 0.4	2.4 ± 0.1	3.3×10^2	1.7 ± 0.3	3.6 ± 0.2	2.1×10^3	NA	NA	NA
2,4-Dichlorophenol	1.25 ± 0.1	0.66 ± 0.02	5.3×10^2	0.4 ± 0.02	1.3 ± 0.02	3.2×10^3	4.8 ± 0.5	2.6 ± 0.1	5.4×10^2
Phenol	1.02 ± 0.08	1.22 ± 0.02	1.2×10^3	0.33 ± 0.02	0.78 ± 0.01	2.36×10^3	0.19 ± 0.02	0.14 ± 0.01	7.3×10^2
Guaiacol	0.056 ± 0.006	0.058 ± 0.001	1.0×10^3	NA	NA	NA	NA	NA	NA
Pyrogallol	4.0 ± 0.6	2.5 ± 0.1	6.2×10^2	10.2 ± 0.8	5.9 ± 0.3	5.8×10^2	11.6 ± 1.0	5.8 ± 0.2	4.9×10^2
Reactive Blue 4	0.12 ± 0.01	1.04 ± 0.03	9.0×10^3	NA	NA	NA	0.21 ± 0.02	1.90 ± 0.06	9.0×10^3
Kraft lignin[b]	0.006 ± 0.001	0.9 ± 0.1	1.4×10^5	NA	NA	NA	0.011 ± 0.001	1.18 ± 0.03	1.6×10^5

For K_M determinations, 1 mM H_2O_2 was used as co-substrate.
[a] For determination of K_M for H_2O_2, 2 mM ABTS was used as co-substrate.
[b] Assuming molecular weight of 10,000. NA, no activity observed.

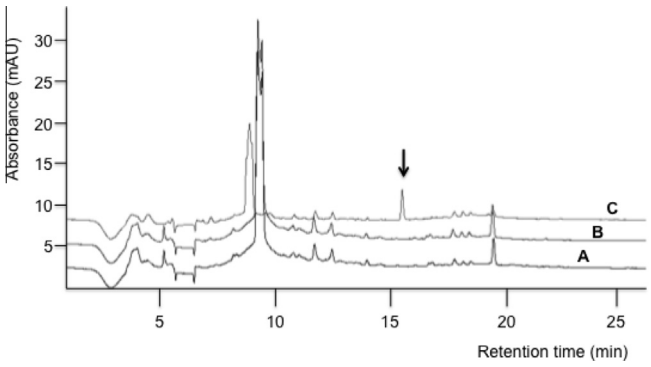

Fig. 4. Reverse phase HPLC analysis of *P. fluorescens* DyP1B incubation with wheat straw lignocellulose, 1 mM hydrogen peroxide and 1 mM $MnCl_2$ showing the formation of a new product peak at 15.6 min (trace C, product marked with arrow). Trace A shows a sample from a control incubation of wheat straw lignocellulose and hydrogen peroxide; trace B shows a sample from a control incubation in the absence of $MnCl_2$.

CCl_3COOH (100%, w/v, 40 μL) and the solution was then centrifuged for 5 min at 10,000 rpm. HPLC analysis was conducted using a Phenomenex Luna 5 μm C_{18} reverse phase column (100 Å, 50 mm, 4.6 mm) on a Hewlett–Packard Series 1100 analyser, at a flow rate of 0.5 ml/min, with monitoring at 310 nm. The gradient was as follows: 20–30% MeOH/H_2O over 5 min, 30–50% MeOH/H_2O from 5 to 12 min, and 50–80% MeOH/H_2O from 12 to 26 min.

Pre-steady state kinetic analysis

Stopped flow experiments were performed on an Applied Photophysics SX.18MV machine, at 25 °C in 100 mM acetate buffer pH 5.5, the concentration of enzyme was 5 μM for all of the enzyme-hydrogen peroxide titration experiments.

Results

Bioinformatic analysis of dyp-type peroxidases in P. fluorescens Pf-5

Bioinformatic searches using the BLAST algorithm in genomes of bacteria in the *Pseudomonas* genus revealed that *P. fluorescens* Pf-5 contains three sequences related to the Dyp family of peroxidase enzymes. As shown in Fig. 1, there is a 35 kDa enzyme (uniprot entry name of Q4KA97_PSEF5), DyP2B, which clusters in the DypB class of enzymes, and has 47% sequence similarity to *R. jostii* DypB. Secondly, there is a 47 kDa heme containing peroxidase (uniprot entry name of Q4KBM1_PSEF5), DyPA, which clusters in the DypA class of enzymes, which has 31.7% sequence similarity to *R. jostii* DypA. Thirdly, there is a 32 kDa enzyme (uniprot entry name of Q4KAC6_PSEF5), DyP1B, which clusters in a group of enzymes slightly distinct from the DypB enzymes, which has 21.4% sequence similarity to *R. jostii* DypB.

Analysis of the DyPs protein sequence shows the presence of conserved residues in the heme-binding site (see Supporting information, Fig. S13 for a sequence alignment). The presence of an aspartate residue replacing the classical distal histidine in a GXXDG motif is characteristic of all discovered DyPs so far [17]. The distal face of the heme interacts with three conserved residues; an aspartic acid (Asp-153 in *R. jostii* DypB), an arginine (Arg-244 in *R. jostii* DypB) and a phenylalanine (Phe-261 in *R. jostii* DypB). The proximal histidine (His-226 in *R. jostii* DypB), the fifth ligand to the heme iron, is also conserved in all of the DyP-type peroxidases. The conserved aspartate is part of the conserved GXXDG motif. Catalytic roles for the distal aspartate and arginine have been proposed based on the structural and mutagenesis studies [17,18]. The distal Asp acts as a proton shuttle in the formation of compound I from H_2O_2 and the arginine stabilizes the negative charge during the heterolytic cleavage of the peroxide group [17–19].

Expression and steady-state kinetic characterisation

Each *P. fluorescens dyp* gene was cloned as a $(His)_6$ fusion protein into the pET151 directional TOPO expression vector, and expressed in *E. coli* BL21 In each case, expression of soluble protein was observed by SDS–PAGE, although lower expression was found for DypA (see Supporting information, Figs. S1–S3). The recombinant enzyme was purified by nickel affinity chromatography, the $(His)_6$ tag removed by TEV protease cleavage, and the native recombinant protein repurified, yielding 30 mg, 26 mg and 5 mg of DyP1B, DyP2B and DyPA enzymes respectively from 2 l bacterial cultures. Since the purified protein was found to exist mainly as the apoprotein form, heme reconstitution was carried out by addition of heme in DMSO, as described in the Methods section. Appearance of a Soret band (at 406 nm for DyP1B, 404 nm for DyP2B, and 409 nm for DyPA, see Supporting information, Figs. S4–S6) indicated the presence of heme in the reconstituted holoenzyme after gel filtration. The observed Rz ratios, (A_{Soret}/A_{280}), obtained from the UV–visible spectra of reconstituted enzyme, were 1.76 for DyP1B, 1.42 for DyP2B, and 0.95 for DyPA.

Upon mixing with hydrogen peroxide over 1–2000 ms, the Soret band of Dyp1B at 406 nm decreased in intensity, with a slight wavelength shift to a new peak at 402 nm, and a less intense, broad UV–visible absorption at 550–600 nm (see Fig. 2A), corresponding to a compound I species similar to that observed for *R. jostii* RHA1 DypB [14]. This species was stable for >2 s as assessed by stopped flow kinetic measurement. Measurement of apparent rate constants for reaction of Dyp1B with varying concentrations of hydrogen peroxide (see Fig. 2B) gave a second order rate constant of $1.22 \times 10^5\ M^{-1}\ s^{-1}$, comparable to that observed for *R. jostii* RHA1 DypB [14].

Each enzyme was characterised using a range of peroxidase and lignin substrates, using UV–visible spectrophotometric assays, and K_M and k_{cat} values measured, as shown in Table 1 (original data shown in Supporting information, Figs. S7–S10). All three enzymes

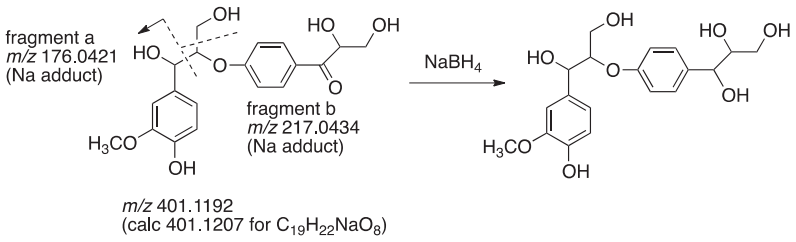

Scheme 1. Molecular structure of Dyp1B oxidation product, showing fragments observed by MS–MS analysis, and the structure of the reduced product after treatment with sodium borohydride.

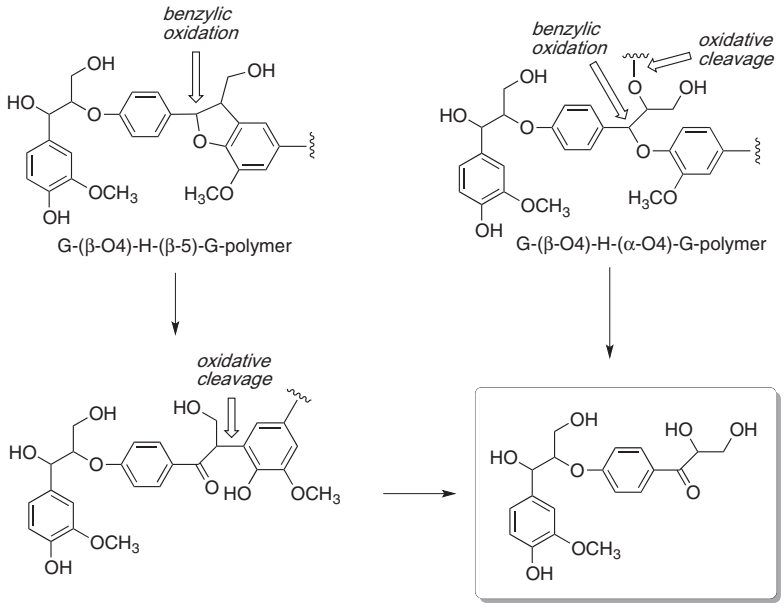

Fig. 5. Possible pathways for formation of DyPB1 product from lignin.

showed catalytic activity with peroxidase substrate ABTS, with k_{cat} values of 10.2–23.1 s^{-1}. Dyp1B and DypA were active with dye substrate Reactive Blue 4, characteristic of the Dyp family of peroxidases [8,17,20–23]. As shown in Fig. 3A, Dyp1B and Dyp2B showed catalytic activity for Mn^{2+} oxidation (k_{cat} 2.4–3.6 s^{-1}, k_{cat}/K_M 330–2100 M^{-1} s^{-1}), whereas DypA showed no activity for Mn^{2+} oxidation. All three enzymes were able to oxidise some phenolic substrates, less efficiently than ABTS, and only Dyp1B showed activity towards guaiacol.

When incubated with alkali Kraft lignin (Sigma–Aldrich), incubation with Dyp1B or DypA gave a time-dependent increase in absorbance at 465 nm (see Supporting information, Fig. S8), also observed previously using *R. jostii* DypB [5], and this absorbance change was found to show Michaelis–Menten kinetic behaviour (see Fig. 3B), implying that Dyp1B and DypA can oxidise Kraft lignin.

Oxidation of wheat straw lignocellulose by Dyp1B

Each peroxidase enzyme was incubated with powdered wheat straw lignocellulose, and product formation monitored by reverse phase HPLC. In the case of Dyp1B, in the presence of 1 mM $MnCl_2$, a visible colour change was observed (see Supporting information, Fig. S11), and time-dependent changes in the HPLC chromatogram were observed after half an hour incubation, and a significant new peak was observed at retention time 15.6 min, as shown in Fig. 4. The new peak was only formed in the presence of $MnCl_2$.

The peak at retention time 15.6 min was collected and analysed by electrospray mass spectrometry, giving a molecular ion at m/z 401.1192, matching molecular formula $C_{19}H_{22}NaO_8$ (calculated m/z 401.1207), consistent with a lignin fragment containing two aryl-C_3 units, containing one G unit and one H unit. MS–MS fragmentation of this species gave fragments at m/z 176.0421 and 217.0434 (see Supporting information, Fig. S12). As shown in Scheme 1, these two fragments are consistent with a molecular structure containing a β-aryl ether lignin dimer with a G unit linked via a β-ether linkage to the 4-*O*-position of an H unit bearing a benzylic ketone and β and γ hydroxyl groups. In order to seek further evidence for the presence of a benzylic ketone in this compound, a sample of this material was treated with an alkaline solution of sodium borohydride, resulting in the disappearance of the HPLC peak at 15.6 min, and the formation of a new peak at 15.0 min, with weaker absorbance (see Supporting information, Fig. S11). Analysis of this new species by mass spectrometry gave m/z 403, two mass units higher than the first species, consistent with reduction of a benzylic ketone to the corresponding alcohol. We therefore propose the structure shown in Scheme 1 for this product. Incubation with larger quantities of Dyp1B resulted in the disappearance of this species, implying that it can be further oxidised by this enzyme.

Conclusions

This study verifies that Gram-negative bacterial strains such as *P. fluorescens* also contain Dyp-type peroxidases that can oxidise lignin. There are homologues for Dyp1B that are found in many *Pseudomonas* strains, also in Burkholderia (e.g., *Burkholderia terrae* BS001, uniprot accession I5CHJ6), and in Bordetella (e.g., *Bordetella bronchiseptica* M85, uniprot accession A0A063K7X2). Unlike *R. jostii* RHA1 DypB, which is targeted to a 60-subunit encapsulin nanocompartment through a C-terminal targeting sequence [24], none of the *P. fluorescens* Dyp-type peroxidases showed a C-terminal targeting sequence, nor was an adjacent encapsulin gene present in the *P. fluorescens* Pf-5 genome.

By expressing and characterising the three *P. fluorescens* Dyp enzymes, we have identified *P. fluorescens* Dyp1B as lignin-oxidising enzyme. Comparing the activity of *P. fluorescens* Dyp1B with that of *R. jostii* DypB, both show activity for Mn(II) oxidation and Kraft lignin oxidation. The Mn(II) oxidation activity of *P. fluorescens* Dyp1B (k_{cat}/K_M 330 M^{-1} s^{-1}) is comparable with that of *R. jostii* DypB (k_{cat}/K_M 275 M^{-1} s^{-1}) [5], but not as high as *Amycolatopsis* sp. 75iv2 Dyp2 (k_{cat}/K_M 1.2 × 10^5 M^{-1} s^{-1}) [7], however, no lignin-oxidising activity was reported for the latter enzyme.

Both *R. jostii* DypB and *P. fluorescens* Dyp1B show time-dependent changes by HPLC when incubated with wheat straw lignocellulose, but uniquely, the *P. fluorescens* Dyp1B liberates a low molecular weight aromatic product from wheat straw lignocellulose. We have identified the molecular structure of this lignin fragment, which contains a G unit linked via a β-aryl ether linkage to an H unit containing a benzylic ketone. The benzylic ketone is

probably the site of oxidative cleavage from the lignin polymer. Two possible pathways for the formation of this product are shown in Fig. 5: the benzylic ketone could be formed from benzylic oxidation of an α-aryl ether linkage to the lignin polymer, or from oxidative cleavage of a phenylcoumarane (β-5) linkage.

The catalytic activities of these bacterial dyp-type peroxidases towards lignin, Mn(II) and a range of aromatic substrates further demonstrates the potential of Dyp peroxidases for biotechnological applications including lignin valorisation, and the potential of pseudomonads for conversion of lignin to aromatic products.

Acknowledgements

We thank the University of Warwick for the award of a Chancellor's International Scholarship to Rahman Rahmanpour, and we thank Dr. Derren Heyes (University of Manchester) for assistance with stopped flow kinetic measurements.

Appendix A. Supplementary data

Supplementary data associated with this article can be found, in the online version, at http://dx.doi.org/10.1016/j.abb.2014.12.022.

References

[1] D.W.S. Wong, Appl. Biochem. Biotechnol. 157 (2009) 174–209.
[2] J. Zakzeski, P.C. Bruijnincx, A.L. Jongerius, B.M. Weckhuysen, Chem. Rev. 110 (2010) 3552–3599.
[3] M. Ramachandra, D. Crawford, G. Hertel, Appl. Environ. Microbiol. 54 (1988) 3057–3063.
[4] T.D.H. Bugg, M. Ahmad, E.M. Hardiman, R. Singh, Curr. Opin. Biotechnol. 22 (2011) 394–400.
[5] M. Ahmad, J.N. Roberts, E.M. Hardiman, R. Singh, L.D. Eltis, T.D.H. Bugg, Biochemistry 50 (2011) 5096–5107.
[6] R. Singh, J.C. Grigg, W. Qin, J.F. Kadla, M.E.P. Murphy, L.D. Eltis, ACS Chem. Biol. 8 (2013) 700–706.
[7] M.E. Brown, T. Barros, M.C.Y. Chang, ACS Chem. Biol. 7 (2012) 2074–2081.
[8] E. van Bloois, D.E.T. Pazmino, R.T. Winter, M.W. Fraaije, Appl. Microbiol. Biotechnol. 86 (2010) 1419–1430.
[9] A. Santos, S. Mendes, V. Brissos, L.O. Martins, Appl. Microbiol. Biotechnol. 98 (2014) 2053–2065.
[10] S. Létoffé, G. Heuck, P. Delepelaire, N. Lange, C. Wandersman, Proc. Natl. Acad. Sci. 106 (2009) 11719–11724.
[11] X. Liu, Q. Du, Z. Wang, D. Zhu, Y. Huang, N. Li, T. Wei, S. Xu, L. Gu, J. Biol. Chem. 286 (2011) 14922–14931.
[12] M. Ahmad, C.R. Taylor, D. Pink, K. Burton, D. Eastwood, G.D. Bending, T.D.H. Bugg, Mol. Biosyst. 6 (2010) 815–821.
[13] C.R. Taylor, E.M. Hardiman, M. Ahmad, P.D. Sainsbury, P.R. Norris, T.D.H. Bugg, J. Appl. Microbiol. 113 (2012) 521–530.
[14] J.N. Roberts, R. Singh, J.C. Grigg, M.E.P. Murphy, T.D.H. Bugg, L.D. Eltis, Biochemistry 50 (2011) 5108–5119.
[15] F.J. Ruiz-Dueñas, M. Morales, M. Pérez-Boada, T. Choinowski, M.J. Martínez, K. Piontek, A.T. Martínez, Biochemistry 46 (2007) 66–77.
[16] S. Ghasempur, S.-F. Torabi, S.-O. Ranaei-Siadat, M. Jalali-Heravi, N. Ghaemi, K. Khajeh, Sci. Technol. 41 (2007) 7073–7079.
[17] Y. Sugano, Cell. Mol. Life Sci. 66 (2009) 1387–1403.
[18] Y. Sugano, R. Muramatsu, A. Ichiyanagi, T. Sato, M. Shoda, J. Biol. Chem. 282 (2007) 36652–36658.
[19] T.L. Poulos, J. Kraut, J. Biol. Chem. 255 (1980) 8199–8205.
[20] S.J. Kim, M. Shoda, Appl. Environ. Microbiol. 65 (1999) 1029–1035.
[21] H.J.O. Ogola, T. Kamiike, N. Hashimoto, H. Ashida, T. Ishikawa, H. Shibata, Y. Sawa, Appl. Environ. Microbiol. 75 (2009) 7509–7518.
[22] C. Liers, C. Bobeth, M. Pecyna, R. Ullrich, M. Hofrichter, Appl. Microbiol. Biotechnol. 85 (2010) 1869–1879.
[23] C. Zubieta, S.S. Krishna, M. Kapoor, P. Kozbial, D. McMullan, H.L. Axelrod, M.D. Miller, P. Abdubek, E. Ambing, T. Astakhova, D. Carlton, H.J. Chiu, T. Clayton, M.C. Deller, L. Duan, M.A. Elsliger, J. Feuerhelm, S.K. Grzechnik, J. Hale, E. Hampton, G.W. Han, L. Jaroszewski, K.K. Jin, H.E. Klock, M.W. Knuth, A. Kumar, D. Marciano, A.T. Morse, E. Nigoghossian, L. Okach, S. Oommachen, R. Reyes, C.L. Rife, P. Schimmel, H. van den Bedem, D. Weekes, A. White, Q. Xu, K.O. Hodgson, J. Wooley, A.M. Deacon, A. Godzik, S.A. Lesley, I.A. Wilson, Proteins 69 (2007) 223–233.
[24] R. Rahmanpour, T.D.H. Bugg, FEBS J. 280 (2012) 2097–2104.